Silicon-based Terahertz Circuits and Systems

Thesis by

Kaushik Sengupta

In Partial Fulfillment of the Requirements
for the Degree of
Doctor of Philosophy

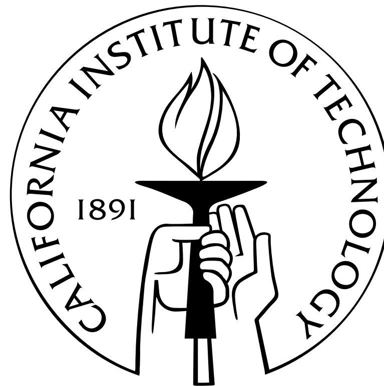

California Institute of Technology
Pasadena, California

2012
(Defended May 31, 2012)

© 2012
Kaushik Sengupta
All Rights Reserved

To Ma, Baba, Ipsita, Dada ...

Acknowledgements

Small perturbations in apparently insignificant events in life can lead to significant changes in future opportunities. My graduate life at Caltech and this thesis would not have come to fruition if this did not hold true.

Five years at Caltech have taught me many things. During my first year at Caltech, I remember past graduates from our lab telling me that one ages twice as fast during these years. As a person, I have evolved significantly and I owe it to these years spent at Caltech. Getting an undergraduate degree from IIT Kharagpur, one of the elite institutions in India, I (along with my majority of my colleagues) considered ourselves as thinking men and cared little for things that needed to get our hands dirty. My romantic vision of path-breaking graduate research consisted of a thinking man stumbling across a 'Eureka' idea. What was missing in that vision was the path that connected the two things together, which often consisted of mundane and routine work, maintaining a strong work ethic, reading and re-reading research papers, critiquing and challenging one's ideas, planning designs ahead of time to meet tape-out deadlines, making sure the design is robust and testable, making a test set-up and laborious hours spent in testing and verifying what may have started as an intellectual exercise on a fine summer afternoon, sipping coffee at Red Door. I cannot say that I have mastered the art, but I have tried and learnt, for sure. Caltech taught me to persevere. It taught me to roll up my sleeves when time comes and get things done, a hard-earned but priceless lesson. It taught me to appreciate work ethic, as much as a momentary flash of intellectual brilliance. Caltech also taught me to try and not play safe. At the end of five years, it has led me to believe, that no matter what, if I throw myself, heart and soul, and persevere, it would probably turn out to be ok and if not, then atleast a lesson learnt

and experience earned. Problems that make a difference are the problems worth solving. Caltech also taught me to appreciate excellence in all spheres of life. I have been fortunate to be a part of this academic institution, its legacy, culture and its people.

I am proud to have my academic genealogy begin stem from my advisor Prof. Ali Hajimiri. He has been more than a source of inspiration to me. There's only a fortunate fraction of students who find a philosophical resonance with their advisors. I belong to that privileged group. The professional world of integrated circuit design often turns on by record-breaking experimental performances of chips. I am indebted to have Ali as my advisor, who have inspired a deeper philosophical approach to research, one that stresses on innovation and long term impact. Beyond academics, I have always enjoyed long discussions on various topics, from philosophy, politics, travel, influences and life. He has always been given me freedom to choose my research topic, and fully supported in my pursuit. I am thankful to him for his encouragement and unreserved support in choosing my career path. I value his mentorship and friendship. He has taught me many a things, that will last a lifetime.

My gratitude goes to my thesis committee. Prof. Changhuei Yang, Prof. Azita Emami, Dr. Sandy Weinreb, Prof. Hyuck Choo and Prof. David Rutledge, who was unavailable for my Ph.D. defense examination, but served on my candidacy committee. Prof. Yang instilled the first seeds of interest in electromagnetics in his first year course, and since then I have been greatly influenced by his research work. I am indebted to Prof. Emami and Dr.Weinreb for their support in research and my career path. I have learnt a lot from my discussions with Prof. David Rutledge, who always gave insights into the problems. I am thankful Prof. Hyuck Choo for his words of advice and encouragement. I would like to specially thank Prof. Ehsan Afshari, Cornell University, for his uninhibited support in research and career.

I would like to acknowledge IBM and UMC for providing fabrication support and IBM for PhD fellowship support. This work was supported partly by the Air Force Research Laboratory.

Part of what makes Caltech a great place to do research is this open environment of exchange of ideas, total absence of bureaucracy and boundaries among various divisions. I

have benefited from the generosity of research labs in Astronomy, Biology to Geology and Planetary Sciences. While setting up a terahertz laboratory, I quickly realized the scarcity of instruments existing in this frequency ranges and the delay and expense in procuring from the few existing vendors. A long chain of email exchanges finally led me to Prof. Zmuidzinas's research lab in Astrophysics and Prof.Blake's laboratory in Geology and Planetary Sciences, who had exactly the instruments I was looking for, lying unused for the moment. I am really thankful to Prof.Zmuidzinas, David Miller, Prof. Blake and Mathew Kelley for letting me borrow the equipment for initial testing. I would also like to acknowledge Prof.Oscar Painter, Applied Physics, who was gracious enough to let me use his equipment. Dr.Peter Siegel has been instrumental in my research work and I am indebted to him for his advice in technical matters and his help in measurement set-ups. This work could have been possible without the generous support of Dr.Siegel and his lab at JPL. I also appreciate my discussions with Prof. Kerry Vahala (Department of Applied Physics), Prof. Scott Fraser and Prof. Ellena Rothenberg (Division of Biology) and Prof.Mark Davis (Department of Chemical Engineering). Prof.P.P.Vaidyanathan has never been short of words of encouragement everytime I meet him at the corridors of Moore and I am grateful to him for that.

My foray into cutting-edge research happened during my undergraduate summer internship days under Prof. Hossein Hashemi, University of Southern California and Prof. Anantha Chandrakasan, MIT and I am thankful to them for their support and encouragement. I made many a friends during my internship days and I would like to thank all of them, specially Harish, Ankush and Ta-shun. I would like to thank all the Prof.T.K.Bhattacharyya and all the professors at IIT Kharagpur, who have contributed significantly in my personal and professional growth.

Graduate life is often painstaking, and would have been impossible to survive if not for my well-wishers and friends. I thank Steve and Kaushik (K_2) for their friendship. The memories of board games, conference travels, Mt.Wilson hike and other 'extravaganzas' will remain forever. Juhwan remains a special friend and a constant companion during sleepless tapeout nights. Kaushik and Bose have been partners-in-crime in many a occasion and I am specially thankful to them. Alex has been an amazing officemate and his zest for starting companies

(mostly imaginary) is infectious. I would like to thank the current and past members of the Caltech High-Speed Integrated Circuits Group lab, specially Amir, Costis, Stephen, Behrooz, Firooz, Hua Wang, Yu-Jiu Wang, Florian Bohn, Aydin Babakhani, Edward Keehr, Joe Bardin, Sho, Tomoyuki Arai, Jay Chen and also members of the MICS group specially Matt, Mayank, Meisam and Manuel and Saman. Hua and Yu-Jiu have been great friends and I thank them for their support. I have had the privilege of co-advising two awesome undergraduate students in Dongjin Seo and Lita Yang and their contribution to this work is immense. No word of thanks is enough for our group administrator Michelle, and department administrators Tanya and Carol, who have been awesome. I would also like to thank Hamdi Mani and Hectar for their help.

A tip of hat to my good friends Palash, Debaojyoti, Iram, Ilona, Teja, Uday, Calyani, Sujit, Pinkesh, Piya, Bharat, Hemanth, Briton for all the good times during graduate school. I owe special thanks to my best friends from undergraduate days, Rajat, Gaurav, Rachit, SSG and Varun. I have had the fortune of having friends for life in Akash, Shishu and Debarshi: *Thanks for everything.*

Finally and most importantly, I would like to thank my parents for their unconditional love and support for everything and much more. I thank Dada and Rohan for being the best brothers, and my grandparents Dadai, ChotoMunna, Amma, Budhha, BoroMunna, who shaped me as a person and taught many things, that shall last my life. Successful graduate research requires collective sacrifices from many a people and no one probably understands this more than my wife, Ipsita. I cannot thank her enough for her support and being on my side for all these years. Sometimes, it never felt that we were two souls separated by 12,000 miles on two opposite of the globe.

Abstract

The Terahertz frequency range, often referred to as the 'Terahertz' gap, lies wedged between microwave at the lower end and infrared at the higher end of the spectrum, occupying frequencies between 0.3-3.0 THz. For a long time, applications in THz frequencies had been limited to astronomy and chemical sciences, but with advancement in THz technology in recent years, it has shown great promise in a wide range of applications ranging from disease diagnostics, non-invasive early skin cancer detection, label-free DNA sequencing to security screening for concealed weapons and contraband detection, global environmental monitoring, nondestructive quality control and ultra-fast wireless communication. Up until recently, the terahertz frequency range has been mostly addressed by high mobility compound III-V processes, expensive nonlinear optics, or cryogenically cooled quantum cascade lasers. A low cost, room temperature alternative can enable the development of such a wide array of applications, not currently accessible due to cost and size limitations. In this thesis, we will discuss our approach towards development of integrated terahertz technology in silicon-based processes. In the spirit of academic research, we will address frequencies close to 0.3 THz as 'Terahertz'.

In this thesis, we address both fronts of integrated THz systems in silicon: THz power generation, radiation and transmitter systems, and THz signal detection and receiver systems. THz power generation in silicon-based integrated circuit technology is challenging due to lower carrier mobility, lower cut-off frequencies compared to compound III-V processes, lower breakdown voltages and lossy passives. Radiation from silicon chip is also challenging due to lossy substrates and high dielectric constant of silicon. In this work, we propose novel ways of combining circuit and electromagnetic techniques in a holistic design

approach, which can overcome limitations of conventional block-by-block or partitioned design methodology, in order to generate high-frequency signals above the classical definition of cut-off frequencies (f_t/f_{max}). We demonstrate this design philosophy in an active electromagnetic structure, which we call Distributed Active Radiator. It is inspired by an Inverse Maxwellian approach, where instead of using classical circuit and electromagnetic blocks to generate and radiate THz frequencies, we formulate surface (metal) currents in silicon chip for a desired THz field profile and develop active means of controlling different harmonic currents to perform signal generation, frequency multiplication, radiation and lossless filtering, simultaneously in a compact footprint. By removing the artificial boundaries between circuits, electromagnetics and antenna, we open ourselves to a broader design space. This enabled us to demonstrate the first 1 mW Effective-isotropic-radiated-power(EIRP) THz (0.29 THz) source in CMOS with total radiated power being three orders of magnitude more than previously demonstrated. We also proposed a near-field synchronization mechanism, which is a scalable method of realizing large arrays of synchronized autonomous radiating sources in silicon. We also demonstrate the first THz CMOS array with digitally controlled beam-scanning in 2D space with radiated output EIRP of nearly 10 mW at 0.28 THz.

On the receiver side, we use a similar electronics and electromagnetics co-design approach to realize a 4x4 pixel integrated silicon Terahertz camera demonstrating to the best of our knowledge, the most sensitive silicon THz detector array without using post-processing, silicon lens or high-resistivity substrate options (NEP $<$ 10 pW/$\sqrt{Hz}$ at 0.26 THz). We put the 16 pixel silicon THz camera together with the CMOS DAR THz power generation arrays and demonstrated, for the first time, an all silicon THz imaging system with a CMOS source.

Contents

Acknowledgements **iv**

Abstract **viii**

1 Introduction **1**

1.1 Contributions . . . 5

1.2 Organization . . . 6

2 The Terahertz Gap: Current THz Technology **8**

2.1 THz Application Space . . . 8

2.2 Current THz Technology . . . 12

2.2.1 Optics-based Technology . . . 13

2.2.2 Solid-State Electronic and Custom Technologies . . . 14

3 Distributed Active Radiation: THz Power Generation in Silicon **17**

3.1 High-Frequency Limitations of DC-RF Power Conversion and Extraction . . 18

3.1.1 DC-RF Power Conversion Below f_{max} . . . 19

3.1.2 Power Generation Above f_{max} . . . 24

3.1.3 High-Frequency Power Extraction from Silicon . . . 27

3.2 Inverse of Maxwell's Law: A Reconfigurable Electromagnetic Surface and Design Evolution of Distributed Active Radiator . . . 32

3.2.1 Conceptual Synthesis of Fundamental and Harmonic Surface Currents in Silicon . . . 35

3.2.2 Active Control of Currents for the Desired Harmonic Radiation . . . 35
3.2.3 Radiative Mechasim for the Desired Harmonic Radiation 38
3.2.4 Active Control of Currents for End-to-End DC-THz Conversion . . . 41
3.2.5 Design, Simulation and Optimization 43
3.2.6 Electromagnetic Simulations 48

4 Electromagnetic Field Analysis 51

4.1 A Hertzian Dipole in a Dielectric with Finite Thickness 54
4.1.1 Far-Field Radiation Pattern and Radiated Power 61
4.1.2 Surface-Wave Fields and Trapped Power 63
4.2 Traveling-Wave Circular Radiator on a Grounded Substrate 71
4.2.1 Surface-Wave Power Suppression in TE Mode 72
4.2.2 Surface-Wave Power in TM Mode 75
4.2.3 Total Radiated Power and Radiation Efficiency 76
4.3 Distributed Active Radiator: Two Traveling-Wave Loops 81
4.4 Arrays of Traveling-wave Loops: Remaining Surface-Wave Suppression . . . 82
4.4.1 Arrays of Hertzian Dipoles in Free-Space 83
4.4.2 Arrays of Traveling-Wave loops: Suppression of Remaining Surface-Wave Power 86

5 Coupled THz Arrays in CMOS 91

5.1 Free-Space Power Combining and Beam-Scanning 93
5.2 Synchronizing Arrays of Distributed Active Radiators 95
5.3 Transmission-Line Coupling 96
5.4 Near-Field Synchronization 101
5.4.1 Sensing the Near-Field 102
5.4.2 Mutual Locking and Electronic Beam-Scanning 105
5.4.3 Frequency Locking Range and Beam-Scanning Analysis 108
5.4.4 Stability Analysis of Near-Field Coupling Mechanism 114

5.5 Design and Implementation 118
5.6 Measurement Results 119
5.6.1 0.3 THz DAR Arrays in 45 nm CMOS 123
5.6.2 0.2 THz DAR Arrays in 65 nm Bulk CMOS 125

6 Integrated 4x4 Power-Generation and Beam-Scanning Array in CMOS at 0.28 THz 132
6.1 THz Beam-Scanning Architecture 132
6.2 Transmitter Circuit Blocks 135
6.2.1 94 GHz Voltage-Controlled Oscillator and Buffers 135
6.2.2 47 GHz Injection-Locked Divide-by-Two 136
6.2.3 47 GHz Phase Rotator 140
6.2.4 141 GHz Injection-Locked Frequency Tripler 141
6.3 Measurement Results 142
6.3.1 Central VCO and the Buffers 143
6.3.2 Quadrature Signal Generation and Phase Rotation 147
6.3.3 Array Measurement 147

7 Multipixel Terahertz Camera in Silicon 155
7.1 Integrated 4x4 Pixel THz Camera in SiGe BiCMOS 157
7.1.1 Architecture, Integrated Antenna, Detector and Baseband 158
7.2 Measurement Results at Room Temperature 163
7.3 All-Silicon THz Imaging 174

8 Robust and Self-Healing High-Frequency Integrated Systems 177
8.1 Sensors 181
8.1.1 DC Current Sensors 181
8.1.2 Input and Output True RF Power Sensing 183
8.1.3 Local Temperature Sensing to measure PA Efficiency 185
8.2 Actuators 187

8.3 Digital Algorithm . . . 188
8.4 Measurement Results Demonstrating Healing . . . 188

9 Other Work **193**
9.1 Power Combining . . . 194
9.1.1 Importance of Power Combining . . . 194
9.1.2 Efficient Power Combining . . . 196
9.2 Architecture and Amplifier Design . . . 197
9.3 Measurement Results . . . 199

10 Conclusion **202**

11 Appendix **204**
11.1 On the possibility of false locking . . . 204
11.2 Derivation of State Equations in the transformed domain for stability analysis 205
11.3 Derivation of linearized state space matrix for stability analysis . . . 206

Bibliography **208**

Bibliography **209**

List of Figures

1.1 The electromagnetic spectral range from low-frequency radio waves to high energy gamma-rays [7]. 3

1.2 A femtosecond-laser based broadband Terahertz system [5]. The photo on the right hand side is the first THz CMOS beam-scanning power generator. [59] . 4

2.1 Molecular transitions in the THz spectrum [13]. 9

2.2 Absorption (α) and refractive indices (n) of tissues at 0.5 and 1 THz [13]. . . 10

2.3 Reflection-based THz image showing strong correlation between acquired image and histological results. The images show tumor tissues with surrounding adipose tissues [24]. 10

2.4 A quasi-three-dimensional image of a transverse slice of a human tooth constructed using depth information from time of flight. Labels E, D and P represent the enamel, dentine and pulp, respectively [13]. 11

2.5 THz absorption spectra of RDX, TNT, HMX. and PETN obtained with THz-TDS [31]. 11

2.6 Solid-state electronics and optics-based THz sources and their typical power output [3]. 13

2.7 Photoconductive-based broadband pulse generation using ultrafast lasers [13]. 14

2.8 CW-wave sources can be generated by beating two CW lasers in nonlinear medium. The right part of the figure shows quantum-cascade-lasers which are powerful narrowband sources but require cryogenic cooling. [3]. 14

2.9 THz broadband time-domain spectroscopy based on photoconductive generation and detection [7]. 15

2.10 A 300 GHz transmitter and a 300 GHz receiver system from Virginia Diodes, Inc. [35] . . . 16
2.11 Silicon-based Terahertz imaging system. . . . 16

3.1 Silicon-based Terahertz imaging system. . . . 17
3.2 Desired high-efficiency conversion from DC power into the chip to THz signals out of the chip. The figure also shows extrapolated plots of high-frequency figures of merits of projected silicon technology. . . . 19
3.3 A physical layout of a MOSFET with four fingers in parallel, showing layout parasitics. . . . 20
3.4 Small signal equivalent model for power gain derivation. . . . 21
3.5 A 2-port S-pamareter model of the gain element. The figure also shows simulated maximum available gain G_{max} and Mason's Invariant U for a 8 µm-wide transistor (1 µm-wide finger) under optimum biasing conditions. Both measures of power gain fall to unity at a frequency of f_{max} near 0.2 THz. . . . 25
3.6 Nonlinear transconductance and capacitance are can be exploited to generate harmonic power above f_{max}. In such a nonlinear dynamical system, output loading needs to be optimized for different harmonics for maximum conversion efficiency. . . . 25
3.7 Variation of second-harmonic power at 300 GHz with the output load consisting of R_L in parallel with L_L. . . . 26
3.8 Chain of conversion from DC to signals at frequencies above f_{max}, consisting of cascaded chain of classical functional elements with tuned matching networks. 29
3.9 Wirebonds and flip-chip interconnects are typical ways of transferring signals out of a chip at frequencies up to few tens of GHz. . . . 29
3.10 Typical cross section of silicon chip consisting of back-end-of-line metal layers and nearly 250–300 µm of lossy doped silicon ($\rho \sim 10$ Ω.cm.) . . . 31

3.11 On-chip antennas on high-dielectric silicon substrate can excite strong surface waves, which either get lost or leaks out in unpredictable ways. An off-chip silicon lens can convert the surface modes into radiative modes, by eliminating total-internal reflections in the planar substrate. 31
3.12 Partitioned approach follows the Divide-and-rule design philosophy. Specifically, for the problem at hand, it separates system design into electromagnetics and circuits, each of which consists of locally optimized standard functional blocks. 32
3.13 Inverse of Maxwell's principle: Formulate the surface currents required to generate a far-/near-file profile and actively synthesize the surface currents with a combination of actives and passives. We remove the artificial between among circuits, electromagnetics, antenna and expand the design space beyond the classical partitioned or block-by-block approach. 34
3.14 Conceptual synthesis of fundamental and harmonic currents for free-space filtering of the fundamental signal and efficient radiation of the desired second harmonic signal. 36
3.15 Second harmonic current pumped in the appropriate phase progression to maintain in-phase traveling and radiating waves in two adjacent loops. 37
3.16 Second harmonic currents above f_{max} are generated from nonlinearities in conductance and capacitance in transistors. 37
3.17 Pseudo-differential pairs driven strongly at the fundamental frequency to create in-phase second harmonic currents pumped into the distributed radiating loops. 38
3.18 The second harmonic return current from the actives channelized through a ground plane. The return currents on the ground are out-of-phase with the forward currents on the loop canceling most of the radiated fields. 39
3.19 The second harmonic return current from the actives channelized through a longer path through a ground aperture plane, creating a 90° phase difference between forward and return path. The radiated fields of two concentric loops add in quadrature in free-space, creating efficient radiation out of the chip. . . 39

3.20 The traveling-wave nature of the currents creates circularly polarized radiation coming out form the backside of the silicon die (ε_r=11.7). 40
3.21 Distributed active radiator: Electromagnetic structure strongly coupled with actives achieving signal generation from DC, frequency multiplication, efficient radiation of desired harmonic and free-space filtering of undesired harmonic simultaneously. 42
3.22 The electromagnetic simulation structure of DAR with 8 ports. Harmonic currents are designed to flow in such a way that each transistor, in the cross-coupled pair, sees a resonator at the fundamental frequency and a radiative impedance at the second harmonic. 45
3.23 A push-push oscillator with an antenna connected at the common-mode point can channelize the second harmonic-current ($2f_0$) to radiate out, after suffering losses in the resonator. In a DAR, the resonator is transparent to the second harmonic current I_{2f0}. Due to the manipulation of surface currents, the same electromagnetic structure behaves like a radiator, and therefore, the second harmonic power gets immediately radiated out instead of suffering losses in the passives. 47
3.24 Instantaneous current configurations at the fundamental frequency showing the forward and return currents on the loops, and almost no current in the ground plane structure. 48
3.25 Instantaneous current configurations at the radiated second harmonic frequency showing in-phase currents on the loops, and near 90° phase-shifted currents in the ground plane structure. 49
3.26 Magnitude of E-field a $2f_0$ in the y-z/x-z plane. The right part shows instantaneous E-field in the y-z plane for the current configuration shown in Fig. 3.25. 49
3.27 Magnitude of H-field a $2f_0$ in the x-z/y-z plane. The right part shows instantaneous H-field in the x-z plane for the current configuration shown in Fig. 3.25 50
3.28 Radiation patterns for DARs in a 0.4 mm x 0.4 mm lossy silicon ($\rho \sim 10$ Ω.cm) for different substrate heights. 50

4.1 An infinitesimal Hertzian dipole in free-space. The radiation patterns in the E and H planes are shown. 51
4.2 An infinitesimal Hertzian dipole at the interface of two dielectrics, air ($\varepsilon_{r,air} = 1$) and a lossless dielectric (with $\varepsilon_{r,diel} = 4.0$). The radiation patterns in the E and H planes are shown [72]. 52
4.3 An infinitesimal Hertzian dipole placed on a semi-infinite dielectric with finite thickness (h). A major fraction of the radiated power can remain trapped in the dielectric as surface waves. 53
4.4 Surface wave patterns in TE and TM modes for an infinitesimal Hertzian dipole placed on a semi-infinite dielectric with finite thickness. 55
4.5 Analytically predicted and electromagnetically simulated E-plane pattern for a Hertzian Dipole for different substrate thicknesses. The substrate of choice is lossless silicon ($\varepsilon_r = 11.7$). 63
4.6 Analytically predicted and electromagnetically simulated H-plane pattern for a Hertzian Dipole for different substrate thicknesses. The substrate of choice is silicon ($\varepsilon_r = 11.7$). 64
4.7 Cylindrical surface wave power excited by a dipole in a semi-infinite grounded substrate. 65
4.8 Total surface wave power broken down into its different modes and the total radiated power for a Hertzian dipole for different substrate thicknesses. 69
4.9 Constituent surface-wave power for different frequencies at a given substrate thickness of h=220 µm and at a frequency of 300 GHz. 70
4.10 Radiation efficiency of a Hertzian dipole against different substrate thicknesses. 70
4.11 Radiation efficiency of a Hertzian dipole against frequency for h= 220 µm. . . 71
4.12 Traveling-wave circular geometries allowing suppression of the trapped power through partial cancelation of the surface-waves. 72
4.13 Variation of TE_0 power suppression with radius of the loop. 74
4.14 TE wavelength variation with substrate thickness. 75
4.15 TM wavelength variation with substrate thickness. 76

4.16 Variation of TM_1 power suppression with radius of the loop. 77
4.17 Total surface wave power broken down into its different modes and the total radiated power for a traveling-wave loop for different substrate thicknesses. The plot shows almost complete suppression of the TE_0 mode. 78
4.18 Constituent surface-wave power for different frequencies at a given substrate thickness of h = 220 µm and at a frequency of 300 GHz. The plot shows almost complete suppression of the TE_0 mode. 79
4.19 Radiation efficiency of traveling-wave loop against different substrate thicknesses. 79
4.20 Analytically predicted and electromagnetically simulated pattern at any constant ϕ plane, for a traveling-wave circular loop of current for different substrate thicknesses. The substrate of choice is silicon ($\varepsilon_r = 11.7$) 80
4.21 Traveling-wave model of a DAR with two concentric traveling-wave current loops separated in phase by $\pi/2$. 81
4.22 Two identical Hertzian dipoles in free-space. 83
4.23 Ratio of total power radiated by a dipole pair to the sum of the individual pair for the configuration in Fig. 4.22. 85
4.24 Two identical Hertzian dipoles in free-space separated along the perpendicular axis. 86
4.25 Ratio of total power radiated by a dipole pair to the sum of the individual pair for the configuration in Fig. 4.24. 87
4.26 2x2 arrays of DARs to suppress TM_1 mode. 87
4.27 Total surface wave power broken down into its different modes and the total radiated power for 2x2 arrays of traveling-wave loops, separated by $d \sim \lambda_{TM1}/2$, for different substrate thicknesses. The plot shows almost complete suppression of the TE_0 and TM_1 modes. 88
4.28 Radiation efficiency of 2x2 arrays of traveling-wave loops, separated by $d \sim \lambda_{TM1}/2$, against different substrate thicknesses. 89
4.29 Radiation efficiency of 2x2 arrays of traveling-wave loops, separated by $d \sim \lambda_{TM1}/2$, against frequency. 89

4.30 Radiated and suppressed surface wave powers for different element spacings. 90

4.31 Analytically predicted and electromagnetically simulated radiation patterns for 2x2 arrays of traveling-wave loops, separated by $d \sim \lambda_{TM1}/2$. 90

5.1 A single Distributed Active Radiator converts DC power into THz power and radiates with a broad beam 92

5.2 Arrays of Distributed Active Radiators can be synchronized to radiate higher power with narrower beam and potentially enabling electronic beam-scanning. 92

5.3 Linear antenna array for power combining and electronic beam-scanning. . . . 93

5.4 Mutual coupling between free-running oscillators synchronizing each other (a). One central frequency reference unilaterally locking multiple autonomous oscillatory elements (b). 95

5.5 Transmission-line based coupling to synchronize two Distributed Active Radiators. 97

5.6 Transmission-line coupling network providing DC power supply. Under locked condition, it presents open-circuit impedances at both fundamental (f_0) frequency as well as at the radiated second harmonic frequency ($2f_0$). 98

5.7 Cross section of the t-line in Fig. 5.5 implemented in 45 nm SOI CMOS process, showing instantaneous electric and magnetic field lines. 99

5.8 The impedance seen by each DAR, under synchronized condition, against frequency. The network provides open-circuit impedances at the designed oscillation frequency of 150 GHz and at the eradiated frequency of 400 GHz. 99

5.9 T-line-based coupling networks required for coherent synchronization of 2x2 arrays of DARs. 100

5.10 Sense antenna picks up the radiated fields of free-running radiating sources and carries the information of phase and frequency of the oscillator cores. If the sense antennas are suitably coupled, the radiated fields will equalize, forcing the oscillators to lock to each other. 101

5.11 The second harmonic current with time rotates about the broadside axis leading to constant magnetic flux through the sense antenna aperture. The sense antenna, therefore, is transparent to the second harmonic radiation. 103
5.12 The out-of-phase fundamental frequency currents in the two branches do not cancel their fields in the near-field region, leading to a periodically changing flux at the fundamental frequency. The sense antenna, therefore, picks up signal only at the fundamental frequency. 103
5.13 Near-field synchronized 2x1 DAR. Coupling network between the sense antenna terminals ensures that no power is dissipated when the sources are synchronized, making it the most stable and lowest energy state. 106
5.14 Optimum value of coupling resistors to maximize locking range. 107
5.15 Two sets of synchronized 2x1 array locked together with two more sense antennas to form 2x2 array of locked DARs. The frequency tuning using varactor enables beam-steering through the synchronization network. 108
5.16 The bias network of each distributed active radiator. The bias network provides open-circuit at both the fundamental frequency of f_0 and the desired radiated second harmonic at $2f_0$, so as to not load the DAR operation. 109
5.17 Injection locking in a self-sustained oscillator and its nonlinear modeling. . . . 110
5.18 Die photos of 2x1 and 2x2 arrays of DARs, synchronized with t-line networks, operating at 0.3 THz. 120
5.19 Die photos of 2x1 and 2x2 arrays of DARs, synchronized with near-field electromagnetic coupling, operating at 0.2 THz. 120
5.20 Calibrated setup to measure EIRP and radiation power of the second harmonic frequency at 0.3 THz for the chipsets in Fig. 5.18 and at 0.2 THz for the chipsets in Fig. 5.19. 121
5.21 Calibrated setup to measure frequency of the received signal and radiation patterns for the chipsets in Fig. 5.18 and Fig. 5.19. 122
5.22 Photo of the measurement setup at 0.3 THz for the chipsets in Fig. 5.18. . . . 122

5.23 Radiation patterns of the second harmonic power near 0.3 THz measured from the backside of the 2x1 array chip in Fig. 5.18. The figure shows the patterns in the two orthogonal planes. 124
5.24 Calibrated locked THz spectrum of the received signal from the 2x2 array chip in Fig. 5.18. 124
5.25 Radiation patterns of the second harmonic power near 0.3 THz measured from the backside of the 2x2 array chip in Fig. 5.18. The figure shows the patterns in the two orthogonal planes. 125
5.26 Radiation patterns of the second harmonic power near 0.2 THz measured from the back side of the 2x1 array chip. The figure shows the patterns in the two orthogonal planes. 126
5.27 Calibrated locked sub-THz spectrum of the received signal from the back side, of the 2x2 array chip in Fig. 5.19. 127
5.28 The received spectrum splits when the DARs go out of locking range due to the change in varactor voltage. 128
5.29 Electronic beam-scanning demonstrated near 0.2 THz, by the 2x2 array of locked DARs using near-field coupling. The figure shows the backside radiation patterns in the θ plane. 128
5.30 Electronic beam-scanning demonstrated near 0.2 THz, by the 2x2 array of locked DARs using near-field coupling. The figure shows the backside radiation patterns in the ϕ plane. 129
5.31 Radiation patterns of the second harmonic power near 0.2 THz from the front side of the 2x2 array chip 129
5.32 Locked second harmonic frequency of the 2x2 array when the varactor voltage of two adjacent DARs are varied simultaneously for beam-scanning in one orthogonal plane 130
5.33 EIRP variation over the beam-scanning range. 131

6.1 Proposed scalable architecture of the integrated THz power generator and beam-steering array in CMOS. 133
6.2 The central VCO with differential buffers and the LO distribution with matching transmission-line driving 8 divide-by-two blocks. The 3D electromagnetic structure for the passives and their placement in the chip are shown. 137
6.3 3D electromagnetic simulation of LO distribution at 94 GHz, feeding the injection-locked frequency dividers. 138
6.4 The injection-locked divide-by-two block showing quadrature signal generation at 47 GHz. Each divider pair drives four phase-rotator blocks whose weights for the quadrature signals are controlled by 6-bit DACs. The placements of these blocks are shown in the chip. 139
6.5 Simulated central frequency of oscillation of the injection locking divide-by-two block with varactor tuning. 140
6.6 Simulated outputs of 4 phase-rotators at 47 GHz separated by 45° in phase difference. The differences in their amplitudes do not translate to the succeeding blocks which are injection-locked. 141
6.7 Injection-locked frequency tripler associated with each DAR showing frequency and phase multiplication from the 47 GHz signal input to the radiated signal at 282 GHz. 142
6.8 Measurement setup for the test structure comprising the central VCO and differential buffers. 144
6.9 Measured VCO frequency tuning against varactor and supply voltage. 145
6.10 Measured single-ended LO buffer power at the pad from the test chip and estimated differential LO buffer output power in the array chip. 145
6.11 Measurement set-up for the test chip comprising of one divide-by-two pair which generates quadrature signals at 47 GHz and drives four phase-rotators. 146
6.12 Measured sensitivity of the injection-locked divide-by-two block for different tuning voltages. The divider-locking bandwidth is marked for the LO buffer output power in the array chip. 148

6.13 Measured phase difference between the output of the two phase shifters in Fig. 6.11 as the 6-bit DAC setting for the phase control voltages of one phase-rotator is varied. 148
6.14 Die micrograph showing placement of individual functional blocks along with a photo of the measurement setup showing the receiver antenna and the harmonic mixer as in Fig. 6.16. 150
6.15 Experimental setup for the absolute power and EIRP measurement at the far]field of the radiating chip mounted on a brass board. 151
6.16 Experimental setup for measurement of the frequency of radiated signal and the 3D radiation pattern. 151
6.17 Calibrated spectrum of the radiated signal at the broadside captured at a far-field distance of 50 mm. The spectrum shows almost 24 dB of fundamental signal suppression near 140.4 GHz and a +9.4 dBm EIRP at the second harmonic frequency of 280.8 GHz 151
6.18 Variation of measured EIRP at the broadside, as the frequency of the radiated signal is controlled using the central VCO varactor tuning setting. 152
6.19 Radiation pattern measured in the elevation and azimuth plane, respectively, at 281 GHz showing a directivity of 16dBi and total electronic beam-steering range of around 80° in the each of the planes. 153
6.20 Chip performance summary 154

7.1 Silicon-based Terahertz imaging system. 155
7.2 Some of the typical and currently used Terahertz direct detection technologies. Golay Cells have typical NEP $\sim$ 200 pW/$\sqrt{\text{Hz}}$ 1001[125], microbolometers $\sim$ 10–200 pW/$\sqrt{\text{Hz}}$ [126], [127], Schottky Barrier Diodes $\sim$ 10–20 pW/$\sqrt{\text{Hz}}$ [128], pyroelectric detectors $\sim$ 400 pW/$\sqrt{\text{Hz}}$ [129]. 157
7.3 Architecture of the 4x4 pixel imager chip. 159

7.4 A full-wavelength loop antenna on an ungrounded substrate maximizes efficiency when front-side and back-side radiated power at the boresight are the same. 161
7.5 A ground plane with an aperture suppresses front-side radiation and increases gain, and therefore responsivity, from backside radiation. 161
7.6 Comparison of radiation patterns in the absence and presence of the ground plane with aperture opening. 162
7.7 THz imaging receiver in silicon with on-chip antenna, front-end detector and baseband amplification with 24.7dB tuning range 163
7.8 Die micrograph and PCB of the THz imager. 164
7.9 Frequency response of the baseband amplification showing a bandpass response which rejects DC offsets and low-frequency drifts. The gain variation with the VGA settings is also shown. 164
7.10 Set-up for measuring responsivity and NEP of the imager. 165
7.11 Measured responsivity and NEP of one pixel in the receiver. 166
7.12 Responsivity and NEP measurements of 16 pixels at 0.25 THz showing sub-10 pW/$\sqrt{Hz}$ for all pixels. 167
7.13 Measurement setup for focusing emitted THz beam to a diffraction-limited spot size on the focal plane which is imaged by the THz receiver by raster-scanning 167
7.14 Measured spot size of the focused beam at 0.26 THz on the focal plane in transmission-mode setup. 168
7.15 Demonstration of Fourier transform of the object on the focus plane of the lens at 0.26 THz. 168
7.16 Transmission-mode imaging setup. 169
7.17 Transmission line imaging examples showing penetrative property of THz through paper, plastic and demonstrating difference of interaction with scatterers of various sizes compared to the wavelength (sugar packets with fine and coarse grained sugar). 170

7.18 Transmission line imaging examples showing near-1-mm resolution, while the RFID chip and the loop antenna inside the conference ID card shows how far technology in conferences has come since the days of paper badges, not so long ago! 170
7.19 Contrast shown between dry and wet leaf due to absorption of THz signals by water. 171
7.20 Transmission difference between adipose and muscle in a sample of chicken tissue at 0.26 THz. 172
7.21 Reflection-mode imaging set-up. 172
7.22 Reflection-based imaging examples. 173
7.23 Contrast between bones, cartilages and muscles in of mouse leg, which is fixed on a glass slide, demonstrating feasibility of noninvasive imaging at THz frequencies. 173
7.24 An all-silicon THz imaging setup with 16-pixel BiCMOS detector array and 2x2 array of locked CMOS DARs near 0.29 THz. 175
7.25 Diffraction-limited spot radiated by the CMOS source and imaged by the silicon detector array. The right figure shows the near-field profile, obtained by scanning the detector array chip, when the two PCBs with the silicon chips are brought into each other's near-fields. 175
7.26 The first THz imaging demonstrated with a CMOS source. 176

8.1 State-of-the-art transistor looks no longer like a textbook transistor. With scaling towards nanometer dimensions, fluctuations in process variations such as line edge roughness, number of dopant atoms can cause significant variations over predictability of transistor performance. 178
8.2 A mixed-signal feedback system that can characterize the performance of the system on-chip and has an actuation space to reconfigure the system to optimize performance over a range of random and systematic variations. 180

8.3 A transmission line based mm-Wave power amplifier with 2-to-1 combiner at 28 GHz with various sensors, ADC, actuators and digital core for on-chip sensing and actuation. 180
8.4 Schematic and layout of the DC sensor of the PA. The current through PA is mirrored by a factor of 100 and sensed, while accomplishing voltage regulation with a headroom of only 10-30 mV. 181
8.5 DC sensor response from measured ADC data, against PA output current showing the spread over 5 chips. 182
8.6 Measured PA drain voltage regulation with DC drawn. The maximum headroom is less than 45 mV over a 2.12 V supply, thereby, not affecting PA efficiency significantly. 182
8.7 RF power sensor schematic and layout showing rectification, low-pass filtering and detection current amplification. 184
8.8 Output and Input RF power sensor response at 28 GHz, from measured ADC data over 6 chips. 184
8.9 Schematic of temperature sensor showing 'hot' sensor diodes interspersed within PA transistor and the simulated thermal profile for 80mW power dissipation in the process. 186
8.10 Layout of the PA transistor with the inter-spaced diodes in between. 186
8.11 Measured temperature sensor output and DC sensor output with increasing DC power dissipation in PA. 187
8.12 Digital core structure. 189
8.13 State-machine description. 189
8.14 Measurement set-up and die micrograph showing PA with sensors, ADC and actuators. 190
8.15 Output power healing for different input power and histogram showing effect of self-healing in narrowing distribution and yield increase. 191
8.16 Self-Healing demonstrating almost 50% less DC power consumption for a constant output power of P_{out}=12.5 dB. 192

8.17 Self-Healing showing improved output power performance over the 4-1 VSWR cycle and histogram showing yield increases for a constant load mismatch at $\Gamma_L = -0.2$ 192

9.1 A conceptual self-similar output combiner for combining currents from four output stages where each output stage is a scaled self-replicated version of the four output stages in an iterative way 194
9.2 Output combiner design for combining current from 16 output stages driven in phase. The combiner also achieves impedance transformation. The spaces in the transmission line network of the combiner represent ports where capacitors were placed as parts of the matching network. It also shows the schematic of the last three stages in each of the four arms of the combiner. It consists of Driver 1, Driver 2 and Output stage which have been illustrated in Fig. 9.4 and Fig. 9.5 195
9.3 Simulated loss (passive efficiency) of the combiner 197
9.4 The PA architecture showing the power splitting, combining networks and power flow among various branches at saturation assuming each stage has 3dB of saturated gain and branches are lossless 199
9.5 Die microphotograph of the 77 GHz amplifier showing the layout placements of the different stages and the power splitting and combining network. 200
9.6 . Measured S-parameters of the power amplifier 201
9.7 Measured output power, gain and PAE at 77 GHz. 201

11.1 On the possibility of false locking. 205

Chapter 1

Introduction

> Nothing, I guess. I do not think that the wireless waves I have discovered will have any practical application.
>
> — Heinrich Hertz, 1886-87

Today, the influence of electromagnetism in our daily lives cannot be over-emphasized. While Maxwell laid out the general theory of electromagnetism, over the years following many new discoveries and inventions, the field branched into separate disciplines of study. The split happened essentially on frequency lines, and the spectrum broke into radio waves, microwaves, mm-waves, terahertz, infrared, optics and so on. Each of them became independent and matured field of research in their own right, influencing our lives significantly but in different ways. Radio waves became the carrier for wireless radio communication, microwave frequencies became a major field of research for radars and defense applications, terahertz and infrared for chemistry and spectroscopy, optics for vision, microscopy, lasers, wireline communication in and among other things. Almost century and half after Hertz's famous misjudgement, we see a re-unification of electromagnetism, unlike ever before, to create cutting-technology for the next-generation systems. Maxwell's equations are the common underlying principles, but the ability to harness, control and use, in an integrated environment, such a large portion of the electromagnetic spectrum with such diverse prop-

erties in their interaction with matter, can lead to the development of a wide range of novel applications with far-reaching impact.

I believe, in the next few years we will see a similar re-unification at a higher level of abstraction, where a wide range of allied fields such as electrical engineering, applied physics and mathematics, material science, chemistry and biology will grow organically, in a mutually synergetic environment, to transform the landscape for the next-generation cutting-edge technology. We are seeing a slight hint of this trend already; silicon integrated circuits are now operable to a wide range of the spectrum from radio waves, microwaves to mm-Wave, sub-THz and THz frequencies; optics, circuits and material science are contributing to opto-electronics and silicon photonics; biology, chemistry and integrated electronics are jointly innovating for future personalized health care. In near future, a host of highly impactful technological innovations will come through this close alliance of multiple scientific disciplines in a holistic collaborative environment. This will not be achieved thorough a mastery of one discipline and a 'black-box understanding' of the allied fields, but through a broader understanding of multiple disciplines and end-to-end design processes.

While human inventions have presided over a major portion of the electromagnetic spectrum, some parts are still less explored, technology less developed and influence in our daily lives, less noticed. One such spectral range is called the Terahertz frequency range, often referred to as the 'Terahertz' gap [1]. It lies wedged between microwave at the lower end and infrared at the higher end of the spectrum, as shown in Fig. 1.1. While the exact frequency range it covers is a matter of semantics and personal opinion, the community generally refers to the frequency spectrum between 0.3-3 THz, as the Terahertz frequency range. In this thesis, in the spirit of scientific research, we use the term 'THz' to refer to frequencies near 0.3 THz.

We see the first references of Terahertz in [1], which called it the 'heat rays of great wavelength'. The 'THz' wavelength ranges from 1 mm-100 µm, which corresponds to photon energies between 1.2-12.4 meV and equivalent blackbody radiation temperatures of 14-140

[1] THz is synonymously referred to as the sub-millimeter wave band, as the wavelength ranges from 1 mm-100 µm

K [2]. Approximately 98% of all photons emitted since Big Bang fall within the THz-far IR band [2]. This explains why in the last hundred years, terahertz has built up a niche place in scientific community for the study of astronomical studies, high resolution spectroscopy, remote sensing as well as chemical sciences and molecular spectroscopy. However, lack of adequate and cost-effective instrumentation development in this spectral region has contributed to it being called the 'THz' gap, which has also adversely affected the development of its application space. However, with new developments in nanotechnology, material science and optics, there has been a resurgence of active research interest in this frequency range and the research community are approaching the technology development from a abroad range of scientific disciplines [3]. Terahertz technology has shown great promise in disease diagnostics such as non-invasive early skin cancer detection [13], [23], [25], [39], label-free DNA sequencing [32], security screening for concealed weapons and contraband detection [27]- [30], global environmental monitoring, nondestructive quality control and ultra-fast wireless communication [3]. In this thesis, we discuss our approach towards development of miniaturizing terahertz technology into silicon-based integrated chipsets.

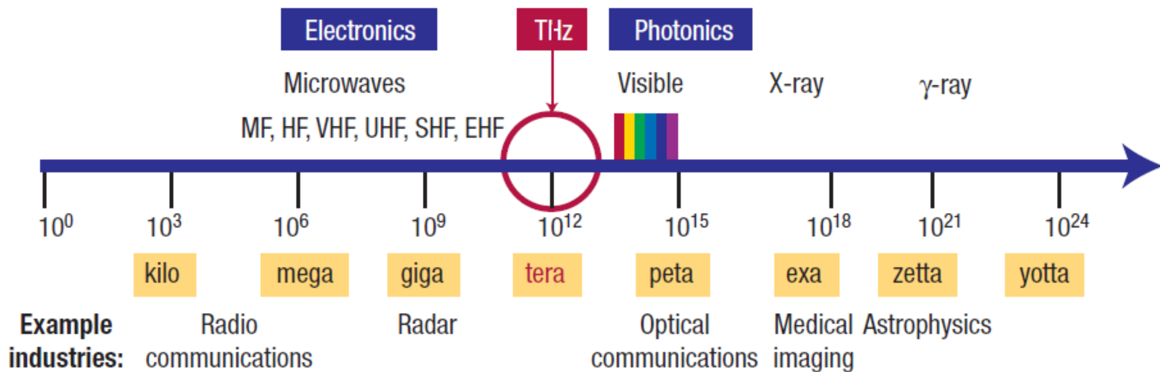

Figure 1.1: The electromagnetic spectral range from low-frequency radio waves to high energy gamma-rays [7].

Silicon-based integrated circuit technology has had a major influence in our lives particularly in the three broad areas of communication, computation and information technology, and health-care. In my lifetime, I have witnessed the sheer force of technology, ushering in the information age in developing countries like India, where the cell-phone market is

expanding at a rate of 40% with a current user base of 919 million users, as of 2012 [4]. The wireless revolution can be felt not just by the fact that every few other miles a new cell-phone tower pops up, one can notice a major change in quality of lives of people in the middle and lower incomes levels. Low-cost technology, implemented in a piece of wireless device, informs farmers the about real-time rates in the nearby marketplace and also availability of necessary health practitioners at the nearest health-care centers. Silicon technology allows this possibility of integrating complex systems into low-cost, single chip solutions. While silicon has almost completely replaced any competing technology in the computational space, due its capability of high integration, excellent process control and unparallel performance of digital CMOS logic, in the realm of wireless communication and RF systems, other technologies such GaAs do co-exist, specially in power generation blocks, where efficiency can offset the extra cost of superior technology. At higher frequencies, such microwave and mm-Wave, other compound III-V devices such InP HBTs and HEMTs have technologically superior performances and almost completely dominate the market. At even higher frequencies such as in the Terahertz band, technology is 'sparse' with only a few compound III-V solid-state electronics and optics-based systems existing. Fig. 1.2 shows a typical femtosecond-laser based broadband Terahertz system (from Teraview [5]), which costs upwards of $200,000. Our vision is to pack the entire functionality into a small silicon chip, which has orders of magnitude smaller form factor and lower cost.

Figure 1.2: A femtosecond-laser based broadband Terahertz system [5]. The photo on the right hand side is the first THz CMOS beam-scanning power generator. [59]

In the last few years, device scaling with increasing cut-off frequencies (f_t, f_{max}) has pushed silicon technologies into the microwave and mm-Wave frequencies. However, as we approach scaling lengths with atomic dimensions focusses on increasing transistor density and improved digital performances, high frequency performances often suffer due to increased gate resistance, short-channel effects, low-resistivity substrates and passive losses in metal structures and therefore the classical cut-off frequencies (f_t, f_{max}) is not guaranteed to increase linearly with scaling. Therefore, new techniques, architectures and topologies need to be invented which can overcome these technological challenges and push performances beyond what conventional design methodologies can achieve. As an example, while the first 77 GHz phased-array was demonstrated in 0.13 µm SiGe BiCMOS process [54], we discuss techniques with which we can push the frequency to a factor of 4x in a technology with lower f_{max} and lower breakdown. In this thesis, we demonstrate the first near-THz CMOS beam-scanning array [59], as shown in Fig. 1.2.

1.1 Contributions

In this work, we propose novel ways of combining circuits and electromagnetics in a holistic design approach which can overcome limitations of conventional block-by-block or partitioned design approach for high-frequency power generation above f_{max}. We demonstrate this design philosophy in an active electromagnetic structure, which we call Distributed Active Radiator. It is inspired by Inverse Maxwellian approach, where we remove the artificial boundaries between circuits, electromagnetics and antenna. Instead of using classical circuit and electromagnetic blocks to generate and radiate THz frequencies, we formulate surface (metal) currents in silicon chip for a desired THz field profile and develop active means of controlling different harmonic currents to perform signal generation, frequency multiplication, radiation and lossless filtering in a compact footprint. This enables us to demonstrate

- The first 1 mW Effective-isotropic-radiated-power(EIRP) THz (0.29 THz) source in CMOS with total radiated power being three orders of magnitude more than previously

demonstrated.

- Demonstration of integrated beam-scanning near 0.2 THz using a proposed near-field synchronization mechanism, which is a scalable method of realizing large arrays of synchronized autonomous radiating sources.

- The first THz CMOS array (4x4 element at 0.28 THz) with digitally controlled beam-scanning in 2D space with nearly 10 mW of EIRP.

We use a similar electronics and electromagnetics co-design approach to realize a 4x4 pixel integrated silicon Terahertz camera demonstrating

- Most sensitive silicon THz detector array without using post-processing, silicon lens or high-resistivity substrate options (NEP<10 pW$\sqrt{Hz}$)

- The first demonstration of an all silicon THz imaging system with a CMOS source.

1.2 Organization

The thesis is organized as follows. Chapter 2 reviews the ever-increasing and diverse THz application space and existing THz technology for signal generation and detection, discussing both solid-state and optics-based approaches. Chapter 3 discusses the challenges of THz frequency generation in silicon-based processes, and extraction of the generated power from the silicon die to the outside world. We argue that the classical partitioned approach, that builds up a system using a cascaded series of standard circuit blocks and interfaces with a classical antenna to radiate out the THz waves, is a sub-optimal approach. We introduce the concept of Distributed Active Radiation (DAR), which combines signal generation, frequency multiplication, radiation and lossless filtering, all simultaneously in an actively controlled electromagnetic structure.

Chapter 4 discusses the theory of DAR from an electromagnetic field perspective. We study in details power lost as surface waves for various kinds of surface current configurations and fundamental limitations of on-chip radiating structures.

Chapters 5-6 discusses arrays of DARs and how many autonomous radiating DARs can be either mutually synchronized or locked to a common sub-harmonic frequency source to achieve power combination in free-space for higher EIRP and electronic beam-scanning. We corroborate our theory with measurement results.

While Chapters 3-6 cover our work on THz power generation in silicon, Chapter 7 discusses THz power detection in silicon-based processes. We demonstrate a 4x4 pixel THz camera in silicon and show imaging results with an all silicon THz imaging system.

Chapter 8 covers my contribution on our collaborative work on robust and self-healing high frequency systems and Chapter 9 discusses my work on CMOS power amplification at mm-Wave frequencies.

Chapter 2

The Terahertz Gap: Current THz Technology

In this Chapter, we will briefly review the ever-developing THz application landscape, currently existing THz source and detector technologies. Comprehensive review articles on this subject can be found in [2], [3], [7], [8], [9], [10], [13], [18], [19].

2.1 THz Application Space

For a long time, THz application space was literally limited to 'space' sciences. However, in the last twenty years, with new developments in THz technology and access to (relatively) increasingly lower-cost technology, there has been extensive research in the application space. Astronomy and space sciences have been drivers for THz technology since vast amounts of spectroscopic information are found in this frequency range. THz-based spectroscopy is purported to have a wide range of applications from carrier concentrations to mobility in doped semiconductors, high temperature superconductor characterization to biomedical applications, facilitated by the fact that collective vibrational modes of many proteins and DNA molecules are expected occur in this range [7]. Many intermolecular vibrational signatures are expected to be present in the THz frequency range, while most intramolecular modes fall in the infrared range [3] (Fig. 2.1). THz waves can also predict conformational states of bio-molecules and polymorphs, which has great potential in pharmaceutical indus-

tries. There has been active research in label-free DNA detection for low cost DNA chips using THz spectroscopy, which can detect the differences between presence and absence of hybridization due to changes in refractive index [32], [33].

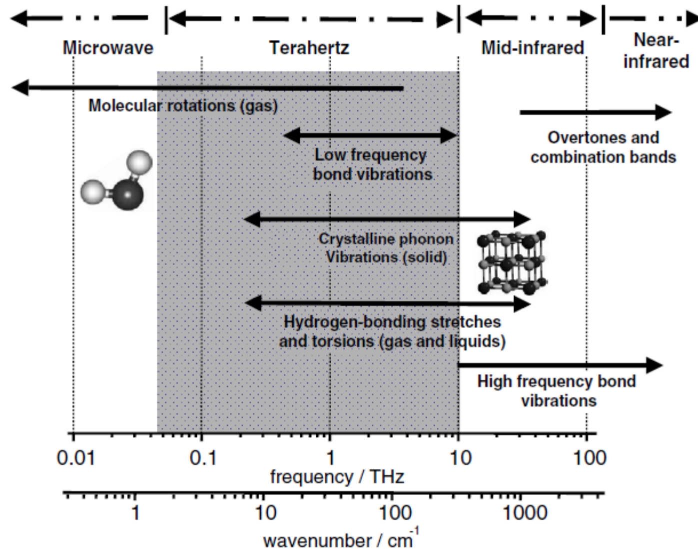

Figure 2.1: Molecular transitions in the THz spectrum [13].

There have been several studies on the diagnosis of cancer, particulary non-invasive early detection of skin cancer, based on dielectric property differences between healthy and cancerous tissues at these frequencies(Fig. 2.2). THz waves, with their low photon energy, are non-ionizing and therefore, safe for medical diagnostics (atleast much safer than X-rays). Due to longer wavelengths, it has higher penetration depth and lower scattering (though higher absorption) than optics , and therefore may have applications in monitoring of tumor boundaries in surgical procedures [24]. This has motivated studies on both pulse-based and CW wave reflection imaging from skin and excised breast tissues. Strong correlation has been observed in THz images and histology results (Fig. 2.3) [25], [13], [23], [25] and research is progressing towards real-time THz image acquisition from ex-vivo samples. THz lends itself amenable to both amplitude and phase detection during image acquisition and therefore, can give depth information and render a three dimensional topographical reconstruction of specimen under test. Fig. 2.4 demonstrates a quasi-three-dimensional image of a transverse slice of a human tooth, showing an example where THz imaging has potential

to be an alternative low-cost and non-ionizing technology against the standard X-rays.

	α (mm^{-1})	α (mm^{-1})	n	n
	0.5 THz	1 THz	0.5 THz	1 THz
Normal skin	11.0	16.8	2.20	2.06
BCC	13.1	19.3	2.26	2.09
Normal breast	10.5	16.4	2.01	1.90
Breast carcinoma	12.5	18.6	2.23	2.08
Breast adipose	1.3	2.2	1.56	1.54
Water	16.3	23.0	2.28	2.09

Figure 2.2: Absorption (α) and refractive indices (n) of tissues at 0.5 and 1 THz [13].

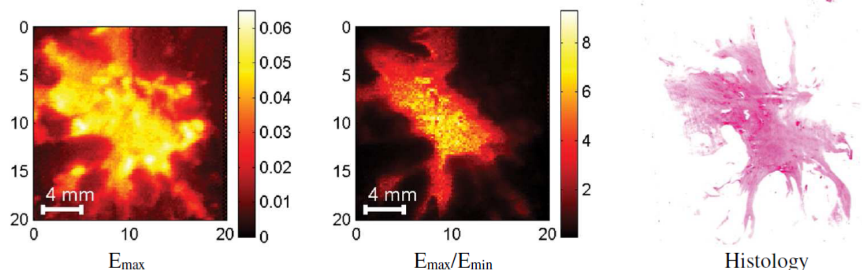

Figure 2.3: Reflection-based THz image showing strong correlation between acquired image and histological results. The images show tumor tissues with surrounding adipose tissues [24].

THz waves can penetrate through clothing, paper, and wood, has higher resolution ($\sim$ 10x) than microwaves and therefore, has great potential in homeland security and defense applications. Potential of stand-off concealed weapon detection with high-enough resolution and contraband detection with THz spectroscopy have been demonstrated [30], [31]. Recently, a 675 GHz solid-state electronic system with mechanical scanning was demonstrated for explosive detection at a stand-off distance of 25 m [28]. Extensive research has gone into various modes of contraband detection from far-off distance, using transmission, reflection, diffuse reflection modes [31]. Due to its see-through properties, it also has tremendous application potential in industrial quality control, electronics, food and agricultural industry which have currently working prototypes based on expensive optics-based THz-TDS systems.

Due to the availability of larger bandwidths at these frequencies, there are applications in development for ultra-fast wireless communication. High-performance point-to-point wireless

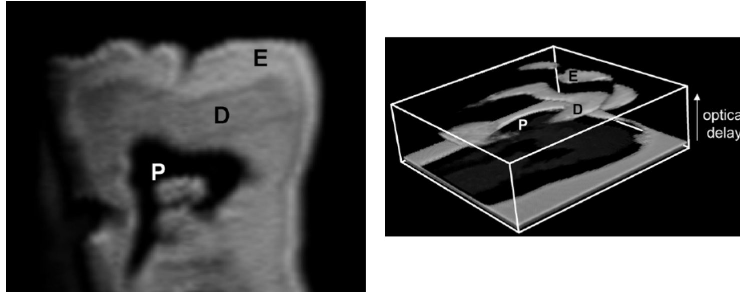

Figure 2.4: A quasi-three-dimensional image of a transverse slice of a human tooth constructed using depth information from time of flight. Labels E, D and P represent the enamel, dentine and pulp, respectively [13].

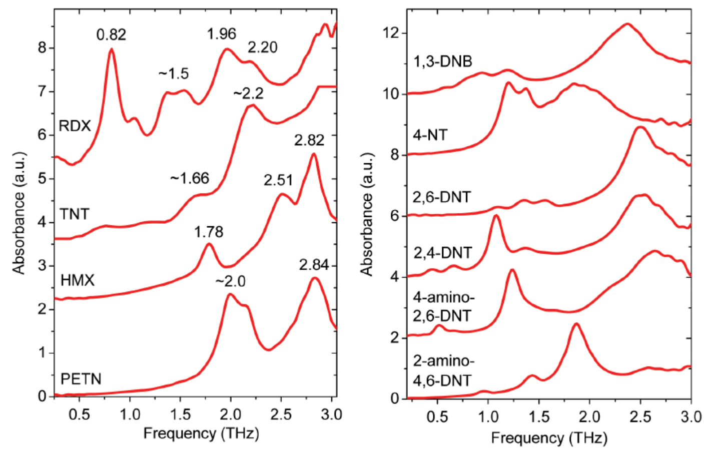

Figure 2.5: THz absorption spectra of RDX, TNT, HMX. and PETN obtained with THz-TDS [31].

connections can be beneficial for communication in rural areas, communication between buildings during disasters, high-data rate delivery for uncompressed video [3]. 120 GHz point-to-point links have already been developed and were used during the Beijing Olympics in China in 2008.

The development of most of these applications depend on the availability of low-cost, high yield technology. Integrated silicon technology, which enabled such explosive growth in computational power in computer chips and cell-phone chipsets at such low-cost, can provide unparalleled signal processing power with billions of transistors and realize complex systems with ultra-small form factors, high reliability, and low cost. Through the technology has matured and developed for digital and lower radio frequencies for cell-phone applications, we have developed new techniques to push silicon beyond its cut-off frequencies into the THz frequency spectrum. Still in the early path of its growth, it will not be entirely surprising if a completely new frontier opens up and grabs the market, however it can be speculated with some confidence that atleast a significant chunk of THz, the 'last' frontier in high-speed electronics, will go the silicon way.

2.2 Current THz Technology

Among the existing THz technology, there is a lack of a high-power, low-cost, portable room-temperature THz source and low-cost, integrated room-temperature detector suitable for video-rate imaging. Current state of the art THz systems are based on expensive optics-based equipment such as femtosecond lasers, electro-optic samplers, nonlinear crystals, and custom photoconductive antennas or discrete module-based solid-state electronic components realized with compound III-V technology or quantum-cascade laser based technology which currently require cryogenic cooling. Fig. 2.6 shows the range of technologies with their typical output power. Silicon-based technology, as reported in [64], [65], [66], have shown generation of tens of nanoWatts of power near 0.3 and 0.4 THz, far too small to be of much practical use.

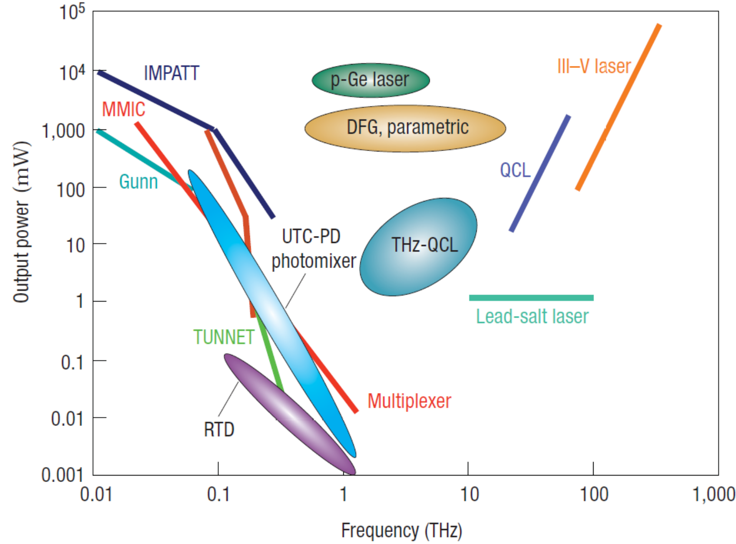

Figure 2.6: Solid-state electronics and optics-based THz sources and their typical power output [3].

2.2.1 Optics-based Technology

Broadband and narrowband continuous-wave THz power generation, based on optical methods, rely on photo-Dember effect and optical rectification effects respectively. When an ultrafast laser pulse shines on a photo-conductive material, electron-hole pairs are generated. The free carries, then accelerate under a static bias field and the transients lead to a broadband pulse which can radiate out. This is explained in Fig. 2.7. Various parameters such as decay times, carrier mass, drift velocity affect power output and bandwidth of the generated pulse [7].

CW-wave sources can be generated by beating two CW lasers, whose frequency difference lies in the THz frequency regime. The lasers are passed through a nonlinear medium and the down-converted signal is extracted. Methods, based on similar nonlinear phenomenon, are optical parametric amplification and Difference Frequency Generation. The nonlinear materials under investigation are GaAs grown at low temperature, GaSe, ZnTe and several others. Tunable THz sources, using parametric amplification, have been demonstrated to produce peak power in excess of 1 W (pulsed) [3]. Quantum-cascade-lasers, which exploits electron relaxation between sub-bands of coupled quantum wells, have demonstrated operation in the infrared as well as in the THz frequency regime from 1-4 THz, but they require

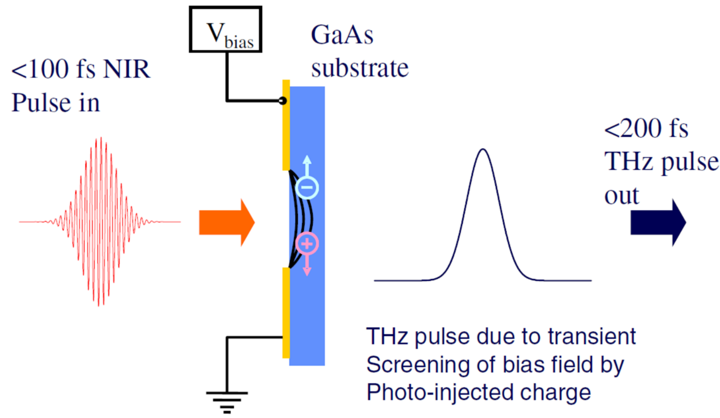

Figure 2.7: Photoconductive-based broadband pulse generation using ultrafast lasers [13].

cooling for their operation, even though recent results have demonstrated their operation near 178 K [34].

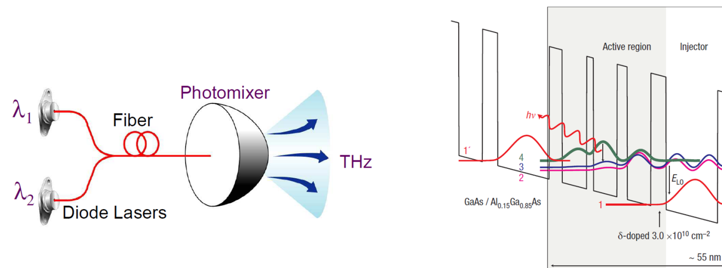

Figure 2.8: CW-wave sources can be generated by beating two CW lasers in nonlinear medium. The right part of the figure shows quantum-cascade-lasers which are powerful narrowband sources but require cryogenic cooling. [3].

The detector technology for pulsed optical systems are either based on photoconductive sampling or electro-optic sampling. Electro-optic samplers use birefringent crystals whose dielectric properties are modulated by the incoming THz pulse, which is translated to polarization modulation in a propagating light wave through the crystal.

2.2.2 Solid-State Electronic and Custom Technologies

Solid-state electronic technology, existing in the THz frequency range, are almost completely based on compound III-V sources. Frequency multiplication based approaches employ a

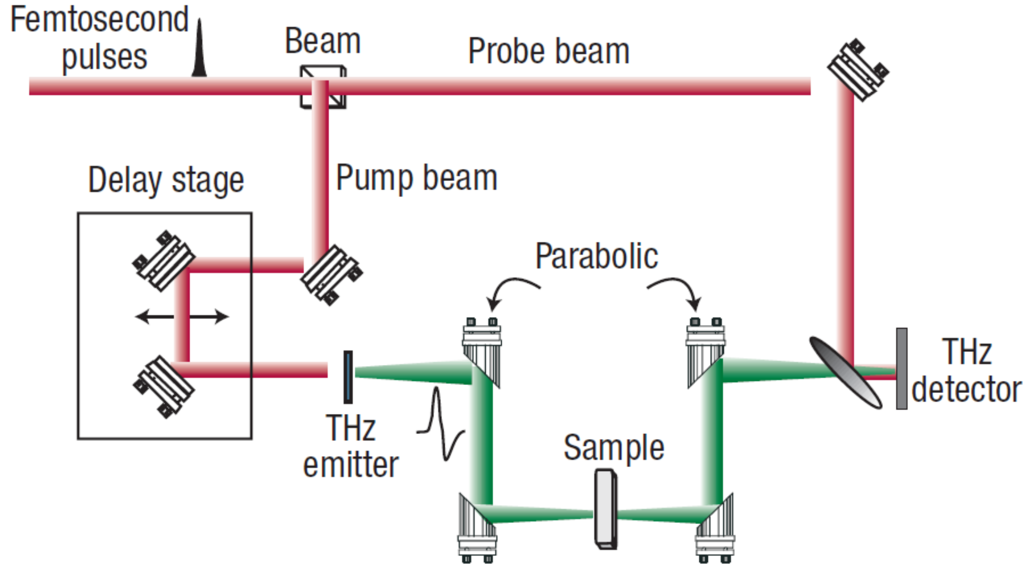

Figure 2.9: THz broadband time-domain spectroscopy based on photoconductive generation and detection [7].

higher power microwave source which drives a chain of frequency multipliers, with amplifiers inserted as per requirements. It is difficult to achieve full system integration even in solid-state MMIC technology and most of the systems are module-based waveguide coupled arrangement. A typical 300 GHz Tx-Rx system from Virginia Diodes, Inc. has been shown in Fig. 2.10 [35]. Each multiplier is generally based on planar GaAs based Schottky diodes and frequencies as high as 2.7 THz with few µW of power has been reached. Higher output power require gas lasers and free-electron lasers, which have shown output powers as high as 30 mW [7]. Until recently, integrated silicon technology did not exist in this frequency range.

Solid-state device based detection system allows for phase detection using down-conversion mixers and GaAs-based Schottky diodes and have reached frequencies of 2.5 THz [7]. Cryogenic cooling is often required for low-noise operation, and super-conducting SIS mixers are often the technology of choice, specially for space-borne applications. Thermal absorption based broadband detectors such as golay cells, pyro-electrical detectors, bolometers are often used as standards for power measurements at these frequencies and they will be compared with our work in Chapter 7. Comprehensive treatise on this subject can be found in [118]

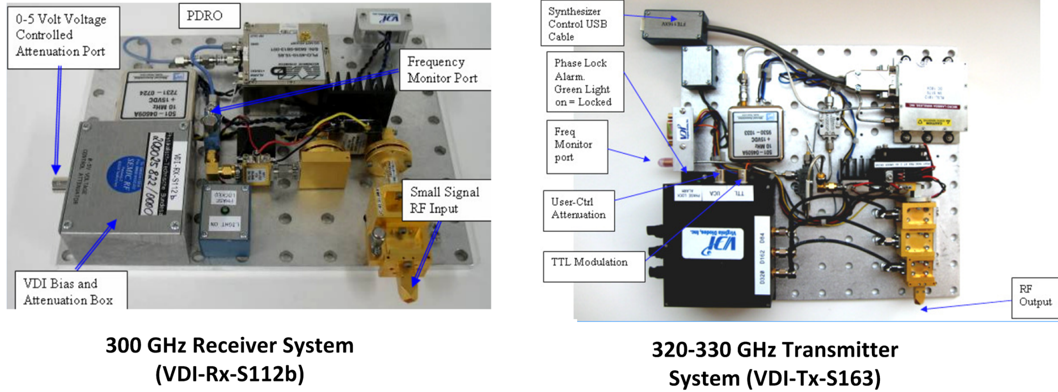

Figure 2.10: A 300 GHz transmitter and a 300 GHz receiver system from Virginia Diodes, Inc. [35]

and [119]. Until recently, there were no silicon-based THz detectors at these frequency ranges. Prior and contemporary work have demonstrated feasibility of silicon technology for THz detection [48], [120]- [122], however they can be power-intensive (> 300mW/pixel) [48], require high resistivity SOI technology (> $1K\Omega$-cm) substrates [121], or rely on external components such as silicon lenses [121], or pos-processing such substrate thinning [122].

In this thesis, we will demonstrate novel techniques that pushes silicon technology into the THz frequency region, demonstrating record output power levels, beam-control and THz detection sensitivity, together enabling an all-silicon THz imager, as shown in Fig. 2.11. Altough, we give examples with imaging applications, the concepts we introduce are equally applicable to communication and sensing systems.

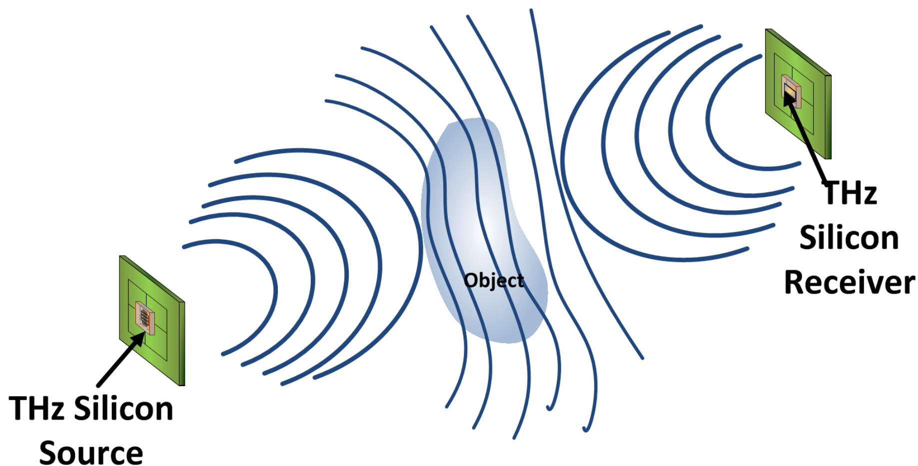

Figure 2.11: Silicon-based Terahertz imaging system.

Chapter 3

Distributed Active Radiation: THz Power Generation in Silicon

> The whole is more than the sum of the parts
>
> *Metaphysics, Aristotle*

In this Chapter, we focus on the problem of THz power generation in silicon and the extraction of the desired power out of the silicon die. In summary, we focus on the transmitted side of Fig. 7.1.

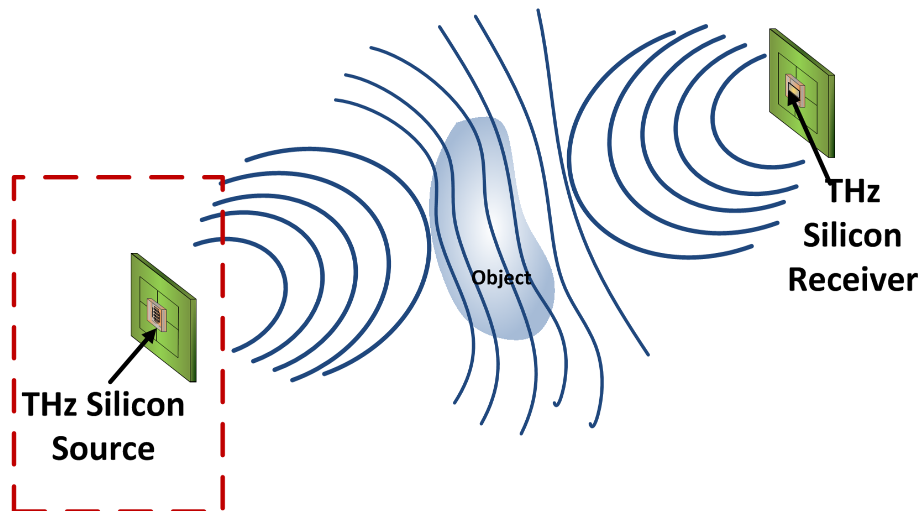

Figure 3.1: Silicon-based Terahertz imaging system.

Due to lower carrier mobility and lower cut-off frequencies of CMOS technology com-

pared to compound III-V technology of similar feature size, direct oscillation at the desired frequency may not be achievable. Further, low breakdown voltage, reduced transistor nonlinearities in short-channel regime, low-quality-factor passives and lossy filtering make on-chip generation and filtering of THz signals very challenging. Extracting the generated power from the silicon die is an equally formidable task. Classical antennas which work well in free-space, are not efficient radiators in silicon. When implemented in silicon the substrate with its high dielectric constant acts as an excellent dielectric waveguide, trapping most of the radiated power into surface wave modes in the substrate [72]– [75]. Previous works have shown radiated THz power in CMOS in tens of nanoWatts of power, far too small to be of much practical use [64], [65], [66]. We will begin by reviewing the challenges of THz power generation and radiation in silicon. We argue that classical partitioned approach that builds up a system using a cascaded series of standard circuit blocks and interfaces with a classical antenna to radiate out the THz waves is a sub-optimal approach. We introduce the concept of Distributed Active Radiation (DAR), which combines signal generation, frequency multiplication, radiation and lossless filtering, all simultaneously in an actively controlled electromagnetic structure. It is inspired by an Inverse Maxwellian approach, where we remove the artificial partitions among circuits, electromagnetics and antenna and approach the power generation and radiation principles from first principles.

3.1 High-Frequency Limitations of DC-RF Power Conversion and Extraction

In this section, we will study the challenges of DC-radiated high-frequency RF conversion in a given technology. As shown in Fig. 3.2, our goal is to maximize the efficiency of conversion from DC power into the chip to THz electromagnetic signal extracted out of the chip. The propagating THz waves in free-space, then, can be used for imaging, sensing or communication or any other application. We will, at first, deal with the circuits part of the problem, which is high-frequency limitation of DC-RF conversion in a silicon chip. A self-

sustained oscillator is an autonomous system which can convert DC power into RF power at a designed frequency. But there are technological limitations on how high of frequency one can achieve in a single-frequency self-sustained oscillator in a given technology. Fig. 3.2, shows extrapolated plots of high-frequency limits of silicon technology. from ITRS in 2007. We will explain the parameters f_t and f_{max} in the next section, but the plot shows the maximum frequency of oscillation one can achieve in a projected technology node. For example, in this thesis, we use extensively the 45 nm SOI CMOS node, with projected $f_{max} \sim 200$ GHz. Therefore, in this technology, no self-sustained oscillation could be achieved above 200 GHz.

After discussing the circuit challenges of high-frequency power generation, we will review the electromagnetic part of the problem, which deals with the extraction of the generated signal from the chip to the outside world for any useful application. Both the problems can be equally challenging and we try to overcome the limitations of conventional design methodology through a holistic approach that combines circuits, electromagnetics, radiation, and nonlinear dynamics. We call our invention, distributed active radiation [57].

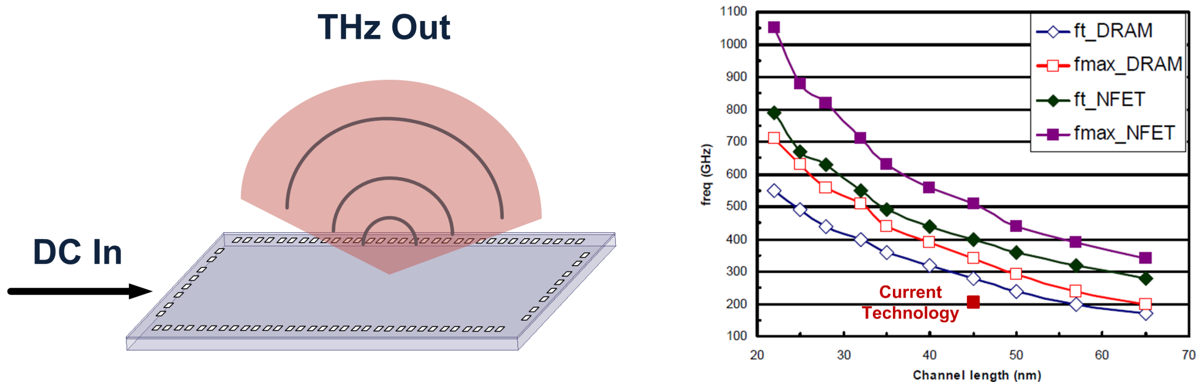

Figure 3.2: Desired high-efficiency conversion from DC power into the chip to THz signals out of the chip. The figure also shows extrapolated plots of high-frequency figures of merits of projected silicon technology.

3.1.1 DC-RF Power Conversion Below f_{max}

An active device, such as a transistor, is denoted as a three-terminal device as shown in Fig. 3.3. The basic operating principle of the device from a circuit perspective may be simple, however, the physical layout of the simplistic model entails interconnections with

metals, polysilicon, vias and the close-spaced nature of the interconnects, distributed current flow, ohmic losses and local current loops, lead to distributed parasitics such as capacitance, resistance and inductance. The transistor, itself, has intrinsic capacitances associated with it due, to the nature of its operation and therefore, overall, a transistor exhibits a dynamic transfer function between any two terminals. At low frequencies, where power gain of the device (defined as P_{out}/P_{in} at a single frequency) is substantial, the parasitics only often contribute to the poles and zeros of the transfer function and therefore may affect stability in a multi-transistor circuit. However, at very high frequencies, when the power gain is limited, RF power dissipation in the distributed resistances become important since it can significantly affect the gain of the device itself. One parameter, which captures this high-frequency limit of a single device is called f_{max} [43], [44]. It is defined as the frequency as which the power gain from the input port to the output load, under the assumption of both input and output conjugate match, falls to unity. A first-order derivation of f_{max}, given basic few parameters of the transistor can be derived as follows.

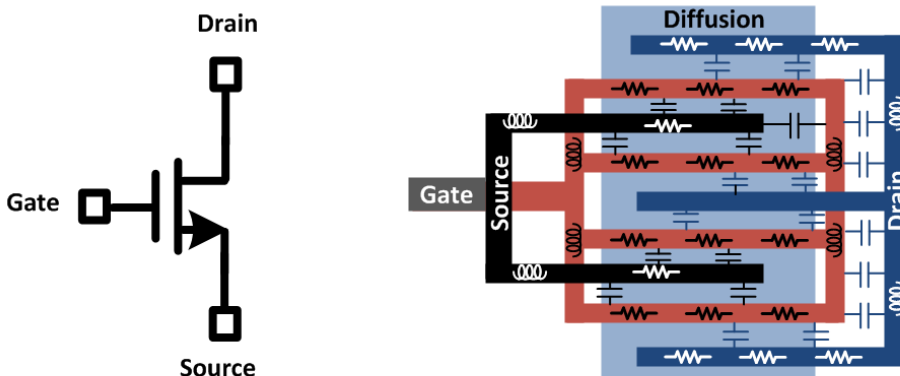

Figure 3.3: A physical layout of a MOSFET with four fingers in parallel, showing layout parasitics.

A NMOS and its typical small-signal equivalent model, biased in saturation, is shown in Fig. 3.4. The parasitic capacitances considered here are C_{gs}, C_{gd} and C_{ds}, and the resistances are the gate resistance R_g (which contributes to the input power dissipation) and the output resistance R_0 (due to channel-length modulation).[1] We assume small-signal operation or

[1] R_g may consist of parasitic physical resistance of the polysilicon gate, the nonquasistatic resistance due to finite transit time effects of the channel [45] and effects of channel resistance due to the feed-forward capacitance C_{gd}.

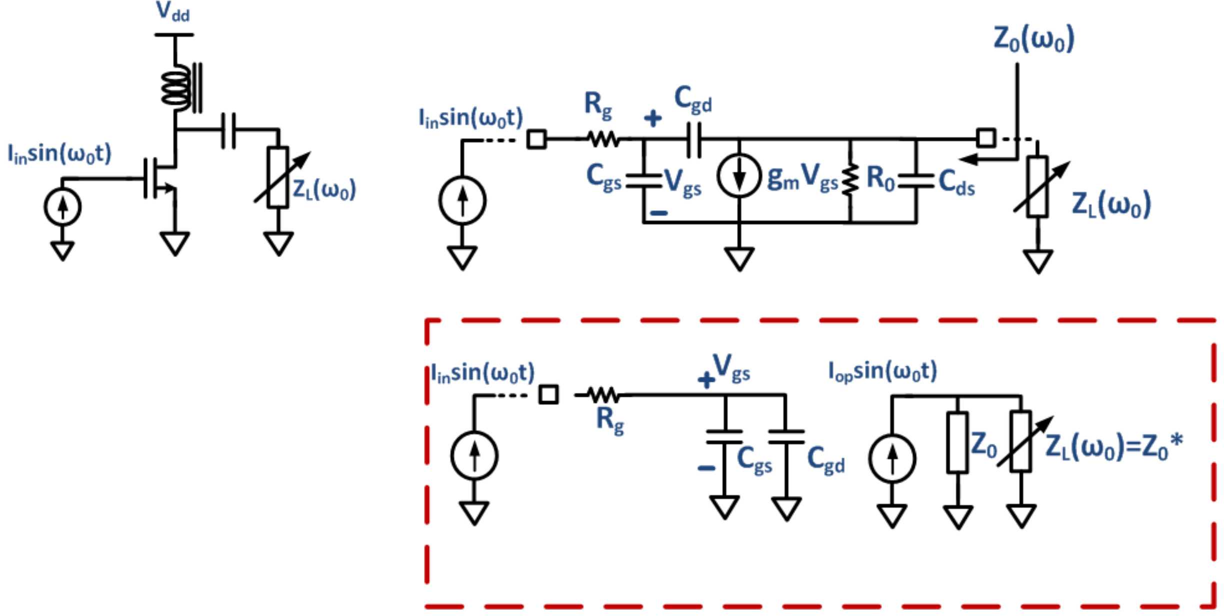

Figure 3.4: Small signal equivalent model for power gain derivation.

linear transfer function. In order to derive a compact first-order model for small-signal power gain, we will make several approximations. Assume that current $I_{in}\sin(\omega_0 t)$ is pumped into the transistor. Neglecting feed-forward current through C_{gd}, the input power is given by

$$P_{in} = \frac{I_{in}^2 R_g}{2} \tag{3.1}$$

We will find the optimum complex load Z_L, that maximizes the power transfer into output load Z_L. By the theorem of maximum power transfer, power dissipation in Z_L is maximized, when $Z_L = Z_0^*$, where Z_0 is the output impedance when the input current source is nulled or kept open. In such a situation, it can be shown that

$$Re(Z_0) \approx \frac{C_{gs} + C_{gd}}{g_m C_{gd}} = \frac{1}{\omega_t C_{gd}} \tag{3.2}$$

where $\omega_t = \frac{g_m}{C_{gs}+C_{gd}}$ is another high-frequency figure of merit, where the short-circuit current gain becomes unity. The magnitude of the output current generated due to the transconduc-

tance and the input perturbation, can be approximated by a short-circuit current assumption, as shown in Fig. 3.4, [44], where $V_{gs} = \frac{I_{in}}{\omega_0(C_{gs}+C_{gd})}$. Therefore,

$$I_{op} = \frac{g_m}{\omega_0(C_{gs} + C_{gd})} I_{in} \approx \frac{\omega_t}{\omega_0} I_{in} \tag{3.3}$$

Therefore at $\omega_0 = \omega_t$, the current gain $\frac{I_{op}}{I_{in}}$ becomes unity. From Fig. 3.4, for output conjugate match, half of the output transconductance current I_{op} flows through Z_0 and the other half through Z_L. The power gain, therefore, can be written as,

$$\begin{aligned} \frac{P_{op}}{P_{in}} &= \frac{\frac{1}{2} I_{op}^2 Re(Z_0)}{\frac{1}{2} I_{in}^2 R_g} \\ &\approx \frac{\frac{1}{2} (\frac{\omega_t}{\omega_0} I_{in})^2 \frac{1}{\omega_t C_{gd}}}{\frac{1}{2} I_{in}^2 R_g} \\ &= \frac{\omega_t}{4\omega_0^2 R_g C_{gd}} \end{aligned} \tag{3.4}$$

It can bee seen that the power gain decreases as the square of the operating frequency. Therefore, in a general sense, higher the output frequency, lower is the efficiency and harder is to generate power. The source of this square-law dependence can be traced to (3.3), where the output current falls inversely as the frequency ω_0. This can be easily understood, since with increase in frequency, the input capacitive impedance ($\frac{1}{\omega_0(C_{gs}+C_{gd})}$) goes down. Therefore, for the same input current and therefore same input power, the voltage perturbation V_{gs} and the output current $I_{op} = g_m V_{gs}$ falls inversely as the frequency.

A realistic transistor layout, specially in the nanometer region, involves much more extensive parasitics, and therefore it is often cumbersome and little enlightening to express f_{max} as an analytical function of all different parasitics. A measurement friendly way is to model the gain element in Fig. 3.4 as a two-port S-parameter block, as shown in Fig. 3.5 [43]. For such a case, different gain parameters can be defined under different input-output loading conditions. Two of them are of interest to us, since they also capture the high-frequency

figure of merit f_{max}. We define the maximum available gain G_{max} as the power gain under input-output conjugate match, which was assumed when we derived f_{max} from transistor small-signal model. We also define the Mason's invariant (U), as the power gain, under conjugate input and output match , after the device has been unilateralized with lossless reciprocal embedding [46]. Given the S-parameter (Y-parameter) matrix, the expressions for G_{max} and U, for a stable device, can be derived as [43],

$$G_{max} = \left|\frac{S_{21}}{S_{12}}\right| \left(K - \sqrt{K^2 - 1}\right) \tag{3.5}$$

$$U = \frac{|Y_{12} - Y_{21}|^2}{4(Re[Y_{11}]Re[Y_{22}] - Re[Y_{12}]Re[Y_{21}])} \tag{3.6}$$

where K is the Kurokawa's stability factor, expressed as $K = \frac{1-|S_{11}|^2-|S_{22}|^2-|S_{11}S_{22}-S_{12}S_{21}|}{2|S_{12}||S_{21}|}$ [46]. For unconditionally stable devices, $K > 1$.

Fig. 3.5 shows the simulated plot of G_{max} and U of a parasitic extracted 8 µm-wide transistor in IBM 45 nm SOI CMOS technology. The transistor is biased at an optimum current density of 0.3 mA/µm and laid out as eight 1 µm wide fingers in parallel. It can be seen that both the figures of power gain fall to unity at the same frequency (f_{max}) near 200 GHz.[2]. This is the definition of f_{max}. It is the frequency at which both G_{max} and U fall to unity. The parameter f_{max} successfully captures the high-frequency limits of frequency operation (atleast small-signal) in that, no power gain is possible above f_{max} between the input and output terminals of a device. This also implies that no self-sustained oscillation is possible beyond f_{max}, since no feedback topology can result in oscillation when the active device's intrinsic power gain is less than unity. *In summary, there is no power gain above f_{max} and therefore, no DC-single frequency RF power conversion is possible beyond f_{max} through a self-sustained oscillator.*

It can be noted that f_{max} is derived under the conditions of conjugate loading and lossless

[2]It can be seen that the G_{max} initially falls as 10 dB/decade, and after a certain frequency, starts falling as 20 dB/decade. The frequency at which the transition occurs is also the frequency the device becomes unconditionally stable ($K > 1$).

matching networks. Often in classical oscillator topology (cross-coupled, Colpitts etc.), the input and output terminals of the active device(s) are not conjugate matched. Moreover, all passive networks have losses associated with them. This implies that the maximum frequency of oscillation possible with any of the classical topologies with passive loss, is infact, less than f_{max}. The limitations in such topologies have been studied in [47]. It can also be noted that, the figure-of-merit f_{max} depends on the the biasing condition and physical layout of the device. Careful layout techniques can reduce distributed resistance, capacitance and achieve higher f_{max}. However, f_{max} is often quoted as a figure-of-merit of a technology, since it gives a rough estimate of the high-frequency limits of operation in that particular technology. In such a case, it is assumed that biasing and layout are both optimized for f_{max}.

With scaling, the high-frequency limits of operation of silicon technology has improved over the years, though not linearly. Digital CMOS technology has demonstrated f_{max} near 0.2 THz [112], SiGe HBTs have reached 0.45 THz [48], while InP HBTs and HEMTs have shown f_{max} near 0.6 THz and even 1 THz [49], [50]. Technology will continue to evolve, frequency limits of technology will be stretched and therefore, with a decade-wide bandwidth in THz to explore, a general method to synthesize and extract/radiate signals efficiently at frequencies above f_{max} of a technology is valuable. Distributed Active Radiation is such a technique of power generation and radiation above f_{max}, which is scalable with power and frequency, and also importable across silicon to III-V technologies.

3.1.2 Power Generation Above f_{max}

In the previous section, it was seen that power generation above f_{max} cannot be achieved frm input DC power in a single self-sustained oscillator. However, almost every integrated technology has inherent nonlinearities present in the operation of its active device, which can be exploited to generate harmonic power beyond f_{max}. A circuit block with converts power at one frequency into its harmonic power is referred to as a frequency multiplier. Various nonlinear techniques, devices and circuit topologies, such as varactor frequency multipliers [51], nonlinear transmission lines [52], FET multipliers, Schottky diode multipliers [53],

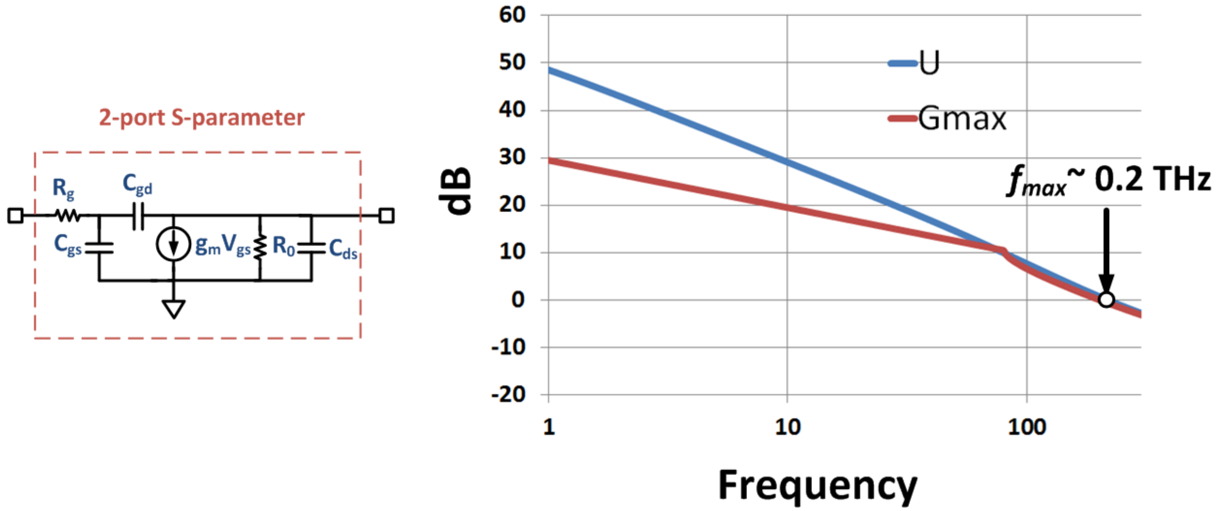

Figure 3.5: A 2-port S-pamareter model of the gain element. The figure also shows simulated maximum available gain G_{max} and Mason's Invariant U for a 8 µm-wide transistor (1 µm-wide finger) under optimum biasing conditions. Both measures of power gain fall to unity at a frequency of f_{max} near 0.2 THz.

injection-locked multipliers [117] can be found in literature. We will review some general characteristics to understand the tradeoffs for efficient frequency multiplication.

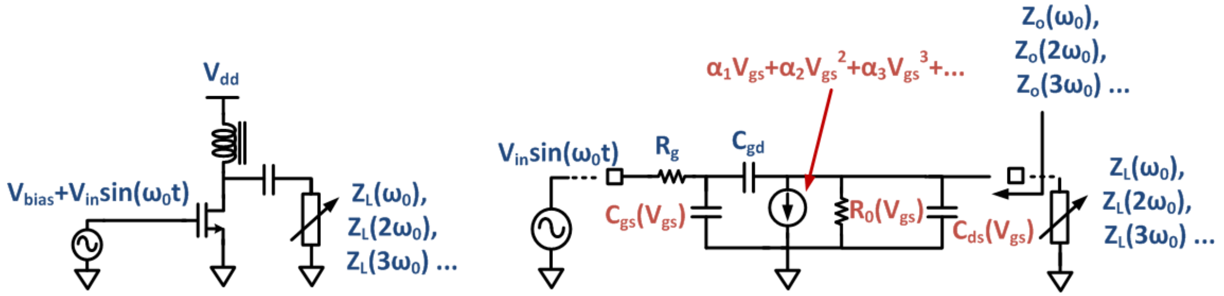

Figure 3.6: Nonlinear transconductance and capacitance are can be exploited to generate harmonic power above f_{max}. In such a nonlinear dynamical system, output loading needs to be optimized for different harmonics for maximum conversion efficiency.

Fig. 3.6 shows that a transistor, when driven into strong nonlinear region, generates higher harmonics due to its nonlinear transconductance, and voltage-dependent capacitance and output resistance. In order to maximize efficiency $P_{out}(nf_0)/P_{in}(f_0)$ for a given drive frequency of f_0, the output load Z_L has to be optimized over various harmonics. Assuming that we are interested in extracting the nth harmonic power, the output impedance $Z_L(n\omega_0)$ directly affects the power transfer of the nth harmonic. However, because of the feed-through

capacitance C_{gd} and nonlinear output-impedance which accomplishes frequency multiplication and nonlinear mixing, the nth harmonic current is also a function of currents at f_0 and other harmonics. A nonlinear harmonic-balance simulation needs to be carried out to optimize the conversion efficiency and an optimum matching network that presents the optimum Z_L over all different harmonics need to be presented at the output of the transistor. Fig. 3.7 shows simulated results of second-harmonic power generation at 300 GHz using the transistor of Fig. 3.5. The transistor is driven in common-source mode at 150 GHz and the output consists of R_L in parallel with L_L, and the plot shows the variation of the output power with the load, under a bias current of 2.5 mA from a 0.6 V supply.

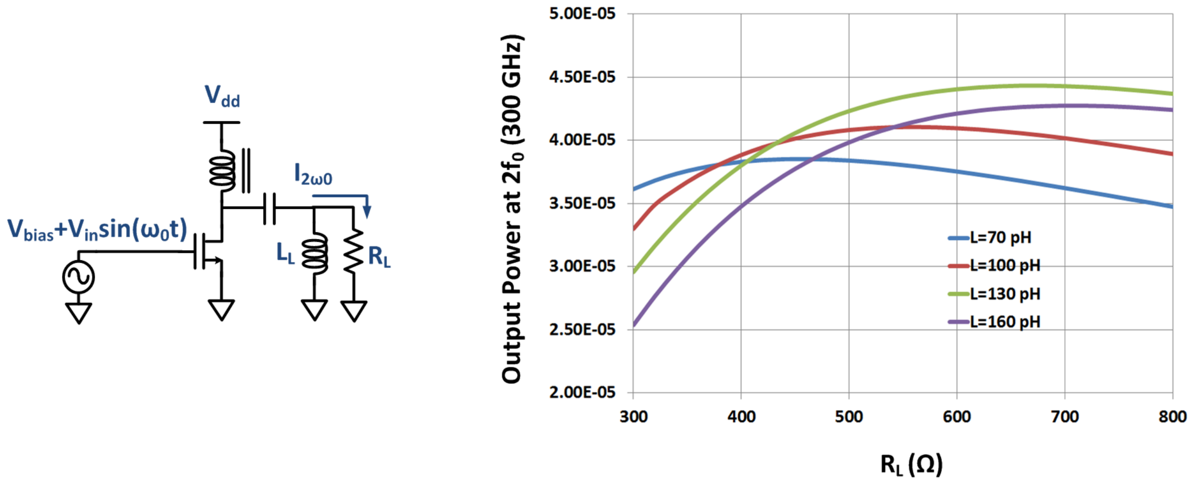

Figure 3.7: Variation of second-harmonic power at 300 GHz with the output load consisting of R_L in parallel with L_L.

It is to be noted that simulation carried out is only to give some insights into how output load affects harmonic conversion efficiency. At different harmonics, the output impedances do not have to look like a constant resistance in parallel with a constant inductance. More sophisticated networks can be synthesized which presents the optimum impedances at the different harmonics. However, such optimum networks can be impractical to realize at such high frequencies and be very lossy. One can do rough estimate on the optimum R_{opt} and L_{opt}. If we neglect the feed-forward current through C_{gd}, then from (3.2), we can derive

$$R_{opt} = \frac{C_{gs} + C_{gd}}{g_m C_{gd}} || R_0 \tag{3.7}$$

$$L_{opt} = \frac{1}{\omega_{2f0}^2 C_{op}} \tag{3.8}$$

where the small-signal parameters are derived from DC operating-point simulation as, g_m=11 mS, f_0=150 GHz, C_{gs}=5.5 fF, C_{gd} =1.8 fF, R_0=690 Ω. This gives a rough estimate of R_{opt}=240 Ω and L_{opt}=140 pH. The estimated vale of L_{opt} matches fairly well with the optimum value for maximum second-harmonic power generation in Fig. 3.7. The calculate value of R_{opt} is, however, different from the simulated results in Fig. 3.7, which is suspected due to ignoring nonlinear effects on output resistance, capacitance and using small-signal quiescent values in making a nonlinear estimate.

In summary, signal power above f_{max} can be ideally generated using a frequency multiplier, which exploits nonlinearity to generate harmonic power. However, this adds another block in the conversion chain. It consumes DC power in most cases and needs input and output impedance matching at THz frequencies, which can be very inefficient, lossy and prone to mismatches. In the next section, we will review the entire chain of conversion from DC-THz above f_{max} and discuss the challenges of extraction of such high-frequency signals from a silicon chip.

3.1.3 High-Frequency Power Extraction from Silicon

From our previous discussions, a frequency multiplier can be driven at frequencies below f_{max} to generate harmonic power above f_{max}, albeit at a lower output power. The entire chain of conversion from DC to power above f_{max} is illustrated in Fig. 3.8. We will summarize our observations here

- A oscillator converts DC power into RF power below f_{max}.
- A buffer amplifier isolates the oscillator from the multiplier and increases the power of the driving signal, to put the multiplier into deep nonlinear regions for higher efficiency.

- The buffer-multiplier interface needs to be power matched through a nonlinear simulation to generate the optimum drive power for the multiplier.

- Passive elements are very lossy at these frequencies. Lumped elements, such as inductors and capacitors, typically have self-resonance frequencies below THz frequencies. Distributed t-lines are often the passive elements of choice, but their ohmic loss often results in a substantial portion of the generated power being dissipated. Resonant matching can also lead to the architecture being prone to modeling inaccuracies, mismatches and parasitic scaling.

- The frequency multiplier needs to be presented the optimum impedance at different harmonics to maximize efficiency. The network, therefore, also needs to function as a filter which will allow only the desired harmonic to propagate and block the fundamental signal, which is typically an order of magnitude stronger. The ideal multiresonant network is often too complicated to realize at these frequencies, and the harmonic power generated at the multiplier output can suffer significant loss in this network itself.

- This approach with cascaded tuned elements does not scale well with frequency or output power. Higher output power will demand larger device sizes which will make it prone to parasitic scaling, mismatches, modeling inaccuracies and matching network detuning.

An efficient mechanism of generating THz power on chip is only half the puzzle solved, the extraction of the generated signal from the chip is also significantly challenging. At these frequencies, wirebonds or flip-chip interconnects add unacceptable amounts of parasitics. Fig. 3.9 shows typical configurations of wire-bonds and flip-chip interconnects with solder bumps. These interconnections work well in transferring signals out of the chip, upto a few 10s of GHz. The typical inductance of a 1 mm long wirebond is 1 nH [44]. At a frequency of 300 GHz, this implies an imaginary reactance of j1884 Ω. Matching with such high impedance is very challenging. Additionally, a slight variation in the bondwire configuration can lead

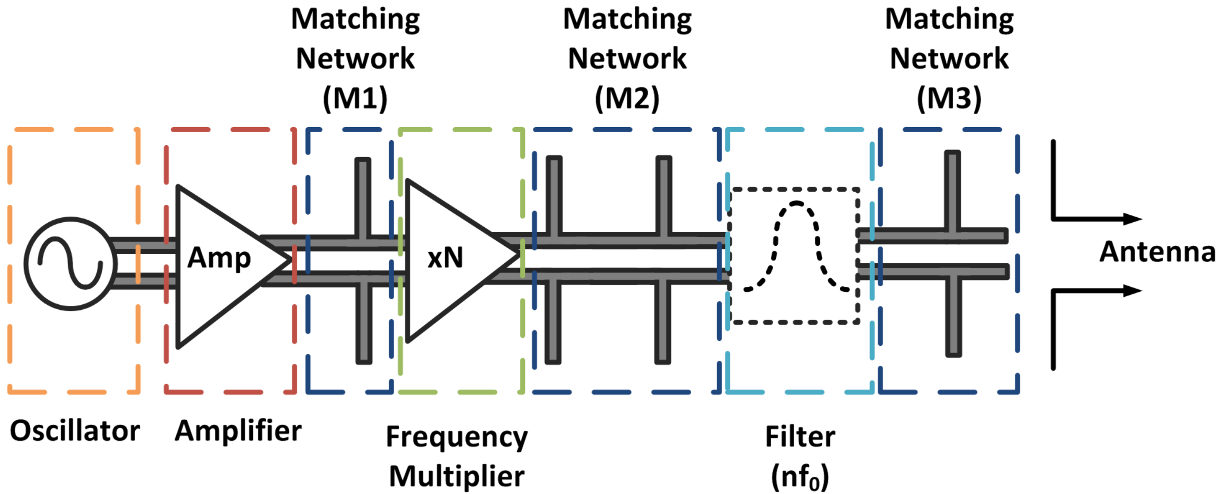

Figure 3.8: Chain of conversion from DC to signals at frequencies above f_{max}, consisting of cascaded chain of classical functional elements with tuned matching networks.

to substantial changes in its inductance and thereby, critically affect the resonant matching. More importantly, the bondwire might itself act as an antenna at these frequencies (λ_0 at 300 GHz is 1 mm $\sim$ bondwire length) and radiate the desired signal, even before it reaches an off-chip transmission line or an off-chip antenna.

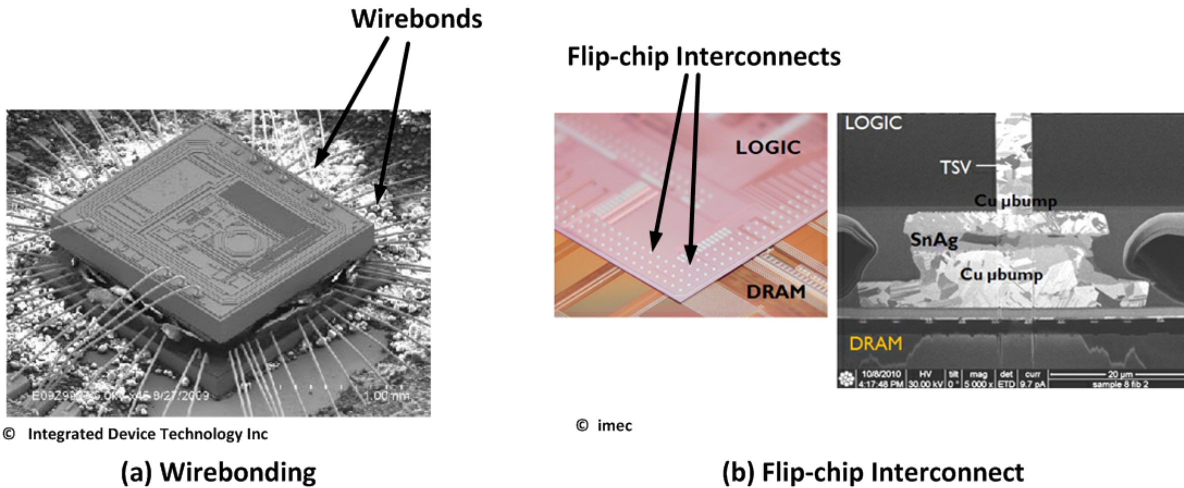

Figure 3.9: Wirebonds and flip-chip interconnects are typical ways of transferring signals out of a chip at frequencies up to few tens of GHz.

Fortunately, at mm-Wave and THz frequencies, the dimension of the silicon die becomes comparable to the wavelength corresponding to the frequency of operation (λ_{si}(300 GHz)$\approx$

300 µm). Therefore, it seems reasonable that antennas could be directly integrated on-chip and the signals could be radiated out from the die itself [54]. The antennas could be made from metal layers available with the chip fabrication technology and therefore radiating the THz signal directly from the silicon die seems the most reliable way. However, classical antennas which work well in free-space do not work well in silicon. Fig. 3.10 shows a cross section of silicon chip showing the back-end-of-line metal layers and a 250-300 µm (after initial thinning) of lossy silicon substrate ($\rho \sim 10$ Ω-cm). Therefore, when an antenna is realized at the interface between free-space and silicon, silicon substrate with its high dielectric constant ($\varepsilon_r = 11.7$) acts as an excellent dielectric waveguide, channeling most of the radiated power into itself. The excitation is often, collectively, referred to as the substrate/surface modes. Since the silicon substrate is lossy, part of the excited surface wave power gets lost and the rest leaks out in unpredictable ways reducing radiation efficiency drastically [72]– [75]. Typically, this is corrected using postprocessing, such as high-resistivity substrate options (for minimizing loss) and off-chip silicon lens that converts the substrate modes into radiative modes [76] and [54], as shown in Fig. 3.11. We will discuss, in details, the concepts of surface waves in the next chapter. However, for now, it can be concluded that classical antennas perform poorly in silicon due to changed boundary conditions and therefore, if we assemble all the parts in this block-by-block partitioned approach, the input DC-radiated THz efficiency is likely to be suboptimal. An example of such a system, with cascaded multipliers and on-chip antenna, achieved an output power of 1.1 µW at a frequency of 820 GHz (1.9x f_{max}), with 3.7 W input DC power and 25 mW input RF power at 18 GHz, implying a conversion efficiency of less than 0.00003 % from DC-THz [48]. Locally optimizing the design blocks forces us to work in an artificially created narrower design space and overlooks the innovations which may lie in a broader design space [55].

In summary, the two major challenges in the realization of a high-power integrated terahertz source in silicon are signal generation and extraction of the signal from the silicon die. Both of these two processes have to be efficient for the realization of integrated source to be feasible especially in any kind of portable applications. The relevant parameter to consider here is the efficiency of conversion from input DC power to total radiated Terahertz

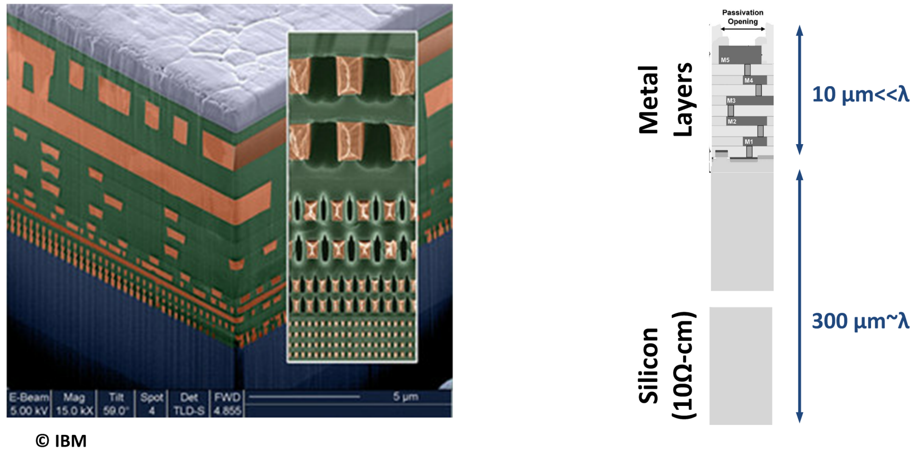

Figure 3.10: Typical cross section of silicon chip consisting of back-end-of-line metal layers and nearly 250–300 µm of lossy doped silicon ($\rho \sim 10\ \Omega$.cm.)

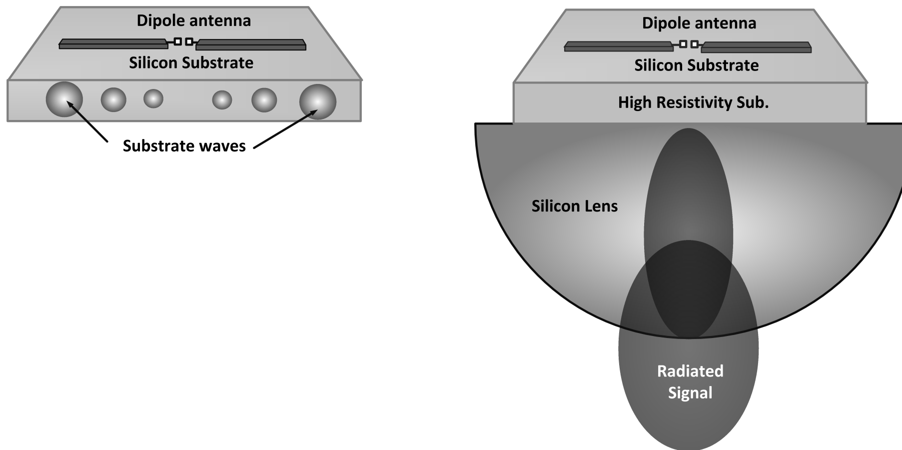

Figure 3.11: On-chip antennas on high-dielectric silicon substrate can excite strong surface waves, which either get lost or leaks out in unpredictable ways. An off-chip silicon lens can convert the surface modes into radiative modes, by eliminating total-internal reflections in the planar substrate.

power and/or Effective-isotropic-radiated power (EIRP). If P_{rad} is the total radiated power with beam directivity D, then ($EIRP = P_{rad} \times D$). EIRP is an useful metric, since at the receiver end, the power captured by the front-end antenna is directly proportional to EIRP of the transmitter. A narrower beam with more focussed energy transfer more power to the receiver than a broader beam with the same radiated power.

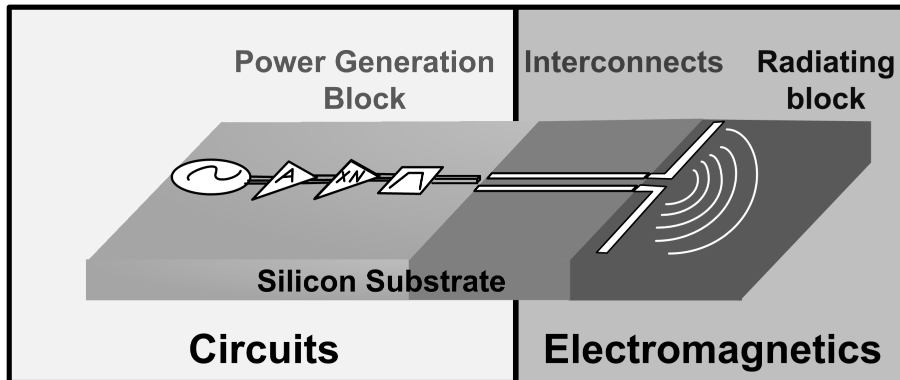

Figure 3.12: Partitioned approach follows the Divide-and-rule design philosophy. Specifically, for the problem at hand, it separates system design into electromagnetics and circuits, each of which consists of locally optimized standard functional blocks.

3.2 Inverse of Maxwell's Law: A Reconfigurable Electromagnetic Surface and Design Evolution of Distributed Active Radiator

Let us analyze the problem at hand from a higher level of abstraction. We are interested in generating radiated electromagnetic fields at THz frequencies of certain strength at a certain far-field/near-field distance. By Maxwell's laws, the radiated fields depend on the surface (metal) currents in the silicon chip. Silicon technology offers the capability of integration of very large number of high-speed transistors and layers of BEOL metal stacks with fine lithographic resolution. Therefore, it may be possible to create complex current configurations and therefore finely controlled electromagnetic field profiles, using a judicious combination of actives and passives, which may not be possible otherwise for a much constricted design

space such as a single-port passive antenna element or in a block-by-block design approach. The concept is illustrated in Fig. 3.13.

Let us suppose that we are interested in creating an electromagnetic near/far-field profile, which needs to be synthesized and possibly dynamically controlled or modulated for some form of versatile communication or sensing mechanism. If the electromagnetic fields are physically realizable, then there exist surface current configuration(s) on the silicon chip, that result in the desired field profiles. The classical approach to system design, as illustrated in Fig. 3.12, is the divide-and-rule approach. The system gets partitioned into the signal generation (circuits part) and radiation (electromagnetics part) at the system level, and each function is accomplished through a cascaded series of standard functional blocks (Fig. 3.12). This eases system design and enables modularity, but also forces us to work in a constrained design space. We remove these artificial partitions between circuits, electromagnetics, antenna and take an inverse Maxwellian approach. We solve for the desired surface currents and then attempt to directly synthesize those surface currents on the silicon chip, with an on-chip control system which may consist of high-frequency THz circuits, complex digital control and custom passive elements. In theory, by actively controlling the surface currents, one may conceive of a reconfigurable electromagnetic surface near the silicon chip, which can be a versatile tool for many practical applications for sensing, imaging and communications.

As a conceptual philosophy, we are essentially taking advantage of the opportunities of silicon integration, which comes with practically unlimited number of transistors, integrated capability of sophisticated digital signal processing and increasingly improved high-frequency transistors. This opens up a new and broader design space, where a holistic approach combining electromagnetics, analog, digital and THz circuits, antenna, control theory, communication, device physics, can allow us to innovate new systems and architectures, which could not be done with the constrained partitioned approach. The design evolution of the Distributed Active Radiator will follow this holistic approach of combining many such apparently partitioned disciplines. We will follow the Inverse Maxwellian approach and begin by formulating surface currents and build up harmonic power generation and radiation mechanisms from basic principles.

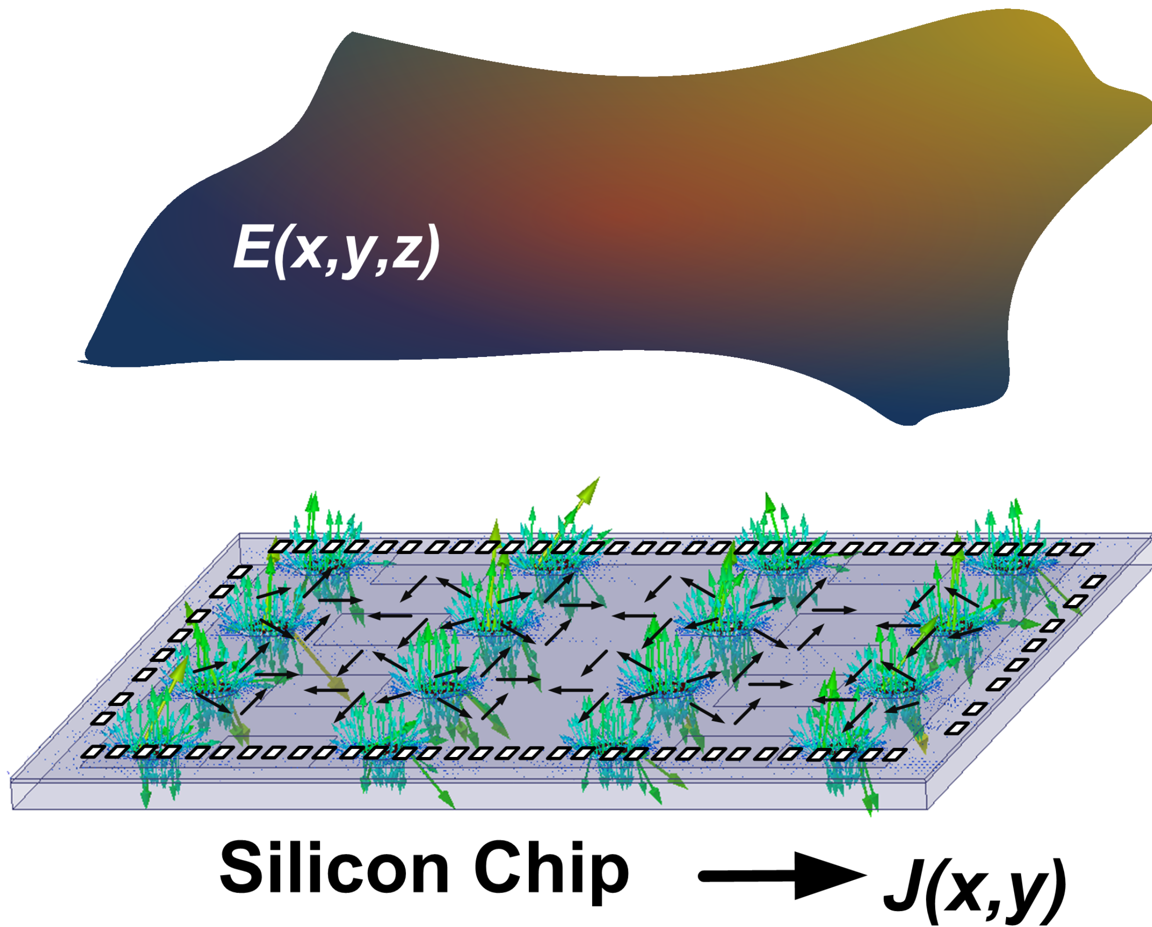

Figure 3.13: Inverse of Maxwell's principle: Formulate the surface currents required to generate a far-/near-file profile and actively synthesize the surface currents with a combination of actives and passives. We remove the artificial between among circuits, electromagnetics, antenna and expand the design space beyond the classical partitioned or block-by-block approach.

Let us suppose that we would like to generate and radiate a pure tone at a frequency above f_{max}. Since self-sustained oscillation at a single frequency is not possible above f_{max}, generating power above f_{max} essentially relies on extracting power from harmonics. The important question is how do we do it efficiently?

3.2.1 Conceptual Synthesis of Fundamental and Harmonic Surface Currents in Silicon

Let us suppose that it is possible to build oscillations at a frequency f_0 near f_{max} and we would like to radiate the second harmonic $2f_0$ (above f_{max}) by filtering the strong fundamental and the other undesired harmonics. Instead of any passive filtering with lossy elements on chip, we would try to achieve this in free-space. Two current elements which are out-of-phase, when placed very closely to each other, cancel their radiated fields, and therefore constitute a poor radiator or a filter as shown in Fig. 3.14. This is primarily the reason why on-chip transmission lines are poor radiators since, the forward and return current being out-of-phase and closely placed cancel their individual radiated fields. However, if the currents are in-phase, they add up their radiated fields. Small loops are, however, inefficient radiators. Let us expand the loops such that their circumferences equal the wavelength at $2f_0$ which we wish to radiate as shown in Fig. 3.14. Therefore, we have two loops sustaining two traveling-waves at $2f_0$ which propagate in phase and radiate continuously and complete $360°$ in one loop traversal. Therefore, we would like to synthesize a transmission-like behavior to filter the fundamental frequency f_0 and a radiative behavior to extract the second harmonic $2f_0$. We will attempt to achieve this in the same electromagnetic structure.

3.2.2 Active Control of Currents for the Desired Harmonic Radiation

In order to sustain radiating traveling-waves at $2f_0$ which constantly lose power, currents at $2f_0$ need to be injected into the loops at the right phases. This is explained in Fig. 3.15 where

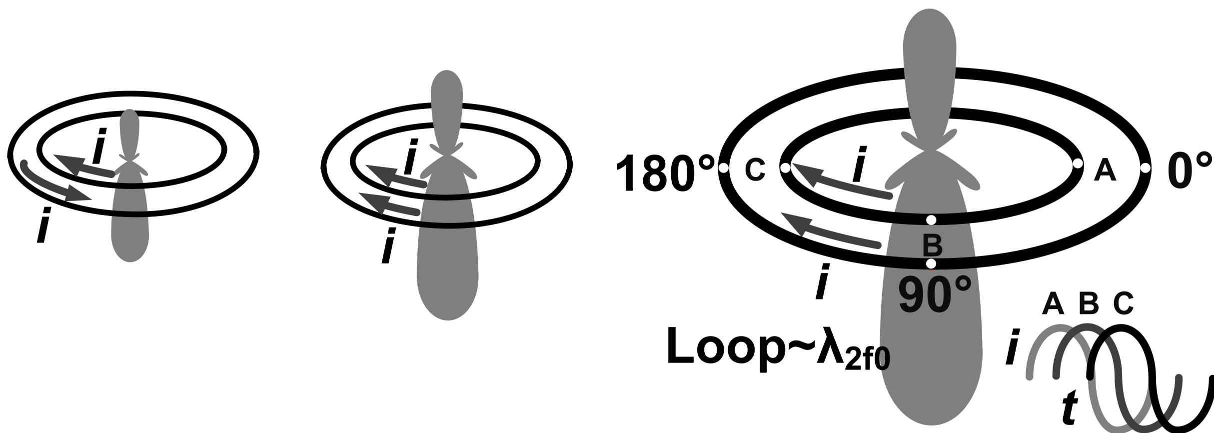

Figure 3.14: Conceptual synthesis of fundamental and harmonic currents for free-space filtering of the fundamental signal and efficient radiation of the desired second harmonic signal.

$2f_0$ currents at 0°, 90°, 180° and 270° are injected into the loops, at appropriate locations and equi-spaced, to complete the total phase change of 360° over the loop [3]. Since the second harmonic $2f_0$ is presumably higher than f_{max}, currents at $2f_0$ cannot be generated directly from DC. This is where we exploit the nonlinearities inherent in integrate circuit technologies efficiently to extract higher harmonics. This is illustrated in Fig. 3.16.

As illustrated in Fig. 3.17, transistor pairs were driven differentially at the fundamental frequency f_0 ($< f_{max}$) into strong nonlinear regions to generate the common mode currents at the second harmonic $2f_0$. Due to frequency multiplication, phase progression of the driving signals at f_0 at the gates of the transistor pairs is half of that of the second harmonic drain currents at $2f_0$. Therefore, as illustrated in Fig. 3.17, transistors were driven differentially at 0° and 180°, 45° and 225°, 90° and 270°, and 135° and 315° to generate $2f_0$ drain currents at 0°, 90°, 180° and 270°, respectively, as shown in Fig. 3.15. We will discuss later, the method for generation of the fundamental frequency signal at the required phase progression. For now, we assume that such signal and phase synthesis is possible. In summary, if transistor pairs were driven differentially at the appropriate phase progression, as shown in Fig. 3.17, it is possible to sustain traveling-waves at the second harmonic $2f_0$ on both the loops which propagate in-phase.

[3]We consider the case of four current injection ports, but there can certainly be multiple injection currents at the appropriate phases distributed over the loop.

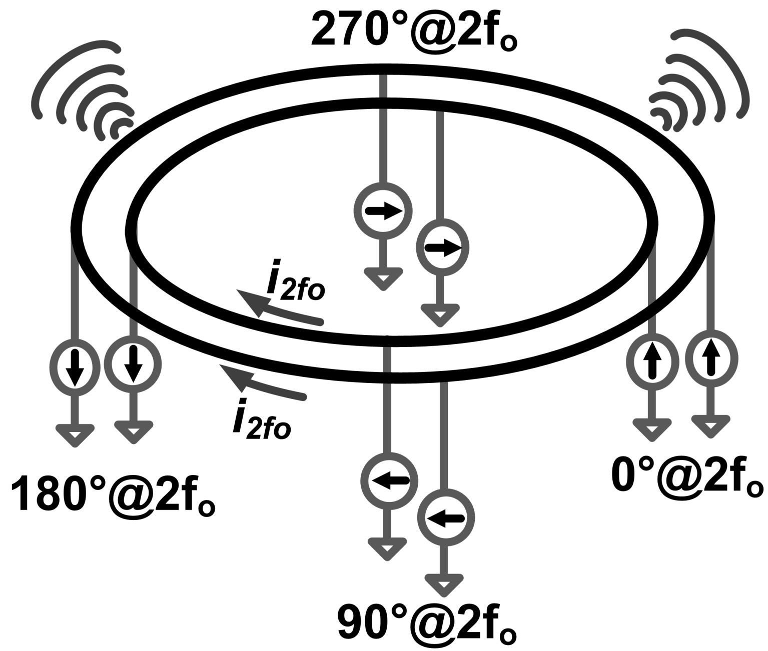

Figure 3.15: Second harmonic current pumped in the appropriate phase progression to maintain in-phase traveling and radiating waves in two adjacent loops.

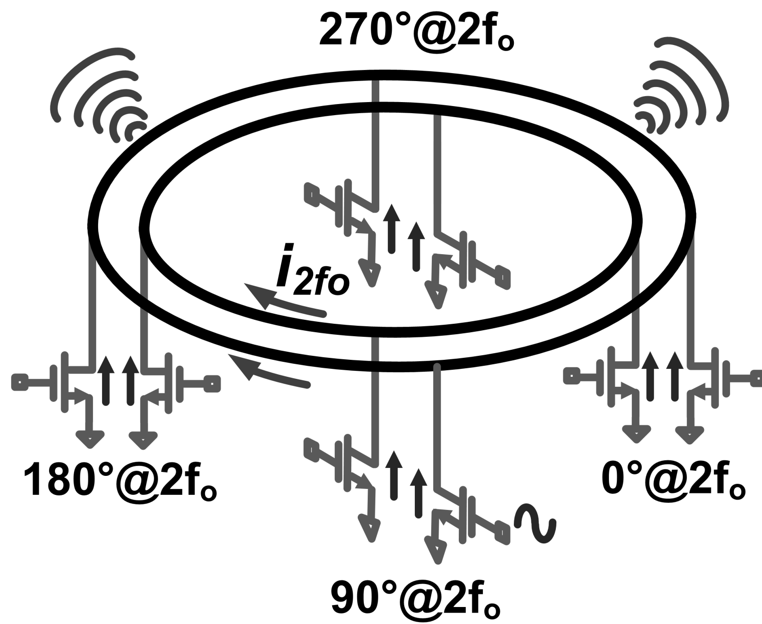

Figure 3.16: Second harmonic currents above f_{max} are generated from nonlinearities in conductance and capacitance in transistors.

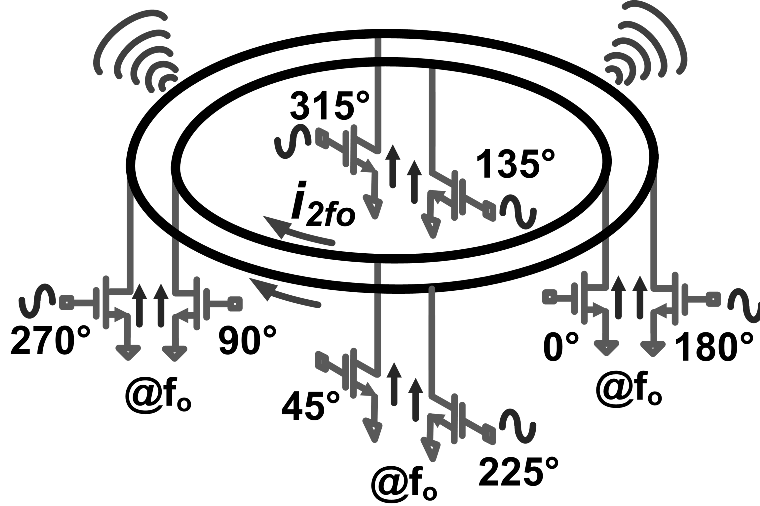

Figure 3.17: Pseudo-differential pairs driven strongly at the fundamental frequency to create in-phase second harmonic currents pumped into the distributed radiating loops.

3.2.3 Radiative Mechasim for the Desired Harmonic Radiation

The radiative mechanism of the traveling-wave loops can be understood by analyzing the entire current configuration at $2f_0$ including the return path through the transistor pairs. If this path is provided by a ground plane as shown in Fig. 3.18, then the loops will essentially behave like microstrip lines for all frequencies and therefore be poor radiators for the same reason on-chip transmission lines are bad radiators. The return $2f_0$ currents from source transistor pairs to sink transistor pairs, will flow in close proximity with the forward propagating waves on the loop. The radiated fields of the two out-of-phase currents at $2f_0$ will cancel. It is apparent that the path of the return current with respect to the forward propagating wave decides how the radiated fields add up. *We, therefore, turn the transmission line behavior into radiative behavior by modifying the manner in which the return current flows.*

Fig. 3.19 illustrates the concept. We follow the same principles of Inverse Maxwell's laws and we formulate the surface currents required to synthesize the desired radiated fields at $2f_0$. This is achieved by creating a phase shifted return path with respect to the forward path and create an electromagnetic configuration which, in totality, behaves like a radiator, but only for $2f_0$. We achieve this by removing the ground plane from below by creating an aper-

ture opening, and channelize the return through an extended path length, creating a phase rotation of 90° as shown in Fig. 3.19. Therefore, instead of two out-of-phase current loops canceling their radiated fields, we have two concentric current loops in phase-quadrature and they add up their power in space. In this way, be reconfiguring the forward and return paths, we modify the transmission line behavior in Fig. 3.18 to radiative behavior in Fig. 3.19. The two loops, along with the ground plane, sustain traveling-waves at $2f_0$, and together they radiate in a distributed fashion.

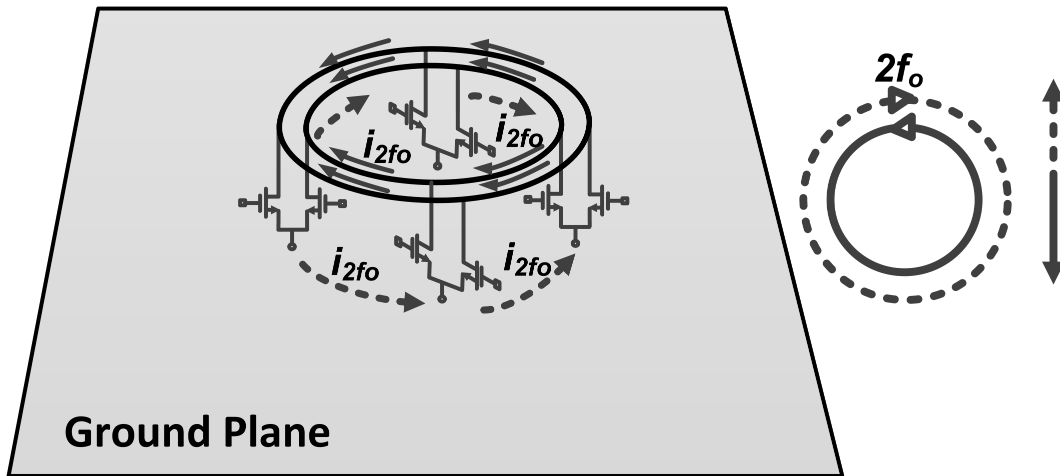

Figure 3.18: The second harmonic return current from the actives channelized through a ground plane. The return currents on the ground are out-of-phase with the forward currents on the loop canceling most of the radiated fields.

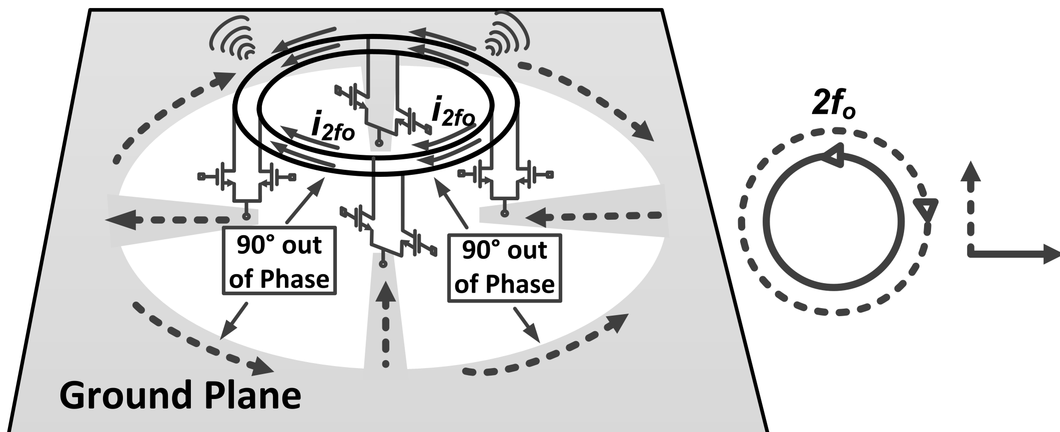

Figure 3.19: The second harmonic return current from the actives channelized through a longer path through a ground aperture plane, creating a 90° phase difference between forward and return path. The radiated fields of two concentric loops add in quadrature in free-space, creating efficient radiation out of the chip.

One can note that as a traveling-wave sets up at the desired second harmonic frequency of $2f_0$, due to phase-controlled current injections by the active devices, it continuously leaks energy in the form of radiation at the desired frequency of $2f_0$. The power at $2f_0$, injected in form of currents by the transistors, therefore does not suffer from the usual propagation loss incurred in the matching networks, filters from the source of generation to the location of radiation in a traditional design. Instead, it immediately gets radiated out as soon as it is generated as demonstrated in Fig. 3.20. The electromagnetic fields from the loop couples to the slot, finds the least impedance path through the high dielectric silicon substrate and comes out from the back side as circularly polarized radiation, because of the traveling-wave nature as shown in Fig. 3.20.

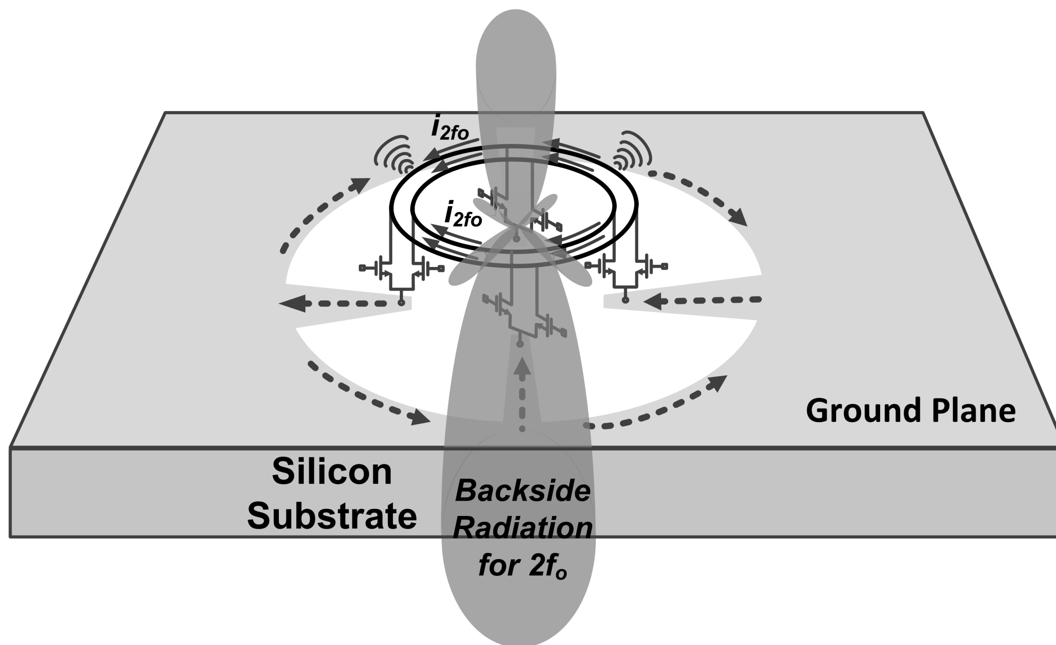

Figure 3.20: The traveling-wave nature of the currents creates circularly polarized radiation coming out form the backside of the silicon die (ε_r=11.7).

3.2.4 Active Control of Currents for End-to-End DC-THz Conversion

We will now address the synthesis of the multiphase differential gate drives at the required phase progression, as shown in Fig. 3.17. Overall, we are interested in putting only DC power into the system and generating all high-frequency signals inside. We generate the drive signal at f_0, and all the required polyphases from the radiating loops themselves. No high-frequency signals are sent from off-chip and in this way we achieve a complete DC-radiated $2f_0$ ($> f_{max}$) conversion.

To create a differential swing at the gates we cross couple the transistors and criss-cross the loops into a Mobiüs strip as shown in Fig. 3.21. This creates a condition where traveling-wave oscillation sets up at a frequency f_o, such that the total loop phase is 180° [56]. The length of the loop, along with the loading parasitics of the transistors, determine the self-oscillation frequency (f_0). The loops act as differential transmission lines for f_o and all its odd-harmonics, which carry the local forward and return currents. The adjacent currents are out-of phase and they cancel the radiation at the fundamental frequency of oscillation f_o and at all its odd-harmonics. As the fundamental wave propagates and creates a differential swing at the gates of the actives, second harmonic currents at $2f_0$ are injected in phase in both the loops and they leak energy continuously. In summary, as soon as the transistor pairs are biased appropriately through the cross-connected loop, a traveling-wave oscillation sets up at f_o, but the fundamental signal gets filtered in space along with all other odd harmonics. The second harmonic wave at $2f_o$, pumped in by multiple active devices in a distributed fashion, travels in phase and radiates efficiently and continuously as it propagates. This leads to a high DC-THz conversion efficiency *and by actively manipulating the surface currents at different harmonics, the same loop behaves as a actively pumped resonator for the fundamental and all odd harmonics, and behaves like a multiphase excited distributed radiator for second harmonic.*

In summary, the distributed active radiator allows signal generation, frequency multiplication, filtration of undesired harmonics and radiation of the desired harmonic, simultane-

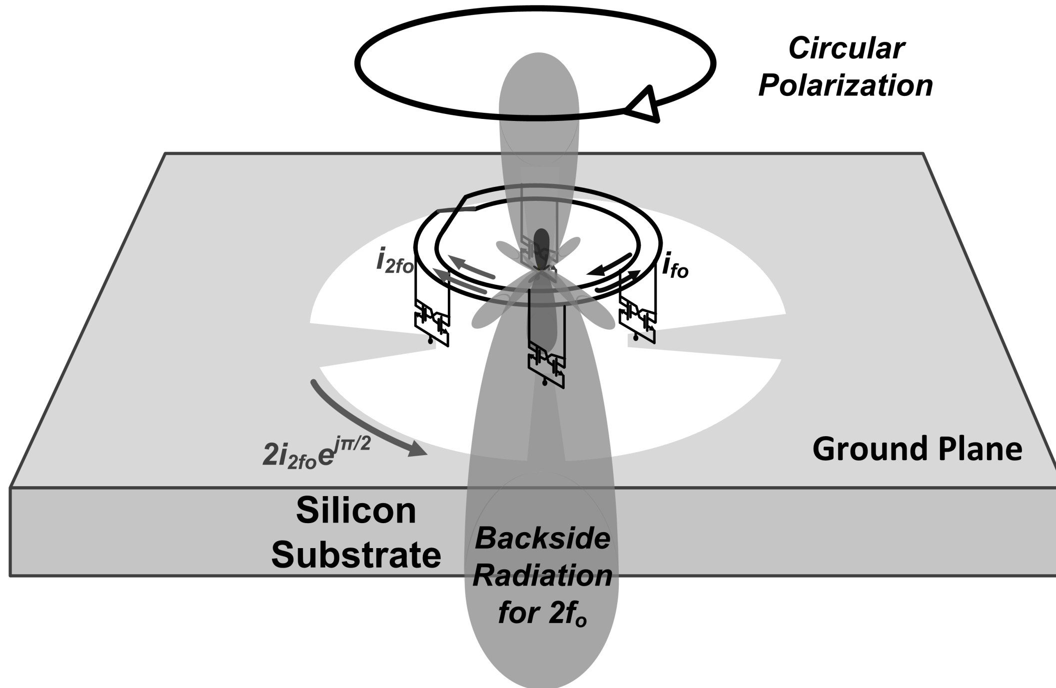

Figure 3.21: Distributed active radiator: Electromagnetic structure strongly coupled with actives achieving signal generation from DC, frequency multiplication, efficient radiation of desired harmonic and free-space filtering of undesired harmonic simultaneously.

ously, all in a compact footprint. The DAR has the following features which addresses some of the challenging problems in power generation and radiation at these frequencies in silicon.

- The DC-THz conversion efficiency is high, since the second harmonic power does not suffer from the usual propagation loss in matching networks, filters from the source of generation to the location of radiation, as in a conventional partitioned design. The power gets immediately radiated as soon as it is generated. The same loops act as a resonator for the fundamental and as distributed radiator for the desired frequency.

- The multiport current injection into the radiating structure in DAR, unlike a conventional single-port driven antenna, allows power combination of several transistors without suffering from parasitic scaling which occurs when all the power transistors are lumped in one place. The distributed design makes the design robust and less sensitive to modeling inaccuracies and process variations.

- The design is symmetric and all transistors see the same impedance. There are no

separate matching networks for maximum harmonic generation. The drain nodes of the cross-coupled pairs see a resonant tank impedance for the fundamental frequency of oscillation and radiation resistance for the desired harmonic frequency. As we shall see, the design encompasses the optimum impedance for maximum harmonic power generation.

- The traveling-wave nature of the DAR creating full-wavelength radiator results in a major part of the surface waves getting canceled, which is a major bottleneck of classical antennas in integrate circuits. We will discuss this, in great details, in Chapter 4.

3.2.5 Design, Simulation and Optimization

The DAR achieves four functions namely signal generation from DC, frequency multiplication, filtering and radiation simultaneously through a careful control of harmonic currents in a electromagnetic structure strongly coupled with actives. The design of the structure, however, can be partitioned into a logical step-wise procedure.

The frequency of oscillation is set by the length of the loop and the capacitive loading of the transistors. At the fundamental frequency, the loop behaves like a differential transmission line of characteristic impedance say Z_0, which is periodically loaded with differential capacitance of the cross-coupled pairs say C_0. Therefore the phase shift θ experienced by the fundamental signal at frequency f_0 as it flows through the t-line of length l loaded in the middle with capacitance C_0 is given by

$$\cos(\theta) = \cos(\beta_0 l) - \pi f_0 C_0 Z_0 \sin(\beta l) \tag{3.9}$$

where β_0 is the propagation constant of the unloaded transmission line at frequency f_0. The periodic loading results in a finite cut-off frequency of the line, resulting in dispersion. The dispersion directly affects the propagation of the fundamental frequency and the odd harmonics for which the structure behaves like a transmission line. The second harmonic signal injected by the actives, however does not see a transmission line but rather a dis-

tributed radiative structure, whose properties are dependent on the aperture and the ground plane configuration which carries the return current, as shown in Fig 3.16. In this design, four active cross-coupled pairs, are distributed across the DAR as shown in Fig. 3.17. The cross-coupled pairs consist of transistors 7.5 µm wide, which results in a differential $C_0 \approx$ 16 fF. The spacing of the loops in the DAR are chosen to be 5 µm on the top 2.1 µm thick Al layer, leading a $Z_0 \approx 80\ \Omega$. With these parameters, the mean radius of the DAR can be derived to be 85 µm from (3.9) for a desired fundamental frequency of oscillation of 140 GHz.

Fig. 3.22 illustrates how each of the active transistor cells see the electromagnetic structure at different harmonics. At the fundamental frequency of oscillation (and all odd harmonics, for that matter), each cross-coupled pair, essentially, sees a resonator with a quality factor of the differential transmission line, *i.e.*, $Z_{f0} = Z_{osc} = R_{osc} + jL_{osc}$, where the differential inductance $2L_{osc}$ resonates with C_0 at f_0 and R_{osc} is contributed by the ohmic loss of the differential t-line.

At the second harmonic, the transmission line behavior is masked. The differential swing at the fundamental frequency creates in-phase second harmonic currents I_{2f0} due to transconductance and capacitance nonlinearity as shown in Fig. 3.22. The drains of the transistors see a radiative impedance $Z_{2f0} = Z_{ant} = R_{ant} + jL_{ant}$, where R_{ant} represents the radiation resistance of the DAR, which results in second harmonic power radiating out of the chip. For maximum second harmonic power generation, there exists a optimum load-pull impedance which the drain of each transistor would wish to see. The radiative impedance Z_{ant} is a function of the aperture opening diameter as well as the width of the metal leads which connect the source of the gm-cells with the ground as shown in Fig. 3.19 and Fig. 3.22. In the limiting cases, when the aperture diameter tends towards zero, the structure becomes similar to Fig. 3.18 and radiation efficiency reduces to near zero. For a large ground aperture, the inductance of the connecting leads affects the second harmonic power generation. In this design, the ground aperture diameter is chosen to be 140 µm and therefore the radiated second harmonic power per DAR is is given by

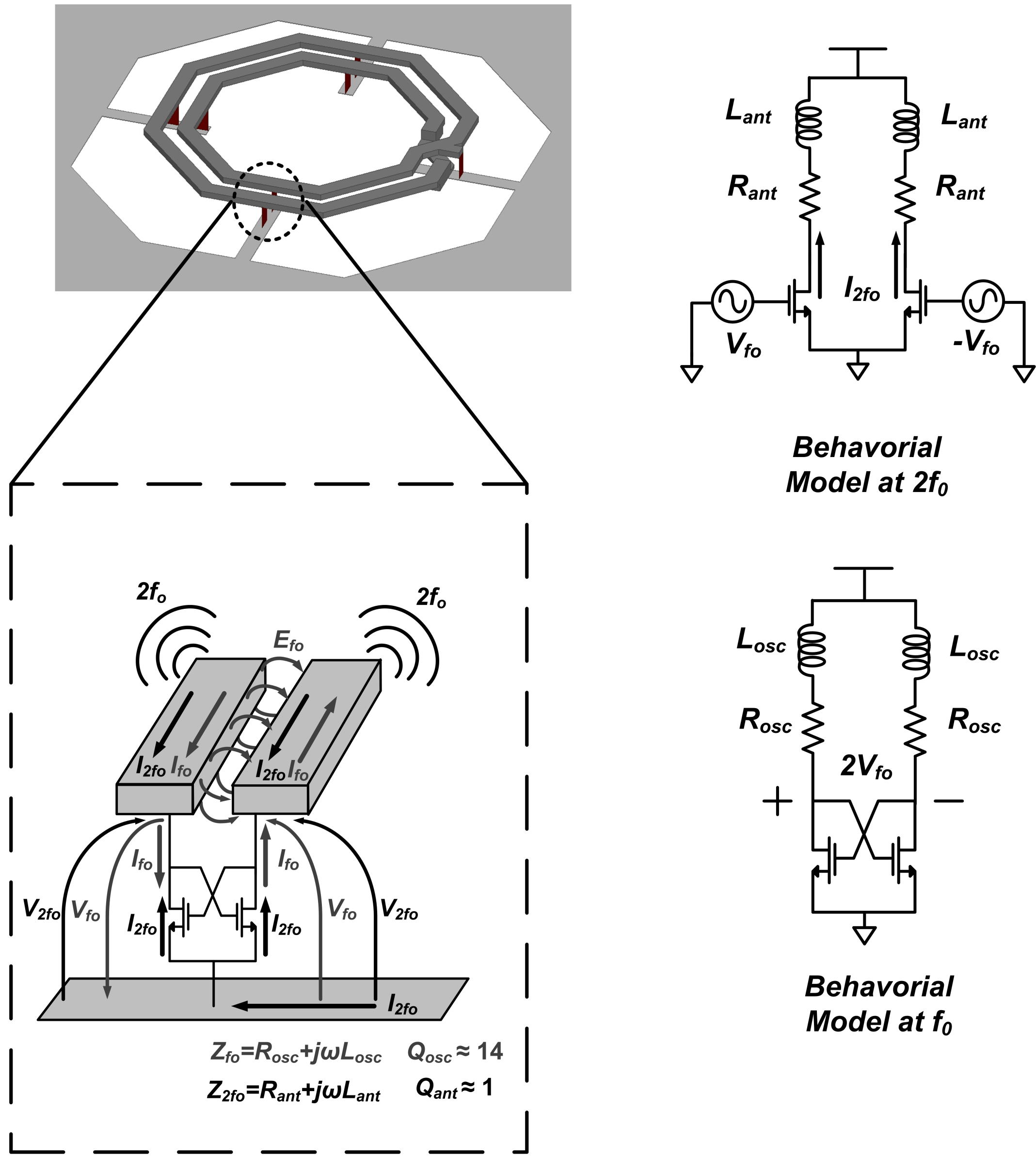

Figure 3.22: The electromagnetic simulation structure of DAR with 8 ports. Harmonic currents are designed to flow in such a way that each transistor, in the cross-coupled pair, sees a resonator at the fundamental frequency and a radiative impedance at the second harmonic.

$$P_{radiated}(2f0) = 4\eta_{2f0}{I_{2f0}}^2 R_{ant} \tag{3.10}$$

where the simulated radiation efficiency $\eta_{2f0} \approx 35\%$ and I_{2f0} is the amplitude of the second harmonic current injected into the DAR as shown in Fig. 3.22. To calculate fundamental power suppression, the total radiated fundamental power can be calculated to be,

$$P_{radiated}(f0) = 4\eta_{f0}{I_{f0}}^2 R_{osc} \tag{3.11}$$

where the simulated radiation efficiency $\eta_{f0} \approx 0.1\%$, I_{f0} is the amplitude of the fundamental frequency current injected into the DAR.

An electromagnetic and circuit cosimulation is carried to capture the signal generation, frequency multiplication, radiation and filtering effects simultaneously. As shown in Fig. 3.22, a 3D electromagnetic simulation with 8 ports is carried out, where the ports signify the terminals of the cross-coupled pairs. A finely swept S-parameter upto a few harmonics of the fundamental is exported to spectre-RF simulator and a harmonic balance analysis is carried out with the extracted models of the negative gm-cells. This captures the self-sustained oscillation, currents and voltages of higher harmonics and also gives the total first and second harmonic power injected into the DAR. The electromagnetic simulation is revisited with the magnitude and phases of current injections at different harmonics to ascertain the radiation efficiency, radiation patterns, total radiated power and EIRP.

We will address a two particular questions, which have been found to arise frequently in mind of people who have followed this work.

How is a DAR different from a loop antenna?

It is important to emphasize that this actively coupled electromagnetic structure is not a reciprocal network and thereby, fundamentally differs from all passive antennas. The multiphase and multiport injected currents by active devices, sustain a traveling-wave in the two core loops, which induce phase-shifted return path in the ground plane. The combined structure, together, radiates out from silicon in a circularly polarized fashion. In a typical loop antenna, with one port excitation, a standing wave pattern in the current sets up with

nulls and maximas distributed over the one-wavelength long antenna. Further, the DAR is a nonlinear structure which combines radiation with efficient frequency multiplication. Additionally, the electromagnetic structure has an active feedback system which generates a traveling-wave oscillation from DC power, unlike a passive radiator. Due to such active manipulation of currents, the DAR has the special property of being an efficient radiator only at the second harmonic, but behaves like a transmission line resonator at the fundamental frequency.

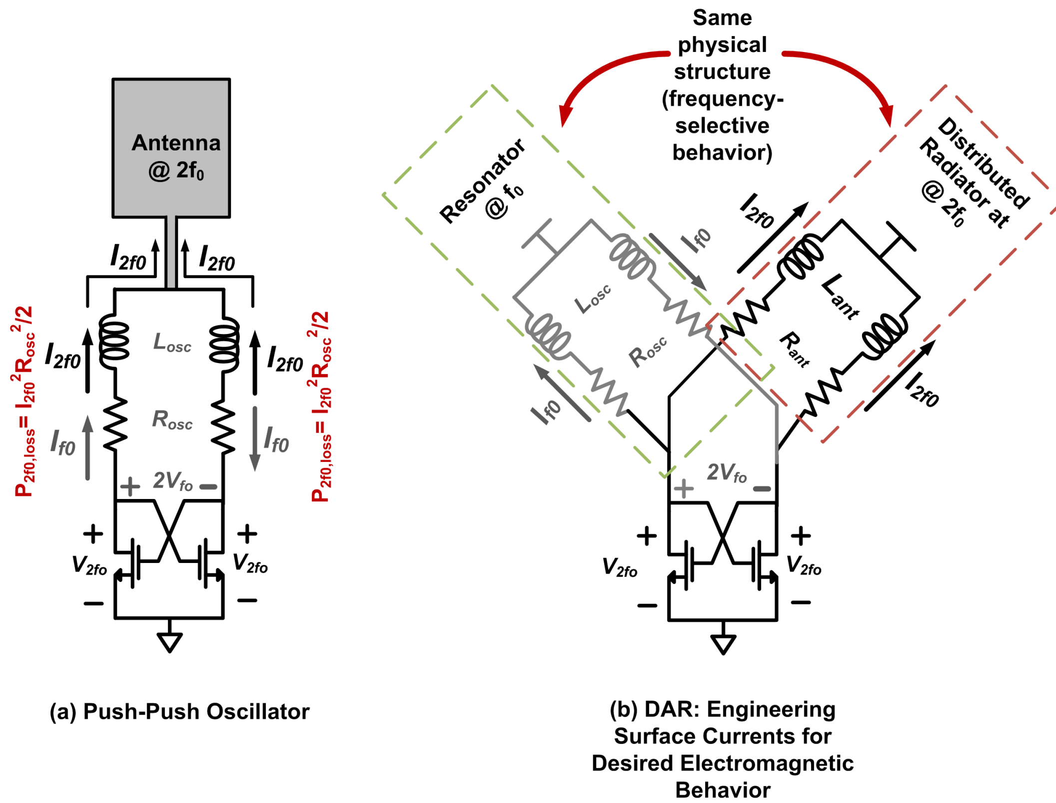

Figure 3.23: A push-push oscillator with an antenna connected at the common-mode point can channelize the second harmonic-current ($2f_0$) to radiate out, after suffering losses in the resonator. In a DAR, the resonator is transparent to the second harmonic current I_{2f0}. Due to the manipulation of surface currents, the same electromagnetic structure behaves like a radiator, and therefore, the second harmonic power gets immediately radiated out instead of suffering losses in the passives.

How is a DAR different from a push-push oscillator with an antenna?

A push-push oscillator with an antenna connected at the common-mode point can channelize the second-harmonic current ($2f_0$) to radiate out, as shown in Fig. 3.23. The $2f_0$

current in a push-push oscillator flows through the same resonator tank and suffers the ohmic loss in the inductor $P_{loss}(2f_0) = I_{2f0}^2 R_{osc}$, as shown in Fig. 3.23. In a DAR, the resonator is transparent to the second harmonic current I_{2f0}. Due to the manipulation of surface currents, the same electromagnetic structure behaves like a radiator, and therefore, the second harmonic power gets immediately radiated out instead of suffering losses in the passives. This is explained in Fig. 3.23. The multi-port, multi-phase excitation of the DAR helps us to combine the output power of several active devices, without suffering from parasitic scaling, which makes it difficult to scale the output power of a push-push oscillator.

3.2.6 Electromagnetic Simulations

Electromagnetics simulations are carried out in a 3D EM software, HFSS and capture radiation properties, current configuration and S-parameter models. Fig. 3.24 illustrates an instantaneous current configurations at the fundamental frequency showing the forward and return currents on the loops, and almost no current in the ground plane structure. However for the desired radiated harmonic frequency of $2f_0$, Fig. 3.25 shows the instantaneous current configurations illustrating in-phase currents on the loops, and near 90° phase-shifted currents near the ground plane aperture.

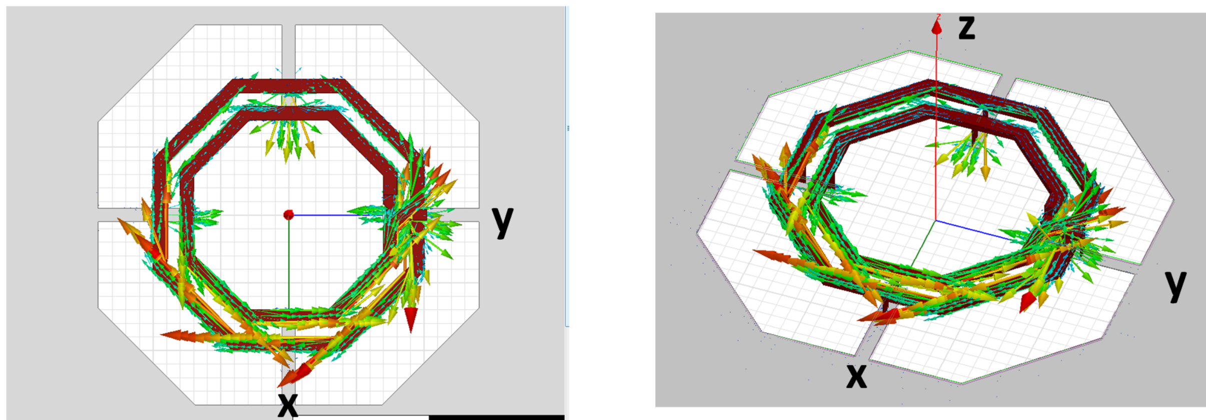

Figure 3.24: Instantaneous current configurations at the fundamental frequency showing the forward and return currents on the loops, and almost no current in the ground plane structure.

The electric field profile, which is rotationally symmetric about the z axis, is shown in

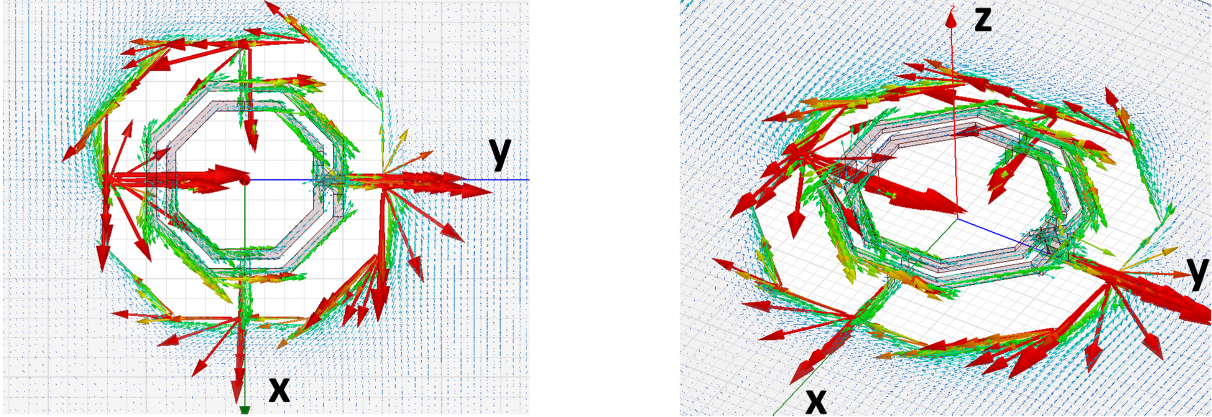

Figure 3.25: Instantaneous current configurations at the radiated second harmonic frequency showing in-phase currents on the loops, and near 90° phase-shifted currents in the ground plane structure.

Fig. 3.26. The radiation pattern can be seen to to mostly directed out of the back of the chip. Fig. 3.26 also illustrates instantaneous E-field in the y-z plane for the current configuration shown in Fig. 3.25. The magnetic field profile, which is also rotationally symmetric about the z axis, is shown in Fig. 3.27. Fig. 3.27 also illustrates instantaneous H-field in the x-z plane for the current configuration shown in Fig. 3.25.

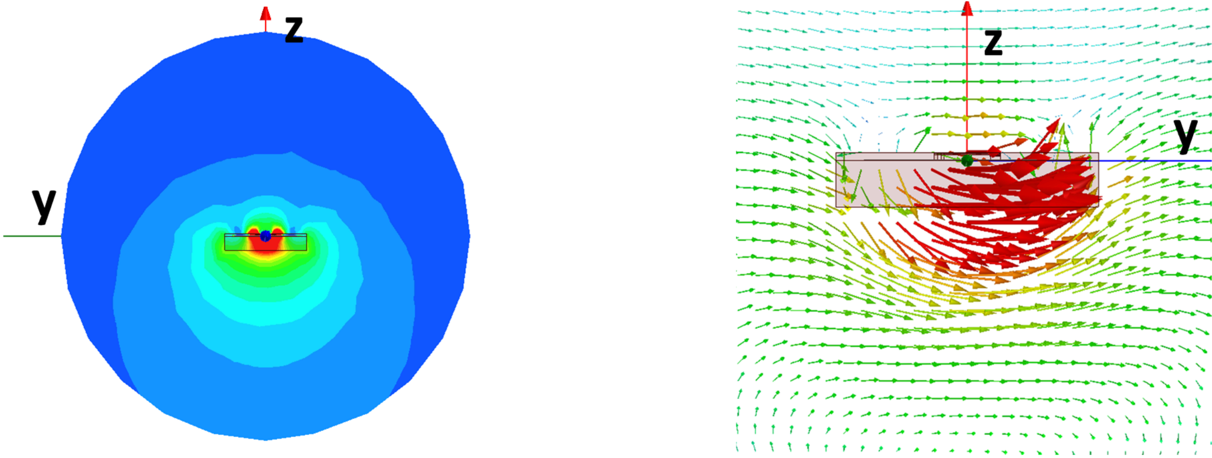

Figure 3.26: Magnitude of E-field a $2f_0$ in the y-z/x-z plane. The right part shows instantaneous E-field in the y-z plane for the current configuration shown in Fig. 3.25.

Fig. 3.28 shows the radiation patterns of DARs implemented in a 0.4 mm x 0.4 mm lossy silicon ($\rho \sim 10$ Ω.cm) for different substrate heights. The patterns show clean radiation profiles and maximum directivity form the back of the chip and are circularly polarized.

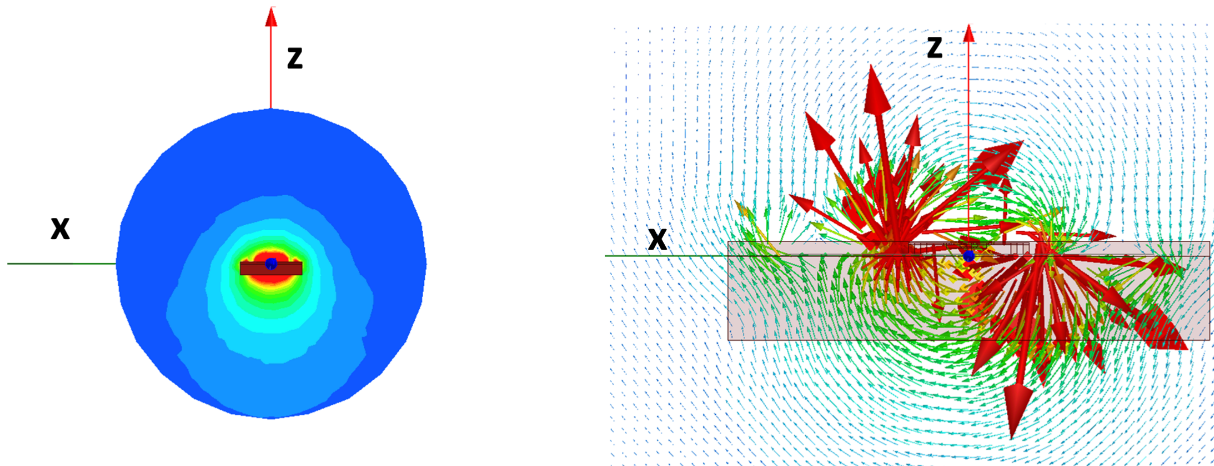

Figure 3.27: Magnitude of H-field a $2f_0$ in the x-z/y-z plane. The right part shows instantaneous H-field in the x-z plane for the current configuration shown in Fig. 3.25

The choice of the substrate heights will be explained, in details, in the next Chapter.

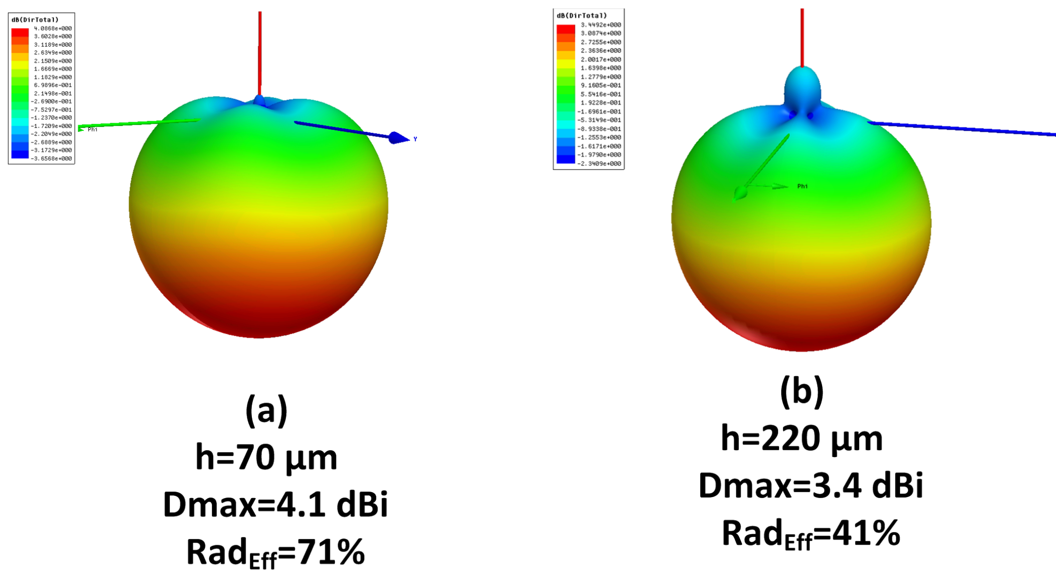

Figure 3.28: Radiation patterns for DARs in a 0.4 mm x 0.4 mm lossy silicon ($\rho \sim 10\ \Omega$.cm) for different substrate heights.

Chapter 4

Electromagnetic Field Analysis

In this Chapter, we will discuss the radiation properties a single and arrays of traveling-wave radiating structure in a silicon integrated circuit environment from an electromagnetic field analysis perspective. An on-chip antenna embedded in a dielectric interface, behaves very differently from a classical antenna in a free-space environment. To understand this, let us consider a infinitesimal Hertzian dipole in free-space ($\varepsilon_{r,air} = 1$) as shown in Fig. 4.1. Let us compare this with another Hertzian dipole placed at the interface of two dielectrics, say air ($\varepsilon_{r,air} = 1$) and a lossless dielectric (with $\varepsilon_{r,diel} = 4.0$), as shown in Fig. 4.2.

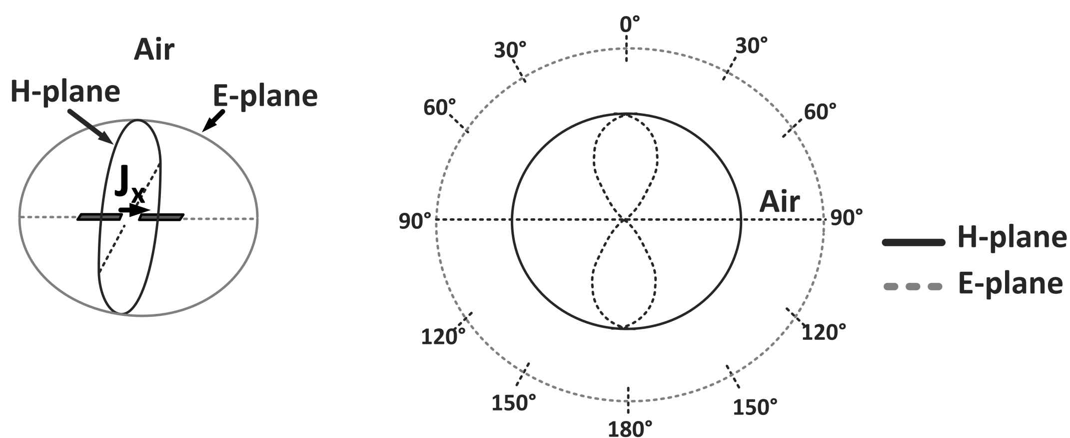

Figure 4.1: An infinitesimal Hertzian dipole in free-space. The radiation patterns in the E and H planes are shown.

The dipole in the free-space radiates uniformly in both halves and the various radiating properties, such as radiation resistance, efficiency, beam patterns, polarization have been discussed in standard antenna textbooks and classical antenna papers [67]– [71]. The electro-

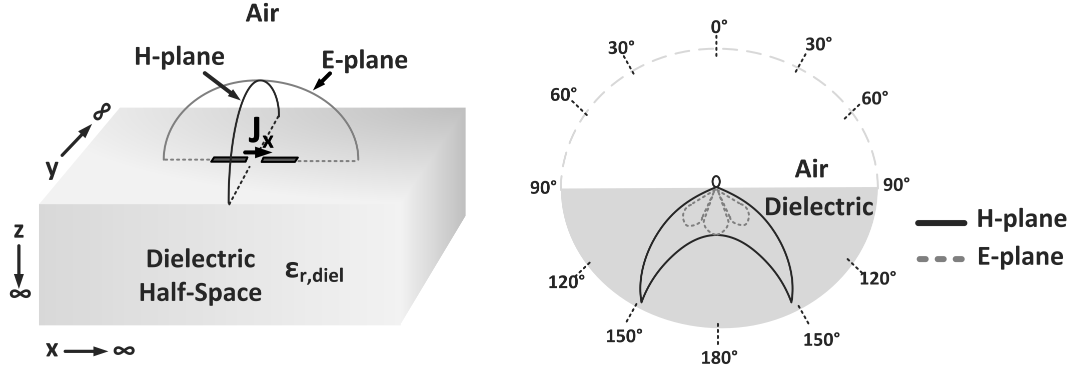

Figure 4.2: An infinitesimal Hertzian dipole at the interface of two dielectrics, air ($\varepsilon_{r,air} = 1$) and a lossless dielectric (with $\varepsilon_{r,diel} = 4.0$). The radiation patterns in the E and H planes are shown [72].

magnetic fields of such a radiating element in free-space have closed-form expressions, both in the near and far fields. However, for a dipole at the interface of a dielectric half-space, the power division is not equal in the two halves. It can be shown that radiated power divides between air and silicon in the inverse ratio of their intrinsic wave impedance, *i.e.*, $P_{air}/P_{si} = \eta_{si}/\eta_{air} = (\varepsilon_{air}/\varepsilon_{si})^{3/2} \approx 1/40$ [72], [73], [75]. One way to think about this is that the antenna sees two environments (air and silicon) in parallel, and silicon with its lower intrinsic impedance channels most of the power into it. The antenna input impedance, as well as the radiation patterns in both E and H-planes are very different from the case where the medium is uniform as depicted in Fig. 4.1 and Fig. 4.2. In summary, integrated antenna behavior needs to be analyzed by a close consideration of the boundary conditions.

For an on-chip antenna, the dielectric thickness (silicon thickness) is finite and comparable to the wavelength of radiation and therefore it is important to consider the reflections from the bottom of the silicon substrate. [1]. Let us consider the case, where the dielectric medium is of finite thickness (h) and has infinite ground plane below. This will be the case when a silicon die is placed on a piece of a very good conductor, such as brass. We will analyze the case, where the substrate is semi-infinite, (*i.e.*, finite in thickness and infinite in lateral dimensions.) This is illustrated in Fig. 4.3. The dipole radiates and parts of that signal suffers multiple reflections from the bottom ground surface and total internal reflections

[1] At 300 GHz, the wavelength in silicon is approximately 300 µm and the silicon die thickness can be of the same order.

from the top silicon-air interface and remains trapped inside silicon and never comes out. This happens essentially because silicon has a high dielectric constant ($\varepsilon_{si} = 11.7$) and in its interface with air, acts as an excellent dielectric waveguide, and channels most of the power in the two-dimensional infinite substrate [73]– [75]. Multiple trapped modes can be excited, depending on boundary conditions. We will refer to them collectively as surface/substrate waves/modes. If the ground is a perfect conductor, then power emitted by the dipole is transferred partly to the radiated power out of the chip into the air, and the rest gets trapped into surface waves. If we now define the radiation efficiency as $P_{eff} = P_{rad}/(P_{rad} + P_{SW})$, then, as a consequence of the excitement of these trapped modes, the radiation efficiency of an antenna in an integrated environment can be substantially less than one even for a lossless media.

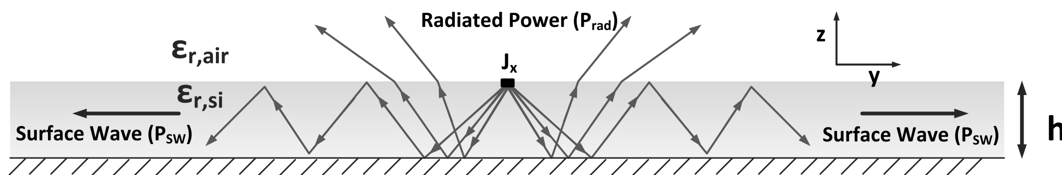

Figure 4.3: An infinitesimal Hertzian dipole placed on a semi-infinite dielectric with finite thickness (h). A major fraction of the radiated power can remain trapped in the dielectric as surface waves.

In this chapter, we will study if engineering surface currents in a suitable way may help us overcome the limitations of radiation efficiency due to excitement of surface waves. We will start with analyzing an impulse dipole and then radiation effects of a traveling-wave surface current configuration will be analyzed with using superposition of these basic impulses. We will find expressions for far-field radiated fields and surface wave fields. The surface wave fields for radiation in a dielectric interface is the classical Sommerfeld problem of an antenna on lossy earth [77], [78]. Determination of exact surface waves require laborious calculations of residues of the poles of Sommerfeld integrals [79] and extensive work on antennas embedded in multilayered dielectrics, based on this method has been reported in [81]– [91]. Dipoles placed on dielectric half-space, as shown in Fig. 4.1, have been analyzed in optics and chemical physics work [96]– [99]. Dipoles on semi-infinite grounded substrates,

as shown in Fig. 4.2, have been studied using complex integral approach in [86]– [88], but such complex methods are only necessary, when one is interested in determining exact solutions of near-fields or in calculating antenna impedances [72]. In this chapter, using first principles and certain approximations, we will try to derive close-form solutions of far-field radiated patterns, surface-wave fields, and compare radiated power with power lost in surface wave for different system and current configurations. This analytical work, in principle, will corroborate some of the results derived in mixed analytical and numerical approaches reported in [92]– [95]. We will then derive traveling-wave solutions of a distributed active radiator as a superposition of suitable current elements.

4.1 A Hertzian Dipole in a Dielectric with Finite Thickness

Imagine an impulse dipole is located on the surface of a dielectric as shown in Fig. 4.3. The impulse is x-directed and located at $(x, y, z) = (0, 0, 0)$. We represent the electrical current impulse as

$$\overline{J_x} = J_x \delta(x)\delta(y)\delta(z)\hat{x} \tag{4.1}$$

Maxwell's equations to be solved to obtain near and far-fields are

$$\nabla \times \overline{E} = -j\omega\mu\overline{H} \tag{4.2}$$

$$\nabla \times \overline{H} = j\omega\varepsilon\overline{E} \tag{4.3}$$

We will use the Fourier transform method to proceed to solve these differential equations [92]. Since the dielectric has a symmetry in infinite two-dimensional plane, we define the two-dimensional Fourier transform of a function $Z(x, y, z)$ as

$$\tilde{Z}(k_x, k_y, z) = \mathcal{F}_{x,y}(Z) = \frac{1}{2\pi}\int_{-\infty}^{\infty}\int_{-\infty}^{\infty} Z(x, y, z)e^{jk_x x}e^{jk_y y}dxdy \tag{4.4}$$

Therefore $\mathcal{F}_{x,y}(\frac{\partial E_z}{\partial x}) = jk_x\tilde{E}_z$, $\mathcal{F}_{x,y}(\frac{\partial E_z}{\partial y}) = jk_y\tilde{E}_z$, $\mathcal{F}_{x,y}(\frac{\partial H_z}{\partial x}) = jk_x\tilde{H}_z$ and $\mathcal{F}_{x,y}(\frac{\partial H_z}{\partial y}) = jk_y\tilde{H}_z$.

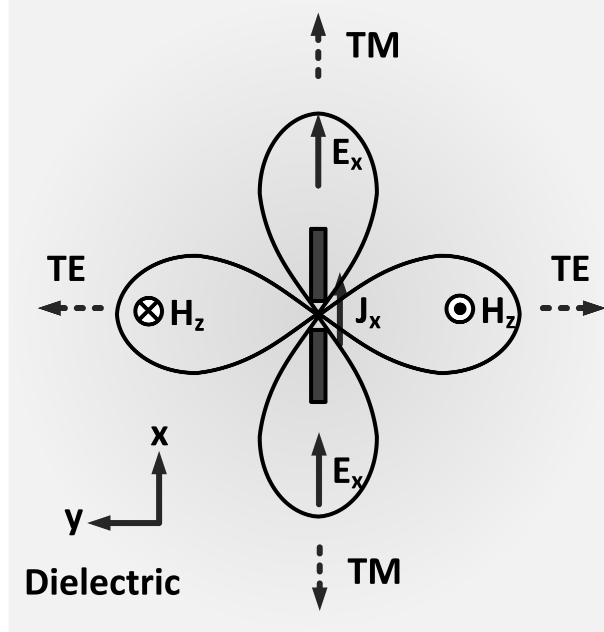

Figure 4.4: Surface wave patterns in TE and TM modes for an infinitesimal Hertzian dipole placed on a semi-infinite dielectric with finite thickness.

Let us argue intuitively which modes of propagation may exist in the two-dimensional infinite silicon substrate. Consider the dipole in Fig. 4.3. The electric field at the origin is aligned in x-direction. This will contribute to a magnetic field H_z in the z direction on the y-axis as shown in Fig. 4.4. A magnetic field in this direction can initiate a TE mode propagation along the y-axis [100]. Similarly, the impulse field at the Hertzian dipole will contribute to a E_x in the x direction on the x-axis. This can initiate a TM mode propagation along the x-axis. Absence of a E_z on the y-axis implies there is no TM propagation along y-axis. Similarly, there is no power in the TE mode along the x-axis. Based on this, an approximate pattern of power contributed by the TE and TM modes is shown in Fig. 4.4.

Therefore, the representative fields for the TE mode is H_z and the TM mode is E_z. We will try to represent the other fields in terms of these representative fields. The Hemholtz

equations in the source-free region in the two dielectrics are given by

$$(\frac{\partial^2}{\partial x^2} + \frac{\partial^2}{\partial y^2} + \frac{\partial^2}{\partial z^2})E_z + k^2 E_z = 0 \tag{4.5}$$

$$(\frac{\partial^2}{\partial x^2} + \frac{\partial^2}{\partial y^2} + \frac{\partial^2}{\partial z^2})H_z + k^2 H_z = 0, \tag{4.6}$$

where $k = \omega\sqrt{\mu_0\varepsilon_0}$ in air and $k = \omega\sqrt{\mu_0\varepsilon_0\varepsilon_r}$ in the dielectric.

In the frequency domain, this translates into

$$\frac{\partial^2 \tilde{E}_z}{\partial z^2} = (-k^2 + k_x^2 + k_y^2)\tilde{E}_z \tag{4.7}$$

$$\frac{\partial^2 \tilde{H}_z}{\partial z^2} = (-k^2 + k_x^2 + k_y^2)\tilde{H}_z \tag{4.8}$$

Therefore, for TM modes, we have

$$\frac{\partial^2 \tilde{E}_{z0}}{\partial z^2} - k_{z0}^2 \tilde{E}_{z0} = 0, \quad z \geq 0 \quad (air) \tag{4.9}$$

$$\frac{\partial^2 \tilde{E}_{zd}}{\partial z^2} + k_{zd}^2 \tilde{E}_{zd} = 0, \quad -h \leq z < 0 \quad (dielectric) \tag{4.10}$$

where $k_{z0}^2 = k_x^2 + k_y^2 - k_0^2$ and $k_{zd}^2 = \varepsilon_r k_0^2 - k_x^2 - k_y^2$.

The solutions for the TM modes are

$$\tilde{E}_{z0}(k_x, k_y, z) = E_{0,TM} e^{-k_{z0}z}, \quad z \geq 0 \quad (air) \tag{4.11}$$

$$\tilde{E}_{zd}(k_x, k_y, z) = E_{d1,TM} \sin(k_{zd}(z+h)) + E_{d2,TM} \cos(k_{zd}(z+h)),$$
$$-h \leq z < 0 \quad (dielectric) \tag{4.12}$$

Similarly, for TE modes, we have

$$\frac{\partial^2 \tilde{H}_{z0}}{\partial z^2} - k_{z0}^2 \tilde{H}_{z0} = 0, \quad z \geq 0 \quad (air) \tag{4.13}$$

$$\frac{\partial^2 \tilde{H}_{zd}}{\partial z^2} + k_{zd}^2 \tilde{H}_{zd} = 0, \quad -h \leq z < 0 \quad (dielectric) \tag{4.14}$$

The solutions for the TE modes are

$$\tilde{H}_{z0}(k_x,k_y,z) = H_{0,TE}e^{-k_{z0}z}, \quad z \geq 0 \quad (air) \tag{4.15}$$

$$\tilde{H}_{zd}(k_x,k_y,z) = H_{d1,TE}\sin(k_{zd}(z+h)) + H_{d2,TE}\cos(k_{zd}(z+h)),$$
$$-h \leq z < 0 \quad (dielectric) \tag{4.16}$$

Equations (4.11)-(4.12),(4.15)-(4.16) represent the all the representative solutions of both the TE and TM modes. The coefficients ($E_{0,TM}, E_{d1,TM}, E_{d2,TM}$) and ($H_{0,TE}, H_{d1,TE}, H_{d2,TE}$) for the TM and TE modes, respectively, are functions of k_x, k_y and other system parameters such as ε_r, h, J_x. Therefore, once we solve of the coefficients using the boundary conditions, one should be able to use use the inverse transform to obtain the *exact* solutions for near as well as far-fields. For example, the solution for E_z within any point in the dielectric in the TM mode could be obtained through an inverse transformation of $\tilde{E}_{zd}$ (4.17).

$$E_{zd}(x,y,z) = \mathcal{F}^{-1}_{k_x,k_y}(\tilde{E}_{zd}) = \frac{1}{2\pi}\int_{-\infty}^{\infty}\int_{-\infty}^{\infty}\tilde{E}_{zd}(k_x,k_y,z)e^{-jk_xx}e^{-jk_yy}dk_xdk_y \tag{4.17}$$

Once we obtain the solutions $\tilde{E}_z$ (TM modes) and $\tilde{H}_z$ (TE modes) (and therefore, E_z and H_z in the spatial domain), we can obtain the EM fields in the other directions, as expressed in (4.18)-(4.21), which can be derived from the relations (4.2)-(4.3).

$$\tilde{E}_x = -\frac{1}{k_x^2+k_y^2}(jk_x\frac{\partial \tilde{E}_z}{\partial z} + \omega\mu k_y\tilde{H}_z) \tag{4.18}$$

$$\tilde{E}_y = -\frac{1}{k_x^2+k_y^2}(jk_y\frac{\partial \tilde{E}_z}{\partial z} - \omega\mu k_x\tilde{H}_z) \tag{4.19}$$

$$\tilde{H}_x = -\frac{1}{k_x^2+k_y^2}(-\omega\varepsilon k_y\tilde{E}_z + jk_x\frac{\partial \tilde{H}_z}{\partial z}) \tag{4.20}$$

$$\tilde{H}_y = -\frac{1}{k_x^2+k_y^2}(\omega\varepsilon k_x\tilde{E}_z + jk_y\frac{\partial \tilde{H}_z}{\partial z}) \tag{4.21}$$

We will now solve for the boundary conditions which will enable us to obtain the desired coefficients in (4.11)–(4.12),(4.15)–(4.16). The ground plane implies that $\tilde{E}_x = 0$ and $\tilde{E}_y = 0$ at $z = -h$. Therefore from (4.11)–(4.12),(4.15)–(4.16) and (4.18)–(4.21), we obtain

$$\left.\tilde{E}_x\right|_{z=-h} = 0 \tag{4.22}$$

$$jk_x k_{zd} E_{d1,TM} + \omega\mu_0 k_y H_{d2,TE} = 0 \tag{4.23}$$

$$\left.\tilde{E}_y\right|_{z=-h} = 0 \tag{4.24}$$

$$jk_y k_{zd} E_{d1,TM} - \omega\mu_0 k_x H_{d2,TE} = 0 \tag{4.25}$$

From (4.23)-(4.25),

$$E_{d1,TM} = 0 \tag{4.26}$$

$$H_{d2,TE} = 0 \tag{4.27}$$

We have four unknowns left ($E_{0,TM}, E_{d2,TM}, H_{0,TE}, H_{d1,TE}$) and we will derive four boundary conditions to solve for them. At the interface $z = 0$, we have

$$\left.\tilde{E}_x\right|_{z=0-} = \left.\tilde{E}_x\right|_{z=0+} \tag{4.28}$$

$$\left.\tilde{E}_y\right|_{z=0-} = \left.\tilde{E}_y\right|_{z=0+} \tag{4.29}$$

This implies from (4.18) and (4.19)

$$\left.\frac{\partial \tilde{E}_z}{\partial z}\right|_{z=0-} = \left.\frac{\partial \tilde{E}_z}{\partial z}\right|_{z=0+} \tag{4.30}$$

$$\left.\tilde{H}_z\right|_{z=0-} = \left.H_z\right|_{z=0+} \tag{4.31}$$

Using the expressions of E_z and H_z in (4.11),(4.12), and (4.15),(4.16) and using the

conditions $E_{d1,TM} = 0$ and $H_{d2,TE} = 0$ from (4.30),(4.31)), we obtain

$$k_{zd} E_{d2,TM} \sin(k_{zd} h) = k_{z0} E_{0,TM} \tag{4.32}$$

$$H_{d1,TE} \sin(k_{zd} h) = H_{0,TM} \tag{4.33}$$

We need two more boundary conditions which will be derived from relations in magnetic fields. One of these is the following

$$\tilde{H}_x \Big|_{z=0-} = \tilde{H}_x \Big|_{z=0+} \tag{4.34}$$

From (4.11)–(4.12),(4.15)–(4.16), and (4.18)–(4.21), and (4.32)–(4.33) using we obtain by simplifying,

$$H_{0,TE} \left(k_{z0} + k_{zd} \cot(k_{zd} h) \right) = E_{0,TM} \omega \varepsilon_0 \frac{k_y}{k_x} \left(1 - \frac{k_{z0} \varepsilon_r}{k_{zd}} \cot(k_{zd} h) \right) \tag{4.35}$$

The other boundary condition is obtained from tangential magnetic fields and the current impulse. At the interface $z = 0$ in the spatial domain,

$$H_y|_{z=0-} - H_y|_{z=0+} = J_x \delta(x) \delta(y)|_{z=0} \tag{4.36}$$

Transforming, this equation into the frequency domain, we obtain

$$\tilde{H}_y \Big|_{z=0-} - \tilde{H}_y \Big|_{z=0+} = \frac{J_x}{2\pi} \tag{4.37}$$

Again, from (4.11)–(4.12),(4.15)–(4.16), and (4.18)–(4.21),

$$\begin{aligned} &(j k_y k_{zd} H_{d1,TE} \cos(k_{zd} h) + \omega \varepsilon_r \varepsilon_0 k_x E_{d2,TM} \cos(k_{zd} h)) \\ &+ (\omega \varepsilon_0 k_x E_{0,TM} + k_y k_{z0} H_{0,TE}) = \frac{J_x (k_x^2 + k_y^2)}{2\pi} \end{aligned} \tag{4.38}$$

Equations (4.32),(4.33),(4.35) and (4.38) represent four equations in four unknowns in

$E_{d2,TM}$,$E_{0,TM}$,$H_{d1,TE}$ and $H_{0,TE}$. Solving for $E_{0,TM}$, we have,

$$E_{0,TM} = \frac{J_x k_x k_{zd} \sin(k_{zd}h)}{2\pi\omega D_{TM}} \tag{4.39}$$

where $D_{TM} = \varepsilon_0(k_{zd}\sin(k_{zd}h) - \varepsilon_r k_{z0}\cos(k_{zd}h))$

From (4.35) and (4.39), we solve for $H_{0,TE}$.

$$H_{0,TE} = \frac{jJ_x k_y \sin(k_{zd}h)}{2\pi D_{TE}} \tag{4.40}$$

where $D_{TE} = k_{z0}\sin(k_{zd}h) + k_{zd}\cos(k_{zd}h)$.

From (4.32) and(4.39), we solve for $E_{d2,TM}$.

$$E_{d2,TM} = \frac{J_x k_x k_{z0}}{2\pi\omega\varepsilon_0 D_{TM}} \tag{4.41}$$

From (4.33) and(4.40), we solve for $H_{d1,TM}$.

$$H_{d1,TE} = \frac{jJ_x k_y}{2\pi D_{TE}} \tag{4.42}$$

It can be noted that the poles of (4.39) and (4.41) which are solutions of $D_{TM} = 0$ give the propagation constants for the surface-wave TM modes [100]. Similarly, the poles of (4.40) and (4.42) which are solutions of $D_{TE} = 0$ give the propagation constants for the surface-wave TE modes.

We have fully solved for $\tilde{E}_z$ and $\tilde{H}_z$ in air and dielectric, in the near as well as in the far-field, albeit in the frequency domain as per (4.11)–(4.12),(4.15)–(4.16). One can solve for the other axial components $\tilde{E}_x$,$\tilde{E}_y$ and $\tilde{H}_x$,$\tilde{H}_y$ from (4.18)–(4.21).

Having, complete field description in the frequency domain, once can perform inverse Fourier transforms as per (4.17), to solve for all the axial fields in the spatial domain. From the expressions (4.39)–(4.42), it can be seen that the inverse Fourier is complicated to be solved analytically. However,often we are not interested in exact near-field behavior, but asymptotic expressions in the far-field in order to calculate radiation patterns and the total

radiated power. In the next subsection, we will analytical expressions for radiation pattern and radiated power.

4.1.1 Far-Field Radiation Pattern and Radiated Power

A useful method to approximate EM fields in the far-field region, is called the stationary method [67]. It can be proved that the following expressions hold true

$$E_\theta(r,\theta,\phi) \approx \frac{je^{-jk_0r}}{r}k_0\left(\tilde{E}_x\Big|_{z=0}\cos\phi + \tilde{E}_y\Big|_{z=0}\sin\phi\right) \tag{4.43}$$

$$E_\phi(r,\theta,\phi) \approx \frac{je^{-jk_0r}}{r}k_0\cos\theta\left(-\tilde{E}_x\Big|_{z=0}\sin\phi + \tilde{E}_y\Big|_{z=0}\cos\phi\right) \tag{4.44}$$

This implies in order to calculate the far-fields, all we need is the frequency domain description of the tangential electric fields at the interface $z = 0$. We solve $\tilde{E}_x|_{z=0}$ from (4.11)and (4.18), and from (4.15), (4.39) and (4.40).

$$\begin{aligned}\tilde{E}_x|_{z=0} &= -\frac{1}{k_x^2+k_y^2}(-jk_xk_{z0}E_{0,TM} + \omega\mu k_yH_{0,TM}) \\ &= \frac{jk_x^2k_{z0}k_{zd}J_x\sin(k_{zd}h)}{(k_x^2+k_y^2)2\pi\omega D_{TM}} - \frac{\omega\mu k_y^2J_x\sin(k_{zd}h)}{(k_x^2+k_y^2)2\pi D_{TE}}\end{aligned} \tag{4.45}$$

Similarly, we solve for $\tilde{E}_y|_{z=0}$ from (4.11) and (4.19), and from (4.15),(4.39) and (4.40).

$$\begin{aligned}\tilde{E}_y|_{z=0} &= -\frac{1}{k_x^2+k_y^2}(-jk_yk_{z0}E_{0,TM} - \omega\mu k_xH_{0,TM}) \\ &= \frac{jk_xk_yk_{z0}k_{zd}J_x\sin(k_{zd}h)}{(k_x^2+k_y^2)2\pi\omega D_{TM}} + \frac{\omega\mu k_xk_yJ_x\sin(k_{zd}h)}{(k_x^2+k_y^2)2\pi D_{TE}}\end{aligned} \tag{4.46}$$

Again from the stationary phase approach, we can relate k_x, k_y, k_{z0} and k_{zd} with k_0, θ, ϕ.

$$k_x = k_0 \sin\theta \cos\phi \tag{4.47}$$

$$k_y = k_0 \sin\theta \sin\phi \tag{4.48}$$

$$k_{z0} = (k_x^2 + k_y^2 - k_0^2)^{1/2} = jk_0 \cos\theta \tag{4.49}$$

$$k_{zd} = (\varepsilon_r k_0^2 - k_x^2 - k_y^2)^{\frac{1}{2}} = k_0(\varepsilon_r - \sin^2\theta)^{\frac{1}{2}} \tag{4.50}$$

Using (4.43), (4.47)–(4.50) and (4.45)–(4.46), we have

$$\begin{aligned}
E_\theta(r,\theta,\phi) \approx & \frac{je^{-jk_0 r}}{r} k_0 \Bigg[\frac{jk_{zd}k_{z0}J_x \sin(k_{zd}h)}{2\pi\omega k_0^2 \sin^2\theta} \left(\frac{k_x^2 \cos\phi + k_x k_y \sin\phi}{D_{TM}} \right) \\
& + \frac{\omega\mu J_x \sin(k_{zd}h)}{2\pi k_0^2 \sin^2\theta} \underbrace{\left(\frac{-k_y^2 \cos\phi + k_x k_y \sin\phi}{D_{TE}} \right)}_{0} \Bigg] \\
& = \frac{je^{-jk_0 r}}{r} \frac{k_0 J_x \eta_0}{2\pi} \cos\phi \left(\frac{\cos\theta(\varepsilon_r - \sin^2\theta)^{1/2}}{j\varepsilon_r \cos\theta \cot(k_0(\varepsilon_r - \sin^2\theta)^{1/2} h) - (\varepsilon_r - \sin^2\theta)^{1/2}} \right) \\
& = \frac{\cos\phi}{r} F_1(\theta)
\end{aligned} \tag{4.51}$$

where $\eta_0 = \sqrt{\mu_0/\varepsilon_0}$ is the wave impedance of free-space.

Similarly, using (4.44), (4.47)–(4.50) and (4.45)–(4.46), we have

$$\begin{aligned}
E_\phi(r,\theta,\phi) \approx & \frac{je^{-jk_0 r}}{r} k_0 \Bigg[\frac{jk_{zd}k_{z0}J_x \sin(k_{zd}h)}{2\pi\omega k_0^2 \sin^2\theta} \underbrace{\left(\frac{-k_x^2 \sin\phi + k_x k_y \cos\phi}{D_{TM}} \right)}_{0} \\
& + \frac{\omega\mu J_x \sin(k_{zd}h)}{2\pi k_0^2 \sin^2\theta} \left(\frac{k_y^2 \sin\phi + k_x k_y \cos\phi}{D_{TE}} \right) \Bigg] \\
& = \frac{-je^{-jk_0 r}}{r} \frac{k_0 J_x \eta_0}{2\pi} \sin\phi \left(\frac{\cos\theta}{j(\varepsilon_r - \sin^2\theta)^{1/2} \cot(k_0(\varepsilon_r - \sin^2\theta)^{1/2} h) - \cos\theta} \right) \\
& = \frac{\sin\phi}{r} F_2(\theta)
\end{aligned} \tag{4.52}$$

We have, now, complete solution of the far-field TEM wave propagation for a Hertzian

dipole on a grounded substrate as shown in Fig. 4.3. The total radiated power is, therefore, determined to be

$$P_{rad} = \frac{1}{2\eta_0} \int_0^{\pi} \int_0^{2\pi} \left(|E_\theta|^2 + |E_\phi|^2\right) r^2 \sin\theta d\phi d\theta \quad (4.53)$$

The flux density given by $|E_\theta|^2 + |E_\phi|^2$ from (4.51) and (4.52) is plotted for different substrate thickness in the E- and the H-pane respectively Fig. 4.5 and Fig. 4.6. The substrate is lossless silicon and the choices for the different substrate heights are based on minimization of power lost in surface modes, which will be discussed in the next section. The plots show a close correspondence between analytically obtained solutions and electromagnetic simulation with semi-infinite substrates, carried out in a method-of-moment-based simulator called IE3D [101].

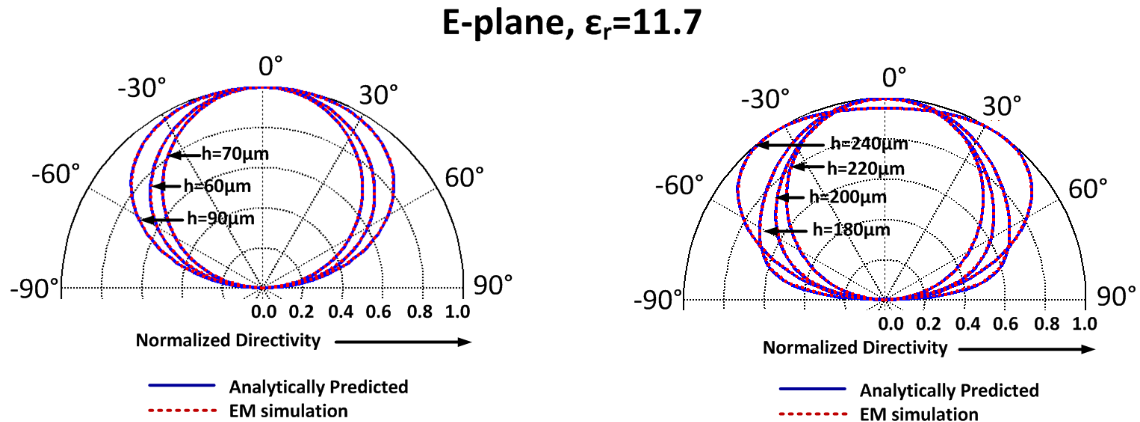

Figure 4.5: Analytically predicted and electromagnetically simulated E-plane pattern for a Hertzian Dipole for different substrate thicknesses. The substrate of choice is lossless silicon ($\varepsilon_r = 11.7$).

4.1.2 Surface-Wave Fields and Trapped Power

We will now analyze the surface waves excited by a dipole on a grounded substrate. We will try to explore the fundamental limits on efficiency due to the power trapped in surface waves and if by engineering novel ways of current flow, power lost in surface waves can be minimized

A Hertzian dipole, as shown in Fig. 4.3, emanates cylindrical surface waves which remain

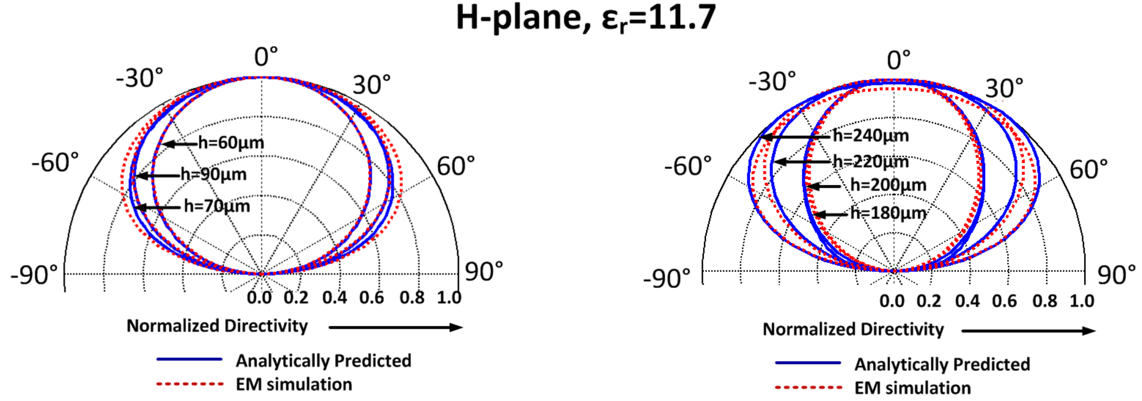

Figure 4.6: Analytically predicted and electromagnetically simulated H-plane pattern for a Hertzian Dipole for different substrate thicknesses. The substrate of choice is silicon ($\varepsilon_r = 11.7$).

trapped in the semi-infinite substrates. Let us consider the TM mode first. Fig. 4.7 shows the configuration for analysis of the surface waves. The final longitudinal electric field in the far-field region for TM surface-wave modes is given by cylindrical wave functions [89]. We will try to derive it from Maxwell's equations for the sake of completeness.

The magnetic vector potential A_z satisfies the wave equation.

$$\bigtriangledown^2 A_z + k^2 A_z = 0 \tag{4.54}$$

The solution can be derived using a method of separation of variables as $A_z(\rho, \phi, z) = R(\rho)P(\phi)Z(z)$. Therefore, transforming (4.54) into the cylindrical coordinates, we have

$$\frac{1}{R}\frac{1}{\rho}\frac{d}{d\rho}(\rho\frac{dR}{d\rho}) + \frac{1}{P}\frac{1}{\rho^2}\frac{d^2P}{d\phi^2} + \frac{1}{Z}\frac{d^2Z}{dz^2} = -k^2 \tag{4.55}$$

where $k = \omega\sqrt{\mu_0\varepsilon_r\varepsilon_0}$. The last term is a constant which results in

$$\frac{1}{Z}\frac{d^2Z}{dz^2} = -k_{zd}^2 \tag{4.56}$$

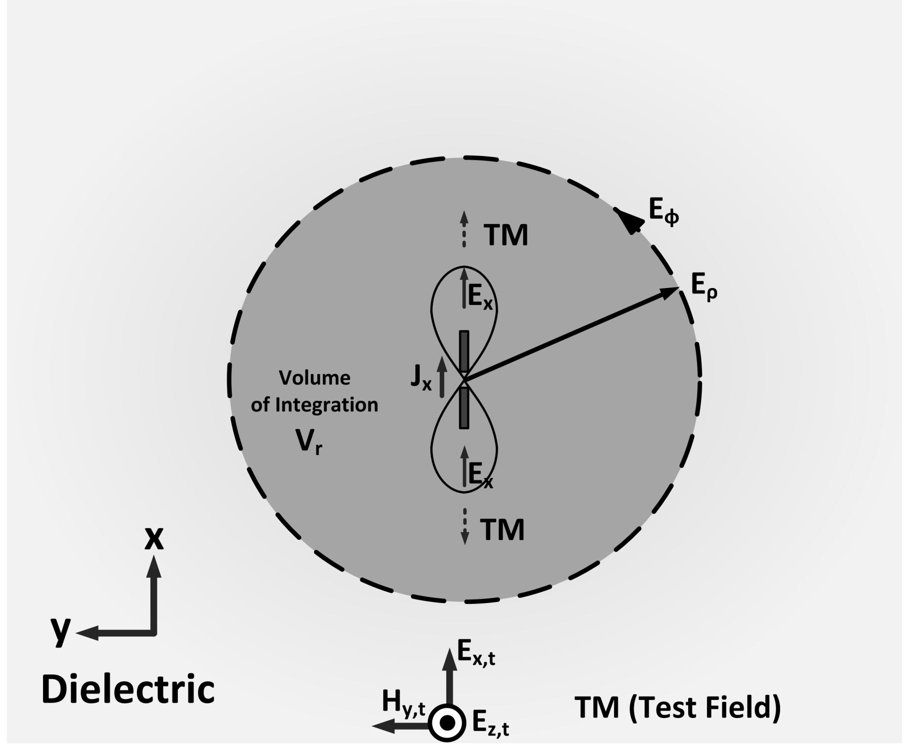

Figure 4.7: Cylindrical surface wave power excited by a dipole in a semi-infinite grounded substrate.

Putting this result in (4.55), we obtain

$$\frac{\rho}{R}\frac{d}{d\rho}(\rho\frac{dR}{d\rho}) + \frac{1}{P}\frac{d^2P}{d\phi^2} = -(\beta\rho)^2 \tag{4.57}$$

where $\beta^2 = k_0^2\varepsilon_r - k_{zd}^2$.

Similarly the last term is also a constant, implying

$$\frac{1}{P}\frac{d^2P}{d\phi^2} = -n^2 \tag{4.58}$$

Putting this result in (4.57), we obtain

$$\rho^2\frac{d^2P}{d\rho^2} + \rho\frac{dR}{d\rho} + [(\beta\rho)^2 - n^2] = 0 \tag{4.59}$$

Solving the three equations (4.56),(4.58) and (4.59), we obtain, in general,

$$Z(z) = M_1 e^{-jk_{zd}z} + M_2 e^{jk_{zd}z} \tag{4.60}$$

$$P(n\phi) = N_1 \cos(n\phi) + N_2 \sin(n\phi) \tag{4.61}$$

$$R(\rho) = R_1 H_n^{(2)}(\beta\rho) \tag{4.62}$$

$$\tag{4.63}$$

where $H_n^{(2)}$ is the n$^{\text{th}}$ order Hankel function of the second kind.

It can be easily proved that the transformation of A_z into E_z follows,

$$E_z = -\frac{j}{\omega\mu\varepsilon}\left(\frac{\partial^2}{\partial z^2} + k^2\right) A_z \tag{4.64}$$

We apply boundary conditions for continuity of fields, and arrive at the known eigenvalue equation for TM mode.

$$k_{zd} \tan(k_{zd}h) = k_{z0}\varepsilon_r \tag{4.65}$$

where $\beta^2 = k^2 - k_{zd}^2$ and $\beta^2 = k_0^2 + k_{z0}^2$.

Substituting the boundary conditions and with further simplification, we obtain,

$$E_{zd} = A_{m1} H_1^{(2)}(\beta\rho) \cos(\phi) \cos(k_{zd}(z + h)) \tag{4.66}$$

It can be noted from (4.66) that the higher-order Henkel functions in (4.62) have been ignored. This can be reasoned from an azimuthal symmetry argument [89]. The coefficient A_{m1} in (4.66) can be solved using reciprocity using an auxillary test field [72]. As shown in Fig. 4.7, a known auxiliary plane wave which consist of a TM wave propagating from $x \to \infty$, arrives and interacts with the Hertzian dipole. We use the following reciprocity

relation to solve for A_{m1}.

$$\oint_{Sr}(\bar{E}_1 \times \bar{H}_2 - \bar{E}_2 \times \bar{H}_1).d\bar{S} = \int_{Vr}(E_2.J_1)dv \tag{4.67}$$

where E_1 and H_1 are the cylindrical surface waves emanated by the Hertzian dipole, E_2 and H_2 are fields due to the test TM plane wave, the surface integral is carried over the imaginary cylindrical surface shown in Fig. 4.7 and the volume contained in the cylinder is denoted by V_r. Solving the equation, and simplifying, we get the following expressions for far-field surface waves for TM modes in the dielectric [90]. In [90] the fields were obtained using complex integrals as discussed in the beginning of this chapter, while we obtained the same result using simpler methods and reciprocity relationships.

$$E_{zd} = -\frac{J_x\eta_0}{2k_0}\cos(\phi)\sum_p \frac{k_{z0}H_1^{(2)}(\beta_p\rho)\beta_p^2}{T_M(\beta_p)}\frac{\cos(k_{zd}(z+h))}{\cos(k_{zd}h)} \tag{4.68}$$

where the summation is carried over all the possible TM modes with propagation constant β_p and $T_M(\beta_p) = \frac{\varepsilon_r\beta_p}{k_{z0}} + \frac{\beta_p\tan(k_{zd}h)}{k_{zd}} + \frac{\beta_p h}{\cos^2(k_{zd}h)}$. As before, the following relations from (4.65) hold true

$$\begin{aligned} k_{z0}\varepsilon_r &= k_{zd}\tan(k_{zd}h) \\ \beta_p^2 &= k^2 - k_{zd}^2 \\ \beta_p^2 &= k_0^2 + k_{z0}^2 \end{aligned} \tag{4.69}$$

Therefore, we have now complete field description of the TM waves. We can follow similar procedure to find field expressions for TE waves, which have a maximum along y-axis, as shown in Fig. 4.4.

$$H_{zd} = -\frac{jJ_x}{2}\sin(\phi)\sum_q \frac{H_1^{(2)}(\beta_q\rho)\beta_q^2}{T_E(\beta_q)}\frac{\sin(k_{zd}(z+h))}{\sin(k_{zd}h)} \tag{4.70}$$

where the summation is carried over all the possible TE modes with propagation constant β_q and $T_E(\beta_q) = \frac{\beta_q}{k_{z0}} - \frac{\beta_q \cot(k_{zd}h)}{k_{zd}} + \frac{\beta_q h}{\sin^2(k_{zd}h)}$. As before, the following relations similar to (4.69) hold true.

$$\begin{aligned} k_{z0} &= -k_{zd}\cot(k_{zd}h) \\ \beta_q^2 &= k^2 - k_{zd}^2 \\ \beta_q^2 &= k_0^2 + k_{z0}^2 \end{aligned} \tag{4.71}$$

The total power in surface waves in TM and TE modes, therefore, can be calculated from (4.68) and (4.70). They are given by

$$P_{SW}^{TM} = \frac{15\pi J_x^2}{k_0}\frac{\beta_p^2}{T_M^2(\beta_p)}\sum_p\left(\frac{k_{zd}^2\tan^2(k_{zd}h)}{\beta_p} + \frac{\varepsilon_r\beta_p^2 h}{\cos^2(k_{zd}h)}\right) \tag{4.72}$$

$$P_{SW}^{TE} = 15\pi J_x^2 k_0 \frac{\beta_q^2}{T_E^2(\beta_q)}\sum_q\left(\frac{1}{\beta_q} + \frac{h}{\sin^2(k_{zd}h)}\right) \tag{4.73}$$

$$P_{SW} = P_{TE} + P_{TM} \tag{4.74}$$

Having obtained the total radiated power in (4.53) and the total power trapped in surface waves in (4.74), we can define radiation efficiency as

$$\eta_{eff} = \frac{P_{rad}}{P_{rad} + P_{SW}} \tag{4.75}$$

The total surface wave power in (4.74) and the total radiated power in (4.53) for different substrate thicknesses at a frequency of 300 GHz, is plotted in Fig. 4.8. It can be seen that the

radiated power maximizes near h=70 µm and h=220 µm. At these substrate thicknesses, the waves radiated at 300 GHz, after suffering reflection from the ground below, add coherently at the top of the substrate. This is the reason, why the radiation patterns where plotted in Fig. 4.5 and Fig. 4.6, for substrate thicknesses near these values.

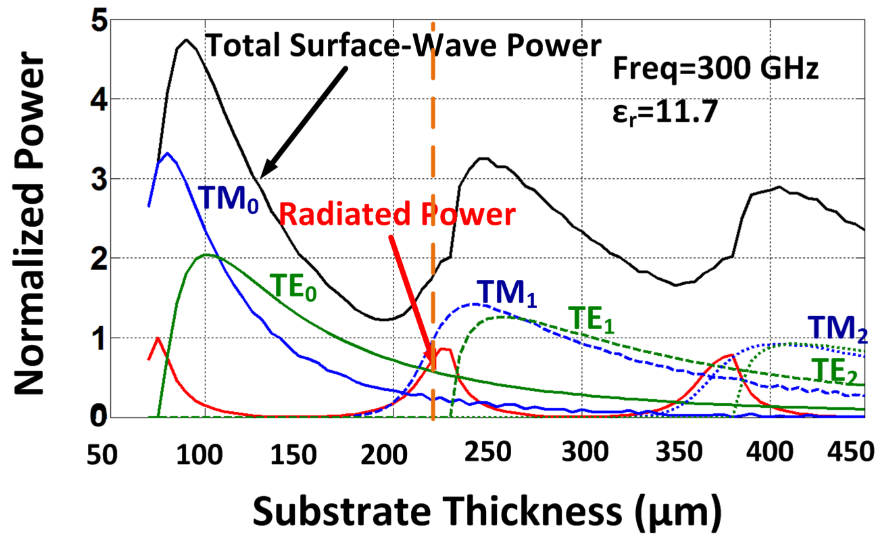

Figure 4.8: Total surface wave power broken down into its different modes and the total radiated power for a Hertzian dipole for different substrate thicknesses.

The power trapped in the constituent individual surface-wave modes, normalized to the maximum radiated power, have also been shown in Fig. 4.8. It is very important to understand, which surface-wave mode carries most of the trapped power, in order to be able to design surface currents that minimize the power lost. The TM_0 mode exists for arbitrarily thin substrates. The next mode TE_0 appears near h=70 µm. The next two modes TM_1 and TE_1 appear near h=180 µm and h=230 µm respectively. Even though the radiated power maximizes near h=70 µm and h=220 µm, with similar radiation efficiencies, the modes carrying the surface-wave power are very different. TM_0 mode is responsible for the entire surface-wave power near h=70 µm, while at h=220 µm, the dominant modes are TE_0 and TM_1. This is illustrated in Fig. 4.9, which shows the constituent surface-wave power for different frequencies at a given substrate thickness of h=220 µm and at a frequency of 300 GHz. The plots are derived from the analytical calculations. It can be clearly seen that the TM_0 mode which was dominant for h=70 µm, is responsible for only 15% of the

surface-wave power, while TM_1 contributes to 52% and TE_0 contributes to the rest 33%. We will revisit this inference later when we analyze a traveling-wave radiative mode in the Distributed Active Radiator and examine how the TE_0 mode is intrinsically canceled in the electromagnetic structure.

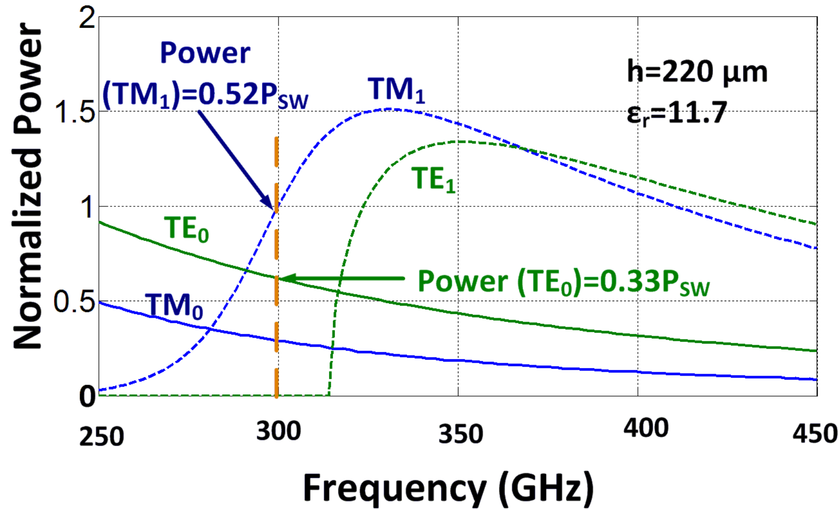

Figure 4.9: Constituent surface-wave power for different frequencies at a given substrate thickness of h=220 µm and at a frequency of 300 GHz.

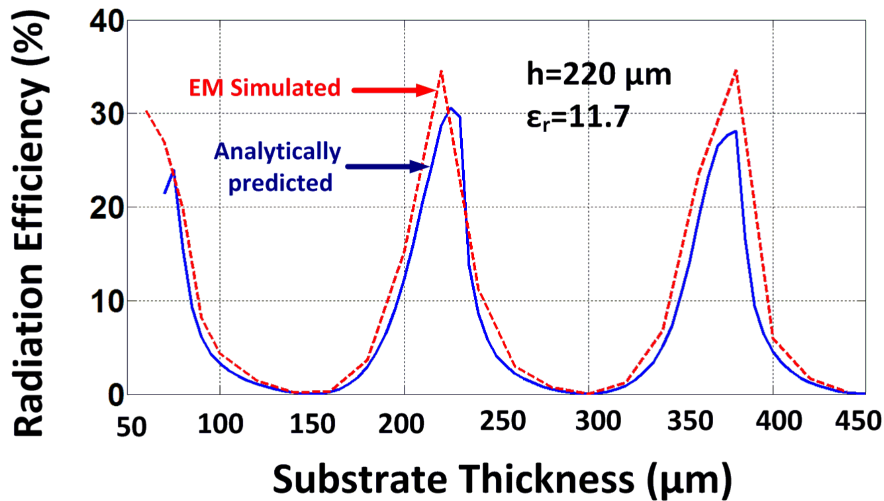

Figure 4.10: Radiation efficiency of a Hertzian dipole against different substrate thicknesses.

The radiation efficiency of the Hertzian dipole is plotted for different substrate thicknesses in Fig. 4.10. As expected from Fig. 4.8, the efficiency peaks near h=70 µm and

h=220 µm, reaching a maximum value near 30%. This implies, that even for completely lossless substrates, only 30% of the power can ever be radiated out from a Hertzian dipole on a grounded substrate. The analytically calculated values match closely with the results obtained using electromagnetic simulation in IE3D. The troughs in the efficiency plot correspond to the thickness where the waves, after suffering reflection from the bottom surface, add destructively at the top of the substrate. The radiation efficiency variation against frequency for a given substrate height of h=220 µm is plotted against frequency. As expected from Fig. 4.8 and Fig. 4.10, the efficiency maximizes for the designed frequency of 300 GHz when the waves, after suffering reflection from the bottom surface, add constructively at the top of the substrate.

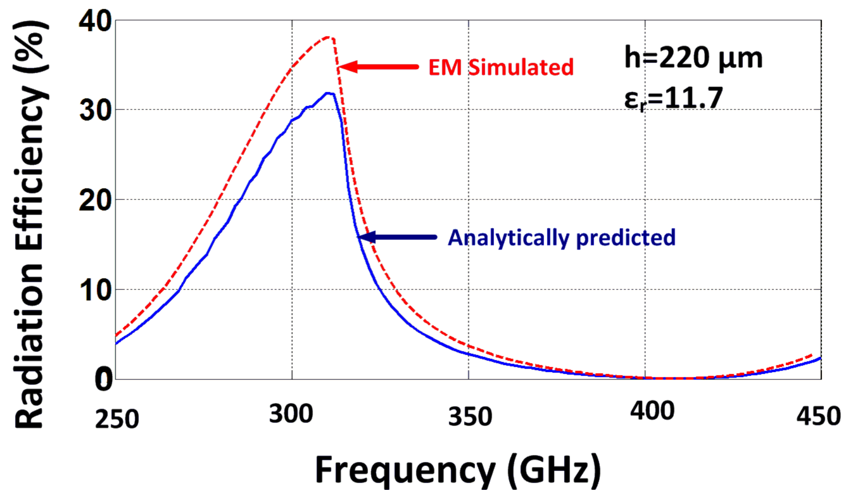

Figure 4.11: Radiation efficiency of a Hertzian dipole against frequency for h= 220 µm.

4.2 Traveling-Wave Circular Radiator on a Grounded Substrate

The distributed active radiator core consists of a traveling-wave radiating structure. In this section, we will examine how surface-wave power in a strong modes can be suppressed in such traveling-wave circular geometries by forcing surface-waves excited by part of the radiative structure to cancel surface-waves excited by another part.

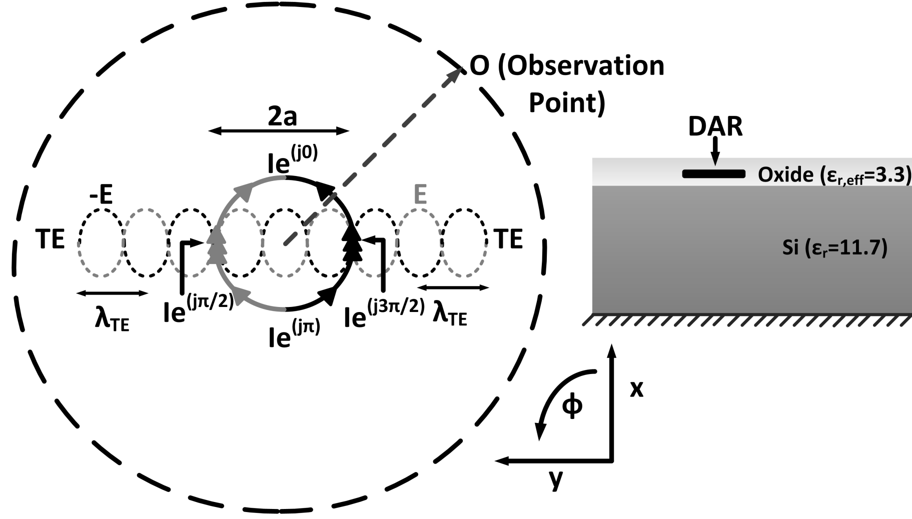

Figure 4.12: Traveling-wave circular geometries allowing suppression of the trapped power through partial cancelation of the surface-waves.

Fig. 4.12 shows the geometry of traveling-wave radiating structure which exists in the core of the DAR. The circular geometry is one wavelength long, which is shown by current configurations of Ie^{j0}, $Ie^{j\pi/2}$,$Ie^{j\pi}$ and $Ie^{j3\pi/2}$. An instantaneous current configuration is also shown on the structure. This traveling-wave radiator can be equivalently represented by a superposition of Hertzian dipoles along the circumference and separated in space, orientation and phase. The analysis of the architecture will proceed along this line of reasoning. Due to the circularly symmetric nature of the traveling-wave radiator, the current configuration just rotates with time and the surface wave power remains constant for all observation points along the circular boundary (containing 'O') and is independent of the azimuth angle ϕ. Therefore, it is enough to analyze the current configuration shown in Fig. 4.12, since at any other time, the field profile will be just a rotation about the vertical z axis.

4.2.1 Surface-Wave Power Suppression in TE Mode

Let us analyze the current elements $Ie^{j\pi/2}$ and $Ie^{3j\pi/2}$, which are located at $\phi = \pi/2$ and $\phi = 3\pi/2$ and separated by the diameter of the loop '2a', as shown in Fig. 4.12. Assuming that the current distribution along the loop for the instant of time shown is $I(\phi) = |I_0 \sin(\phi)|$, the current elements $\phi = \pi/2$ and $\phi = 3\pi/2$ carry the maximum current I. Therefore, the

dominant TE modes along the y-axis (as revealed in (4.70) and Fig. 4.4) will be contributed primarily by the elements located near $\phi = \pi/2$ and $\phi = 3\pi/2$. Now, imagine that the diameter of the loop is chosen such that traversing along the diameter '2a' the TE wave suffers a phase shift of 180°, *i.e.*, $2a = (2n-1)\lambda_{TE}/2, n \subseteq I^{+}$. Therefore, the TE surface waves of wavelength λ_{TE} emanated from the $\mathrm{Ie}^{\mathrm{j}\pi/2}$ will suffer a phase shift of 180°, as it traverses through the diameter and reaches the current element $\mathrm{Ie}^{3\mathrm{j}\pi/2}$ and vice versa. This should result in major part of the dominant TE wave being canceled. Suppressing the TE mode can substantially reduce the total surface wave power, as TE_0 contributed to 33% of the surface-wave power in a Hertzian dipole, as demonstrated before in Fig. 4.9. Assuming an instantaneous current distribution as $I(\phi) = I_0 \sin(\phi)$ and using the relation in (4.70), the longitudinal magnetic field in the TE mode at any observation angle (ϕ_O) due to a current element I_0 located at an angle ϕ is given by

$$H_{zd}(\phi, \phi_O) = H_{zd0} \sin(\phi) \cos(\phi - \phi_O) \tag{4.76}$$

Therefore, the resultant H_{zd} due to the traveling-wave loop of current is given by

$$H_{zd,loop}(a) = \max_{-\pi/2 \le \phi_O \le \pi/2} \left\{ \int_0^{2\pi} H_{zd0} \sin\phi \cos(\phi - \phi_O) e^{-ja\beta_{TE}\cos(\phi-\phi_O)} d\phi \right\} \tag{4.77}$$

The maximization is done over the observation angle because the TE surface-wave power is independent of observation angle ϕ_O and due to the partial cancelation of TE surface wave, the TE maximum may shift to a different angle than $\phi_O = \pi/2, 3\pi/2,$. The effect of radius on the total surface-wave power in the dominant TE_0 mode has been shown in Fig. 4.13. It can be seen that when the phase shift corresponding to one diameter traversal ($2a\beta_{TE0}$) corresponds to near 200°, the TE_0 mode is considerable suppressed. The angle is slightly more than 180°, due to the contribution of the current elements along the circumference of the loop and not just at $\phi = \pi/2$ and $\phi = 3\pi/2$.

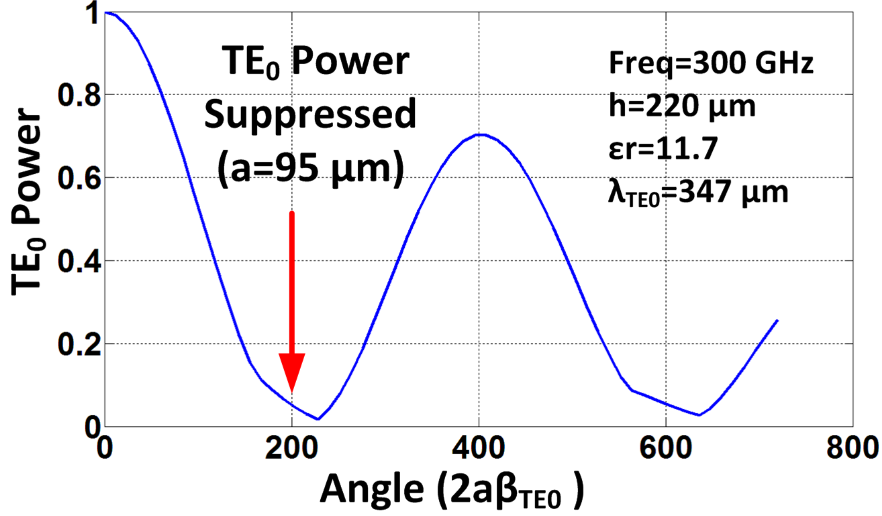

Figure 4.13: Variation of TE_0 power suppression with radius of the loop.

In summary, if we design the loop judiciously, then a substantial portion of the surface wave power in a dominant TE_0 mode may be canceled. However, the diameter of the core loop in a DAR is not independent of the frequency of operation and is set by the boundary condition required traveling-wave oscillation, as described in Chapter 3. The circumference of the loop needs to be equal to half-wavelength long at the fundamental frequency (f_0, half the radiated frequency) in the transmission-line mode of propagation in the oxide layer. Fortunately, this approximately corresponds to the diameter equaling half-wavelength long at the radiated frequency of $2f_0$.

$$\begin{aligned} 2\pi a &= \frac{\lambda_{f0,oxide}}{2} \approx \lambda_{2f0,oxide} \\ \Rightarrow 2a &= \frac{\lambda_{2f0,oxide}}{\pi} \approx \frac{\lambda_{2f0,si}}{2} \end{aligned} \tag{4.78}$$

Therefore, we use the exploit of the relative dielectric constant differences between the oxide layer (which decides the dimensions for the traveling-wave oscillation at the fundamental frequency of f_0) and silicon (which decides propagation for the radiated second harmonic frequency of $2f_0$). It can be noted that the wavelengths corresponding to the various TE

modes are substrate thickness dependent (and in general not equal to $\lambda_0/\sqrt{\varepsilon}_{r,si}$). The TE wavelengths for different substrate thicknesses are shown in Fig. 4.14, for a frequency of 300 GHz and for lossless silicon. It can be seen for a substrate height of h=220 µm (which maximized radiation efficiency of a Hertzian dipole in Fig. 4.10), the dominant TE_0 wavelength corresponds to 347 µm ($\lambda_0/\sqrt{\varepsilon}_{r,si} \approx 300$ µm). This implies that for TE_0 mode suppression, the radius 'a' should be $a = \lambda_{TE0}/4$, which corresponds to $a \approx 95$ µm, as shown in Fig. 4.13. For this value of the radius, the loop circumference $2\pi a = 596$ µm $\approx \frac{\lambda_{0,150GHz}}{2\sqrt{\varepsilon_{r,eff}(\text{oxide})}}$, where $\varepsilon_{r,eff}$(oxide) is the effective dielectric constant of the oxide in its interface with air, as shown in Fig. 4.12. Therefore, due to the relative dielectric constants between silicon and the oxide, resonant frequency of DAR also corresponds to the radius which suppresses the TE mode. In reality, due to parasitic capacitance, the radius of the DAR will be less than optimum. In the design, the required radius still suppressed the TE mode by around 50%.

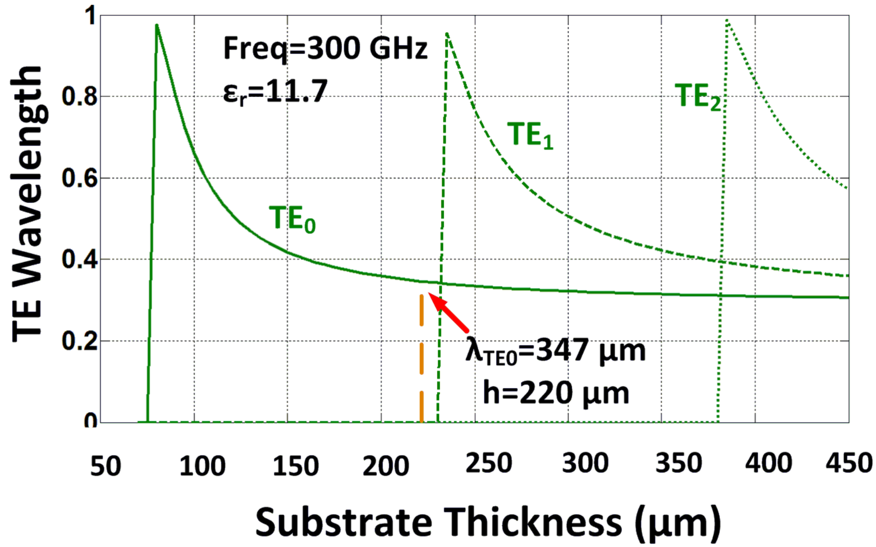

Figure 4.14: TE wavelength variation with substrate thickness.

4.2.2 Surface-Wave Power in TM Mode

The previous section showed surface-wave power in the TE_0 mode suppression due to field cancelation along $\phi = \pi/2$ direction. The TM mode, however, is maximum in the $\phi = 0$ direction, as shown in (4.68) and Fig. 4.4. Along the direction, the maximum current

elements at $\phi = \pi/2$ and $\phi = 3\pi/2$ add in phase. Therefore, we expect much less cancelation of the TM modes. Similar to (4.77), we can derive field expressions for the TM modes.

$$E_{zd,loop}(a) = \max_{-\pi/2 \leq \phi_O \leq \pi/2} \left\{ \int_0^{2\pi} E_{zd0} \sin\phi \sin(\phi - \phi_O) e^{-ja\beta_{TM}\cos(\phi-\phi_O)} d\phi \right\} \tag{4.79}$$

The dominant TM mode for the designed substrate height of 220 µm, is the TM_1 mode as shown in Fig. 4.9. The wavelength corresponding to this mode for the substrate height of 220 µm can be shown to be 782 µm, as illustrated in Fig. 4.15. This implies a corresponding phase shift of $2\beta_{TM1}a = 0.46\pi$ across the diameter (as opposed to $2\beta_{TE0}a = \pi$), and the total power in the TM_1 surface-wave mode can be calculated from (4.79). The result is shown in Fig. 4.16. As expected, the TM_1 is not suppressed significantly and with the TE_0 mode almost being canceled, the TM_1 is expected to be the dominant surface-wave mode left.

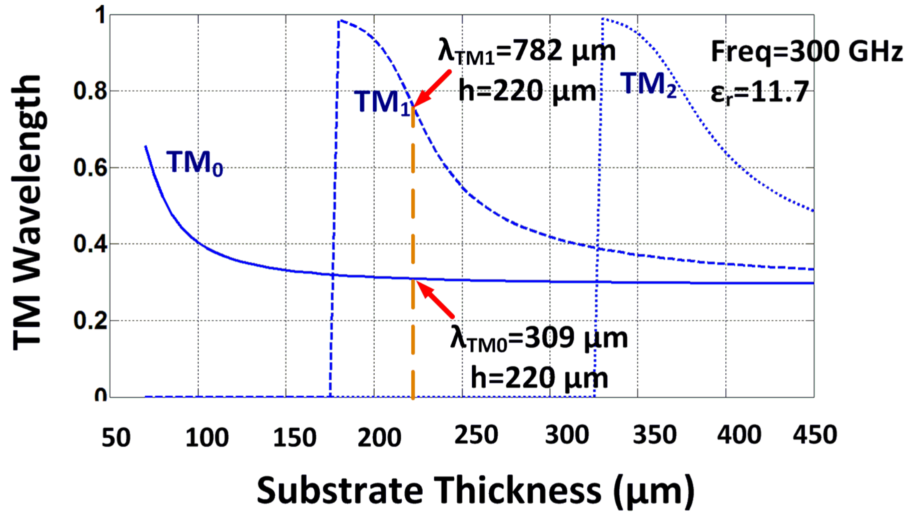

Figure 4.15: TM wavelength variation with substrate thickness.

4.2.3 Total Radiated Power and Radiation Efficiency

As explained in the previous two sections, the TE_0 is canceled by ensuring near π phase, as the wave propagates across the diameter, *i.e.*, $2a\beta_{TE0} \approx \pi$. The TM_1 mode is much

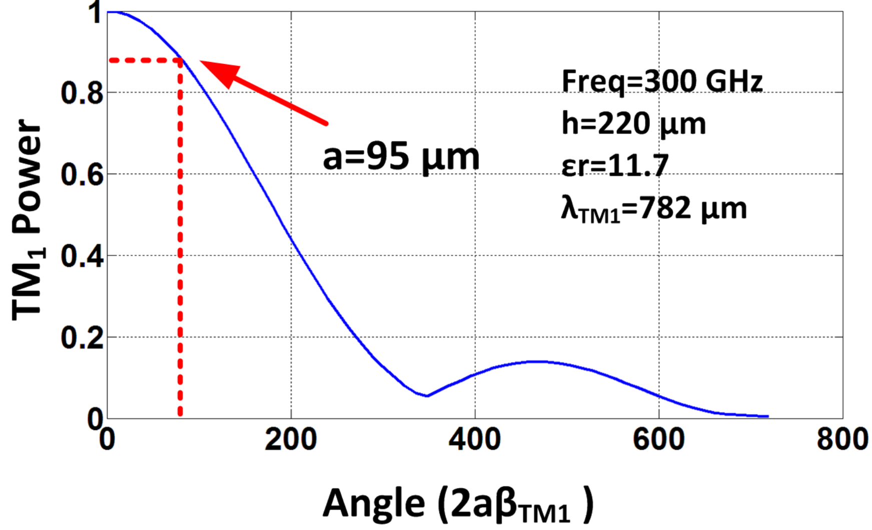

Figure 4.16: Variation of TM_1 power suppression with radius of the loop.

less affected since the dominant current elements add their individual TM_1 surface waves in phase. Also, due to a larger wavelength of TM_1 ($\lambda_{TM1} > 2\lambda_{TE0}$),the phase change between any two current elements in the loop a an direction is less than $\pi/2$ ($2a\beta_{TM1} < \pi/2$). Therefore, for the power which is radiated out in free-space, we expect even less suppression since $\lambda_0 > \lambda_{TM1} > \lambda_{TE0}$. For the designed loop radius of a=95 µm, the phase change over one diameter is given by $2a\beta_0 \approx \pi/5$. Therefore, the phase difference of the radiated waves between any two elements on the loop on the z=0 plane is less than $\pi/5$. For any elevation θ, the maximum phase difference is even smaller and given by $2a \sin\theta\beta_0$. Therefore, the resultant radiated far-fields from the traveling-wave loop can be calculated from (4.43) and (4.44) as

$$E_{\theta,loop}(a,r,\theta,\phi) = \frac{F_1(\theta)}{r} \max_{-\pi/2 \le \phi_O \le \pi/2} \left\{ \int_0^{2\pi} \sin\phi \sin(\phi - \phi_O) e^{-ja\beta_0 \cos(\phi - \phi_O)} d\phi \right\} \quad (4.80)$$

$$E_{\phi,loop}(a,r,\theta,\phi) = \frac{F_2(\theta)}{r} \max_{-\pi/2 \le \phi_O \le \pi/2} \left\{ \int_0^{2\pi} \sin\phi \cos(\phi - \phi_O) e^{-ja\beta_0 \cos(\phi - \phi_O)} d\phi \right\} \quad (4.81)$$

The total radiated power from the traveling-wave loop can be calculated as

$$P_{rad,loop} = \frac{1}{2\eta_0}\int_0^{\pi}\int_0^{2\pi}\left(|E_{\theta,loop}|^2 + |E_{\phi,loop}|^2\right)r^2 \sin\theta d\phi d\theta \quad (4.82)$$

Fig. 4.17 shows the variation of the total radiated power and the surface wave power along with its constituent components, each power being normalized to the maximum radiated power. Similar to a single Hertzian dipole in Fig. 4.8, the radiated power maximizes near h=70 µm and h=220 µm, when the waves, after suffering reflection from the bottom surface, add constructively at the top of the substrate. However, at the designed substrate thickness of 220 µm, we see an almost complete suppression of the TE_0 mode (compare this to Fig. 4.8). The TM_1 mode is suppressed in the same ratio as shown in Fig. 4.16.

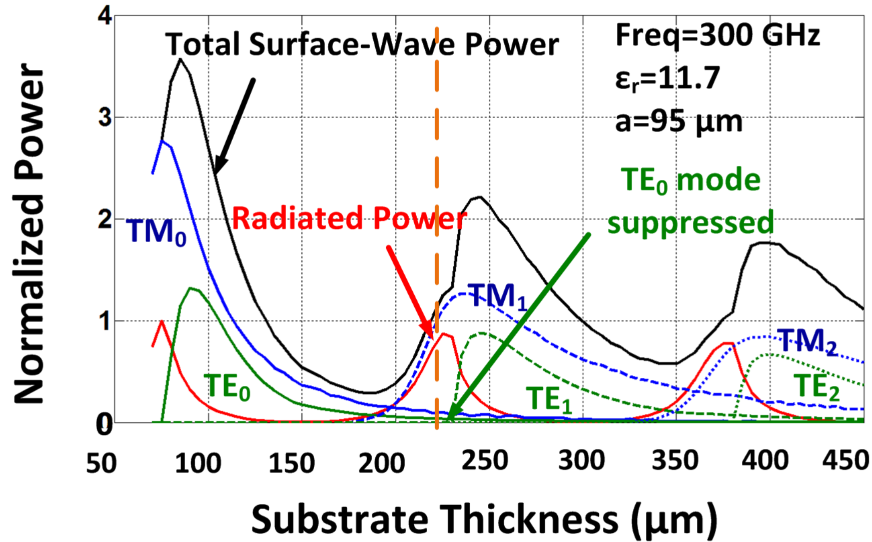

Figure 4.17: Total surface wave power broken down into its different modes and the total radiated power for a traveling-wave loop for different substrate thicknesses. The plot shows almost complete suppression of the TE_0 mode.

This is again reflected in Fig. 4.18, where we see a similar suppression of the TE_0 mode (compare this to Fig. 4.9). The absolute power in the TM_1 mode does not increase, however it now contributes to 88% of the total surface wave power. Because of the lower total surface wave power, the radiation efficiency shows an almost 10% increase reaching a maximum of 40% as shown in Fig. 4.19.

Due to the rotational symmetry of the traveling-wave circular-loop of current, the radi-

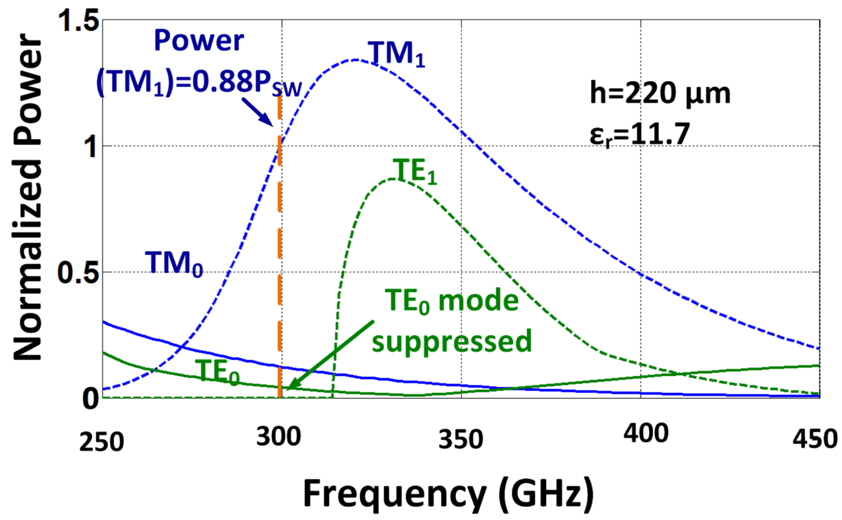

Figure 4.18: Constituent surface-wave power for different frequencies at a given substrate thickness of h = 220 µm and at a frequency of 300 GHz. The plot shows almost complete suppression of the TE_0 mode.

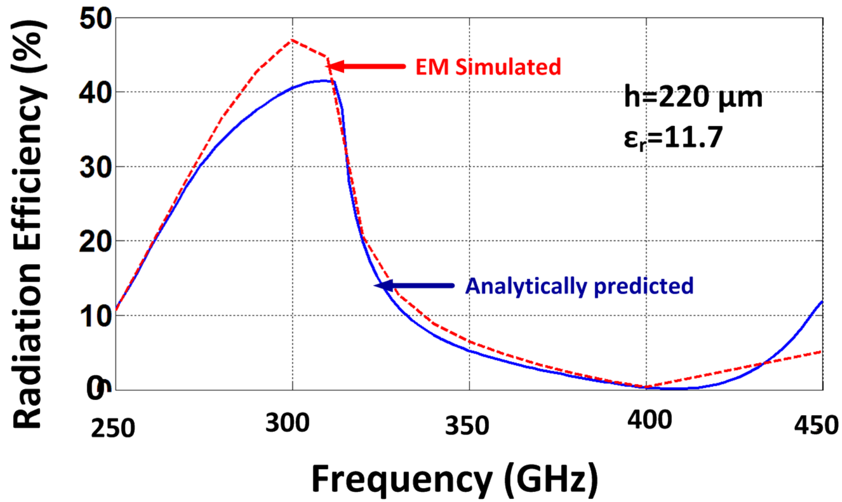

Figure 4.19: Radiation efficiency of traveling-wave loop against different substrate thicknesses.

ation pattern, similar to the surface-wave pattern, will be independent of ϕ. The patterns, analytically calculated from (4.80) and (4.81), are shown in Fig. 4.20 for different substrate thicknesses. The patterns show very close correspondence from the ones obtained from electromagnetic simulation.

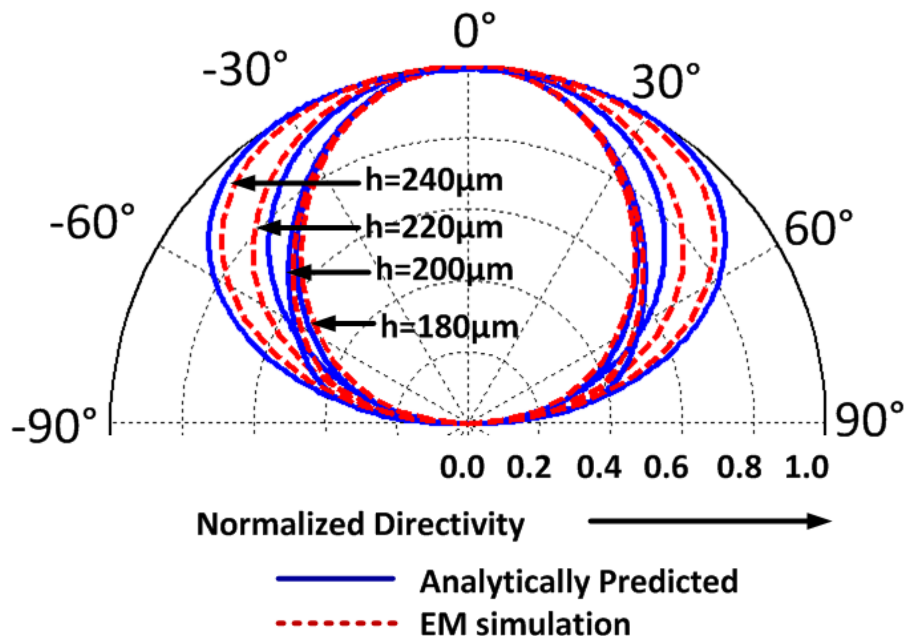

Figure 4.20: Analytically predicted and electromagnetically simulated pattern at any constant ϕ plane, for a traveling-wave circular loop of current for different substrate thicknesses. The substrate of choice is silicon ($\varepsilon_r = 11.7$)

In summary, radiation characteristics, power trapped in surface waves and radiation efficiency, are dependent on the surface current configuration. The distributed active radiator, with its traveling-wave configuration, not only achieves generation of RF signal from DC, frequency multiplication, filtering, but also radiates it efficiently by engineering surface currents in such a wave that one dominant surface-wave mode gets almost completely suppressed.

4.3 Distributed Active Radiator: Two Traveling-Wave Loops

In a DAR, we have one inner core loop of traveling-wave current and also another loop of current through the ground plane, which is phase shifted by $\pi/2$. Now, one can approximate the electromagnetic behavior of a DAR, with two concentric current loops, separated in phase by $\pi/2$. It is to be kept in mind that this equivalence model is very simplistic and only holds for very thin loops of current. If the ground plane is widened, then the distribution of the current in the plane needs to be considered. Due to the current loop being actively controlled with transistors, the return current density on the DAR ground plane will be concentrated near the edge of the aperture and therefore will behave like a loop of current. However, for wider ground planes, one needs to account for multiple reflections of waves between this ground plane of the DAR and the ground plane below the substrate as shown in Fig 4.12, and in the limit, the aperture will behave more like a slot.

In this anlaysis, we will assume the case where the loop approximation holds and we will approximate the DAR electromagnetic behavior with the equivalent traveling-wave model as shown in Fig. 4.21.

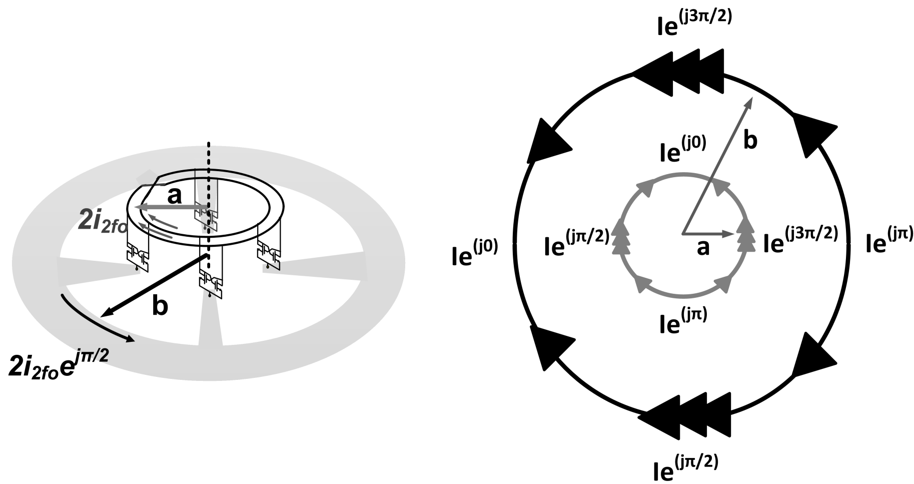

Figure 4.21: Traveling-wave model of a DAR with two concentric traveling-wave current loops separated in phase by $\pi/2$.

The net resultant radiated field due to two concentric traveling-wave currents can be

calculated from (4.80) and (4.81).

$$E_{\phi,DAR} = E_{\phi,loop}(a,r,\theta,\phi) + e^{j\pi/2} E_{\phi,loop}(b,r,\theta,\phi) \tag{4.83}$$

$$E_{\theta,DAR} = E_{\theta,loop}(a,r,\theta,\phi) + e^{j\pi/2} E_{\theta,loop}(b,r,\theta,\phi) \tag{4.84}$$

Also, the surface-wave fields in TE and TM modes can be calculated from (4.77) and (4.79)to be,

$$H_{zd,DAR} = H_{zd,loop}(a) + e^{j\pi/2} H_{zd,loop}(b) \tag{4.85}$$

$$E_{zd,DAR} = E_{zd,loop}(a) + e^{j\pi/2} E_{zd,loop}(b) \tag{4.86}$$

As we can see, from (4.83)-(4.86), the radiated as well as the surface-wave fields are in quadrature and therefore, add in power. As a result, they act as *two independent noninteracting sources* and it is reasonable, therefore, to advance the analysis with one traveling loop, keeping in mind, the presence of another loop in quadrature whose effects can be later added. This will be clear in the next section.

4.4 Arrays of Traveling-wave Loops: Remaining Surface-Wave Suppression

Recalling from the results, previously derived, the traveling-wave radiator suppresses TE_0 mode almost completely and therefore the remaining TM_1 mode is almost entirely responsible for the remaining surface-wave power. In this section, we will discuss how to suppress the TM_1 mode with multiple traveling-wave loops.

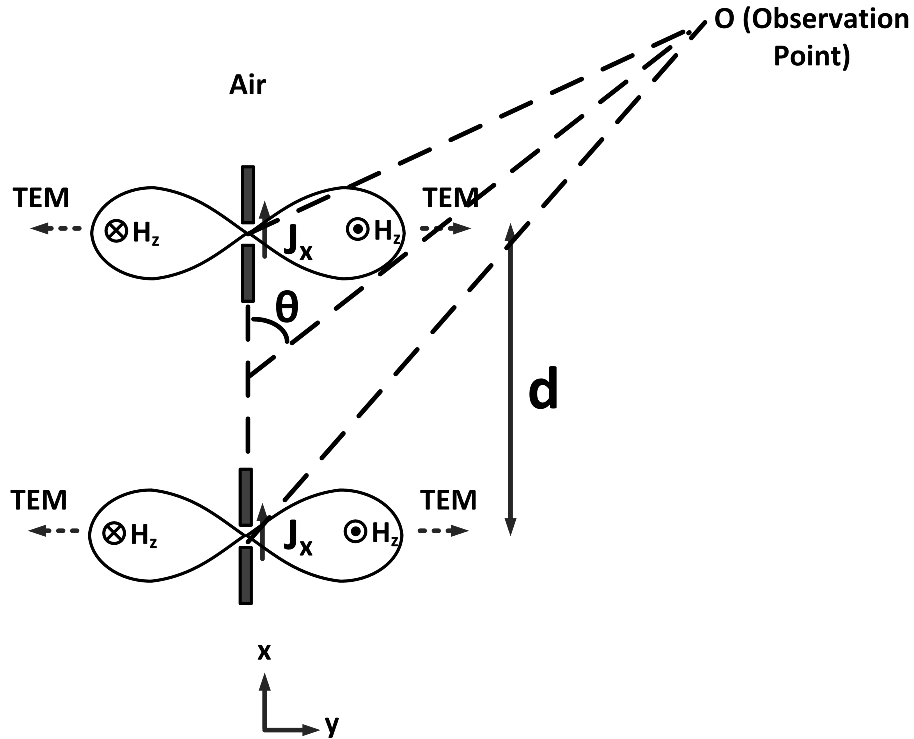

Figure 4.22: Two identical Hertzian dipoles in free-space.

4.4.1 Arrays of Hertzian Dipoles in Free-Space

Let us begin by considering *two identical noninteracting* Hertzian dipoles in free-space along the dipole axis, as shown in Fig. 4.22. It can be shown that, at the far-field of an individual dipole, only E_θ exists and is a function of the elevation as

$$E_{\theta,d} = \frac{E_0}{r} \sin\theta \tag{4.87}$$

Therefore,the total power radiated by a single dipole is given by

$$
\begin{aligned}
P_{rad,d} &= \frac{1}{2\eta_0}\int_0^{\pi}\int_0^{2\pi}|E_\theta|^2 r^2 \sin\theta d\phi d\theta \\
&= \frac{\pi E_0^2}{\eta_0}\int_0^{\pi}\sin^3\theta d\theta \\
&= \frac{4\pi E_0^2}{3\eta_0}
\end{aligned} \tag{4.88}
$$

The electric-field due to the dipole pair at any elevation angle θ can be obtained using superposition.

$$
\begin{aligned}
E_{\theta,dpair} &= \frac{E_0}{r}\sin\theta(1+e^{-j\beta_0 d\cos\theta}) \\
&= \frac{2E_0}{r}\sin\theta\cos(\frac{\beta_0 d}{2}\cos\theta)e^{-j\frac{\beta_0 d}{2}\cos\theta}
\end{aligned} \tag{4.89}
$$

The common assumption for noninteracting arrays of radiating sources is that due to interference, fields add coherently in certain parts of space and they destructively interefere in certain areas, keeping the total radiated power to be constant. We will now calculate the total power radiated by the dipole pair.

$$
\begin{aligned}
P_{rad,dpair} &= \frac{1}{2\eta_0}\int_0^{\pi}\int_0^{2\pi}|E_{\theta,dp}|^2 r^2 \sin\theta d\phi d\theta \\
&= \frac{\pi E_0^2}{\eta_0}\int_0^{\pi} 4\sin^3\theta\cos^2(\frac{\beta_0 d}{2}\cos\theta)d\theta
\end{aligned} \tag{4.90}
$$

The total power of the dipole pair, as a fraction of twice of the power of a single dipole, is plotted against distances of separation. It can be seen that the ratio progresses towards unity for $d > 2\lambda$, when the dipoles behave as noninteracting. However for $d < 2\lambda$, there is a significant variation in the total radiated power, which can be greater or less than the additive power of individual dipole elements. Even for a typical design separation of $d = \lambda/2$, the dipole pair radiates almost 30% more than the additive power of two individual dipoles.

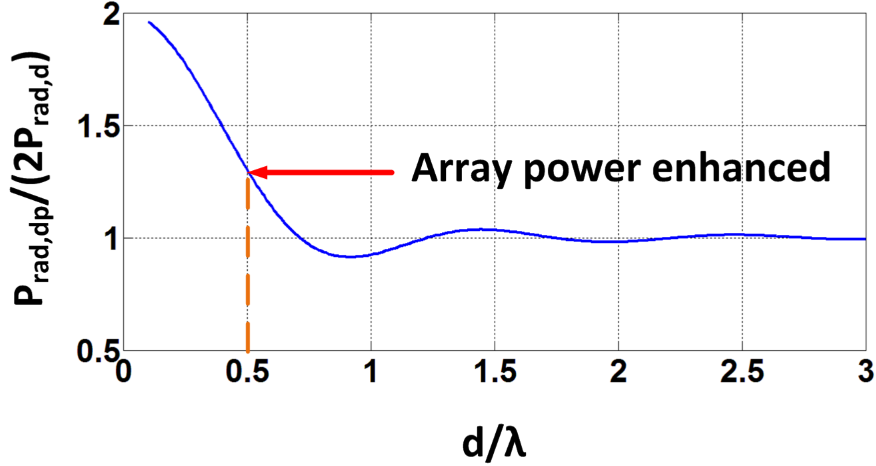

Figure 4.23: Ratio of total power radiated by a dipole pair to the sum of the individual pair for the configuration in Fig. 4.22.

This is not obvious, since we started with the assumption of noninteracting dipoles and applied superposition principles. However, the analysis reveals that one cannot ignore the near-field effects and the total radiated power in an array can be significantly different from the sum of the individual radiated power. Since, we have used current impulses, this analysis is valid. However, with any finite driving point impedance one has to consider the impedance variations due to non-negligible near-field interactions. One may note that the electric field E_x of an individual dipole towards the other dipole, only vanishes in the very far-field and one cannot, in general, ignore that effect.

Let us consider another example of two identical Hertzian dipoles in free-space along the perpendicular axis, as shown in Fig. 4.24. The total power radiated by the dipole pair can be found similar to (4.90) as

$$\begin{aligned} P_{rad,dpair2} &= \frac{1}{2\eta_0}\int_0^{\pi}\int_0^{2\pi}|E_{\theta,dp2}|^2 r^2 \sin\theta d\phi d\theta \\ &= \frac{\pi E_0^2}{\eta_0}\int_0^{\pi} 4\sin^3\theta\cos^2(\frac{\beta_0 d}{2}\sin\theta)d\theta \end{aligned} \quad (4.91)$$

As before, the total power of the dipole pair, as a fraction of twice the power of a single dipole, is plotted against distances of separation. The result is shown in Fig. 4.25. It can be

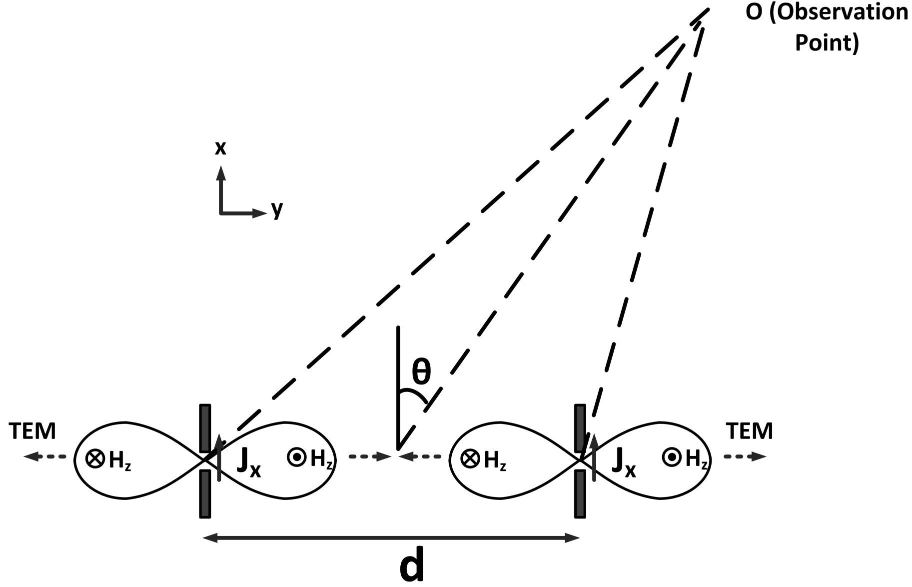

Figure 4.24: Two identical Hertzian dipoles in free-space separated along the perpendicular axis.

seen that the variation is much more significant compared to Fig. 4.23 and for distance of separation of $d = \lambda/2$, almost 90% of the radiated power can be canceled. Even though the power may add up in some other areas, the total integrated power is only 10% of the sum of the individual radiated power. The configuration shown in Fig. 4.24 is similar to the case of the traveling-wave radiator, with its remnant TM_1 surface-mode. If we employ an array of the traveling-wave loops separated by $d = \lambda_{TM1}/2$, then the surface-wave power contained in TM_1 can be significantly reduced. However, in the intended direction of radiation, the configuration will be similar to Fig. 4.22, where the radiated fields add up, leading to a boost in radiated power, as demonstrated in Fig. 4.23.

4.4.2 Arrays of Traveling-Wave loops: Suppression of Remaining Surface-Wave Power

We proceed to use a similar analysis to analyze 2D arrays of DARs, which can be expected to suppress the cylindrical TM_1 surface modes, if the spacing between the array elements is optimized. However, at boresight direction in air, arrays of synchronized DARs will combine their power coherently. The set of 2x2 arrays of DARs under analysis is shown in Fig. 4.26.

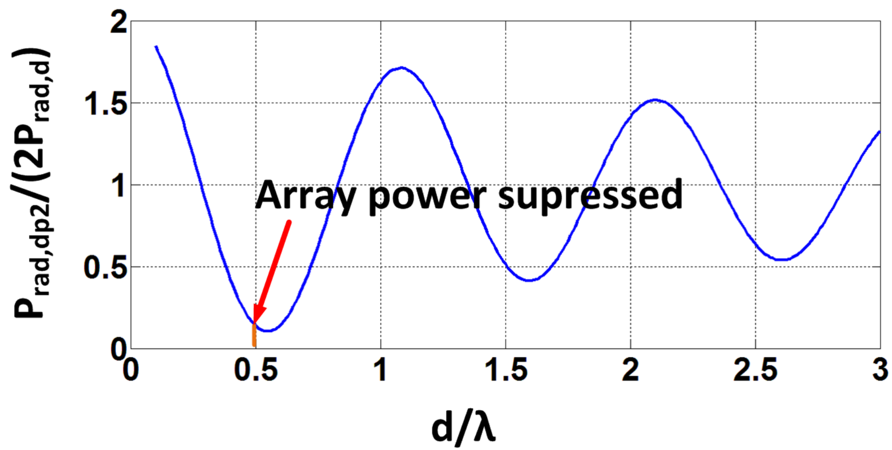

Figure 4.25: Ratio of total power radiated by a dipole pair to the sum of the individual pair for the configuration in Fig. 4.24.

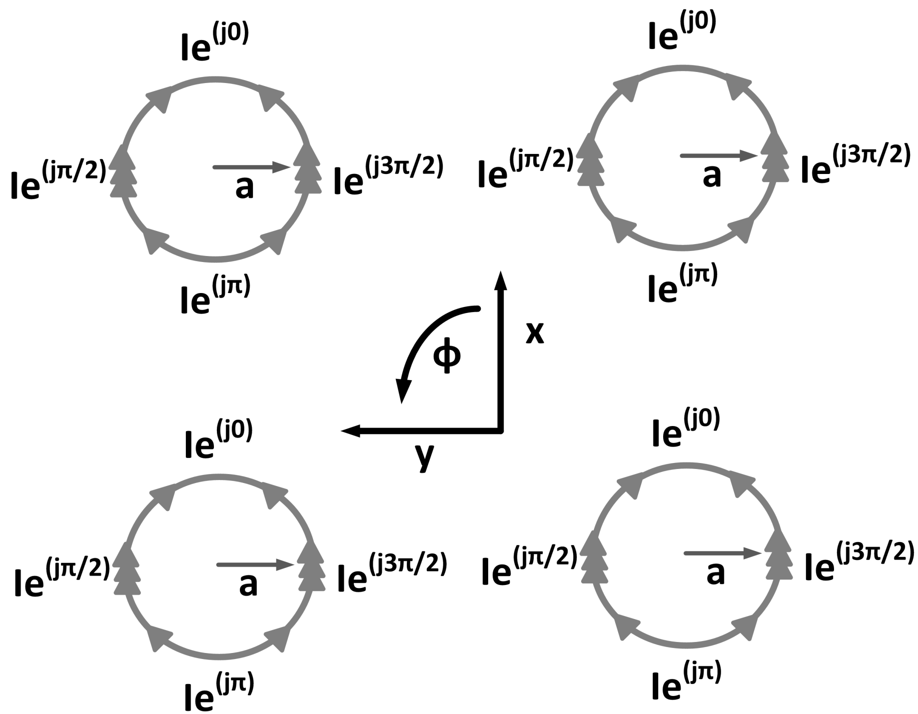

Figure 4.26: 2x2 arrays of DARs to suppress TM_1 mode.

We will demonstrate this with an example. The wavelength corresponding to the dominant TM_1 mode for h=220 µm is λ_{TM1}=782 µm as shown in Fig. 4.15. We keep the element spacing at $d \approx \lambda_{TM1}/2 \approx 400$ µm. The radiated power, total surface wave power and its components have been plotted in Fig. 4.27 for different substrate heights. At h=220 µm, it shows almost complete suppression of both the surface wave modes, namely TE_0 (due to the traveling-wave loops themselves) and TM_1 (due to array configuration). One can compare this against Fig. 4.8 and Fig. 4.17.

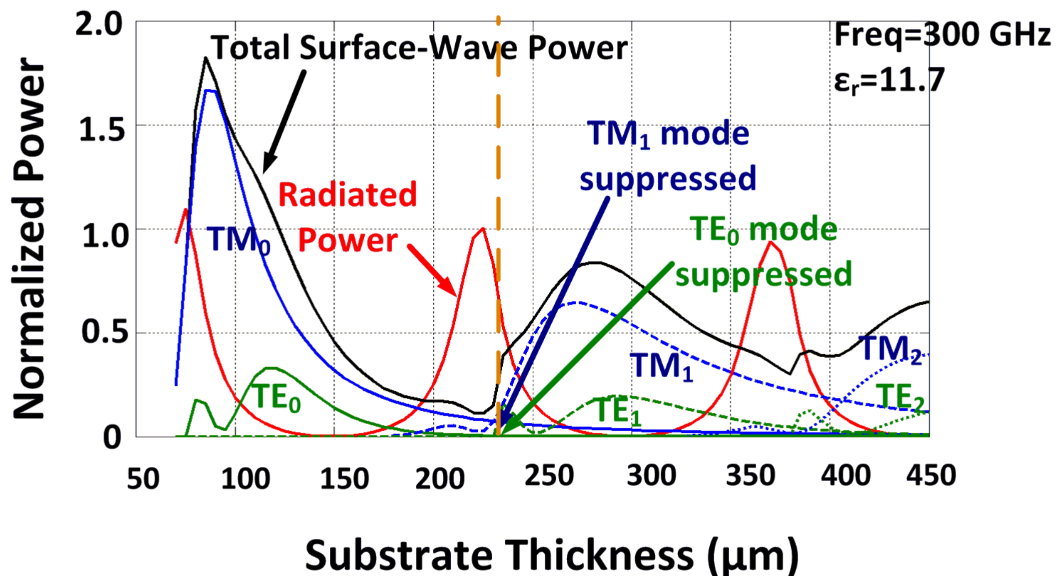

Figure 4.27: Total surface wave power broken down into its different modes and the total radiated power for 2x2 arrays of traveling-wave loops, separated by $d \sim \lambda_{TM1}/2$, for different substrate thicknesses. The plot shows almost complete suppression of the TE_0 and TM_1 modes.

The radiation efficiency for different substrate heights, has been shown in Fig. 4.28. At h=220 µm, due to almost complete suppression of surface-waves, radiation efficiency has increased to 90% and this has been verified by corroboration with EM simulations, as shown in Fig. 4.29. Again, one can compare this with Fig. 4.11 and Fig. 4.19.

At the optimum spacing, the local derivative of array power with spacing is zero. Therefore, the suppressed surface-wave power is not very sensitive to element spacing, as shown in Fig. 4.30, which shows the efficacy of array structures in reducing surface wave power. The radiation patterns, analytically predicted and EM simulated, for the 2x2 arrays of traveling-

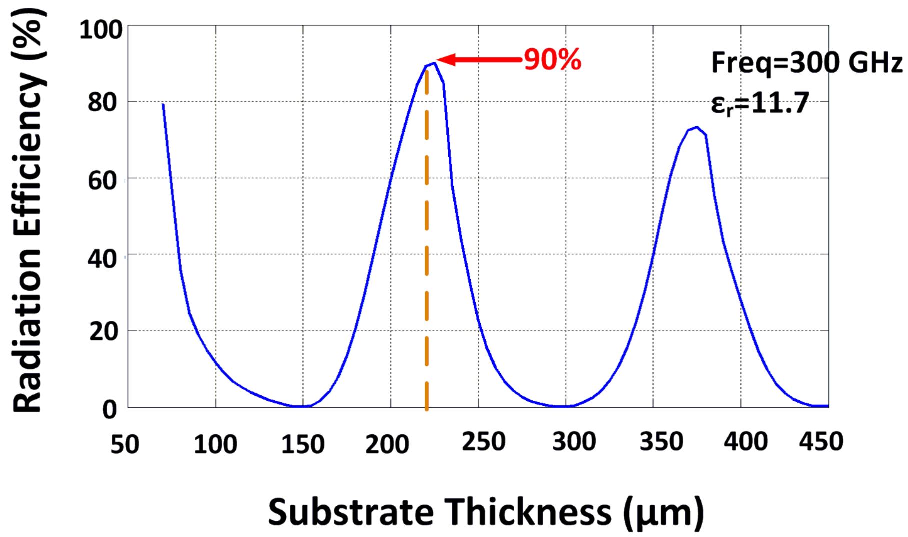

Figure 4.28: Radiation efficiency of 2x2 arrays of traveling-wave loops, separated by $d \sim \lambda_{TM1}/2$, against different substrate thicknesses.

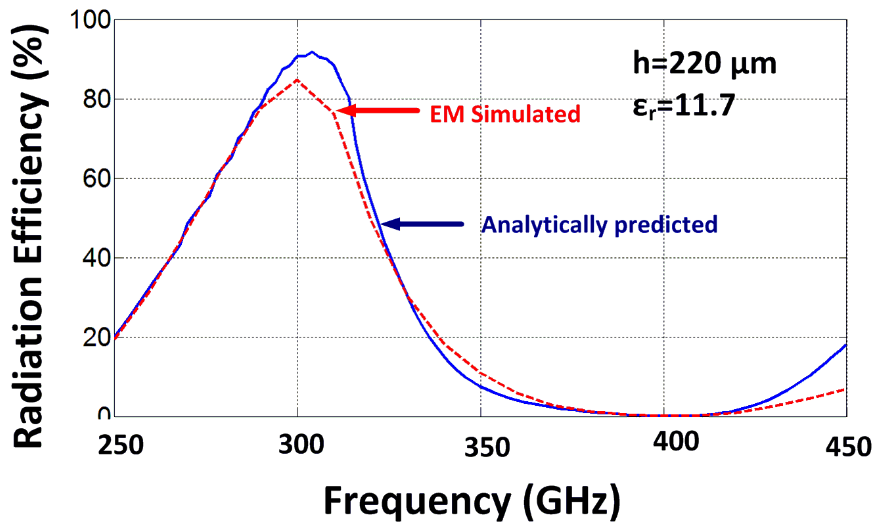

Figure 4.29: Radiation efficiency of 2x2 arrays of traveling-wave loops, separated by $d \sim \lambda_{TM1}/2$, against frequency.

wave loops, are shown in Fig. 4.31.

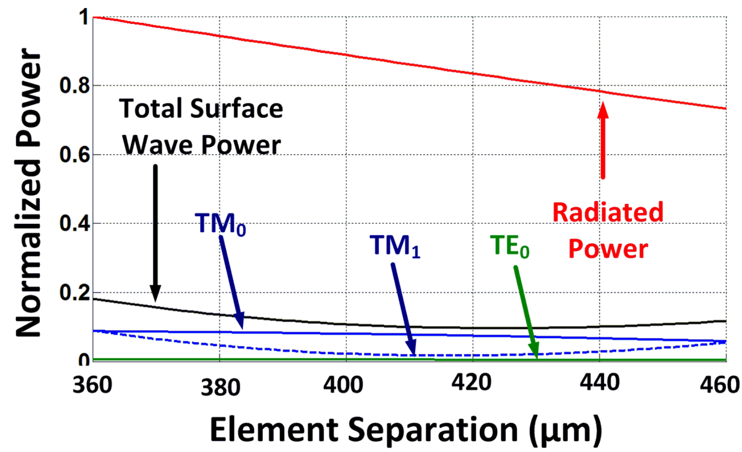

Figure 4.30: Radiated and suppressed surface wave powers for different element spacings.

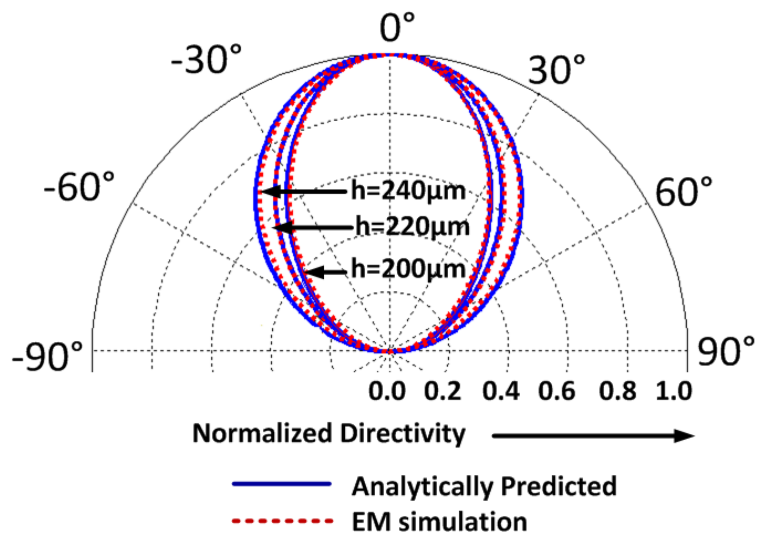

Figure 4.31: Analytically predicted and electromagnetically simulated radiation patterns for 2x2 arrays of traveling-wave loops, separated by $d \sim \lambda_{TM1}/2$.

Chapter 5

Coupled THz Arrays in CMOS

In Chapter 3, we showed distributed active radiator to be an efficient method of conversion from DC power into radiated THz power in silicon processes. While DAR is a distributed structure in itself, in order to generate higher power and higher EIRP, arrays of such structures can be synchronized to each other so that the radiated power coherently combines in free-space without loss. As discussed in Chapter 4, the total radiated power and EIRP scale as N and N^2, respectively, where N is the total number of array elements. This is pictorially represented in Fig. 5.1 and Fig. 5.2, where the radiated beam gets more directive (sharper) with increased number of elements. This happens essentially because the aperture of the radiating surface (A_{eff}) increases with number of elements which results in increased directivity (D) by the reciprocity relation ($D = \frac{4\pi}{\lambda^2}A_{eff}$) [67]. As shown in Fig. 5.2, such an array realization also enables us to perform electronic beam-steering in space by having individual phase control in each of the radiating elements [67], [68], [102].

In this Chapter, we will discuss the challenges of synchronizing large-scale 2D arrays of coherently locked oscillating THz sources for beam-forming and beam-steering. We will also discuss the various methods we have proposed, implemented and analyze them theoretically. We will conclude with measurement results corroborating our theory.

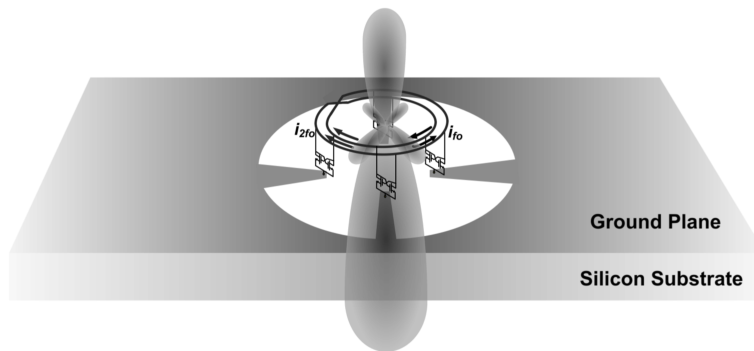

Figure 5.1: A single Distributed Active Radiator converts DC power into THz power and radiates with a broad beam

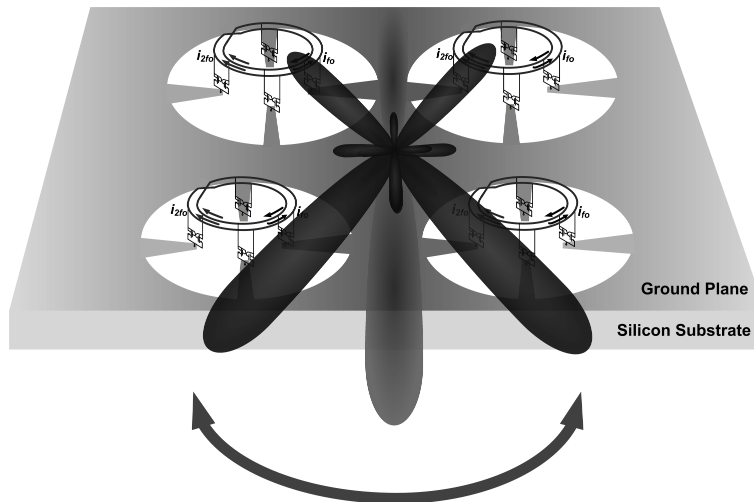

Figure 5.2: Arrays of Distributed Active Radiators can be synchronized to radiate higher power with narrower beam and potentially enabling electronic beam-scanning.

5.1 Free-Space Power Combining and Beam-Scanning

Let us consider a linear array of 'N' identical radiating sources, each with radiation pattern R(ϕ) and separated by distance 'd', as shown in Fig. 5.3. Let us suppose that we can control the phase and amplitude of the excitation of each on of them. The theory of combining many coherent sources in space for lossless power combination and beam-scanning has been covered extensively in scanning array and phased-array literatures [67], [68], [102]– [104]. We will give a brief description for the sake of completion.

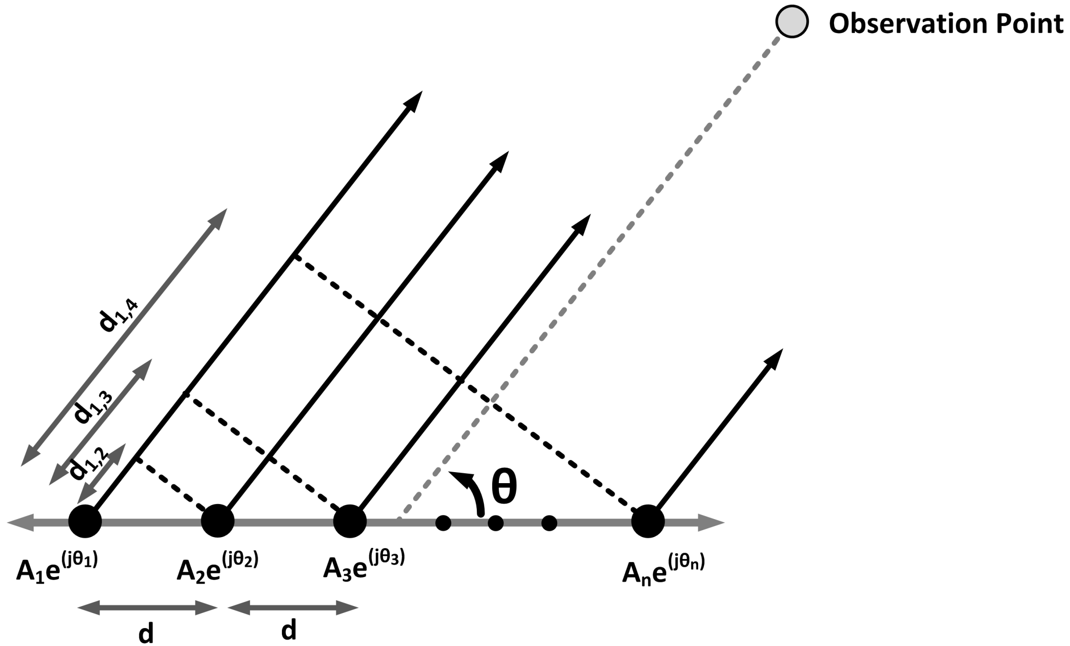

Figure 5.3: Linear antenna array for power combining and electronic beam-scanning.

Let A_m and θ_m be the amplitude and phase of the mth element in the N element linear array. At an observation point 'O', which is at angle of θ from the array axis, as shown in Fig. 5.3, the amplitude of the 'N' interfering waves will be given by

$$A(\theta) = R(\theta) \sum_{m=1}^{N} A_m e^{j\theta_m - \beta d_m} \quad (5.1)$$

where $\beta = 2\pi/\lambda$ is the propagation constant, d_m is the distance from the mth radiating

element to the observation point 'O', the product βd_m is the total phase change suffered by the wave as it propagates from the mth element source to the observation point and $R(\theta)$ is the gain of an individual radiator.

Therefore, if we want the resultant beam to tilt towards the direction of 'O', then all the waves need to interfere constructively at 'O'. This can be achieved if the phases of individual sources are adjusted such that the waves from the 'N' sources arrive in-phase at 'O'. Therefore, from (5.1), we have

$$\begin{aligned} \theta_m &= \beta d_m \\ \Rightarrow \theta_m &= m\beta d \cos\theta, \qquad \text{since } d_m \approx md\cos\theta \end{aligned} \tag{5.2}$$

This implies we need a linear phase progression among the elements. Assuming equal amplitude excitations, *i.e.*, $\mathrm{A_m} = \mathrm{A}$, and using the relation in (5.2), we have

$$A(\theta) = R(\theta) \sum_{m=1}^{N} A_m \tag{5.3}$$

At any other observation point at an angle Φ, we have

$$\begin{aligned} A(\Phi) &= R(\Phi) A \sum_{m=1}^{N} e^{jm\beta d\cos\theta - m\beta d\cos\Phi} \\ &= R(\Phi) A \frac{\sin[\frac{N}{2}(\beta d\cos\theta - \beta d\cos\Phi)]}{\sin[\frac{1}{2}(\beta d\cos\theta - \beta d\cos\Phi)]} \end{aligned} \tag{5.4}$$

The radiation pattern of the N sources with equal amplitudes and linear phase progression in (5.2) is given by (5.4). The resultant beam pattern is the product of the individual beam pattern $R(\Phi)$ and the array pattern. It can be easily observed, that the array pattern has a maximum at an angle θ at the observation point 'O'. In summary, one can control the individual phase relationships among an array of radiating sources to electronically control the direction of the radiated beam and combine power coherently in free-space.

5.2 Synchronizing Arrays of Distributed Active Radiators

In this section, we will discuss various methods, design tradeoffs and implementation for arrays of autonomous radiating elements. Depending on the synchronization modality, they are can be broadly of two categories, as illustrated in Fig. 5.4. They are

- Mutually coupled system
- Unilaterally and centrally locked to one frequency reference

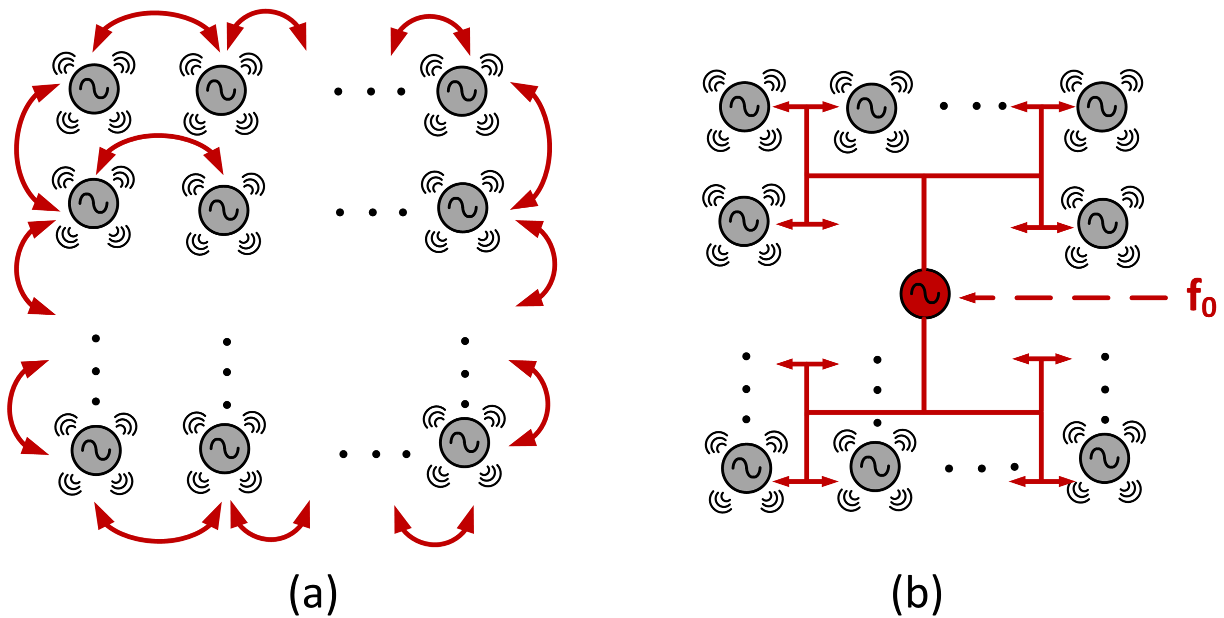

Figure 5.4: Mutual coupling between free-running oscillators synchronizing each other (a). One central frequency reference unilaterally locking multiple autonomous oscillatory elements (b).

The concepts are illustrated in Fig. 5.4. Arrays of DARs could be mutually coupled to each other in a suitable way so that the synchronization condition is the most stable condition. This is illustrated in Fig. 5.4(a). Such a general system of mutually coupled nonlinear dynamical elements may have multiple steady-state solutions. It is, therefore, important to design the coupling network in such a way that the synchronized state is the only stable state, and any initial condition will ultimately relapse into this stable locked state.

The frequency of radiation for such a system is governed by the common locking frequency of the coupled oscillators and thus collectively free-running in nature. If $f_1, f_2 ... f_N$ be the closed-spaced free-running frequencies of oscillation of the individual elements, then the common oscillation frequency in the locked case will be approximately $f_c \approx \frac{1}{N}\sum_{i=1}^{N} f_i$ [105]– [108]. For such a system, it is difficult to determine the output frequency accurately, and in general, it will vary with fabrication processes and on external conditions, such as temperature and power supply changes. This may be acceptable for applications, where the receiver is not sensitive to slight variations in incoming signal frequency, such as in non-coherent receivers and energy detectors for imaging purposes. However, in communication systems, we would often require accurate control over the emitted frequency so that receiver can effectively decode the information. Fig. 5.4(b) illustrates such a case, where all the elements are locked to one central oscillator which can be synchronized to a low-frequency stable reference (f_0). In this Chapter we will discuss the case of the mutually coupled system. The case for the centrally locked reference will be discussed in Chapter 6.

We will discuss our two proposed methods of mutual synchronization of multiple DAR elements. They are

- Transmission-line based synchronization
- Near-field coupling based synchronization

5.3 Transmission-Line Coupling

Assume that there are M cross-coupled pairs distributed uniformly in a single DAR as shown in Fig. 5.5. We would like to mutually lock two such identical DARs so that they combine coherently in the broadside direction as depicted in Fig. 5.2. This would be achieved if all the M corresponding cross-coupled pairs oscillate and radiate in phase in both the DARs. Assume, for now, that we can lock two such cross-coupled pairs by a coupling network, as shown in Fig. 5.5. We will discuss the requirements and design of the coupling network, but for now, assume that the coupling network ensures that the two cross-coupled pairs which

are connected to the network oscillate in phase.[1] In order to ensure phase-coherence in all the M cross-coupled pairs, we however, do not need M such coupling networks between each corresponding pair. It can be easily argued that two judiciously placed networks will ensure a synchronized state, as long as the start-up condition for the traveling-wave oscillation is satisfied for each DAR [57]. We will give a short intuitive reasoning here. Let us place one coupling network between cross-coupled pairs $P_{1,1}$ and $P_{2,1}$ between the two DARs as shown in Fig 5.5. This ensures that $P_{1,1}$ and $P_{2,1}$ are in phase, but the wave can still travel in two different directions in the two DARs. A second coupling network, as shown in Fig. 5.5, between another corresponding pair $P_{1,i}$ and $P_{2,i}$ ensures that the direction of wave travel is also same in both of them, guaranteeing phase-coherence in all the corresponding oscillators in the two DARs.

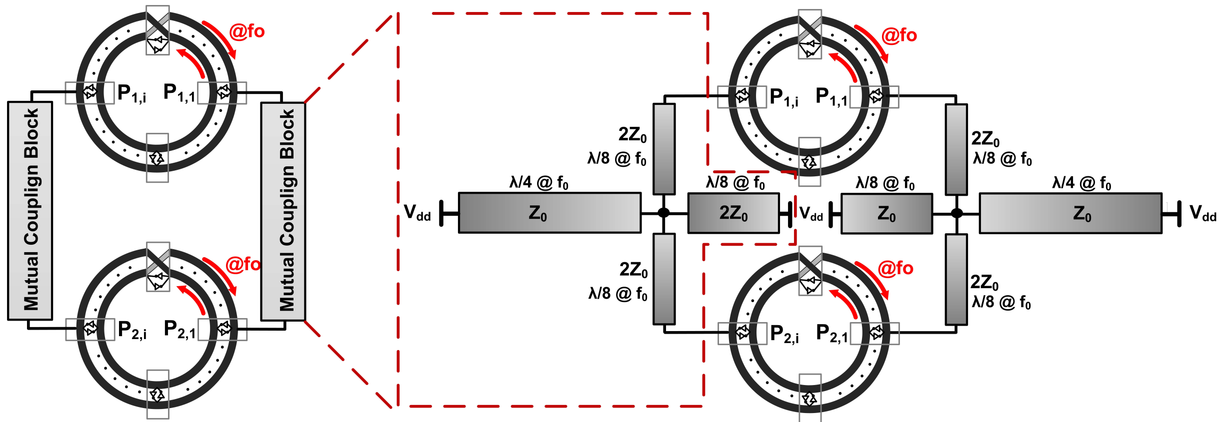

Figure 5.5: Transmission-line based coupling to synchronize two Distributed Active Radiators.

The network needs to satisfy certain properties in order to function as the locking network.

1. Due to DAR spacings, the physical dimension of the network will be comparable to the wavelength of operation and therefore, the network is distributed.

2. Secondly, in the locked state, the network should present open-circuit impedance to the connected DARs at both the frequency of oscillation (f_0) and the frequency of radiation

[1]If the network is an infinitesimally short piece of wire, then the two oscillators shorted together would obviously oscillate in phase.

$(2f_0)$. This will ensure that the coupling network doesn't affect the operation of the DAR core.

3. Additionally, the network should ensure that the mutually locked condition is the lowest energy state of the system and therefore, any perturbation from any other state will bring back the DARs into the locked state.

An implementation of such network, based on transmission lines, is shown in Fig. 5.5. The network mutually forces mutual synchronization in the DARs it connects, while providing DC voltage to the nodes. The network also provides open-circuit impedances at both the frequency of oscillation (f_0) and the frequency of radiation $(2f_0)$. This operating principle is explained in Fig. 5.6. Under locked condition, the instantaneous currents from the two symmetrically coupled nodes add in phase at the junction, as shown in Fig. 5.6. Therefore the resultant impedance at f_0, that each DAR sees, consists of two $\lambda/8$ t-lines of effective characteristic impedance $2Z_0$ in series and shorted at the end. This results in an open-circuit impedance. The network also provides an open circuit impedance at the second harmonic frequency $(2f_0)$ as also illustrated in Fig. 5.6.

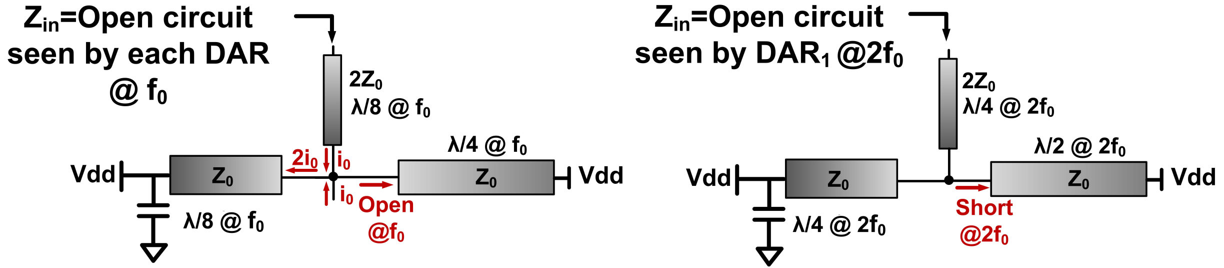

Figure 5.6: Transmission-line coupling network providing DC power supply. Under locked condition, it presents open-circuit impedances at both fundamental (f_0) frequency as well as at the radiated second harmonic frequency $(2f_0)$.

The t-line network was implemented in 45 nm SOI CMOS process for a fundamental frequency (f_0) of 150 GHz and a radiated frequency of 300 GHz [57]. The chip results will be discussed in later part of this chapter. The cross section of the t-line is shown in Fig. 5.7. The signal line is 2.1 µm thick and separated by 8.4 µm from the bottom ground plane. The

network was simulated in IE3D and the resultant impedance observed by each DAR under the condition of synchronization has been shown in Fig. 5.8. As observed in the plot, each DAR sees almost open-circuit impedances both at the fundamental and radiated frequencies of 150 GHz and 300 GHz. The network is doubly resonant at these frequencies. The variation of the impedance for other frequencies from 100 GHz to 400 GHz has been shown in Fig. 5.8.

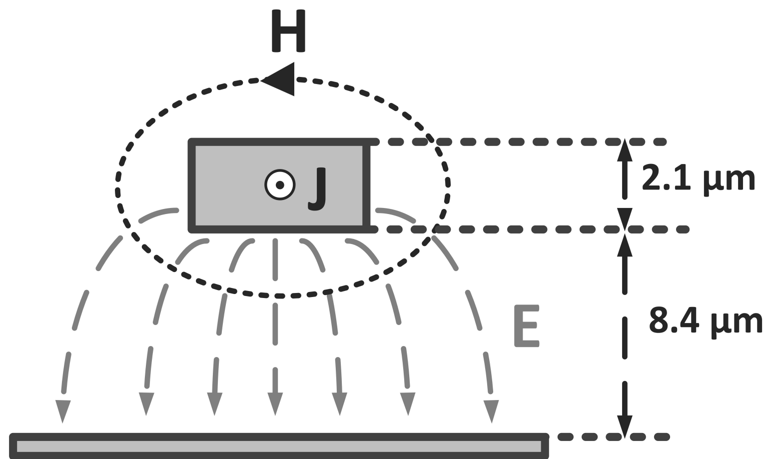

Figure 5.7: Cross section of the t-line in Fig. 5.5 implemented in 45 nm SOI CMOS process, showing instantaneous electric and magnetic field lines.

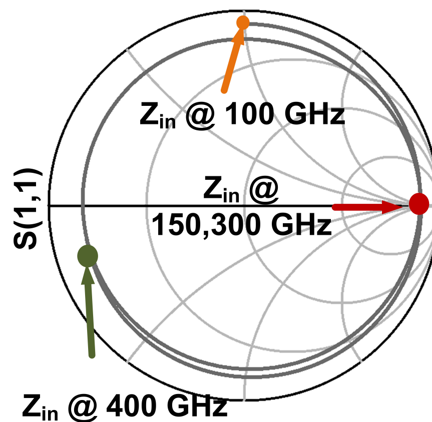

Figure 5.8: The impedance seen by each DAR, under synchronized condition, against frequency. The network provides open-circuit impedances at the designed oscillation frequency of 150 GHz and at the eradiated frequency of 400 GHz.

The t-line method is a straightforward robust method to lock multiple DARs, as demonstrated in [57]. While this method was possible to lock a 2x2 array, for larger arrays, the

network of t-lines become too complex. The physical dimensions become major impediments to layout; some transmission lines have to cross over each other and it is difficult to accommodate such multiple networks for large-scale arrays. More importantly, the length of the t-lines connecting the DARs dictate the separation of the radiator cores. This is not optimal since the DAR placement can be optimized to partially cancel the substrate waves excited by each other in a large-scale array, as discussed extensively in Chapter 4. This can lead to a substantial improvement in radiation efficiency, output power and clean radiation patterns. Near-field locking, as will be discussed now, not only addresses these constraints, but removes the function of mutual synchronization to another level of abstraction. This allows independent optimization of the power generating elements, the radiator cores and their placements, while ensuring mutual synchronization happens at the background. It should be noted that the concept of near-field synchronization is general and is applicable to arrays of any form of free-running autonomous radiating sources.

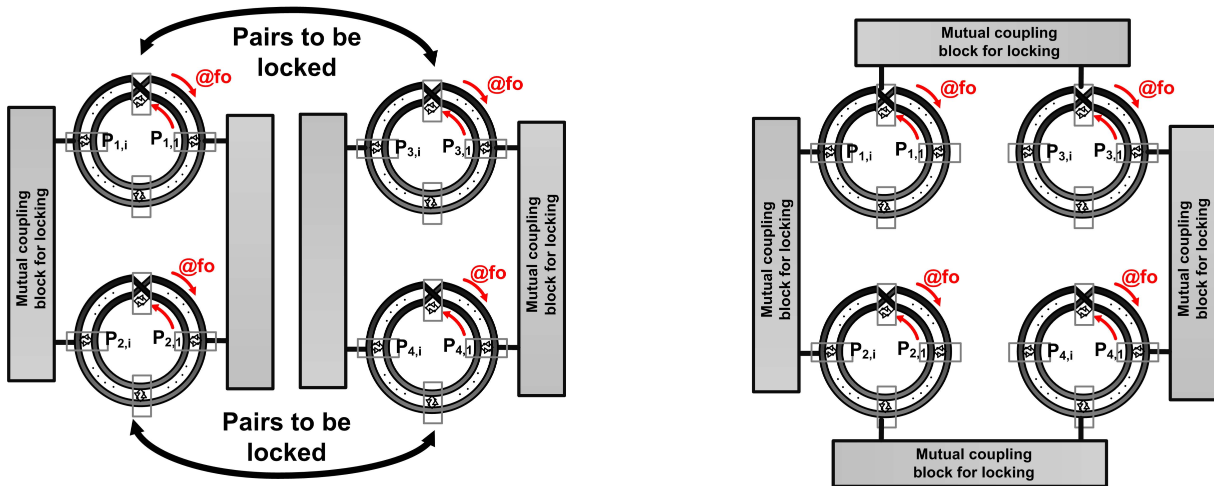

Figure 5.9: T-line-based coupling networks required for coherent synchronization of 2x2 arrays of DARs.

5.4 Near-Field Synchronization

Let there be two *uncoupled*[2] near-identical oscillators running at almost the same frequency. Even though the oscillators are identical in design, the difference in their frequencies of oscillation can be attributed towards active and passive mismatches. Further assume, that during oscillation, they radiate the fundamental frequency or any of its harmonics. In the absence of strong enough coupling, the oscillations will occur at nearly the same frequencies but at random phases. However, the electromagnetic (EM) waves, both in the near and far-fields, radiated by each of these structures will carry the information of the corresponding frequency and phase. The central idea behind near-field synchronization is to sense the radiated fields of each of them separately, and create a condition which forces the fields to equalize. Such forced equalization of the boundary conditions will result in that information being propagated back towards the source of the boundary conditions forcing the oscillators to lock to each other.

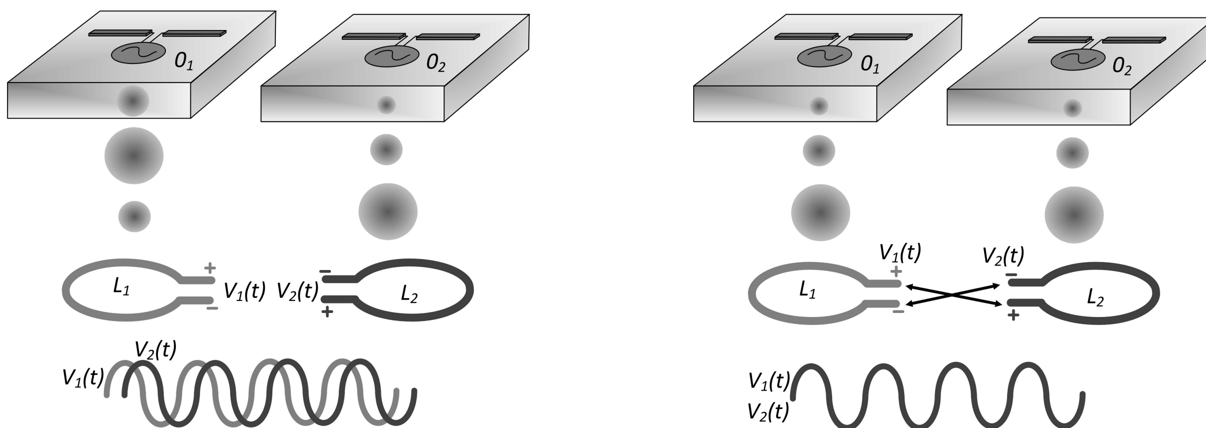

Figure 5.10: Sense antenna picks up the radiated fields of free-running radiating sources and carries the information of phase and frequency of the oscillator cores. If the sense antennas are suitably coupled, the radiated fields will equalize, forcing the oscillators to lock to each other.

The conceptual idea is illustrated in Fig. 5.10. Let there be two uncoupled free-running oscillators O_1 and O_2 radiating in space. To probe the individual radiated fields, we place two identical 'sense' antennas L_1 and L_2 at exactly the same relative position with respect

[2] We define the state *'uncoupled'* when coupling is too small for the near-identical oscillators to lock to each other

to the sources O_1 and O_2, respectively. Assume, for now, that the sense antenna L_1 (L_2) only receives radiation from the corresponding oscillator O_1 (O_2) and does not pick up any spurious fields from the oscillator O_2 (O_1). Without any locking mechanism, as discussed before, O_1 and O_2 will oscillate at similar frequencies but at random phases. The voltages at the terminals of the corresponding sense antennas L_1 and L_2 will be exactly at the same frequencies and at the same relative random phases. Now, if we couple the sense-antennas appropriately, so that the lowest energy state or most stable condition of the system is when the terminal voltages equalize, then it will also force the frequency and phase of the source oscillators to equalize. Thereby, the free-running oscillators O_1 and O_2 can be 'wirelessly' locked as shown in Fig. 5.10. *This removes the necessity of complicated multinodal transmission networks for synchronized large 2D arrays (Fig. 5.5) and frees up the possibility of optimized design and placement of the radiator cores.* It relegates the function of locking to the background, making it transparent to system design. This method of locking, does not suffer from constraints like other radiative coupling methods where radiating oscillators need to be placed very closely to each other for the coupled radiative fields to force locking [109].

5.4.1 Sensing the Near-Field

For implementation in silicon, both the radiators and the sense antennas are realized with back-end of the line metal layers in the die. Therefore, the sense-antennas, will be in the near-field of the radiator cores. It is important to understand how the presence of the sense-antennas will affect the near-field and therefore the far-field radiation patterns, and how different harmonics contribute to the locking mechanism. While intuition would like us to believe that the sense antenna will only pick up the radiated second harmonic fields, we will show that, only the fundamental frequency fields, which cancel in the Fraunhofer region, are picked up by the near-field sense antenna. The desired second harmonic radiation is unaffected by the presence of the sense antenna network.

Fig. 5.11 shows a three-dimensional layout of radiator cores along with the sense antenna and the ground plane with the aperture opening. Let us assume the DAR has a fundamental

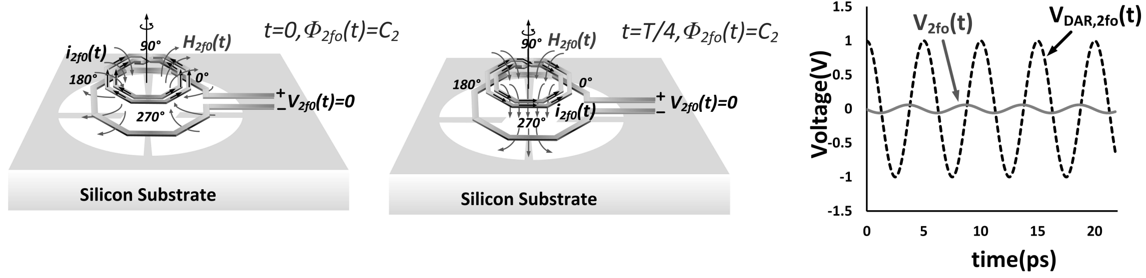

Figure 5.11: The second harmonic current with time rotates about the broadside axis leading to constant magnetic flux through the sense antenna aperture. The sense antenna, therefore, is transparent to the second harmonic radiation.

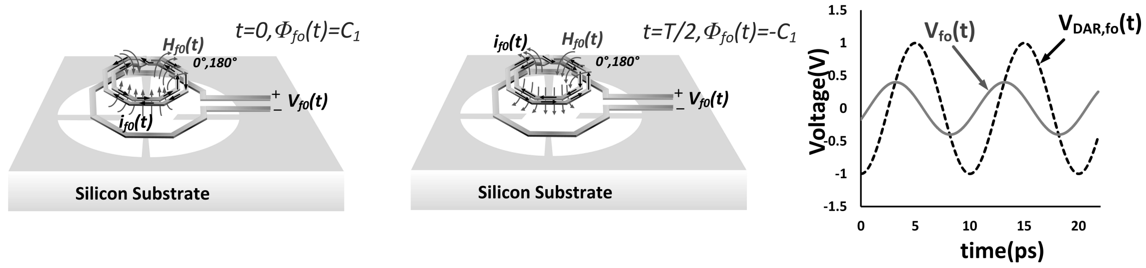

Figure 5.12: The out-of-phase fundamental frequency currents in the two branches do not cancel their fields in the near-field region, leading to a periodically changing flux at the fundamental frequency. The sense antenna, therefore, picks up signal only at the fundamental frequency.

frequency of oscillation of f_0 and the desired radiation frequency of $2f_0$. The current configurations along the DAR for the second harmonic is shown in Fig. 5.11. The $2f_0$ currents in both the branches are in phase and the total phase change over one loop is 360°, as shown in Fig. 5.11. Now, the second-harmonic voltage at the terminal of the sense antenna is related to the rate of change of magnetic flux at $2f_0$, generated by the DAR, coupled through the sense-antenna. Therefore, if $\mathbf{V_{2f_0}(t)}$ is the voltage at $2f_0$ at the sense antenna terminal and $\mathbf{\Phi_{2f_0}(t)}$ is the second harmonic magnetic flux linked to the sense-antenna, then

$$\mathbf{V_{2f_0}(t)} = \frac{d}{dt}\mathbf{\Phi_{2f_0}(t)} \tag{5.5}$$

It it to be noted that the second harmonic currents form in-phase traveling-wave in both the branches. Therefore, with time, the $2f_0$ current configuration and the magnetic fields, essentially, rotate about the broadside axes as shown in Fig. 5.11. Hence, by rotational symmetry, the $2f_0$ magnetic flux linkage to the sense antenna whose surface is perpendicular

to the broadside axis, remains constant with time. Therefore by (5.5), we have

$$\mathbf{\Phi_{2f_0}(t)} \approx C(constant) \tag{5.6a}$$

$$\mathbf{V_{2f_0}(t)} \approx 0 \tag{5.6b}$$

This implies that the sense antenna does not pick up any second harmonic radiation and does not affect the near-fields at $2f_0$. Assuming that a second harmonic traveling-wave of amplitude $1V$, exists on the DAR, the voltage picked up at the sense antenna terminal, as illustrated in Fig. 5.11, is shown to be negligible. In reality, the $2f_0$ wave amplitude on the DAR will be much less than 1 V and therefore, the sense antenna $2f_0$ voltage will be even lesser. In summary, *even though the second-harmonic is the dominant radiated power, the near-field sense antenna does not pick up its power or affect its radiation characteristics, which also suggests that second harmonic power generation does not contribute to the locking mechanism.* [3]

The current distribution of the fundamental frequency does not possess the rotational symmetry of its second harmonic as shown in Fig. 5.12. The out-of-phase currents in the two branches cancel their radiation only in the far-fields, but in the near-field the distance of the two loop branches from any point on the aperture of the sense antenna is significantly different. As a result, the strength of the fields contributed by the out-of-phase currents at such a closely placed point are different. This results in a periodically changing non-zero magnetic flux linkage with the sense antenna aperture. The concept is illustrated in Fig. 5.12 where the direction of the instantaneous fundamental current in the two loops interchanges over one time period leading to a periodically changing magnetic flux and a significant pick-up in the sense antenna terminal. This is illustrated in Fig. 5.11 which shows

[3] The reasoning of rotational symmetry and constant magnetic flux holds for far-field regions too. Therefore if the sense antenna is placed in the far-field in the same way as shown in Fig. 5.11, the magnetic flux would still remain constant and no radiation will be picked up. This happens because the receiving radiation pattern of the sense antenna is not aligned to the incoming radiation from the DAR and the magnetic flux is parallel to the sense antenna aperture. The antenna needs to be rotated so that the aperture is parallel to the broadside axis, for the magnetic field to have a nonzero flux coupled to the antenna.

the f_0 voltage swing at the sense antenna terminal due to a 1 V traveling-wave oscillation at the fundamental frequency. Therefore, *even though fundamental radiation gets canceled off in the far-field, the sense antenna selectively picks up the near-field of the fundamental frequency which can be exploited for the purpose of synchronization.*

In summary, in this method of near-field synchronization, the generated second harmonic power gets radiated out unaffected by the presence of the sense network, while a small fraction of the fundamental power is be 'sniff'ed out during the transient phase of locking as will be shown in the next subsection. Once the system is locked, almost no power gets wasted in the coupling network.

5.4.2 Mutual Locking and Electronic Beam-Scanning

In the previous subsection, we discussed how we gather the information of phase and frequency of 'uncoupled' DARs by sensing the near-fields. In this subsection, we will see how we synchronize multiple such sources by equalizing the near-fields through a coupling network.

Fig. 5.13 shows the implementation. The two DARs share the same silicon substrate and are identical. The sense-antenna of DAR 2 is rotated around the broadside axis to facilitate the layout of the coupling network. The terminal voltage of the sense antenna is only related to the rate of change of coupled magnetic flux, which remains unchanged by any such rotation around the broadside axis. The sense antenna terminals are now coupled by optimally chosen resistors such that if the DARs were synchronized, no steady-state current will flow along the resistors and therefore, no power will be dissipated in the coupling network. This happens because when synchronized, the terminal voltages of both the sense antennas will equalize leading to no current flow in the resistors. *Such a network, thereby, creates a condition where the minimum energy state is the synchronized state.* Any perturbation from the synchronized state will result in transient currents flowing along the resistors and the sense antenna, injecting currents back into the DARs, such that they finally fall back into the mutually locked state which is the lowest energy state.

In order to maximize the locking range, the value of the resistor is chosen such that if

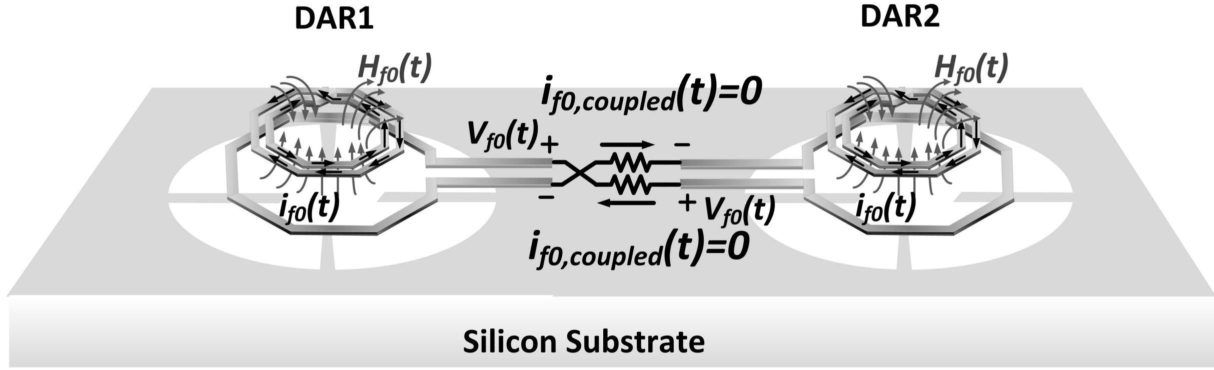

Figure 5.13: Near-field synchronized 2x1 DAR. Coupling network between the sense antenna terminals ensures that no power is dissipated when the sources are synchronized, making it the most stable and lowest energy state.

the DARs were oscillating out of phase, the power dissipation in the network is maximum. This is illustrated in Fig. 5.14, which shows the optimum resistance in the coupling network for the distributed active radiator implemented in this paper. The DAR has a simulated fundamental frequency of f_0=110 GHz. The core structure along with the sense antennas are simulated in a 3D electromagnetic simulation tool. It is to be noted that there exists two current configurations on the DAR, with wave travel in opposite directions, which can result in the same sense antenna voltage. However, a false locking state with two DARs in the above two states, is an unstable state. We have discussed the details in Appendix A, but, in implementation in a silicon die, any form of residual coupling through substrate or otherwise is enough to suppress this undesired locking state and this is verified in simulations and experiments.

2D arrays of coherent radiating sources can be synthesized by similar principles. For 2x2 array, two sets of synchronized 2x1 arrays are locked together with another set of sense antennas as shown in Fig. 5.15. The method can be extended for even larger arrays. It can be seen that the placement of the radiator cores is no longer constrained by the locking network. For different distances of separation of the radiator cores, the terminal voltages at the sense antennas will vary, but the coupling resistors can be optimized for the same locking range. In this way, large-scale arrays of radiating power sources can be laid out in silicon, while a background mesh of coupled sense antennas ensure seamless synchronization

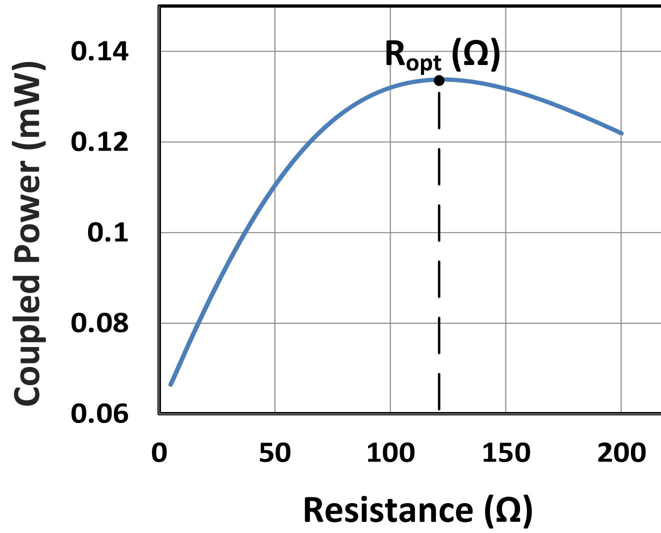

Figure 5.14: Optimum value of coupling resistors to maximize locking range.

for coherent power combination and high EIRP generation.

It is to noted that near-field synchronization is very different from a lumped transformer coupling network. The dimension of the sense antenna is comparable to the wavelength at the frequency of operation and as a result the phase of induced fundamental current changes by almost 180° along the sense antenna circumference. The amount of fundamental energy coupled to the sense loop is dependent on its close near-field electromagnetic interaction with the DAR which is strongly dependent on the frequency. This gives the sense desired differential behavior at the fundamental frequency (f_0) and second harmonic ($2f_0$), unlike a transformer.

In a t-line based coupling network, the DC is supplied by the network itself, as shown in Fig 5.5. In a near-field synchronization, the network is only electromagnetically coupled to the DARS, as shown in Fig. 5.13. Therefore, a separate biasing network needs to be implemented to provide the DC current. This is shown in Fig. 5.16. Each DAR is biased by a network of transmission line which provides open-circuit impedance at both the frequency of oscillation f_0 as well as the desired radiation frequency of $2f_0$ so that it does not affect the DAR operation. As shown in Fig. 5.16, at f_0, the $\lambda/4$ shorted t-line stub presents an open impedance at the network junction. Therefore, at the fundamental frequency of f_0,

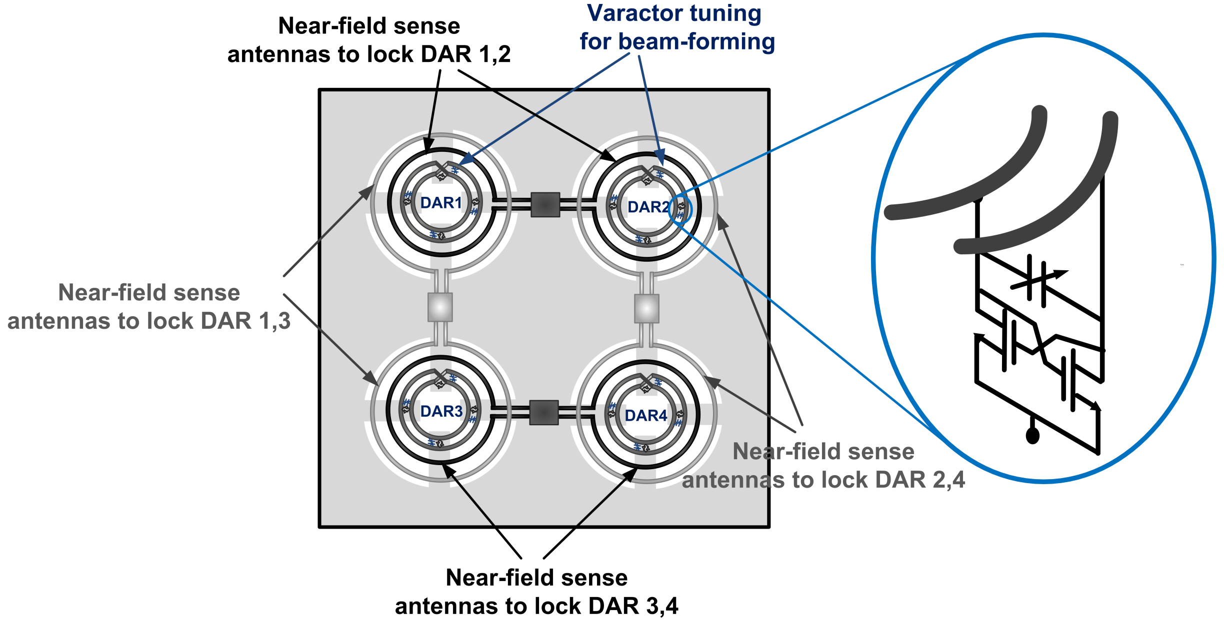

Figure 5.15: Two sets of synchronized 2x1 array locked together with two more sense antennas to form 2x2 array of locked DARs. The frequency tuning using varactor enables beam-steering through the synchronization network.

the DAR sees a resultant $\lambda/4$ shorted t-line stub due to the two $\lambda/8$ t-lines in series. At $2f_0$, the $\lambda/4$ (@f_0) and therefore $\lambda/2$ (@$2f_0$) shorted t-line stub presents a short at the network junction. This results in the DAR seeing a resultant open-circuit presented by a $\lambda/8$ (@f_0) and therefore $\lambda/4$ (@$2f_0$) shorted t-line stub. The transmission lines are realized as microstrip lines on the 3.2 m thick top copper metal with ground-shielded tub structure.

5.4.3 Frequency Locking Range and Beam-Scanning Analysis

In order to incorporate the ability to scan the THz beam electronically in 2D space, one needs to control the phase of the emitted radiation from each radiator core. The method to introduce phase control in an array of coupled oscillators by controlling the tuning frequency of the end elements was shown in [106]– [108]. We use a method where we control the frequency of resonance of each DAR element in the array by changing the voltages of varactors distributed along the resonator as shown in Fig. 5.15. It should be noted that since the second harmonic is the radiated power, a phase difference of, say ϕ, induced by the near-field network

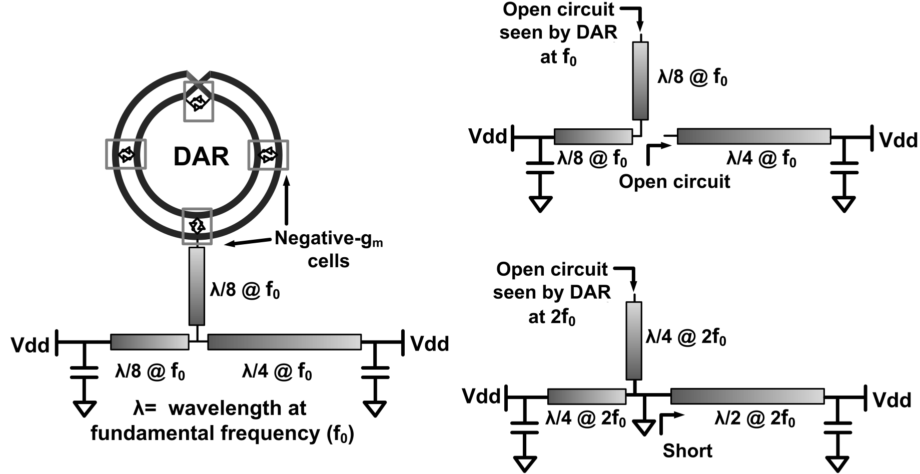

Figure 5.16: The bias network of each distributed active radiator. The bias network provides open-circuit at both the fundamental frequency of f_0 and the desired radiated second harmonic at $2f_0$, so as to not load the DAR operation.

at the fundamental frequency translates to a phase difference of 2ϕ of the desired radiated beam, within the locking range.

In order to gain deeper understanding of the design tradeoffs, locking range, induced phase rotations and the stability of the system, we perform a nonlinear analysis that explores the transient behavior of the system. It has to be remembered that, because of the distributed nature of near-field coupling network and the resonator structure with distributed negative-g_m cells, one has to be careful to consider the pulling effects on transconductance cells in one DAR due to a combined effect of the transconductance cells in the coupled DAR. As a result, one cannot apply directly the arguments and results derived for a linear coupled system with nearest neighbor coupling [106]– [108]. The analysis, we perform, is based on the Stroboscopic concept [111], where we observe the transient build-up of amplitude and phase and derive conditions for the stability of the possible steady-state solutions.

Let us consider a self-sustaining LC oscillator with a negative-g_m cell, a lossy tank tuned at ω_t, and under an injected current $i_{inj}(t)$, as shown in Fig. 5.17. Since mutual injection locking is essentially a nonlinear phenomenon, one needs to consider the nonlinear transconductance of the cross-coupled pair which is represented by $i = f(v)$, where the odd-function $f(v)$ captures the nonlinear current-voltage relationship in the cross-coupled pair. If g_m

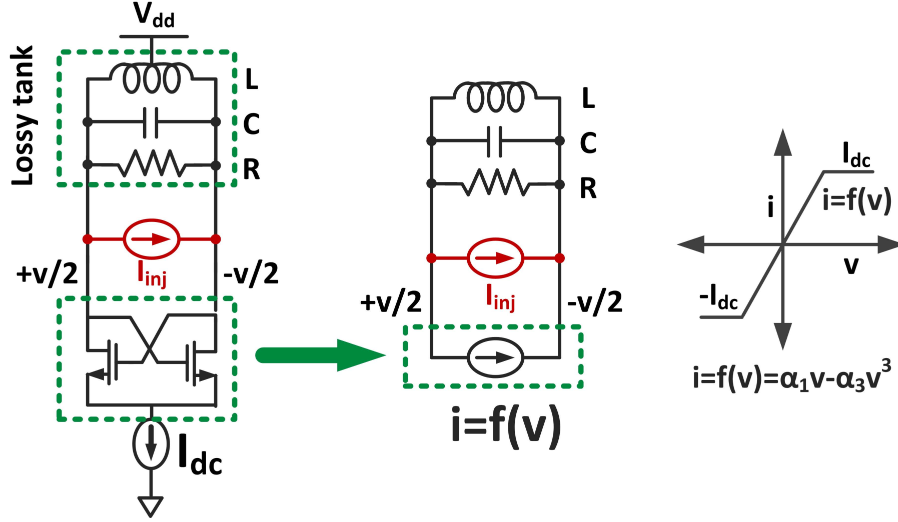

Figure 5.17: Injection locking in a self-sustained oscillator and its nonlinear modeling.

is the small-signal transconductance of a single transistor in the cell, then it can be seen $f'(v) = di/dv = g_m/2$. When the frequency of oscillation is pushed towards f_{max}, the cross-coupled pair will not undergo a hard-switching of current between the transistors and effect of the higher-order nonlinear terms will diminish. Therefore, we model the nonlinear block $f(v)$ by a third-order polynomial expansion $f(v) = \alpha_1 v - \alpha_3 v^3$, where $\alpha_1 = g_m/2$. This enables us to develop intuitive understanding and derive close-form expressions while still capturing the important aspects of the nonlinear dynamics in play. The system is governed by second-order dynamics due to the LC tank and by applying KCL in Fig. 5.17, we can derive the state equation

$$i_L + C\frac{dv}{dt} + i_R = f(v) + i_{inj} \tag{5.7}$$

$$\frac{1}{\omega_t^2}\frac{d^2v}{dt^2} + \frac{1}{Q\omega_t}(1 - g_m R + 3\alpha_3^2 R v^2)\frac{dv}{dt} + v - L\frac{d_{inj}}{dt} = 0 \tag{5.8}$$

where $\omega_t = 1/\sqrt{LC}$ is the resonant frequency of the tank with quality factor $Q = R/(\omega_t L)$.

Let us consider Fig. 5.13 where two identical DARs are coupled together through a near-

field coupling network, where frequency of resonance of each can be adjusted with varactors. Under locked condition, with same tuning in both DARs, there is no current $i_{coupled}$ flowing through the coupling resistors. Now assume, that one of the two coupled DARs is slightly detuned. Within the locking range, the two DARs will still be mutually pulled towards a common frequency. However, there will be a phase difference, say ϕ, at the fundamental frequency, induced between any two and therefore, every corresponding cross-coupled pairs in the two structures. In such a distributed system with multiple negative-g_m cells pulling each other through distributed coupling network, the current injected (i_{inj}) induced in each cross-coupled pair will, in general, be a function of voltages of all the other transconductance cells in the two DARs with different delays. While this would seemingly make the problem intractable, well-reasoned symmetry arguments can help to break the problem down.

Let us assume N cross-coupled pairs are distributed in each DAR and let us denote the voltages at the fundamental frequency of the ith pairs in the two DARs as $v_{1,i} = A_{1,i}\cos(\omega t)$ and $v_{2,i} = A_{2,i}\cos(\omega t + \phi)$. Since in a traveling-wave oscillation, amplitude remains constant over the resonator, $A_{1,i} = A_1$ and $A_{2,i} = A_2$. Further assuming identical DARs, we conclude $A_1 = A_2 = A$. To quantify the coupling, the current injected into the coupling resistors as shown in Fig. 5.13 is given by $i_{coupled} = (v_{s1} - v_{s2})/R_{opt}$, where v_{s1} and v_{s2} are the induced voltages at the two sense antenna terminals. Now because of the distributed structure of the DAR and the sense antenna, there is a delay or phase shift, say $\theta_{1,i}$ ($\theta_{2,i}$), between the chosen oscillator voltage $v_{1,i}$ ($v_{2,i}$) and the induced sense antenna terminal voltage v_{s1} (v_{s2}). Therefore, $v_{s1} \propto A\cos(\omega t + \theta_{1,i})$ and $v_{s2} \propto A\cos(\omega t + \phi + \theta_{2,i})$. The current through the coupling resistors $i_{coupled} = (v_{s1} - v_{s2})/R_{opt}$, will travel along the sense antenna, suffer different delays and inject currents in each cross-coupled pair distributed over the DAR. Now, because of reciprocity, $i_{coupled}$ will have exactly the same delay or phase difference $\theta_{1,i}$ and $\theta_{2,i}$ with the injected current in the ith pair in the two DARs. Hence, the current injected i_{inj} in the ith cross-coupled pair in each DAR, due to $i_{coupled}$ is given by $|i_{inj}| \propto |(v_{1,i} - v_{2,i})/R_{opt}| = |(A\cos(\omega t) - A\cos(\omega t + \phi))/R_{opt}$. This expression of i_{inj} is independent of i, $i.e$, the location of trans-conductance cell in the DAR. This implies every cross-coupled pair will experience the same $|i_{in}|$ due to the near-field coupling network and is proportional to the difference between

its voltage and the corresponding pair in the coupled DAR. Therefore, *the entire dynamics of nonlinear synchronization is captured by analysis of any two corresponding cross-coupled pairs in the two coupled DARs.*

This could also have been reasoned by an argument of rotational symmetry. Since the sense antenna terminal voltage does not change if we rotate the antenna around the broadside axis, the effect of injected current in each cross-coupled pair and sense antenna voltage has to be exactly the same.

Let $\omega_{t,1}$ and $\omega_{t,2}$ be the angular resonant frequencies of two mutually locked DARs oscillating at a common angular fundamental frequency of a ω_0. Let $v_1 = A\cos(\omega_0 t)$ and $v_2 = A\cos(\omega_0 t + \phi)$ be the steady-state voltages of two corresponding cross-coupled pairs in the DAR 1 and DAR 2, respectively. The injected current i_{inj} in cross-coupled pair in DAR 1, as argued before, can be represented as $i_{inj,1} = \varepsilon(v_2 - v_1) = \varepsilon A(\cos(\omega_0 t + \phi) - \cos(\omega_0 t))$. Putting these values in (5.8) for DAR 1, we obtain,

$$
\begin{aligned}
\cos(\omega_0 t)\left[\left(1 - \frac{\omega_0^2}{\omega_{t,1}^2}\right) + \varepsilon L\omega_0 \sin(\phi)\right] = \\
\sin(\omega_0 t)\left[\frac{\omega_0}{Q\omega_{t,1}}\left(1 - g_m R + \frac{3}{4}\alpha_3^2 R A^2\right)\right] \\
+ \sin(\omega_0 t)\left[\varepsilon L\omega_0(1 - \cos(\phi))\right]
\end{aligned}
\tag{5.9}
$$

Equation (5.9) can hold true if both the coefficients of $\cos(\omega_0 t)$ and $\sin(\omega_0 t)$ are zero. Given $\omega_{t,1}$ and $\omega_{t,2}$ and the other system parameters, we would like to solve for the locked frequency ω_0, induced phase difference ϕ and the amplitude A. Therefore, from (5.9), equating the coefficients of $\cos(\omega_0 t)$ to zero, we get,

$$
1 - \frac{\omega_0^2}{\omega_{t,1}^2} + \varepsilon L\omega_0 \sin(\phi) = 0 \tag{5.10}
$$

Similarly, for the coupled resonator DAR 2, we have

$$1-\frac{\omega_0^2}{\omega_{t,2}^2}-\varepsilon L\omega_0\sin(\phi)=0 \tag{5.11}$$

Solving (5.10) and (5.11), we obtain

$$\omega_0 = \frac{\sqrt{2}\omega_{t,1}\omega_{t,2}}{\sqrt{\omega_{t,1}^2+\omega_{t,2}^2}} \tag{5.12}$$

$$\sin(\phi) = \frac{1}{\varepsilon L\omega_0}\frac{\omega_{t,2}^2-\omega_{t,1}^2}{\omega_{t,1}^2+\omega_{t,2}^2}\approx\frac{2\Delta\omega_t}{C\omega_0} \tag{5.13}$$

where $\Delta\omega_t=\omega_{t,2}-\omega_{t,1}$ and $C\approx\varepsilon L\omega_0$ denotes the coupling strength. The expressions make intuitive sense since, for $\omega_{t,1}\approx\omega_{t,2}$, the locked frequency is almost the mean of the two resonant frequencies, *i.e.*, $\omega_0\approx(\omega_{t,1}+\omega_{t,2})/2$. Also, for higher coupling strength C, the phase difference ϕ decreases, as expected. Since $|\sin(\phi)|\leq 1$, the locking bandwidth can be expressed as

$$\Delta\omega_t=\frac{C\omega_0}{2} \tag{5.14}$$

It can be seen that the locking bandwidth is independent of the quality factor of the two resonator in the two DARs as long as the quality factors are of the same value. An intuitive way of understanding the result is as follows. Consider an oscillator with an external current injection i_{inj}, where the locking bandwidth is given by the Adler's expression $\Delta\omega_t=i_{inj}/(2i_{osc}Q\omega_0)$ [110]. For a given injection current, the bandwidth decreases with Q. However, in our case of mutually locked DARs, the injection current $i_{inj}=\varepsilon(v_2-v_1)$ also increases proportionately with Q since both v_1 and v_2 increases linearly with Q for given oscillator currents. This makes the bandwidth independent of thee quality factor, to a first order, as long as the oscillation amplitude is current-limited.

For the DAR implemented in this paper, we see from Fig. 5.14, $i_{coupled}\approx 1.5$ mA, when the DAR is completely out of phase in which case $|v_2-v_1|\approx 1$ V. The simulated injected current, under such a condition, is $i_{inj}\approx 750$ µA implying $\varepsilon\approx 750$ µS. The simulated

resonator parameters are $L\omega_0 \approx 50\ \Omega$ and $Q \approx 6$ which results in the coupling coefficient to be $C \approx 2\%$. The locking bandwidth from (5.14) is then estimated to be approximately 2.1 GHz for a fundamental frequency of 100 GHz.

5.4.4 Stability Analysis of Near-Field Coupling Mechanism

In the previous subsection, we studied the steady-state behavior of the coupled DAR system and derived the expressions for locking bandwidth and phase changes due to frequency tuning during beam-scanning. In this subsection, we will study the stability of the locked system under perturbation to ensure the system always falls back into the synchronized state, which is the lowest energy state.

In order to do that, we perform a stroboscopic analysis on the dynamic behavior of the amplitude and phase of the voltages v_1 and v_2 of any two corresponding cross-coupled pairs in the two DARs. We assume a locked frequency of ω_0 and observe the dynamics of the amplitude and phase every time period $T = 2\pi/\omega_0$. Thereby, we observe a discrete set of points in the amplitude and phase space, which then become the state equations and we analyze the stability of the steady-state solution in this new formed phase space [111]. If the system reaches a stable steady oscillatory state with angular frequency ω_0, the amplitude and phase observed every time period T will remain the same, and any perturbation will bring back the system into this steady-state solution in the new phase space.

We begin by transforming the second-order system in (5.8) into two first-order equations in the state space variables r and ϕ, where

$$v = r\cos(\phi) \tag{5.15a}$$

$$\frac{dv}{dt} = \omega_0 r \sin(\phi) \tag{5.15b}$$

Arguing as before, $i_{inj} = \varepsilon(v_2 - v_1)$, we obtain the following state equations for cross-coupled

pair in DAR 1 from (5.8) using (11.1a) and (11.1b), as derived in Appendix .

$$\begin{aligned}
\frac{dr_1}{dt} &= \frac{1}{2}\omega_0 r_1 \sin(2\phi_1) - \frac{\omega_{t,1}^2}{2\omega_0} r_1 \sin(2\phi_1) \\
&- \frac{\omega_{t,1}}{Q} r_1 \sin^2(\phi_1)(1 - g_m R + 3\alpha_3^2 R r_1^2 \cos^2(\phi_1)) \\
&+ \varepsilon\omega_{t,1}^2 L \sin(\phi_1)(r_2 \sin(\phi_2) - r_1 \sin(\phi_1)) \\
&= F_1(r_1, \phi_1, r_2, \phi_2) \qquad (5.16a) \\
\frac{d\phi_1}{dt} &= -\omega_0 \cos^2(\phi_1) - \frac{\omega_{t,1}^2}{\omega_0} \cos^2(\phi_1) \\
&- \frac{\omega_{t,1}}{2Q} \sin(2\phi_1)(1 - g_m R + 3\alpha_3^2 R r_1^2 \cos^2(\phi_1)) \\
&+ \varepsilon\omega_{t,1}^2 L \cos(\phi_1)(\frac{r_2}{r_1} \sin(\phi_2) - \sin(\phi_1)) \\
&= G_1(r_1, \phi_1, r_2, \phi_2) \qquad (5.16b)
\end{aligned}$$

If we observe r_1, ϕ_1, r_2, ϕ_2 every time period T, and we designate the observed variables as $r_{1,T}, \phi_{1,T}, r_{2,T}, \phi_{2,T}$ which are the new state space variables, then we can conclude from (5.15a) and (5.15b) $\phi_1 = \phi_{1,T} - \omega_0 t$ and $\phi_2 = \phi_{2,T} - \omega_0 t$. For moderately high-Q systems, the r_1, ϕ_1 are slowly varying functions over time and will remain almost constant over one time period T. Therefore, form (5.16a) and (5.16b), integrating out the periodic terms, we obtain,

$$\begin{aligned}
\frac{dr_{1,T}}{dt_T} &= \frac{r_1(T) - r_1(0)}{T} \\
&= \frac{1}{T}\int_0^T F_1(r_1, \phi_1, r_2, \phi_2) dt \\
&\approx -\frac{\omega_{t,1}}{2Q} r_{1,T} \left(1 - g_m R + \frac{3}{4}\alpha_3^2 R r_{1,T}^2\right) \\
&+ \frac{C\omega_0}{2}(r_{2,T} \cos(\phi_{2,T} - \phi_{1,T}) - r_{1,T}) \\
&= F_{1,T}(r_{1,T}, \phi_{1,T}, r_{2,T}, \phi_{2,T}) \qquad (5.17)
\end{aligned}$$

$$
\begin{aligned}
\frac{d\phi_{1,T}}{dt_T} &= \frac{\phi_1(T)-\phi_1(0)}{T} \\
&\frac{1}{T}\int_0^T G_1(r_1,\phi_1,r_2,\phi_2)dt \\
&= \Delta\omega_t + \frac{C\omega_0}{2}\frac{r_{2,T}}{r_{1,T}}\sin(\phi_{2,T}-\phi_{1,T}) \\
&= G_{1,T}(r_{1,T},\phi_{1,T},r_{2,T},\phi_{2,T}) \qquad (5.18)
\end{aligned}
$$

where t_T is the new time variable denoting sampling of t every time period T. Similarly, we can derive,

$$
\begin{aligned}
\frac{dr_{2,T}}{dt_T} &= \frac{r_2(T)-r_2(0)}{T} \\
&= \frac{1}{T}\int_0^T F_2(r_1,\phi_1,r_2,\phi_2)dt \\
&\approx -\frac{\omega_{t,2}}{2Q}r_{2,T}\left(1-g_mR+\frac{3}{4}\alpha_3^2Rr_{2,T}^2\right) \\
&+ \frac{C\omega_0}{2}(r_{1,T}\cos(\phi_{2,T}-\phi_{1,T})-r_{2,T}) \\
&= F_{2,T}(r_{1,T},\phi_{1,T},r_{2,T},\phi_{2,T}) \qquad (5.19)
\end{aligned}
$$

$$
\begin{aligned}
\frac{d\phi_{2,T}}{dt_T} &= \frac{\phi_2(T)-\phi_2(0)}{T} \\
&= \frac{1}{T}\int_0^T G_2(r_1,\phi_1,r_2,\phi_2)dt \\
&= -\Delta\omega_t + \frac{C\omega_0}{2}\frac{r_{1,T}}{r_{2,T}}\sin(\phi_{1,T}-\phi_{2,T}) \\
&= G_{2,T}(r_{1,T},\phi_{1,T},r_{2,T},\phi_{2,T}) \qquad (5.20)
\end{aligned}
$$

At steady state, from (5.18) and (5.18), we conclude $\sin(\phi_{1,T}^0-\phi_{2,T}^0) = 2\Delta\omega_t/(C\omega_0)$ (verifying (5.13)) and $r_{1,T}^0 \approx r_{2,T}^0 = \sqrt{4(g_mR-1)/(3\alpha_3^2R)}$. To check the stability of this steady-state solution, we linearize the dynamical equations (5.17)–(5.20) around the equilibrium point and check the eigenvalues of the state-space matrix, say A. We will construct

the time-dependent behavior of the perturbation state space variables near the equilibrium point and verify if they decay exponentially to zero. From (11.2a)–(11.3d), as derived in Appendix, we have

$$\begin{aligned} A &= \begin{pmatrix} \frac{\partial F_{1,T}}{\partial r_{1,T}} & \frac{\partial F_{1,T}}{\partial \phi_{1,T}} & \frac{\partial F_{1,T}}{\partial r_{2,T}} & \frac{\partial F_{1,T}}{\partial \phi_{2,T}} \\ \frac{\partial G_{1,T}}{\partial r_{1,T}} & \cdots & \cdots & \frac{\partial G_{1,T}}{\partial \phi_{2,T}} \\ \frac{\partial F_{2,T}}{\partial r_{1,T}} & \cdots & \cdots & \frac{\partial F_{2,T}}{\partial \phi_{2,T}} \\ \frac{\partial G_{2,T}}{\partial r_{1,T}} & \cdots & \cdots & \frac{\partial G_{2,T}}{\partial \phi_{2,T}} \end{pmatrix} \\ &= \begin{pmatrix} -\beta & r_T^0 \Delta\omega_t & \gamma & -r_T^0 \Delta\omega_t \\ \frac{\Delta\omega_t}{r_T^0} & -\gamma & -\frac{\Delta\omega_t}{r_T^0} & \gamma \\ \gamma & r_T^0 \Delta\omega_t & \beta & -r_T^0 \Delta\omega_t \\ \frac{\Delta\omega_t}{r_T^0} & \gamma & \frac{\Delta\omega_t}{r_T^0} & -\gamma \end{pmatrix} \end{aligned} \tag{5.21}$$

where the steady-state value $r_T^0 = r_{1,T}^0 \approx r_{2,T}^0 = \sqrt{4(g_m R - 1)/(3\alpha_3^2 R)}$, $\Delta\phi_T^0 = \Delta\phi_{1,T}^0 - \Delta\phi_{1,T}^0$, $\beta = -\frac{2\omega_{t,1}}{Q}(g_m R - 1) - \frac{C\omega_0}{2}$, $\gamma = \frac{C\omega_0}{2}\cos(\Delta\phi_T^0)$.

It is trivial to prove that the determinant of the matrix A is 0, which implies one eigenvalue $\lambda_1 = 0$. It can be shown that the other eigenvalues are $\lambda_2 = -2\gamma < 0$, $\lambda_3 = -(\gamma+\beta) < 0$ and $\lambda_4 = -(\beta-\gamma) < 0$. Solving for the eigenvectors, it is easy to show that any perturbation in state space variables dies down as

$$\delta r_{1,T}/\delta r_{2,T} = C_1 e^{\lambda_2 t} + C_2 e^{\lambda_3 t} + C_3 e^{\lambda_4 t} \tag{5.22a}$$

$$\delta(\phi_{1,T} - \phi_{2,T}) = C_4 e^{\lambda_2 t} + C_5 e^{\lambda_3 t} \tag{5.22b}$$

where $\lambda_2, \lambda_3, \lambda_4 < 0$. Since the initial phase is arbitrary, we only consider perturbation in the difference of the phase variables of the two DARs ($\delta(\phi_{1,T} - \phi_{2,T})$) which is shown exponentially decay to zero. This implies, that the steady-state solution which exists within the locking range is stable.

The analysis can be extended to larger arrays of mutually coupled DARs where the derived stability conclusions still hold. We conclude, therefore, near-field synchronization is a scalable and also stable and robust method for realizing large scale arrays of radiative power sources. As long as the oscillator voltage swings are in the current-limited region, this form of coupling, to a first-order is independent of the quality factor of the coupled DARs and can also be used for beam-scanning by controlling the resonant frequencies of one or more of the coupled distributed active radiators.

5.5 Design and Implementation

In order to demonstrate t-line and near-field locking, two sets of chips were designed in two different CMOS processes. Two arrays 2x1 and 2x2 DARs, based on t-line locking, are designed in IBM 45 nm CMOS SOI process with estimated $f_{max} \sim 0.2$ THz [112]– [114]. The fundamental frequency of oscillation is designed to be near 150 GHz and the second harmonic radiated frequency is, therefore, near 300 GHz ($> f_{max}$) [57], [61]. The design of the DAR has been discussed in Chapter 3 and the locking scheme and the t-line implementation has been discussed in a previous section in this chapter. The silicon-on-insulator technology does not offer the option of a high-resistivity substrate for low loss passives and radiating structures. The insulator comprises of a 0.225 µm thick buried oxide and the bulk resistivity of the silicon substrate below is typically 13.5 Ω-cm which is comparable to other bulk processes. The 2x2 array chip measures 800 µm × 800 µm.

Another set of 2x1 and 2x2 arrays of DARs with near-field synchronization network are designed in 65 nm bulk CMOS process with sub-200GHz f_{max}. The fundamental frequency of oscillation f_0 is chosen to be 110 GHz, which implies that the desired radiated power is at $2f_0$=220 GHz. The difference in frequency of operation in the two designs are based on the different operable frequency limitations of the two CMOS processes. The concepts behind the different modes of locking are equally applicable to each other. Each cross-coupled pair consist of NMOS transistors of W/L=12 µm/65 nm, biased at 6 mA under 0.8 V. The DAR metal loop is realized on 3.2 µm thick top copper metal layer with four cross-coupled pair

distributed along the circumference to sustain the traveling-wave oscillation. The distributed active radiator is designed to have a radius of 55 µm with 10 µm separation between the adjacent branches for the fundamental frequency of oscillation to be near 110 GHz.[4] For the 2x1 array, the sense antennas, as shown in Fig. 5.13 are realized on a 0.9 µm thick copper metal, one metal layer below the radiator loop. The ground aperture is designed to have a radius of 95 µm for the optimum radiative impedance seen by the drain terminals for the maximum second harmonic power generation.

The DARs, in the near-field setting, are separated by nearly 600 µm which approximately corresponds to the optimum spacing for the dominant surface mode at 220 GHz to partially cancel. This flexibility of the sense mash network allows us this optimal placement, which otherwise, is constrained by the coupling network dimensions. This leads to much higher radiation efficiency which ultimately leads to higher THz power and EIRP.

5.6 Measurement Results

The die photos for the two sets of chips are shown in Fig. 5.18 and Fig. 5.19. The 0.3 THz DAR arrays in Fig. 5.18, based on t-line coupling, are designed without any frequency tuning. The 2x2 array in Fig. 5.19, based on near-field coupling, has varactor tuning capability for beam-steering operation. The bulk substrate is near 270 µm with 10 Ω-cm resistivity. The substrate is not thinned and no silicon lens is used for surface wave correction.

The second harmonic radiation in the WR-3 (220–325 GHz) band for the chipsets in Fig. 5.18 and in the WR-5 band (140–220 GHz) for the chipsets in Fig. 5.19, is captured from the back side of the die as shown in Fig. 5.20. The front-end of the receiver is a WR-3/WR-5 25 dB gain rectangular horn antenna connected to an Erickson power meter, which is a calorimeter-based power measurement instrument between 75–2000 GHz [115]. The frequency of the received THz signal is measured by down-converting the signal using a harmonic mixer and then amplifying the down-converted signal with low-noise amplifiers and

[4]The process supported circular inductors which were modified into the DARs. However, they can very well be realized with hexagonal resonators as in [57]

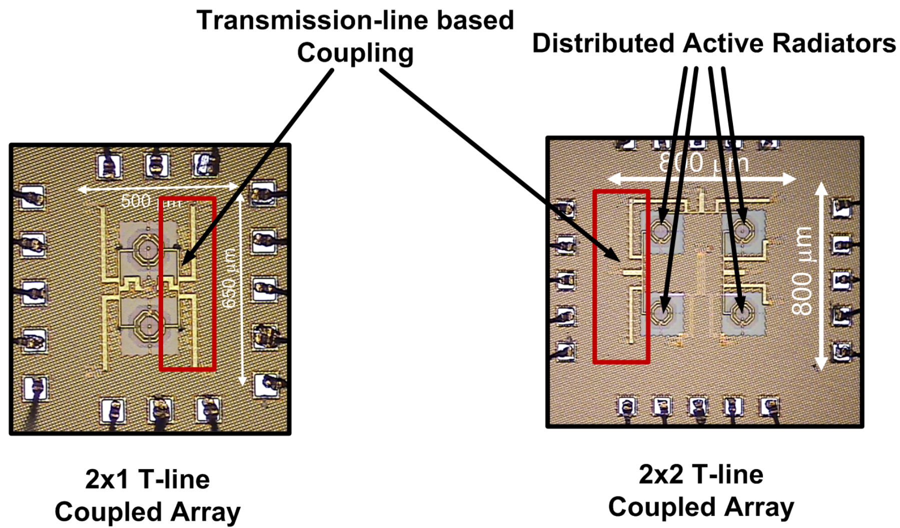

Figure 5.18: Die photos of 2x1 and 2x2 arrays of DARs, synchronized with t-line networks, operating at 0.3 THz.

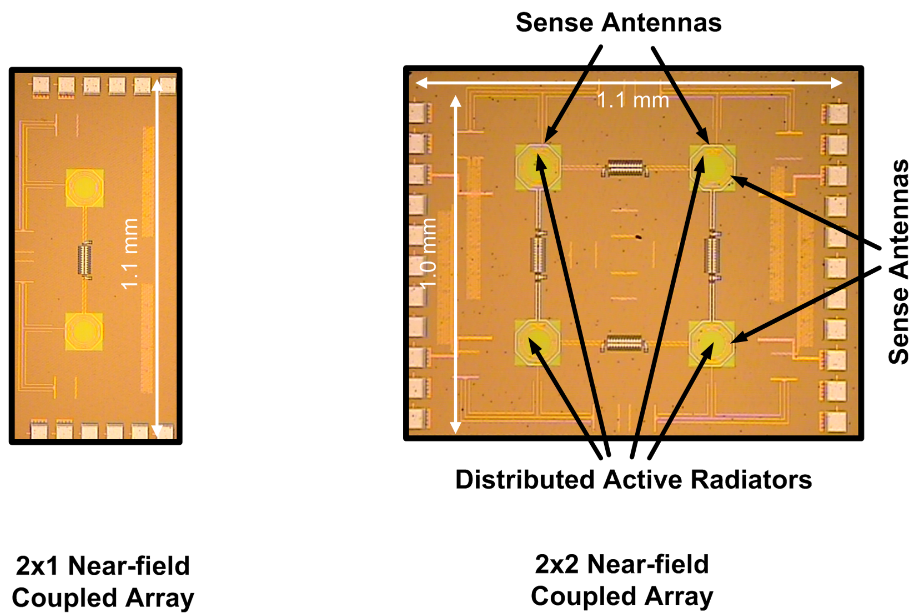

Figure 5.19: Die photos of 2x1 and 2x2 arrays of DARs, synchronized with near-field electromagnetic coupling, operating at 0.2 THz.

then observed in a spectrum analyzer. This is illustrated in Fig. 5.21. This entire receiver chain is calibrated using WR-3/WR-5 sources and Erickson power meter. Since the harmonic mixer produces IF products due to mixing of the incoming signal with various LO harmonics, the frequency of the received signal is measured by ascertaining which harmonic of the LO is responsible for the observed IF. This is determined by changing the LO frequency by say, Δf_{LO} and observing the change in frequency of the IF say, Δf_{IF}. The ratio of the frequency shifts, given by, $|\Delta f_{IF}/\Delta f_{LO}|$, is the desired LO harmonic responsible for the observed IF. The received THz signal frequency is then given by $f_{RF} = nf_{LO} \pm IF$, depending on whether IF increases or decreases with increase in LO frequency. The photograph of the measurement set-up at 0.3 THz for the chipsets in Fig. 5.18, is shown in Fig. 5.22.

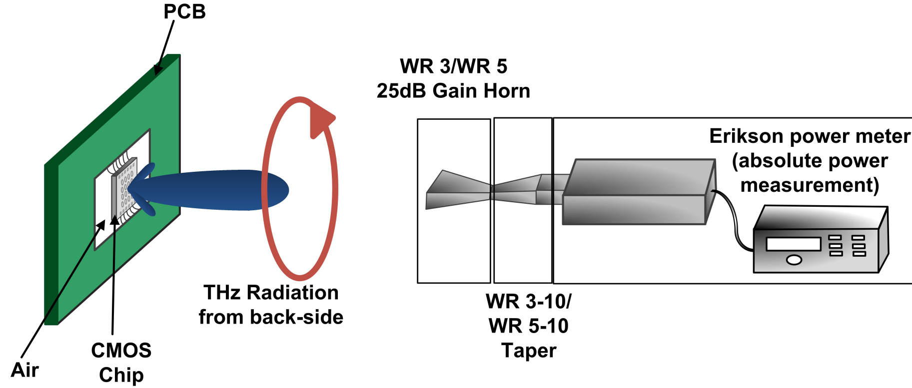

Figure 5.20: Calibrated setup to measure EIRP and radiation power of the second harmonic frequency at 0.3 THz for the chipsets in Fig. 5.18 and at 0.2 THz for the chipsets in Fig. 5.19.

The effective isotropic radiated power or EIRP, in any given direction, is measured directly from the power captured power at the receiver antenna in Fig. 5.20 at a far-field distance from the CMOS chip. If at a particular frequency, the power captured by the polarization-matched receiver antenna with gain of G_r, at a far-field distance of R be P_r, then EIRP of the source in that direction is given by

$$EIRP(\theta, \phi) = \left(\frac{4\pi R}{\lambda}\right)^2 \frac{P_r}{G_r} \tag{5.23}$$

where λ is the free-space wavelength at the measured frequency and (θ, ϕ) denotes the measurement direction in azimuth and elevation. The total radiated power, and hence

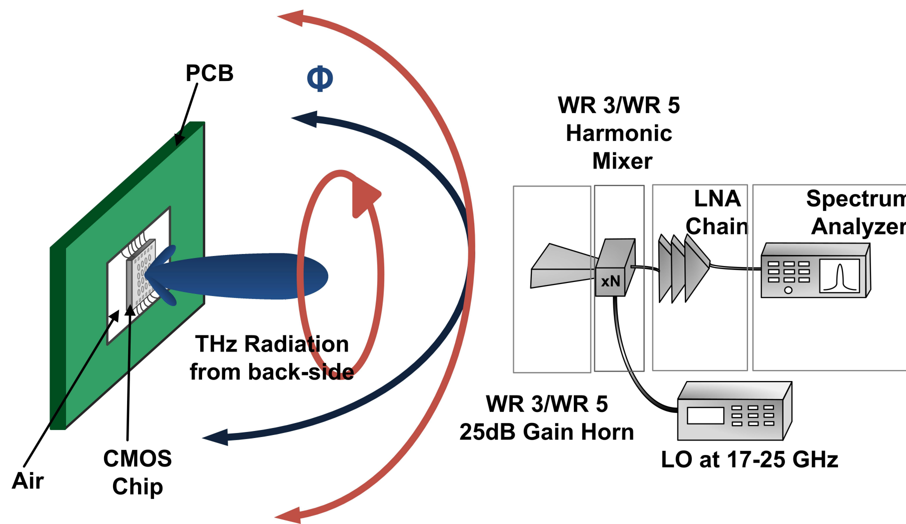

Figure 5.21: Calibrated setup to measure frequency of the received signal and radiation patterns for the chipsets in Fig. 5.18 and Fig. 5.19.

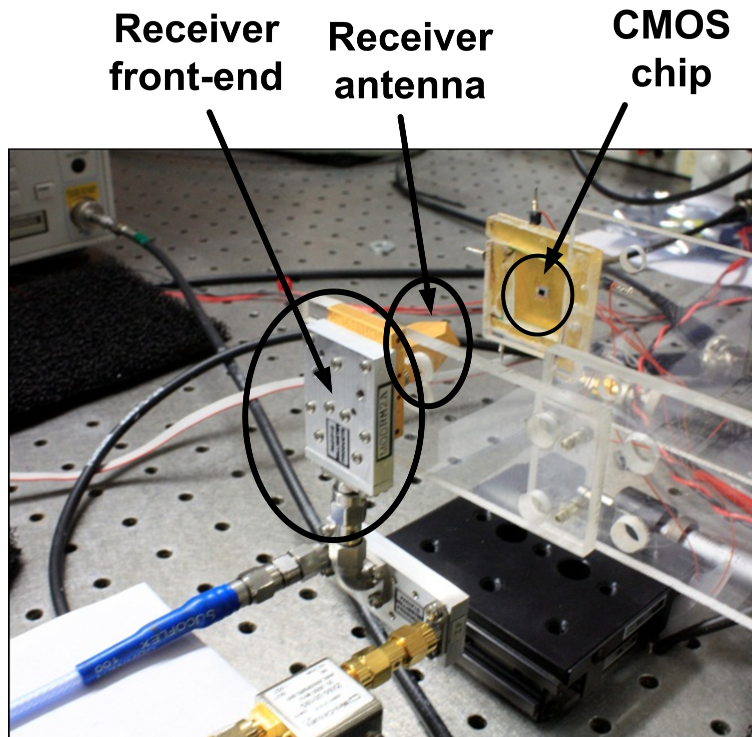

Figure 5.22: Photo of the measurement setup at 0.3 THz for the chipsets in Fig. 5.18.

the directivity is measured by integrating the power density, measured from the radiation pattern over space. It should be noted, that unlike traditional antenna systems, we can only measure the directivity and not separately the gain of the radiating structure in DAR. Since the actives and radiating passives are strongly coupled in the self-oscillatory, frequency multiplying radiating structure of DAR, it is not possible to measure how much of second harmonic power in injected by the transistors to be radiated. As a result, we can only measure the radiated power at far-field after it has suffered the losses in the substrate and the passives. The measured pattern gives us a measure of directivity.

5.6.1 0.3 THz DAR Arrays in 45 nm CMOS

The radiated signal from the back side of the 2x1 array in Fig. 5.18 is detected at 299 GHz. The radiation is expected to be circularly polarized which was verified by rotating the receiver antenna around its boresight axis and no significant change was observed in the power captured. Calibrating for half the power lost due to polarization mismatch of circularly polarized radiation and linearly polarized receiver antenna, the bore-sight EIRP is measured to be -13 dBm. The far-field radiation pattern in the two orthogonal planes is shown in Fig. 5.23. The directivity is measured by integrating over the measured 3D radiation pattern profile. The directivity is measured to be 6 dBi which translates to total radiated power of 13 µW. Each DAR draws 22 mA of current from 0.85 V DC supply.

The calibrated spectrum for the 2x2 array is shown in Fig. 5.24, showing a strong second harmonic signal at 292 GHz due to the efficient radiative behavior of DAR, and a suppressed fundamental frequency signal at 146 GHz due to the quasi-optical filtering effect of the out-of-phase fundamental currents. The bore-sight EIRP is measured to be -1 dBm at 0.29 THz. This is the first ever near 1 mW THz source in CMOS, by around three orders of magnitude. The radiation pattern, measured at 0.29 THz in the two orthogonal planes, is shown in Fig. 5.25. The pattern is symmetrical about the axes due to the traveling-wave nature of the DARs. The measured directivity is 10 dBi, implying total radiated power of 80 µW. This is near three orders of magnitude more radiated power compared to previous works [65]– [66].

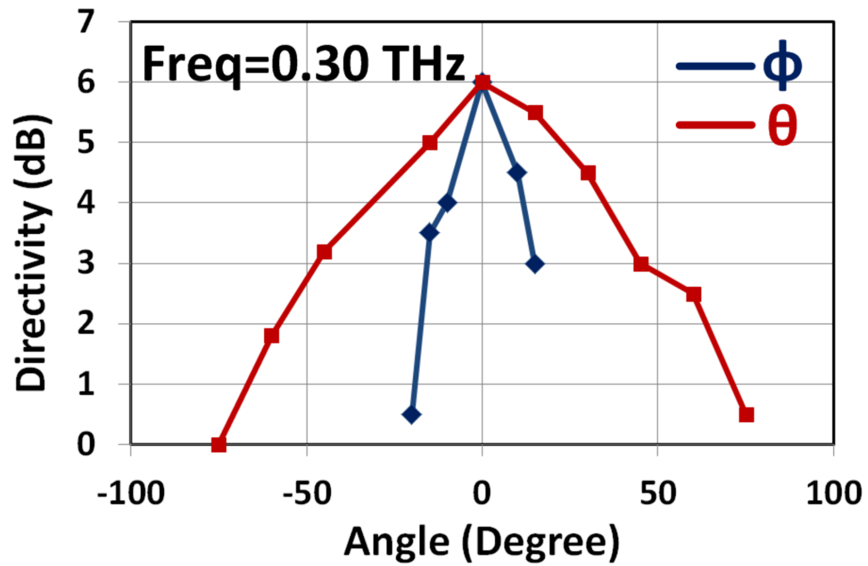

Figure 5.23: Radiation patterns of the second harmonic power near 0.3 THz measured from the backside of the 2x1 array chip in Fig. 5.18. The figure shows the patterns in the two orthogonal planes.

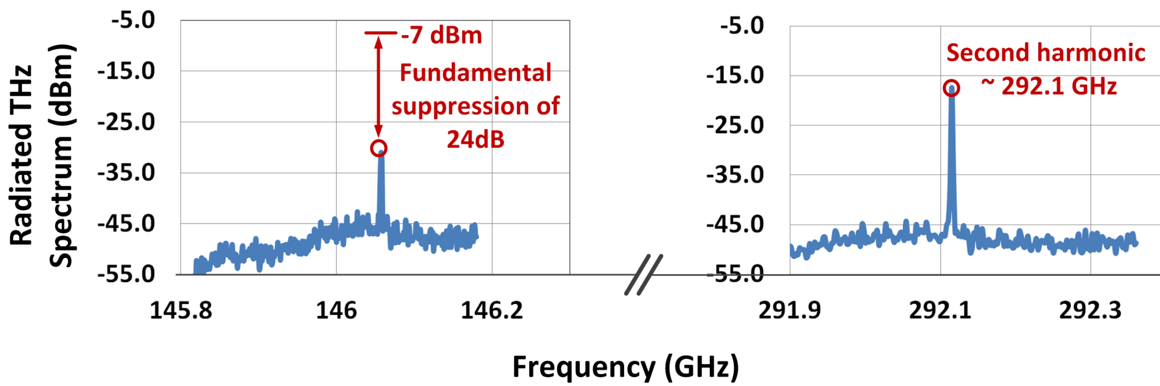

Figure 5.24: Calibrated locked THz spectrum of the received signal from the 2x2 array chip in Fig. 5.18.

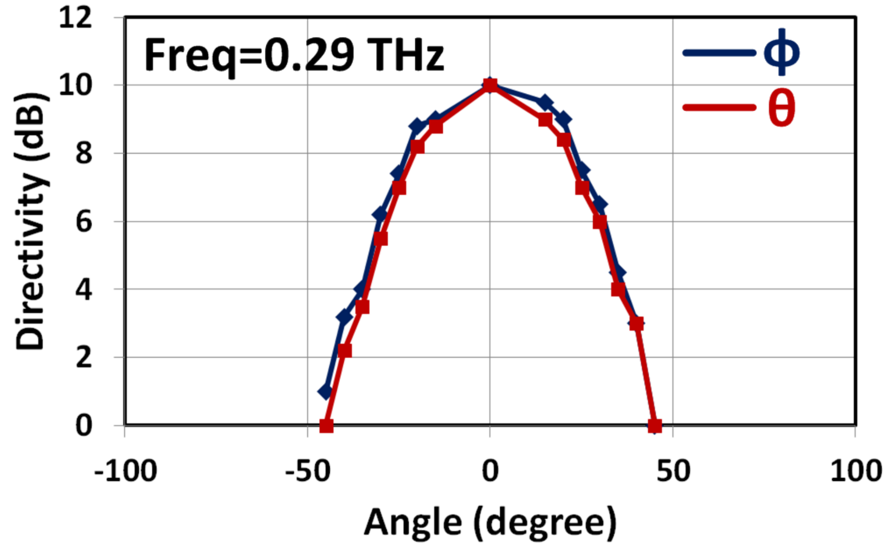

Figure 5.25: Radiation patterns of the second harmonic power near 0.3 THz measured from the backside of the 2x2 array chip in Fig. 5.18. The figure shows the patterns in the two orthogonal planes.

The distributed active radiator relies on the closed-space out-of-phase currents in the first harmonic to suppress radiation at the fundamental frequency. The measured spectrum of the fundamental frequency near 146 GHz is also shown in Fig. 5.24. The spectrum at the fundamental frequency is adjusted for the same receiver antenna aperture for a fair comparison of the radiation power density. The desired $2f_0$ radiation power density at 292 GHz is shown to be 14 dB higher than that of the fundamental frequency at 146 GHz, showing an almost 24 dB fundamenal suppression due to the quasi-optical filtering effect. The fundamental suppression is estimated from a simulated value of RF power at the fundamental frequency injected into the resonator and the antenna aperture area corresponding to the physical chip dimensions

5.6.2 0.2 THz DAR Arrays in 65 nm Bulk CMOS

For the 2x1 array, the radiated second harmonic signal, as shown in the measurement setup in Fig. 5.20, is detected at a frequency of 198 GHz. The bore-sight EIRP is measured to be -9.2 dBm. The frequency is slightly less than the simulated frequency of 220 GHz, which is due transistor parasitic modeling inaccuracies at these frequencies. As discussed before, the

radiation is expected to be circularly polarized which was verified by rotating the receiver antenna around its bore-sight axis and no significant change was observed in the power captured. The radiation pattern measured in two orthogonal planes is shown in Fig. 5.26. The maximum directivity is measured to be 5.9 dBi, at a slight offset to the bore-sight axis, believed to be because of mismatch in the two locked DARs, which results in a phase difference between them under locked condition. The total radiated power at 198 GHz is measured to be 30 µW generated from a total DC current of 48 mA from a 0.8 V supply. The radiation from the front side of the chip is also measured, which contributed to a larger total radiated power and lower directivity of the back side radiation, than reported in [58].

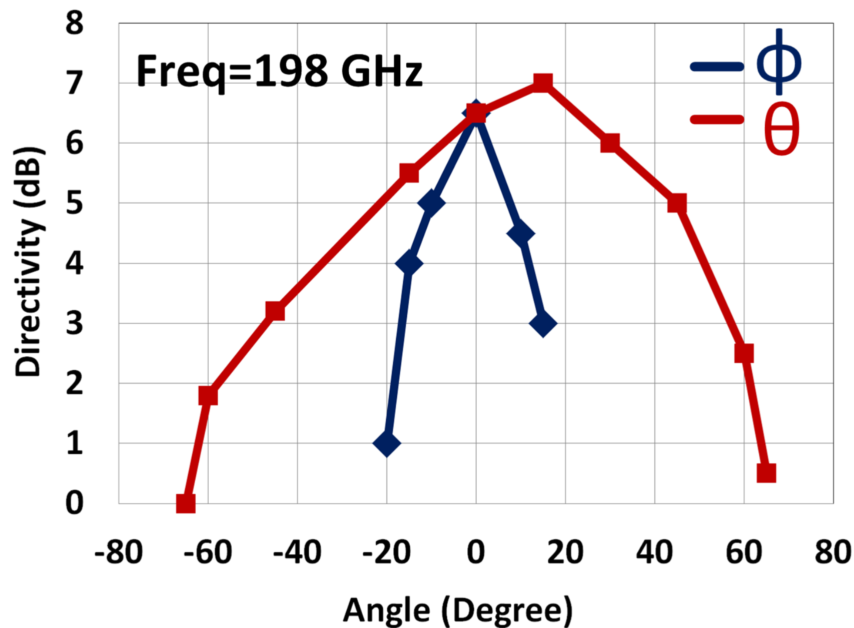

Figure 5.26: Radiation patterns of the second harmonic power near 0.2 THz measured from the back side of the 2x1 array chip. The figure shows the patterns in the two orthogonal planes.

The 2x2 array, with near-field locking, has varactor tuning embedded in each of its oscillating radiative cores to be able to control phase of individual DARs for the purpose of beam-steering. For the nominal tuning, the THz spectrum when all the four cores are locked together is shown in Fig. 5.27. The signal is detected at a frequency of 191.2 GHz and the power captured by the 25 dB gain receiver antenna is 8 µW at a far-field distance of 20 mm. This translates to an measured EIRP of -1.9 dBm by (5.23). As before, the signal is measured

to be almost circularly polarized. Near-field effects or standing waves in measurement can cause errors in estimation of radiated power. Hence the receiver antenna was placed over a range of far-field distances (R) from 20 mm to 60 mm. The received power followed closely the $1/R^2$ law and the measured EIRP remained almost constant. By changing the varactor voltages, the frequency of oscillation of each individual DARs can be tuned and the near-field synchronization network will pull them towards a common frequency within the locking range. When the coupled DARs go outside the locking range, the spectrum splits as also shown in Fig. 5.28.

The spectrum at the fundamental frequency, adjusted for the same receiver antenna aperture for a fair comparison of the radiation power density, is also shown in Fig. 5.27. The desired $2f_0$ radiation power density at 191 GHz is shown to be 11 dB higher than that of the fundamental frequency at 95.5 GHz. To obtain a lower bound of the filtering effect of the DAR, we assume estimate the radiation density for the fundamental power injected into the DAR. The quasi-optical filtering suppresses the first harmonic by atleast 22 dB showing the efficacy of lossless filtering achieved in the DAR through manipulation of out-of-phase currents at f_0 in the two adjacent branches.

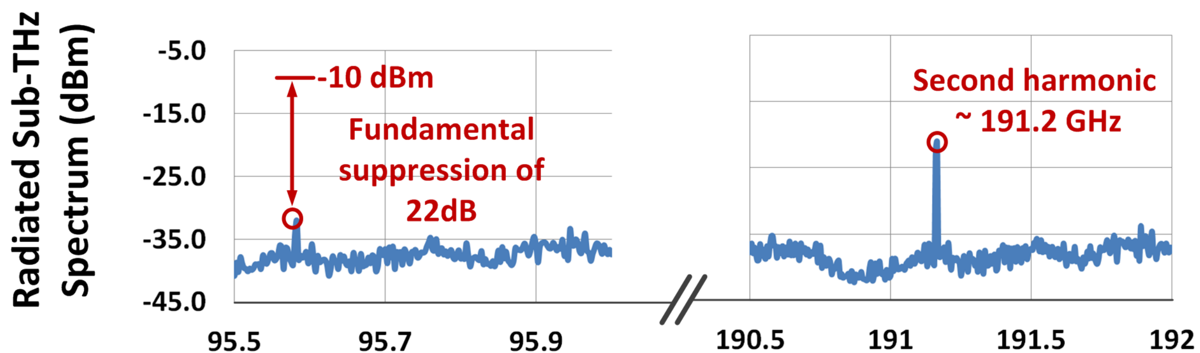

Figure 5.27: Calibrated locked sub-THz spectrum of the received signal from the back side, of the 2x2 array chip in Fig. 5.19.

Fig. 5.30 shows the measured radiation patterns, for the signal received form the backside of the 2x2 array chip as shown in Fig. 5.21. The patterns are fairly rotationally symmetric due to the nature of the circularly polarized radiation from the symmetric 2x2 array. Beam-scanning is demonstrated over two orthogonal planes by changing the varactor voltages of

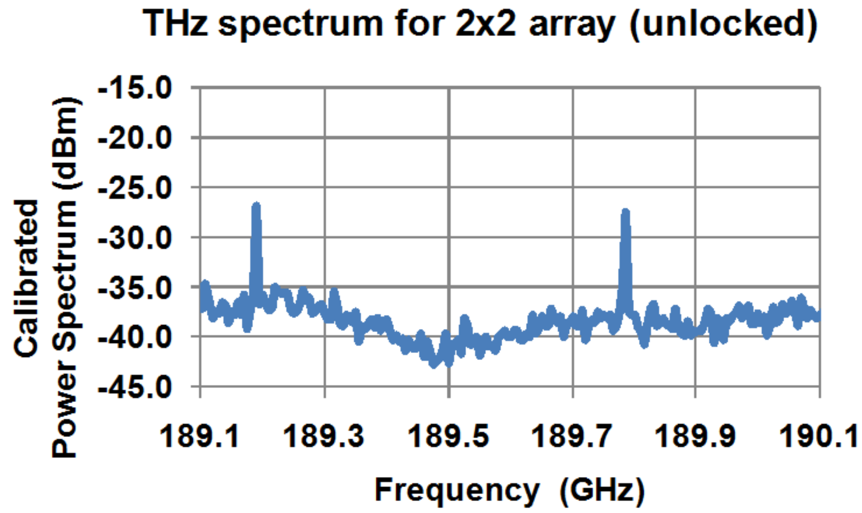

Figure 5.28: The received spectrum splits when the DARs go out of locking range due to the change in varactor voltage.

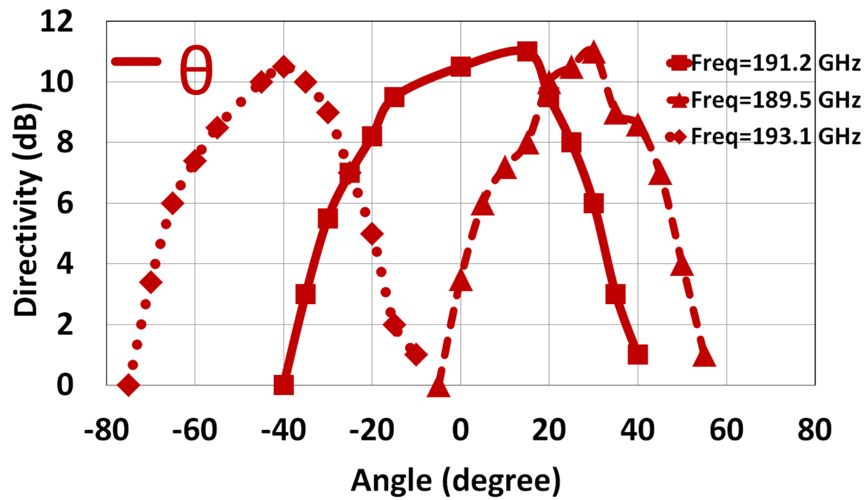

Figure 5.29: Electronic beam-scanning demonstrated near 0.2 THz, by the 2x2 array of locked DARs using near-field coupling. The figure shows the backside radiation patterns in the θ plane.

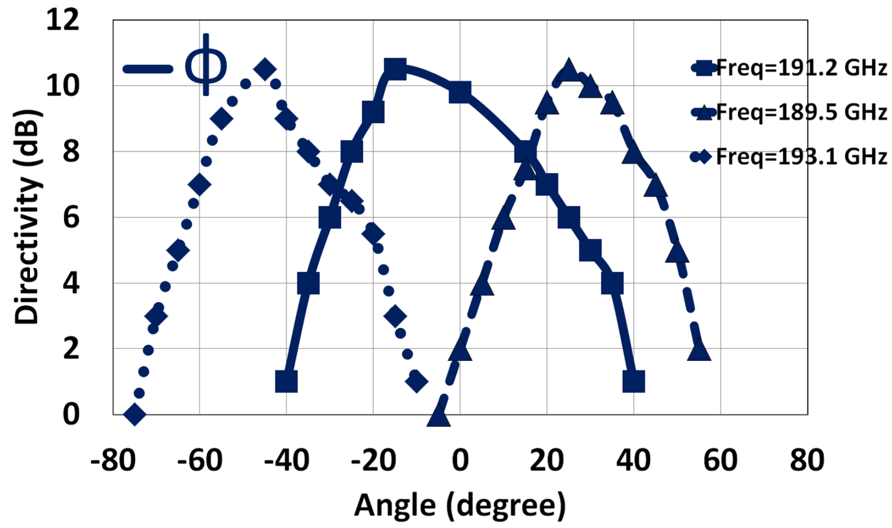

Figure 5.30: Electronic beam-scanning demonstrated near 0.2 THz, by the 2x2 array of locked DARs using near-field coupling. The figure shows the backside radiation patterns in the ϕ plane.

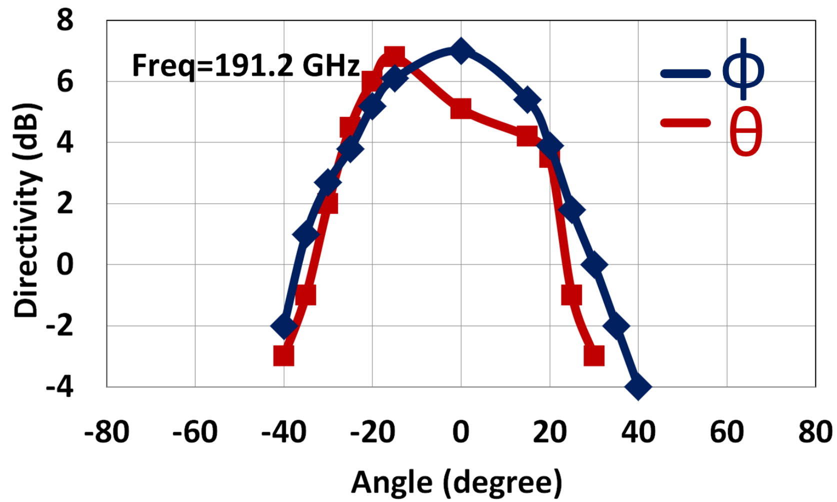

Figure 5.31: Radiation patterns of the second harmonic power near 0.2 THz from the front side of the 2x2 array chip

two adjacent DARs and measuring the pattern change over the intended plane of variation. Total electronic beam-scanning range is observed to be more than 70° in each of the two orthogonal axes. We proved in the previous section, that at the edges of locking the phase difference between the near-field coupled DARs at the fundamental frequency approaches 90°. However in practice, due to mismatches in passives, transistors and loading effects of the bias network, the locking bandwidth will decrease. Let us assume that at the locking edge, the phase difference at f_0 between two adjacent DARs approaches 45°. Therefore, the phase difference at the radiated frequency of $2f_0$ becomes approximately 90°. Under such a condition, for the on-chip separation of d_s=600 µm, we expect a total beam scanning range of $2\sin^{-1}(\lambda\Delta\phi_{2f_0}/(2\pi d_s)) \approx 82°$ which is reasonably close to measured results. The front side radiation pattern is also measured in the two orthogonal planes for nominal tuning, as shown in Fig. 5.31. The power radiated from the front side resulted in a total radiated power of 90 µW, and a lower directivity of 8.5 dBi, compared to that reported in [58].

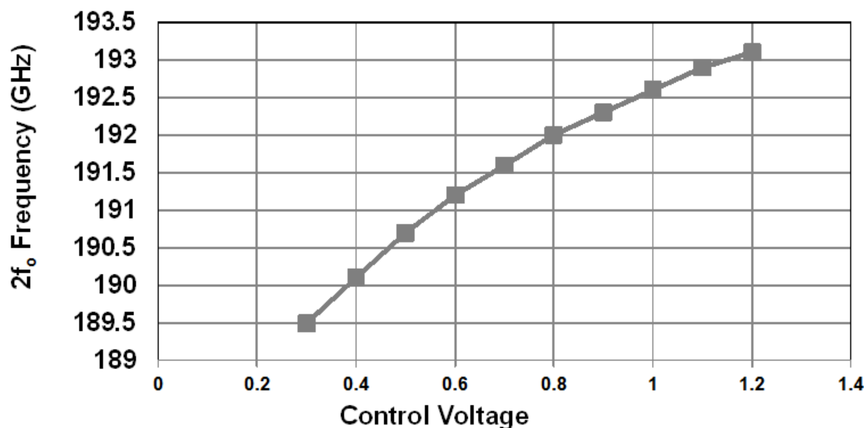

Figure 5.32: Locked second harmonic frequency of the 2x2 array when the varactor voltage of two adjacent DARs are varied simultaneously for beam-scanning in one orthogonal plane

In this method of beam-scanning using coupled DARs, the frequency of radiation varies with intended direction. Fig. 5.32 shows the variation of the locked second harmonic frequency with control voltage. As shown in (5.12), for small frequency offsets, the fundamental oscillation frequency, approximately, follows the mean of the resonant frequencies of the coupled DARs. Therefore, the maximum variation in the resonant frequencies of the adjacent

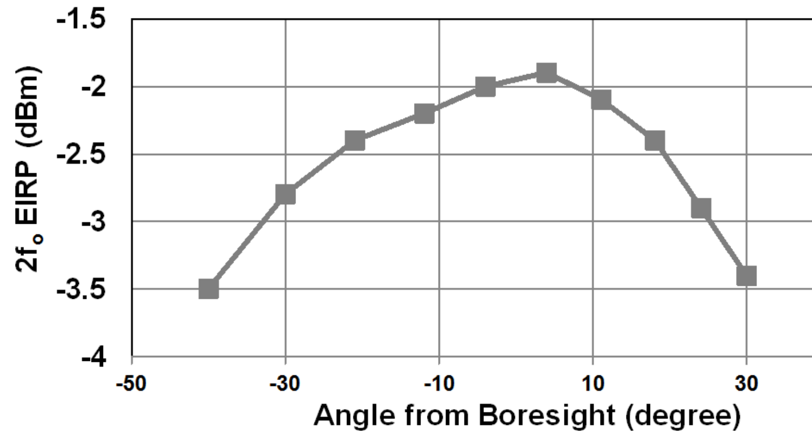

Figure 5.33: EIRP variation over the beam-scanning range.

DARs within the locking range, is measured to be 3.5 GHz from Fig. 5.32. This is close to the value of 2.1 GHz estimated in the analysis in the section that follows (5.13). EIRP, measured from the backside of the chip, over the beam-scanning range of over 70° in one orthogonal plane shows a fairly flat response for a total variation of less than 1.6dB.

Chapter 6

Integrated 4x4 Power-Generation and Beam-Scanning Array in CMOS at 0.28 THz

In Chapter 5, mutual synchronization networks using transmission lines and nearfield coupling, was demonstrated to implement 2x1 and 2x2 arrays of distributed active radiators. The frequency of oscillation of such a mutually injection locked system is determined by the common oscillation frequency of individually free-running oscillators [110]. In a practical system, we may often desire a central frequency reference controlling the frequency of the transmitted beam. Also in a mutually locked setting it is difficult to scale the array to a large number of elements. In this Chapter, we present a scalable power-generation and beam-steering architecture, which uses a central frequency reference to lock a multiple number of radiating sources, compatible to phase and frequency locking to a lower-frequency source.

6.1 THz Beam-Scanning Architecture

The beam-scanning and power generation architecture is shown in Fig. 7.3. The key element in the overall architecture is that desired harmonic power is generated locally and radiated immediately, which happens at the front-end of the transmitter in the individual DARs. This ensures high conversion efficiency from DC-THz. Therefore, the architecture simply enables a scalable frequency and phase control of the individual DARs and is not based on

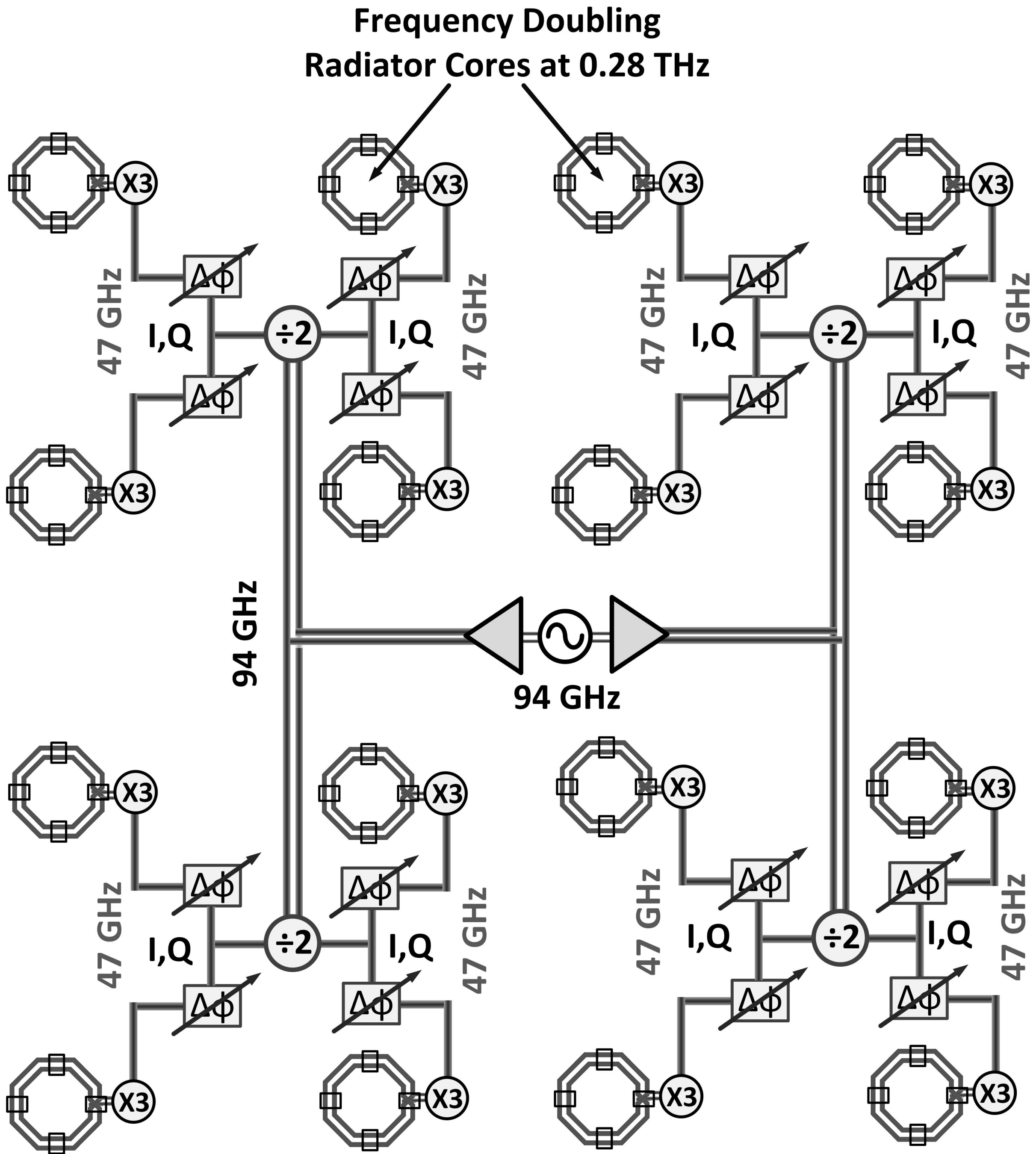

Figure 6.1: Proposed scalable architecture of the integrated THz power generator and beam-steering array in CMOS.

propagation of harmonic power from the source of generation through multipliers, matching networks, filters and radiating elements, similar to the partitioned approach, discussed in Chapter 3.

As shown in Fig. 7.3, a central frequency reference distributes signals at subharmonic frequencies to the entire chip to minimize losses in signal distribution. An on-chip VCO with differentials buffers constitute the central frequency reference. The VCO is tunable around 94 GHz with a 6 GHz tunable bandwidth. The central frequency of oscillation is one-third of the final radiated signal power near 0.28 THz. The buffers following the VCO distributed the 94 GHz differential signal to four symmetric junction points with equal delays, as show in Fig. 7.3, through impedance-matched differential transmission lines.

Once the signals are distributed globally at the four junction points, the t-lines are terminated by single-ended injection-locked divide-by-two blocks. The frequency dividers convert the differential signals at 94 GHz gets into differential quadrature signals, I and Q at 47 GHz. An alternative approach would have been to generate the quadrature signals at 47 GHz centrally and then distribute the four signals across the chip. However, this would have required simultaneous differential I and Q routing with good isolation which is difficult to achieve within area constraints. The quadrature signals at 47 GHz can now be added with different weights to generate 16 independent phase-rotated signals differential signals at 47 GHz, each of which in the end gets frequency and phase-locked to the 16 DAR cores. This facilitates control of phase of the radiated signal from each of the individual radiating cores enabling beam-forming and beam-steering in 2D space. The outputs 16 such phase rotators drive 16 injection-locked frequency triplers which are tuned at 140 GHz, each of which are locked to the fundamental frequency of oscillation of the final DARS at 140 GHz. Since the DARs only radiate the second harmonic, the chip generates and radiates power at 280 GHz with on-chip electronic beam control. Therefore the phase rotation, say θ, induced at 47 GHz gets translated to 6θ at the radiated frequency of 280 GHz. This does not imply that the sixth harmonic of 47 GHz gets radiated, instead, the signal at 280 GHz is generated and radiated locally at each of the DARs. Therefore the power is primarily determined by the voltage supply and current in each of the DAR which was analyzed in the previous chapters.

The signal distribution across the chip at mm-Wave frequencies is enabled through transmission lines which are carefully modeled using 3D electromagnetic simulation. Since the load impedances are dependent on length of the t-lines, the input to the circuit blocks, such as divide-by-two and the frequency triplers, are matched to the characteristic impedance of the interconnect t-lines, details of which will be discussed in the following section. This decouples the design of the output matching network of the previous stage with the exact placement of the blocks. The preceding circuit blocks, such as the oscillator buffers and the phase-shifters, drive load-pull impedances that ensure maximum power transfer to the succeeding blocks, such as the divide-by-two and the frequency triplers.

6.2 Transmitter Circuit Blocks

6.2.1 94 GHz Voltage-Controlled Oscillator and Buffers

The central VCO is realized cross-coupled transistors with a differential transmission-line based inductor as shown in Fig. 6.2. The cross-coupled pair consists of two 12 μm transistors, biased at 0.4 mA/μm for a total current of 9.6 mA from a 1 V supply. The transistors are laid out as 12 fingers in parallel, where each finger has a W/L of 1 μm/45 nm. The differential inductance of 38 pH is realized with differential coplanar strip lines placed in a ground tub, in order to shield the lossy silicon substrate, as shown in Fig. 6.2. The t-line is realized on 1.2-μm-thick copper metal with cheesing, and has simulated quality factor of 14 at 94 GHz. The varactors are realized with 32 μm wide NMOS transistors and the VCO has a tunable frequency range of 6%.

The buffers draw 11 mA each from a 1 V supply and each of the 12 μm wide transistors of the differential pair drive load-pull impedance for maximum power transfer to the succeeding frequency dividers. As can be shown in Fig. 6.2, the input of the divide-by-two blocks are matched to 100 Ω differential impedance which gets translated to 50 Ω by matched transmission lines at the split junction as shown in Fig. 6.2. This impedance is matched to the buffer differential load pull impedance for maximum power transfer through the t-line

shunt-series matching network, which also providing DC supply to the buffers, as illustrated in Fig. 6.2. Each of the output buffers drive 1.5 mW of RF power at 94 GHz into the t-line distribution network and approximately 180 μW of power reaches the single-ended input of each divide-by-two block based on a simulated loss of 3 dB in the LO distribution network as shown in Fig. 6.2. A 3D electromagnetic simulation of the LO distribution network, which feeds the divider blocks, is carried out, as shown in Fig. 6.3.

6.2.2 47 GHz Injection-Locked Divide-by-Two

The differential signal at 94 GHz from the output buffers, drives the input of two single-ended frequency dividers as shown in Fig. 6.4. The inputs of the frequency dividers are translated to 50 Ω single-ended by t-line matching networks and decoupling capacitors, which terminate the differential LO distribution t-line with odd-mode impedance of $Z_{00,diff}$=50Ω. The divide-by-two achieves the quadrature signal generation, I and Q at half the LO frequency, which are added with controllable weights to achieve a unique phase-rotated signal to be locked to a final radiating DAR. Each divide-by-two pair drives 4 phase-rotator blocks in its vicinity which locks to four unique radiating DARs as shown in Fig. 6.4.

The self-oscillation frequency of the divider is designed around to be around 47 GHz which is half of the center frequency of the central VCO. In order to ensure that the locking bandwidth covers the entire tuning range of the VCO in presence of process variations, the quality factor of the transmission-line-based inductor is designed to be lower (Q $\approx$ 7) for a differential inductance of 58 pH. The inductors of the divide-by-two pair are realized as differential coplanar transmission lines isolated by a ground tubs. Fig. 6.4 illustrates the placement of the individual blocks in the chip and since each divider drives the phase-rotators directly without buffers, parasitic capacitance has to be carefully extracted to ensure accurate resonance frequency. The varactor allows around 1.8 GHz tuning range in addition as shown in Fig. 6.5. Each divider draws 5.5 mA of current from a 1 V supply.

Figure 6.2: The central VCO with differential buffers and the LO distribution with matching transmission-line driving 8 divide-by-two blocks. The 3D electromagnetic structure for the passives and their placement in the chip are shown.

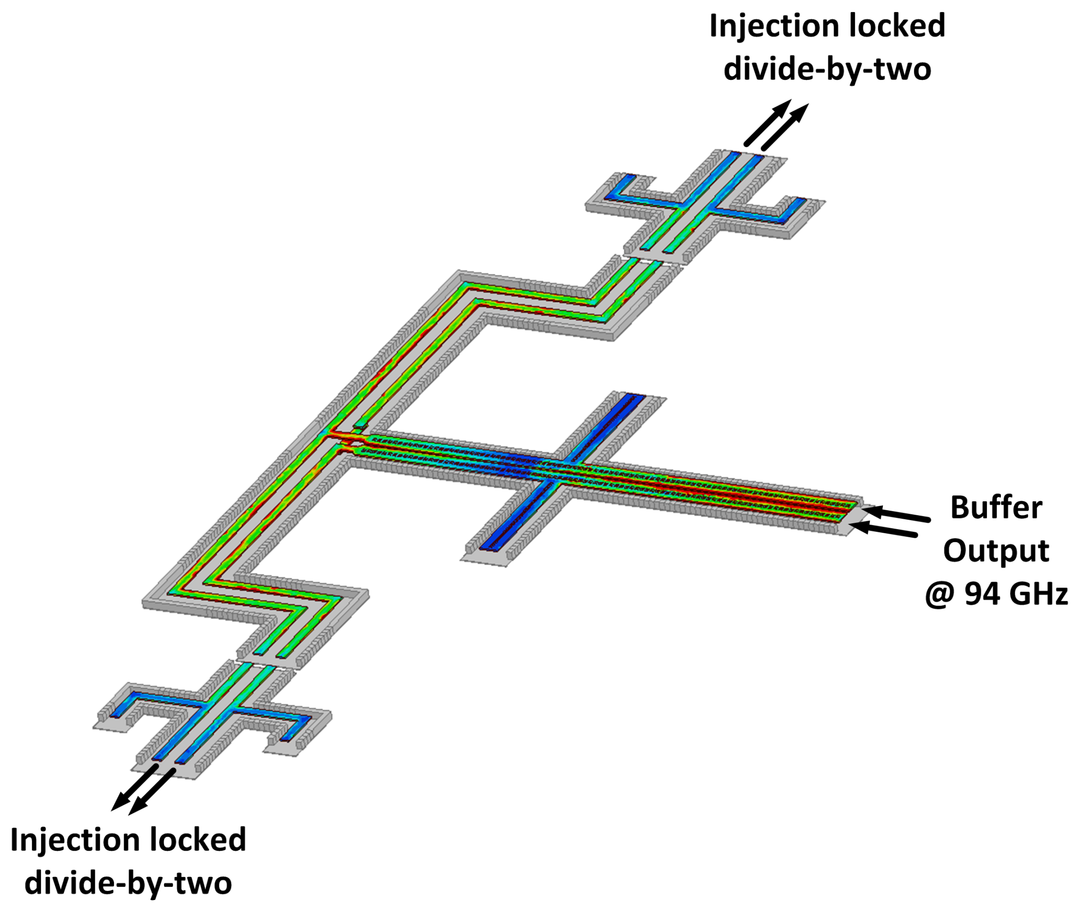

Figure 6.3: 3D electromagnetic simulation of LO distribution at 94 GHz, feeding the injection-locked frequency dividers.

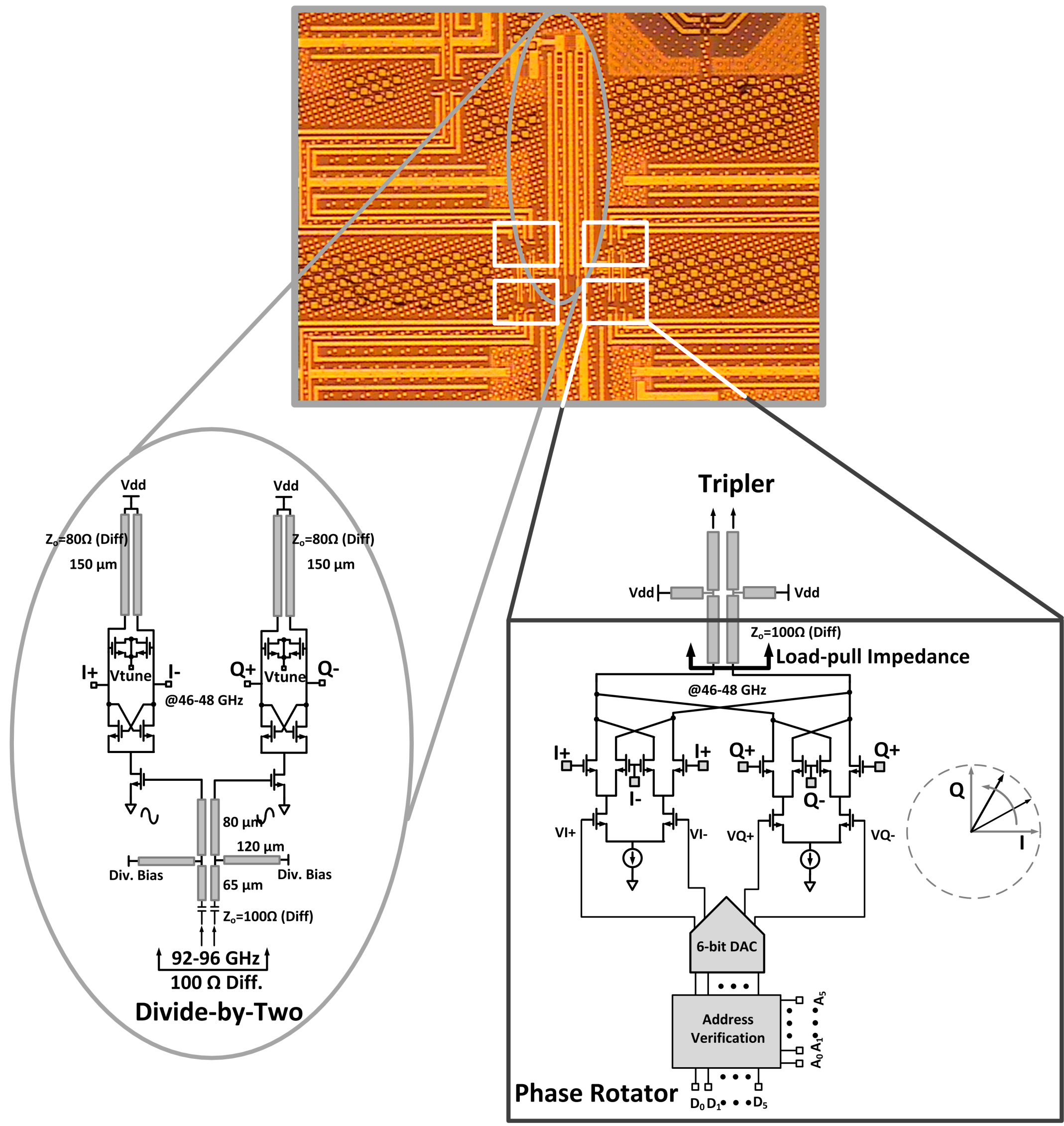

Figure 6.4: The injection-locked divide-by-two block showing quadrature signal generation at 47 GHz. Each divider pair drives four phase-rotator blocks whose weights for the quadrature signals are controlled by 6-bit DACs. The placements of these blocks are shown in the chip.

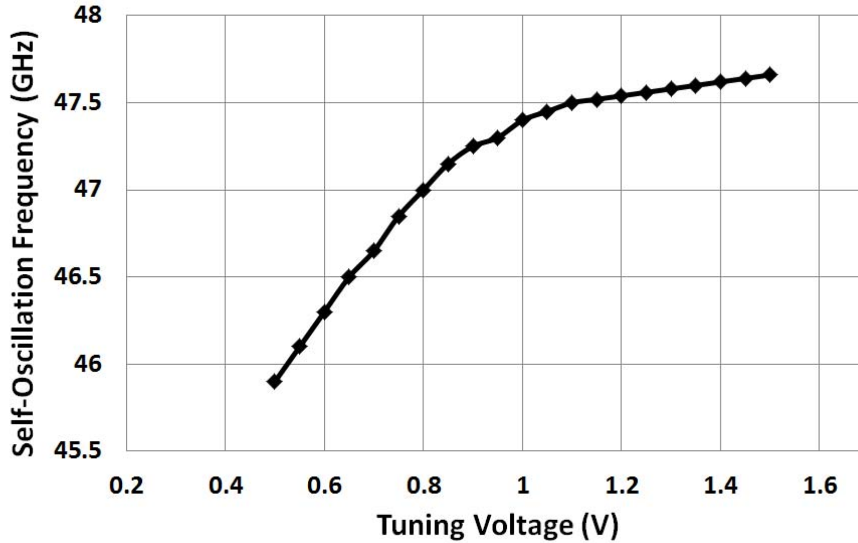

Figure 6.5: Simulated central frequency of oscillation of the injection locking divide-by-two block with varactor tuning.

6.2.3 47 GHz Phase Rotator

Phase rotation is achieved using a weighted summation of the quadrature signals at 47 GHz using two current-commuting Gilbert cells as shown in Fig. 6.4 [116]. The four phase control voltages (VI+,VI-,VQ+,VQ-) are generated using a 6-bit DAC with a serial interface. To address sixteen such phase-synthesis blocks for the 4x4 array, a 6-bit address is assigned to each phase-rotator element. The outputs of the Gilbert cells are current combined through a t-line matching network to generate the phase-rotated signal at 47 GHz which drives an injection-locked tripler to generate the phase-rotated signals at 141 GHz.

In such a scheme, the magnitude of the output current, and therefore RF power at 47 GHz, is a function of the phase-angle generated as shown in Fig. 6.6. When both the quadrature signals are added in equal weights to generate a 45° signal, the output current is $\sqrt{2}$ times the current when only one of the quadrature signal is passed. This difference in amplitude, however, does not propagate into the succeeding blocks, since the output swing of the injection-locked tripler is primarily determined by the biasing condition and design of the tripler. However, to ensure that the tripler locking is achieved under the condition of minimum current swing in presence of process variations, the output of the phase-rotator

is matched to the load-pull impedance for maximum power transfer as shown in Fig. 6.4. With a 6-bit control, a phase resolution of approximately 1.5° is achieved at 47 GHz which translates to a phase resolution of 9° at the radiated frequency of 0.28 THz. Each phase rotator dissipates 22 mA of current from a 1 V supply.

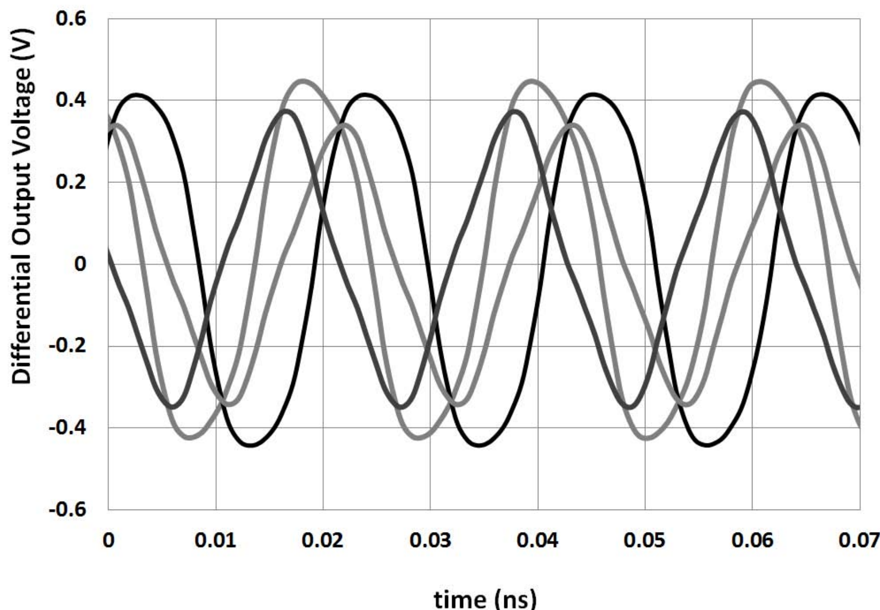

Figure 6.6: Simulated outputs of 4 phase-rotators at 47 GHz separated by 45° in phase difference. The differences in their amplitudes do not translate to the succeeding blocks which are injection-locked.

6.2.4 141 GHz Injection-Locked Frequency Tripler

The schematic of the tripler whose output locks to the self-oscillation frequency of the DAR is shown in Fig. 6.7. The output signal from the phase-shifters at 47 GHz drive a differential current injection in a cross-coupled oscillator tuned at 141 GHz [117]. As shown in the Fig. 6.7, the 47 GHz signal with a phase-angle of θ locks to an output signal of 141 GHz with phase angle 3θ which ultimately translates to a radiated signal at 282 GHz with a phase angle 6θ. The frequency tripler draws 4 mA of current from a 1 V supply.

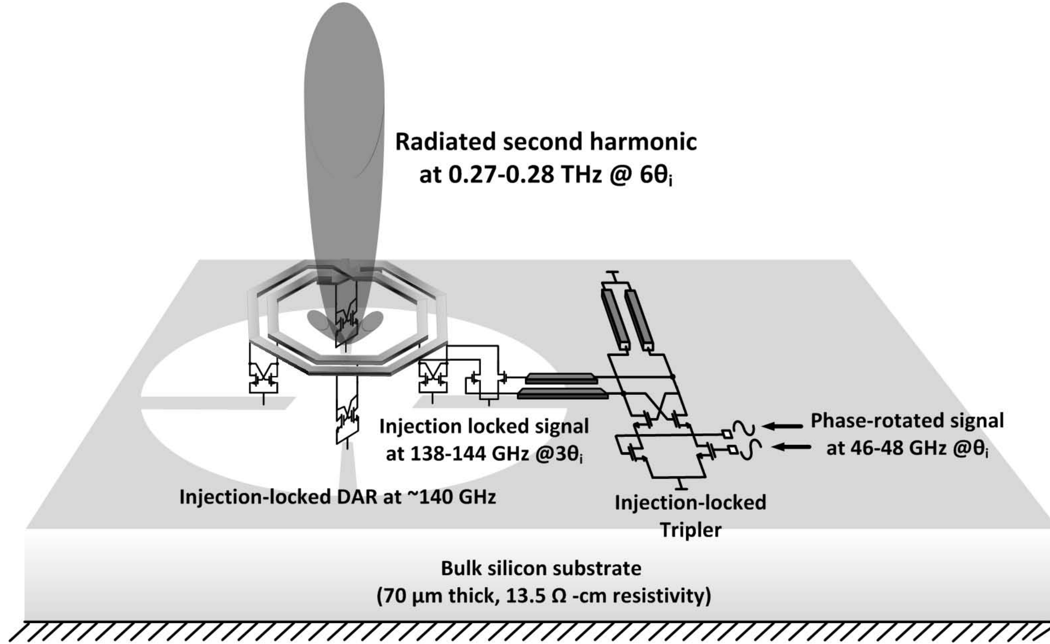

Figure 6.7: Injection-locked frequency tripler associated with each DAR showing frequency and phase multiplication from the 47 GHz signal input to the radiated signal at 282 GHz.

6.3 Measurement Results

The 280 GHz beam-scanning array is implemented in 45 nm SOI CMOS digital process with measured typical $f_t/f_{max} \sim$ 190–200 GHz [112], [113], [114]. The silicon-on-insulator technology does not offer the option of a high-resistivity substrate for low-loss passives and radiating structures. The insulator is only 0.225-μm-thick buried oxide and the bulk resistivity of the silicon substrate below is typically 13.5 Ω.cm, comparable to other bulk processes. The chip occupies 2.7 mm x 2.7 mm as shown in Fig. 6.14.

The chip is mounted on a brass for a good thermal pathway and radiates from the top side as shown in Fig. 6.7 and Fig. 6.14. The substrate is thinned to 70 μm such that the waves reflected from the backside brass mount interfered almost coherently with the topside radiation at 0.28 THz. Simulations showed that the radiation efficiency is not sensitive to the 10 μm tolerances of the thinning procedure. Previous works on DARs [57], [58] needed no substrate thinning and demonstrated radiation of signal from the backside of the silicon die, the integrated 4x4 array chip with local phase control, centralized LO distribution and

digital programming, presented in this paper dissipates near 800 mW of DC power and needs a reliable thermal pathway. While this could have been achieved using epoxies with good thermal conductivity and still radiating from the backside, in this paper the chip is mounted on a brass board and wire bonded to the PCB with carries only the digital programming and DC supply lines. While the array performance is quantified with free-space measurements, several breakouts of the array are measured as test-structures separately on wafer.

6.3.1 Central VCO and the Buffers

In order to characterize the central frequency reference, a stand-alone VCO test-structure with differential output buffers is measured with WR-10 waveguide probes as shown in Fig. 6.8. In the 4x4 array chip, the VCO buffers drive load-pull impedances which are matched from 50 Ω differential impedances as shown in Fig. 6.2. However, in the absence of differential probes in the WR-10 band, one of the output lines in the differential t-line structure on each side in the test chip is terminated with on-chip single-ended 50 Ω load. The other single-ended t-line is brought out to a 100 μm × 100 μm Al pad. A waveguide WR-10 probe is used to measure the frequency and output power of the two single-ended outputs, on either side, as shown in Fig. 6.8. The VCO has a central frequency of oscillation at 94 GHz and can be tunable from 91.8–96.5 GHz for a supply of 1.1 V. The tuning of the oscillation frequency with varactor voltage and V_{dd} is shown in Fig. 6.9. The phase noise of the free-running oscillator is measured to be -112 dBc/Hz at 10 MHz offset. The core oscillator and the buffers together draw 30 mA of current from V_{dd}=1.1 V.

A measurement of interest is the output power delivered by the oscillator buffers in the array, since it is critical in determining the locking range of the succeeding frequency dividers. However, because of the difference in output impedance seen by the buffers in the test chip and the array chip, the RF power, delivered by the buffers in the 4x4 array, is estimated from a measurement of output power from the test chip and 3D electromagnetic simulation of t-line network in the two chips. The measured output power at the pads in the VCO test chip and the estimated RF power at the buffer output in the array chip are shown in

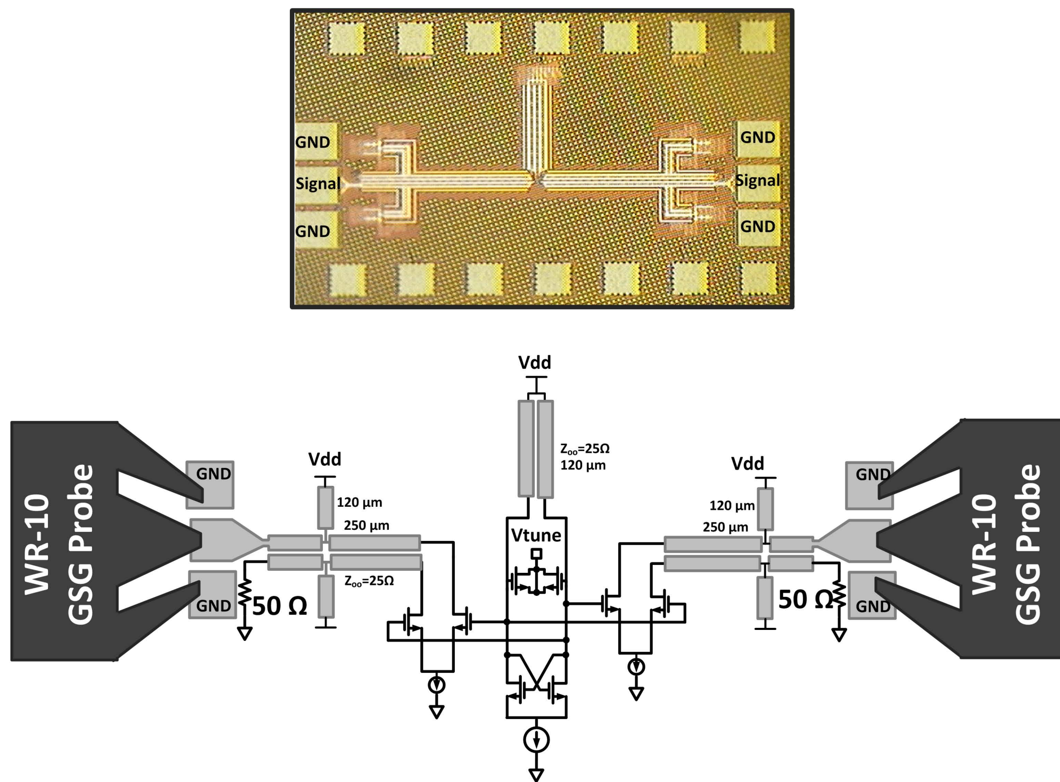

Figure 6.8: Measurement setup for the test structure comprising the central VCO and differential buffers.

Fig. 6.10. The output power delivered by each buffer at 94 GHz is 1.2 mW, out of which a simulated 50% is lost in the LO distribution network, implying 150 μW power would drive each divide-by-two block.

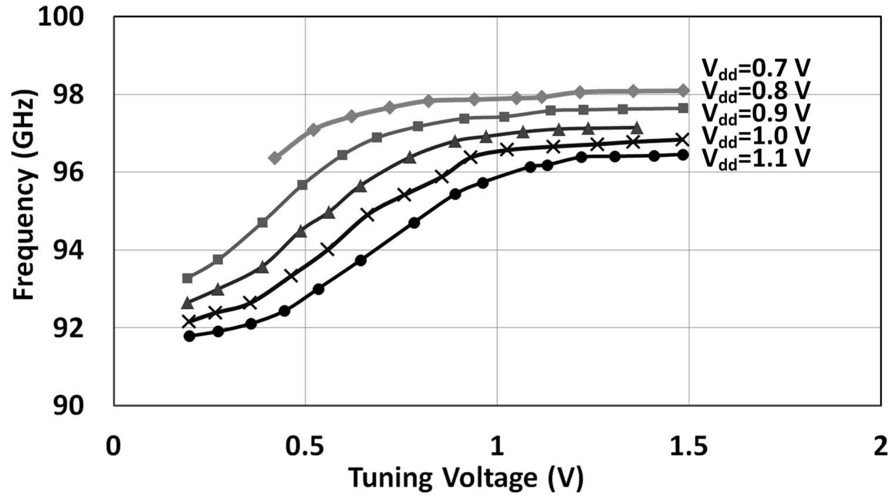

Figure 6.9: Measured VCO frequency tuning against varactor and supply voltage.

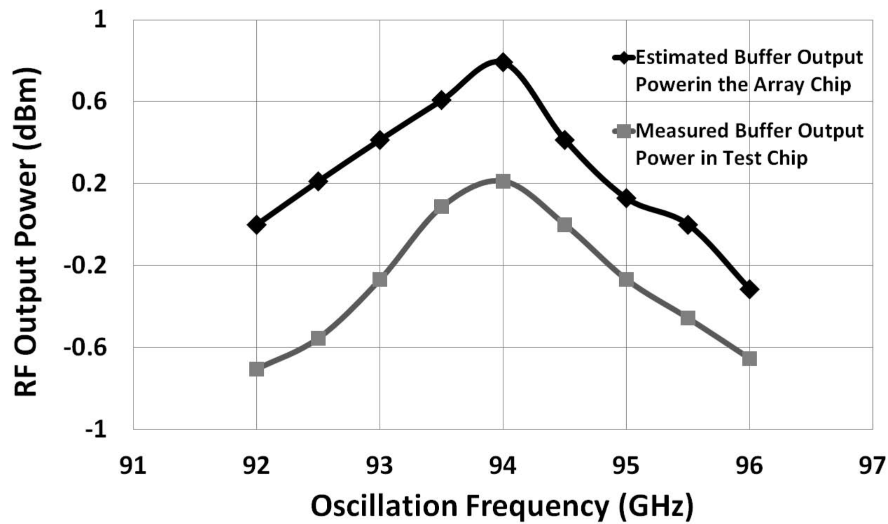

Figure 6.10: Measured single-ended LO buffer power at the pad from the test chip and estimated differential LO buffer output power in the array chip.

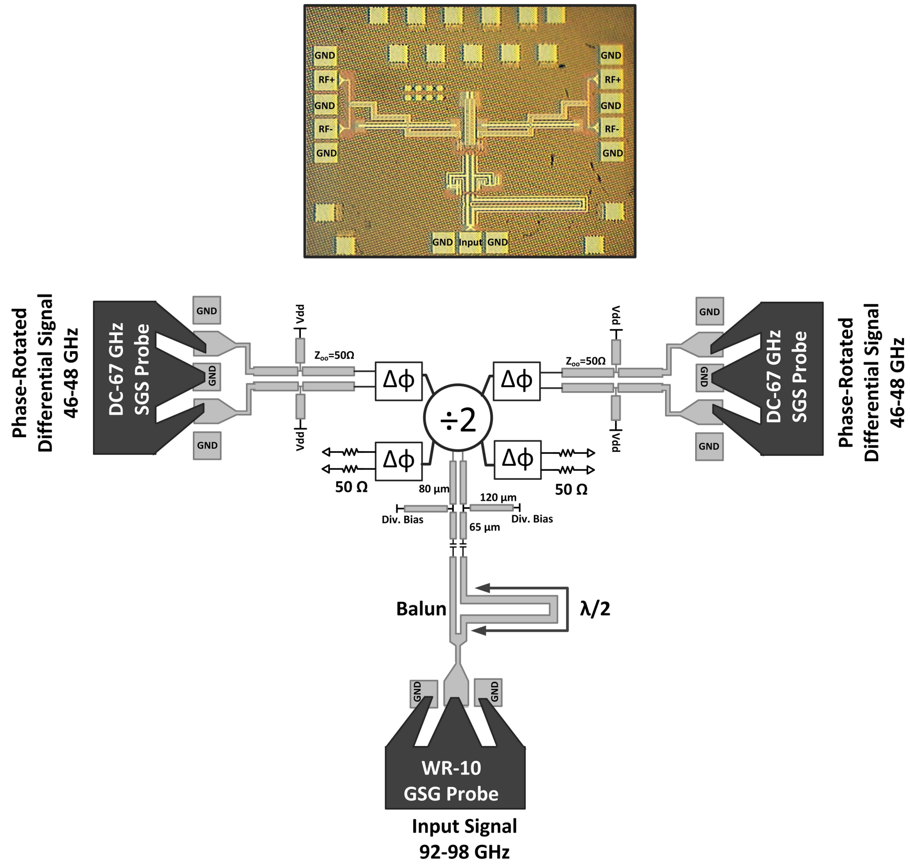

Figure 6.11: Measurement set-up for the test chip comprising of one divide-by-two pair which generates quadrature signals at 47 GHz and drives four phase-rotators.

6.3.2 Quadrature Signal Generation and Phase Rotation

A test-structure comprising of the frequency divider generating the quadrature signal generation at 47 GHz, which drives four phase-rotators, is measured. Due to the absence of the differential probe at the WR-10 band, a GSG waveguide probe feeds a single-ended W band signal which is converted into differential mode through an on-chip balun as shown in Fig. 6.11. The input matching network of the divider and the output network of the phase-rotators are identical to the array chip. The measured sensitivity of the divider, which is the input power necessary to achieve locking and frequency division, is shown in Fig. 6.12, calibrating for the loss of the on-chip balun from electromagnetic simulations. The divider locking range for the measured VCO output power for an estimated 3 dB power loss in the LO distribution is shown in Fig. 6.12. The range covers the entire 92–96 GHz tuning range of the VCO for a single tuning voltage of V_{tune}=1.0 V for the divider. The central frequency of the locking range can be varied using varactor tuning in the divider. The phase-rotator performance is measured using differential SGS probes by measuring the outputs of two of the phase rotators while the other two are terminated on chip as shown in Fig. 6.11. The phase mismatch of the probes and the measurement equipment on the two sides are calibrated out. To ensure minimum sensitivity to offset voltages and transistor mismatches, the quadrature signals are added with equal weights in one of the phase rotators such that $V_{pr1} = |VQ_{max}+VI_{max}|$, while the control for the other is varied from $V_{pr2} = |VQ_{max}+VI_{max}|$ to $V_{pr2} = |VQ_{max} - VI_{max}|$ by the 6 bit DAC setting. The measured phase-difference between the outputs is shown in Fig. 6.13. The measurement shows a full range of 90° of phase rotation with low initial offset of 5°.

6.3.3 Array Measurement

The die photo and the PCB is shown in Fig. 6.14. The chip micrograph shows the placement of the central VCO with LO distribution, frequency dividers, phase-rotators, injection locking triplers and the frequency doubling DAR cores. The free-space measurement set up for 4x4 array chip is shown in Fig. 6.15. The radiated power is captured at a a distance of 50 mm, by

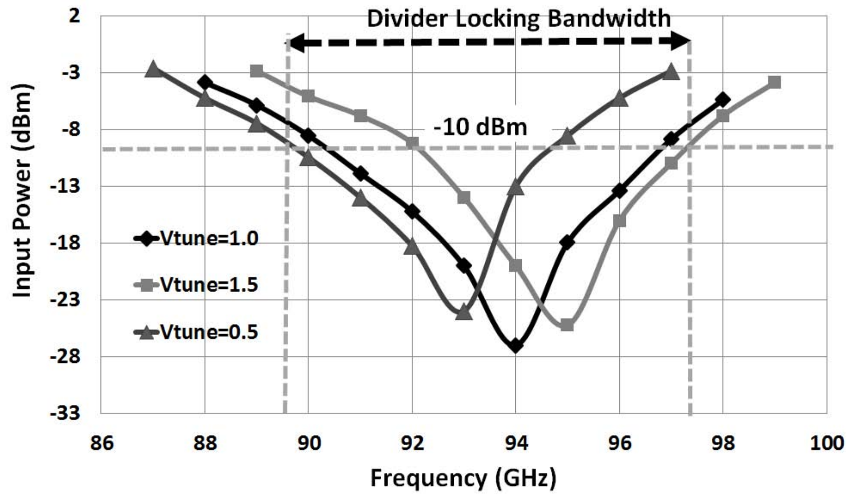

Figure 6.12: Measured sensitivity of the injection-locked divide-by-two block for different tuning voltages. The divider-locking bandwidth is marked for the LO buffer output power in the array chip.

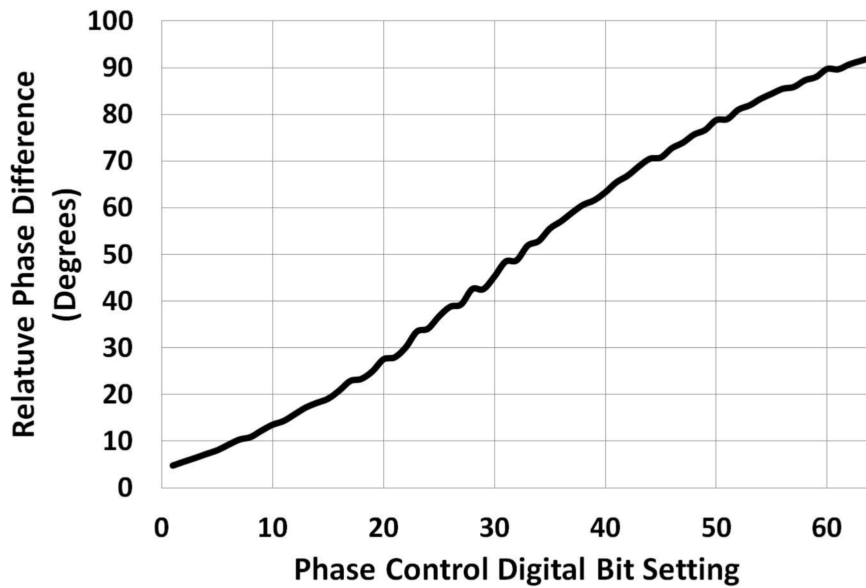

Figure 6.13: Measured phase difference between the output of the two phase shifters in Fig. 6.11 as the 6-bit DAC setting for the phase control voltages of one phase-rotator is varied.

a WR-3 (225–325 GHz) 25 dB standard-gain horn antenna. The absolute power is measured using an Erickson power meter, which is a calorimeter based power measurement instrument between 75–2000 GHz [115]. The measurement of the power is similar to the procedure described in Chapter 5.

The power captured by the receiver antenna with a given aperture is proportional to both the total radiated power from the chip and the directivity of the beam. This measure, defined as Effective Isotropic Radiated Power (EIRP), at any given direction is enumerated directly from the power captured by the receiver antenna connected to the Erickson power meter as shown in Fig. 6.15, as explained in Chapter 5.

Because of the traveling nature of the surface currents in the DAR, the radiated fields are expected to be circularly polarized. This is experimentally verified by rotating the linearly polarized receiver antenna around its broadside axis linearly polarized receiver antenna. The power captured changed by less than 0.5 dB over the entire rotational angle verifying the circularly polarized nature of the radiation. When all the DARs are radiating in phase, the beam has the highest directivity near broadside. Calibrating for half the power lost due to polarization mismatch, the power captured at the far-field distance of 50 mm in the broadside direction is 8 μW at 282 GHz which translated to an EIRP of +9.4 dBm. Near-field effects or standing wave formation can cause errors in power measurement. The receiver antenna is placed over a range of far-field distances and the received power followed closely $1/R^2$, and the measured EIRP remained constant.

The frequency of the radiated signal is measured by down converting the signal with a harmonic mixer, amplified by low-noise amplifiers and then analyzed in a spectrum analyzer. The entire receiver chain is calibrated between 110–170 GHz and 220–325 GHz using separate WR-6 and WR-3 sources, respectively, along with the Erickson power meter. The calibrated spectrum of the radiated signal is shown in Fig. 6.17 for the central oscillator setting of V_{tune}=1 V. Fig. 6.17 illustrates the strong second harmonic component at 280.8 GHz with EIRP of +9.4 dBm due to the efficient radiative behavior of DAR, and the quasi-optical filtering effect resulting in an estimated 24 dB fundamental power suppression at 140.4 GHz. The power of the fundamental frequency has been scaled to the same receiver aperture for a

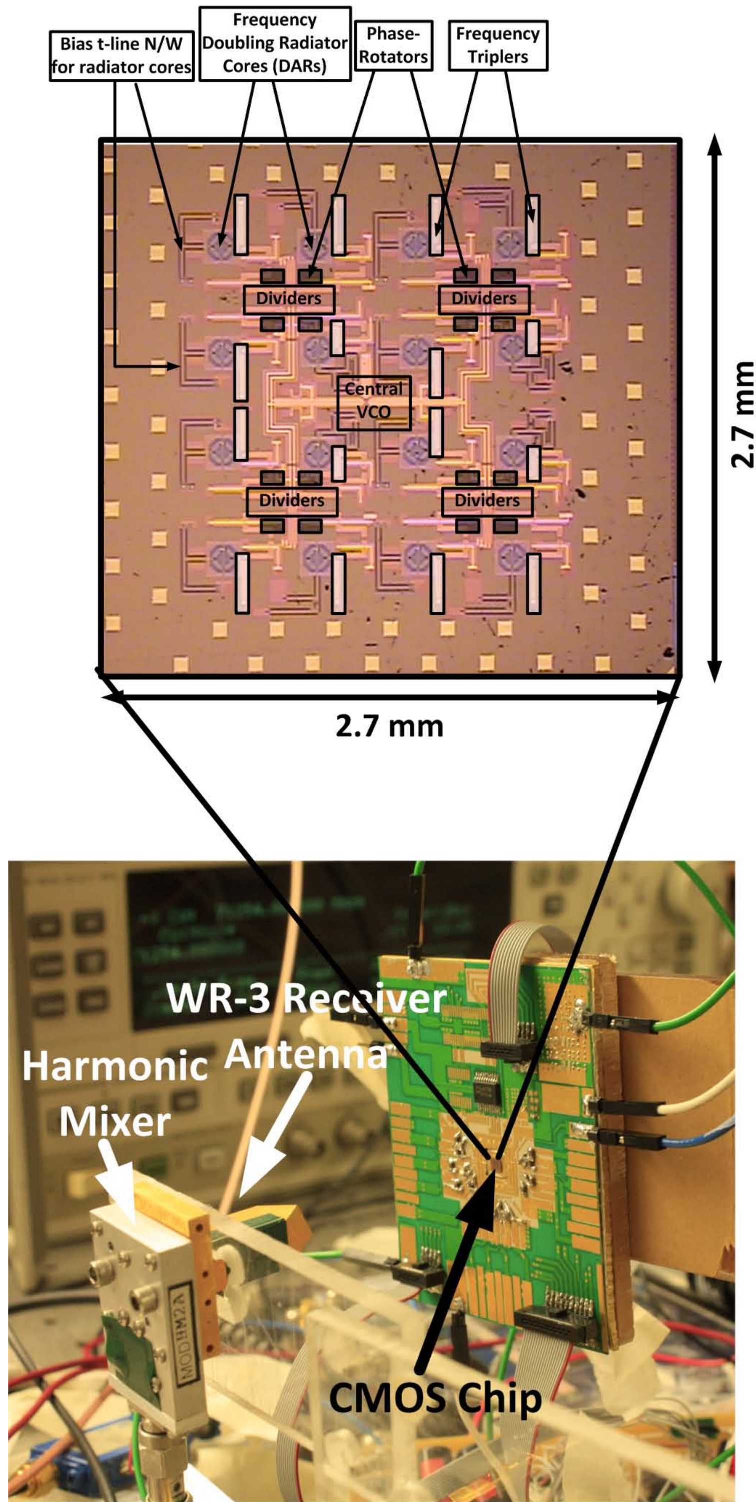

Figure 6.14: Die micrograph showing placement of individual functional blocks along with a photo of the measurement setup showing the receiver antenna and the harmonic mixer as in Fig. 6.16.

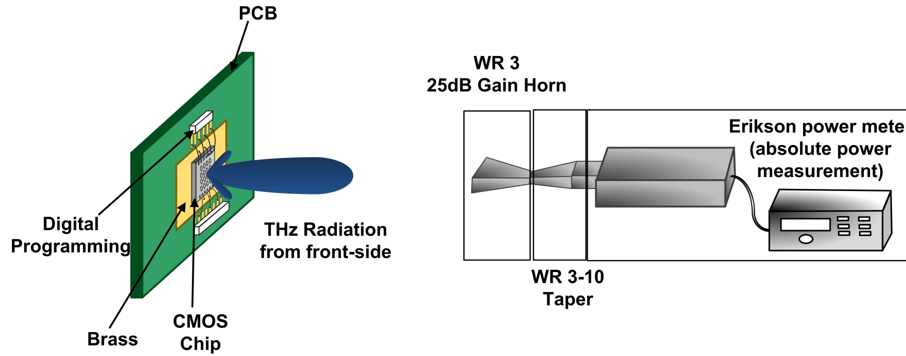

Figure 6.15: Experimental setup for the absolute power and EIRP measurement at the far]field of the radiating chip mounted on a brass board.

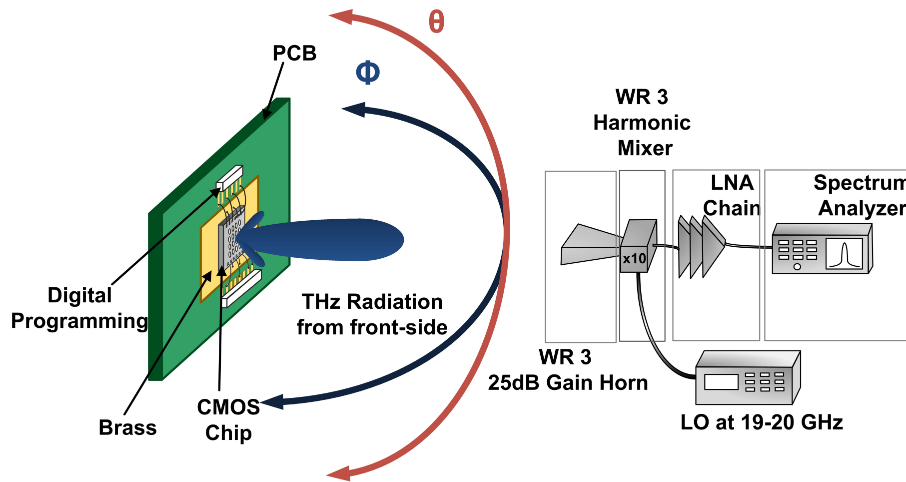

Figure 6.16: Experimental setup for measurement of the frequency of radiated signal and the 3D radiation pattern.

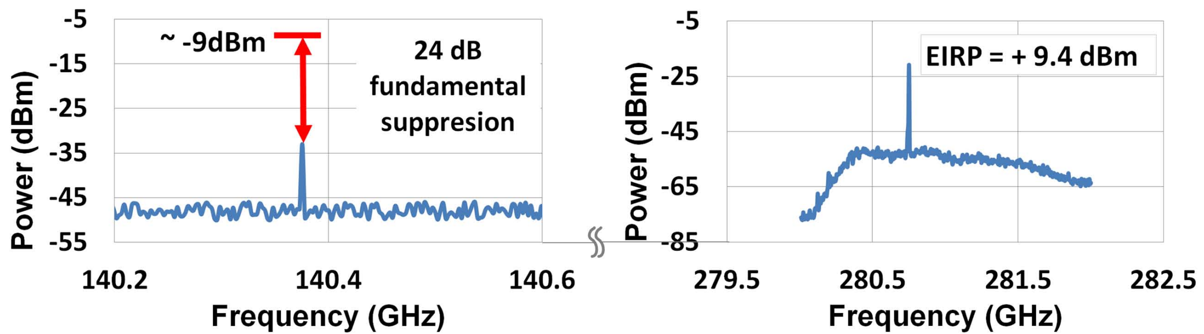

Figure 6.17: Calibrated spectrum of the radiated signal at the broadside captured at a far-field distance of 50 mm. The spectrum shows almost 24 dB of fundamental signal suppression near 140.4 GHz and a +9.4 dBm EIRP at the second harmonic frequency of 280.8 GHz

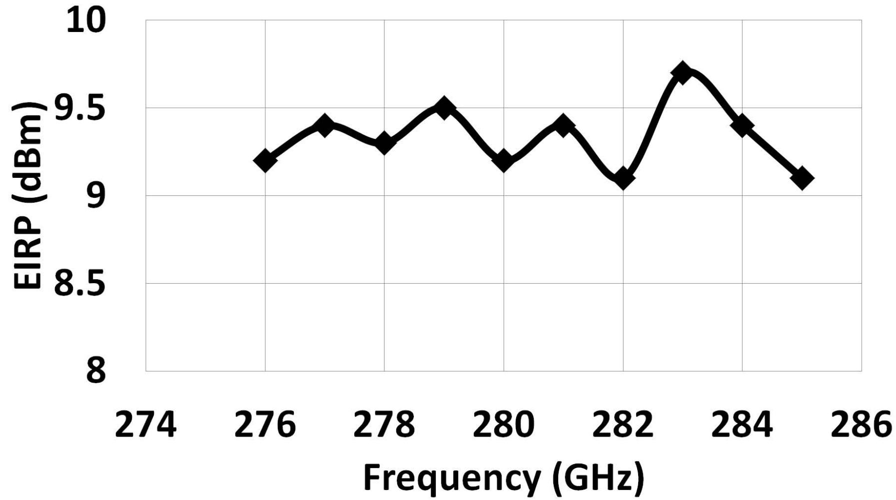

Figure 6.18: Variation of measured EIRP at the broadside, as the frequency of the radiated signal is controlled using the central VCO varactor tuning setting.

fair comparison.[1] The transmitted signal frequency can be adjusted between 276–285 GHz as the central VCO is tuned from 92-95 GHz. The output signal loses locking if the VCO is tuned beyond this range. Since the frequency doubling happens only locally at the radiator cores themselves, the EIRP remains fairly constant and varies less than 0.5 dB over the entire tuning range as shown in Fig. 6.18.

To demonstrate electronic beam-steering, a progressive phase shift between the adjacent radiators is created in each of the two orthogonal axes. This is achieved using the digital phase-rotation settings at the lower frequency of 47 GHz, which is up-converted in phase and frequency at the radiated frequency of 282 GHz. The radiation patterns are measured by rotating the Tx chip in three-dimensional space as shown in Fig. 6.16. The measured radiation patterns at 282 GHz in azimuth and elevation are shown in Fig. 6.19. The clean array pattern with one major lobe indicates the effectiveness of surface wave cancelation in the silicon chip. While the gain of the array could not be measured because of the self-sustained oscillatory nature of the DAR, the directivity (shown in dB in Fig. 6.19) is measured by integrating the measured 3D profile of the radiation pattern. The rotational symmetry

[1]The fundamental suppression is estimated from a simulated value of RF power at the fundamental frequency injected into the resonator and the antenna aperture area corresponding to the physical chip dimensions.

of the DAR results in a similar symmetry along the direction of maximum directivity. The patterns, therefore, are symmetrical in both the two orthogonal planes. The maximum directivity is measured to be approximately 16 dB and the total radiated power is 190 μW for an EIRP of 9.4 dBm at 281 GHz. Fig. 6.19 shows an approximately 80° of beam-scanning control in each of the 2D axes. To effect a beam tilt of $\Delta\alpha = 40°$ from the broadside direction at 282 GHz, the phase shift, $\Delta\beta$, between adjacent radiators separated by approximately 500 μm is given by $\Delta\beta = 180° \sin(\Delta\alpha) \times \frac{2.8}{3.0} \approx 108°$. This implies a phase-difference of 19° at the subharmonic locking frequency of 47 GHz which is easily achieved using the 6 bit control for the phase-shifters. The chip performance is summarized in Fig. 6.20.

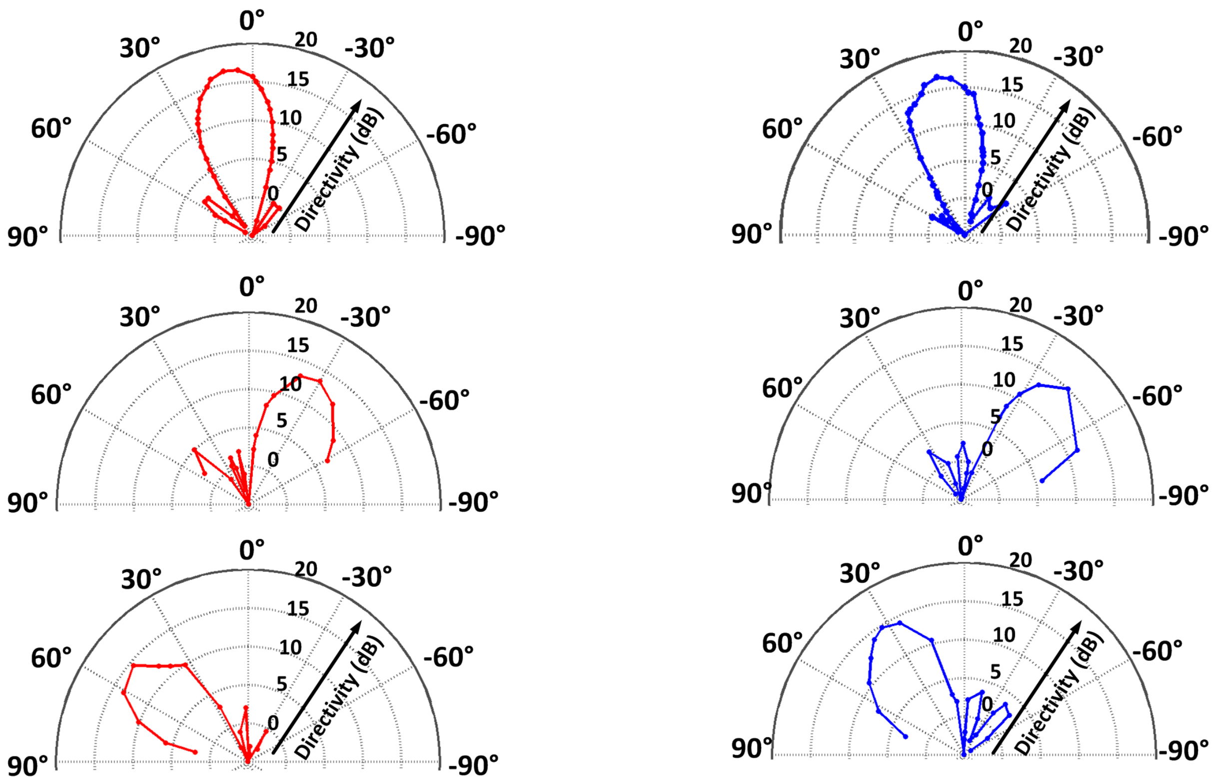

Figure 6.19: Radiation pattern measured in the elevation and azimuth plane, respectively, at 281 GHz showing a directivity of 16dBi and total electronic beam-steering range of around 80° in the each of the planes.

Chip performance summary

Transmitter Performance

Frequency of operation	276-285 GHz
Maximum broadside EIRP	+9.4dBm
Total radiated power (broadside)	190µW
EIRP flatness	less than 1dB
Beam-steering	80° in in 2D space
Beam-steering resolution	limited by DAC res.
Side lobes ratio	>10dB
Central time-base VCO tuning range	90.2-98.5 GHz

Power consumption

Central VCO and Buffers@1.1V	30mA
Divide-by-two elements (total of 8) @1.1V	8mA per element
Phase-rotators (total of 16)@1.1V	22mA per element
Triplers (total of 16) @1.1V	4mA per element
Distributed active radiators (total of 16) @0.8V	20mA per element

Figure 6.20: Chip performance summary

Chapter 7

Multipixel Terahertz Camera in Silicon

In Chapters 3-6, we discussed, integrated terahertz sources, radiators and beam-scanners in integrated silicon technology. In order to enable the realization of an all-silicon THz imager, we will now concentrate on the second part of the transceiver system, namely the receiver, as shown in Fig. 7.1.

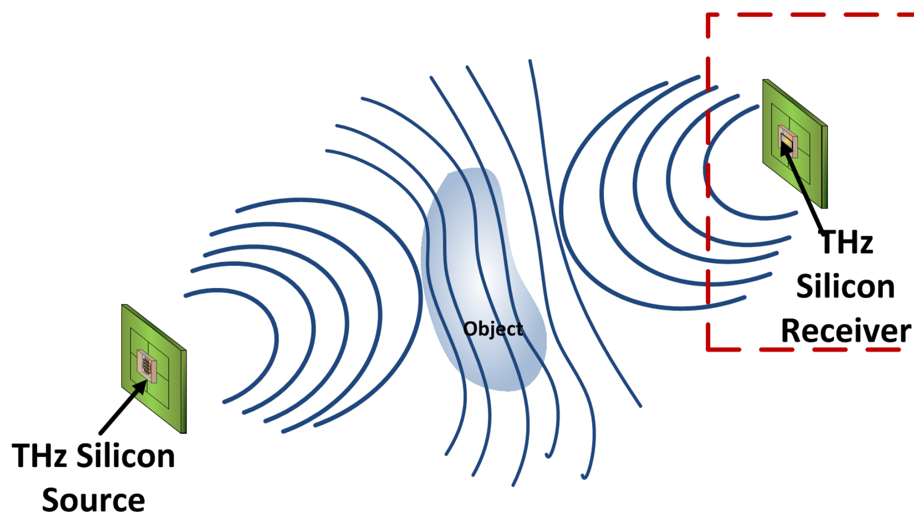

Figure 7.1: Silicon-based Terahertz imaging system.

Terahertz receivers and imagers, for a long time, have been fields of study in astronomy and chemical sciences for high-resolution spectroscopy and remote sensing areas. In recent years, there has been significant research devoted to Terahertz technology and because of some of its unique properties it is emerging as an attractive tool for a wider range of applica-

tions such as security screening (due to its ability to penetrate through clothing, plastic and packaging materials with higher resolution than microwaves and mm-Waves) [2], noninvasive medical imaging (lower scattering compared to optics, contrast in water absorption and tissue density and safe due its nonionizing photon energies) [8], [23], spectroscopic studies and label-free biosensing [32], contraband detection [30], and industrial and process control. Current THz detector technology consist of discrete and custom devices, which are often bulky and expensive, while not sensitive enough at room temperature. They can be optics-based (such as nonlinear crystals or electro-optic samplers), calorimetric detector technologies (such as bolometers, golay cells, pyroelectric detectors which are limited by thermal-time constants for their use in video-rate imaging), or solid-state hybrid III-V MMICs (which have higher cost and are less amenable to integration) [118] and [119]. Fig. 7.2 illustrates some typical THz detector technology currently in use for astronomical sciences. Comprehensive articles on this subject can be found in [118]- [119]. The important figure of merits for a detector are Responsivity ($\mathfrak{R}_\mathfrak{v}$) and Noise-equivalent-power (NEP). Responsivity is defined as the change in output DC voltage with a unit change in input RF power. NEP is defined as as the input power for which the signal-to-noise ratio is unity for an integration time of 1 second. Therefore, if v_n be the output rms noise voltage, NEP is defined as

$$NEP = \frac{v_n}{\mathfrak{R}_\mathfrak{v}} \tag{7.1}$$

Typical NEP achieved in the conventional technology at room temperature are mentioned in Fig. 7.2. Golay cells achieve typical NEP of 200–300 pW/$\sqrt{\text{Hz}}$ [125], microbolometers range from 10–200 pW/$\sqrt{\text{Hz}}$ [126], [127], Schottky Barrier Diodes 10–20 pW/$\sqrt{\text{Hz}}$ [128] and pyroelectric detectors 400 pW/$\sqrt{\text{Hz}}$ [129], [130]. If silicon technology can achieve competitive performance, then with its level of integration, it can pave the way for low-cost fully integrated THz imaging systems for large-volume applications spanning from defense to consumer and medical electronics.

Prior work and contemporary work have demonstrated the feasibility of silicon tech-

nology for THz detection [48], [120]– [122], however they can be power-intensive (> 300 mW/pixel) [48], require high-resistivity substrates (> $1K\Omega$-cm) substrates [121], or use modifications such as silicon lenses [121] or substrate thinning [122]. The main reason necessitating the use of these modifications is the low efficiency of on-chip receiving antennas. It is easier to see these challenges in the context of a transmitter antenna, but the reasoning still applies to a receiving antenna due to reciprocity. In this chapter, we will discuss the design and implementation of a lens-less multipixel THz receiver with antenna and detector codesign on a 250 μm bulk silicon substrate with 10 Ω-cm resistivity [62].

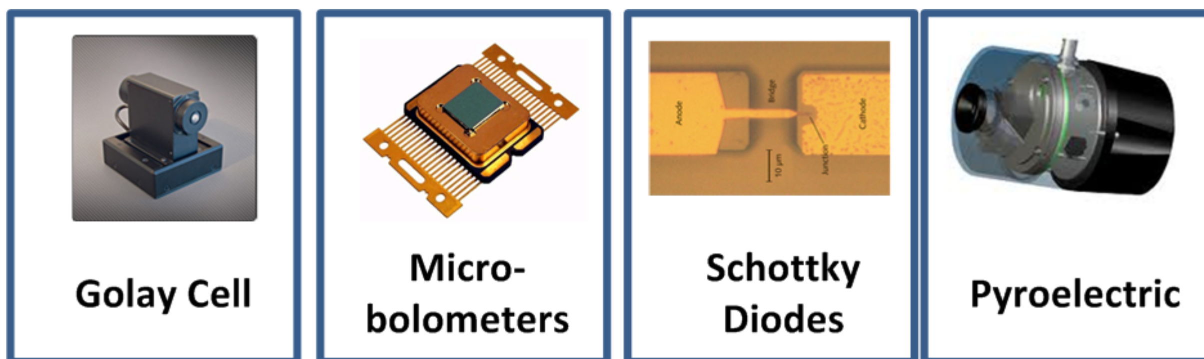

Figure 7.2: Some of the typical and currently used Terahertz direct detection technologies. Golay Cells have typical NEP $\sim$ 200 pW/$\sqrt{\text{Hz}}$ 1001[125], microbolometers $\sim$ 10–200 pW/$\sqrt{\text{Hz}}$ [126], [127], Schottky Barrier Diodes $\sim$ 10–20 pW/$\sqrt{\text{Hz}}$ [128], pyroelectric detectors $\sim$ 400 pW/$\sqrt{\text{Hz}}$ [129].

7.1 Integrated 4x4 Pixel THz Camera in SiGe BiCMOS

In this section, we will describe the design and implementation of direct-detection-based 4x4 pixel THz camera in 0.13 μm SiGe BiCMOS process.

The chip is implemented in the IBM8hp process, which is a 0.13 μm SiGE BiCMOS process. The process provides 120 nm NPN bipolar transistors with peak f_T/f_{max} of 200/285 GHz. This process has substrate resistivity of about 10 Ω-cm and five levels of copper metal layers, including M1, M2, M3 and M4 (each with a thickness of 0.32 μm), and M5 (with a thickness of 0.55 μm), as well as two levels of aluminum (with thicknesses of 1.25 μm and 4

μm).

7.1.1 Architecture, Integrated Antenna, Detector and Baseband

The choice of a front-end for an architecture which can be scaled to a large number of pixels is critical with respect to its sensitivity, scalability and power dissipation. Operating near and above f_{max} of a technology, the incoming signal captured by the antenna cannot be amplified by a high-gain front-end LNA. For the lowest noise performance, the signal can either be directly converted to DC through rectification or brought down to an intermediate frequency through harmonic mixing. While a down-converting architecture gives additional phase information and low noise performance due to optimum receiver architecture, it poses major challenges such as routing of LO, maintaining phase coherence to all pixels, occupation of substantially large silicon area and excessive power consumption. Scaling a down-converting architecture to a high-resolution imager with more than 100$\times$100 pixels is therefore prohibitive. In this work, we choose a direct detection scheme for the 16 pixel camera. The architecture is shown in Fig. 7.3. 16 identical pixels are distributed across a 2.5 mm$\times$ 2.5 mm size chip. Each pixel has an integrated antenna with a square law detector and an associate baseband with variable gain and adjustable bandwidth. The differential output of all the pixels come out to the pads.

The pixel spacing is kept at 500 μm for antenna spacing of $\lambda_0/2$ at 300 GHz. The antenna consists of a near-full-wavelength loop, which has a property of reducing surface-wave power lost in TE_0 modes as discussed in Chapter 4. The chip was designed to have maximum sensitivity for radiation from the backside of the substrate. As shown in Fig. 7.4, for an ungrounded substrate, the paths length between the primary A_{f1} and the different secondary sources (A_{f2}, A_{f3}, etc.) on the front side of the silicon die, after suffering multiple reflections, is the same as the primary source A_{b1} and the different secondary sources (A_{b2}, A_{b3}, etc.) on the backside of the silicon die, after suffering multiple reflections. It can be shown that the efficiency of the antenna is maximized, when the sources (A_{b1}, A_{b2}, A_{b3}, etc.) on the backside add coherently in phase [72]. This implies that total path length

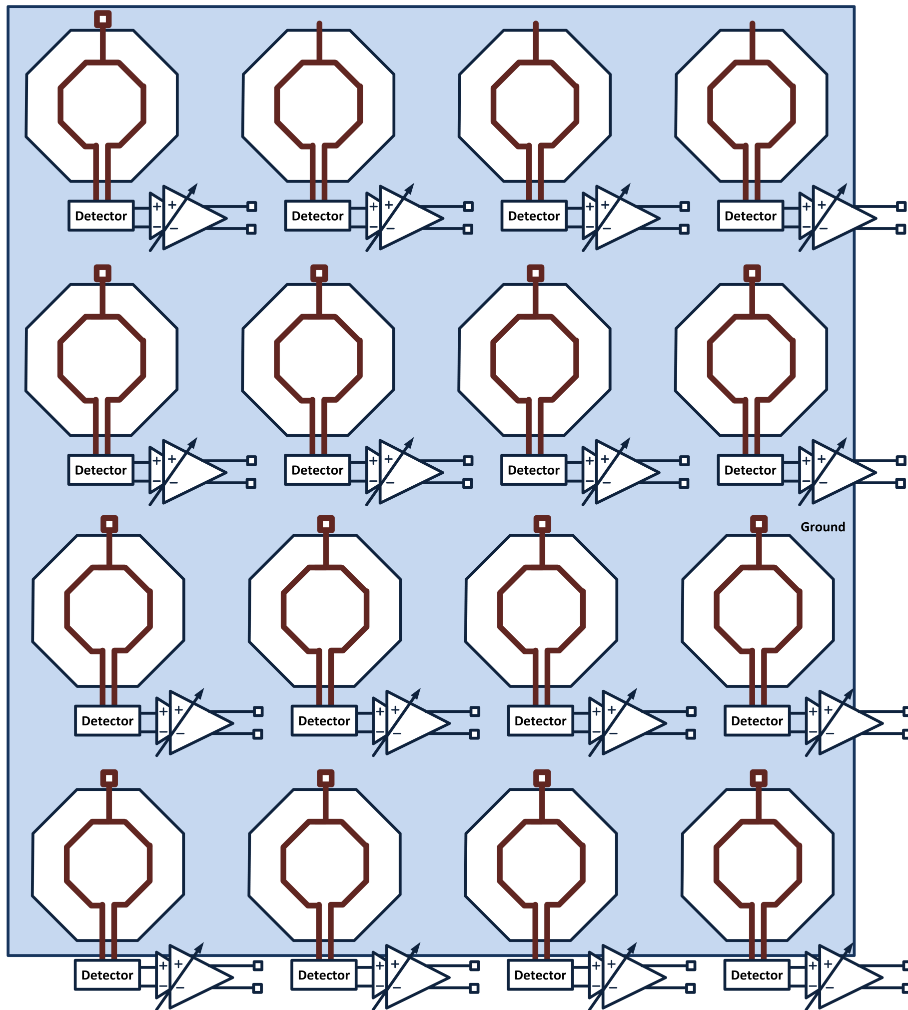

Figure 7.3: Architecture of the 4x4 pixel imager chip.

($\sim 2h = \lambda_{si}$). However, this also maximizes radiation from the front-side of the die due to phase coherence between A_{f1}, A_{f2}, A_{f3}, etc., implying the the gain of the antenna gets halved [72]. In order to block front-side radiation, a ground plane with an aperture opening is placed on metal 1, as shown in Fig. 7.5. Now, the reflected waves at the ground plane, suffer an additional phase difference of π, as shown in Fig. 7.5. Therefore for a substrate of $h \sim (2n-1)\lambda_{si}/2, n \subset I^{+}$, the secondary sources at the backside (A_{b1}, A_{b2}, A_{b3}, etc.) are in phase, while the front-side (A_{f1}, A_{f2}, A_{f3}, etc.) will be out-of-phase.

The radiation properties of the grounded and ungrounded loop antennas are shown in Fig. 7.6. The substrate height is optimized for efficiency, which implies h=150 μm in the absence of ground plane and h=220 μm in the presence of ground plane at an operating frequency of 300 GHz. As explained previously, for the ungrounded substrate, we see equal directivity in the front and backside lobes (12.5 dBi), while for the die with the ground plane, the front-side radiation is suppressed by almost 6 dBi compared to the back-side radiation (16.8 dBi). Due to the absence of the ground lane, the substrate mode configuration also changes. For the ungrounded substrate, the cut-off frequencies for both TE_0 and TM_0 modes are zero. It can be shown that for the substrate height of h=150 μm that maximizes efficiency, the only modes existing are the TM_0 and TE_0, each with wavelengths of 500 μm, of which TM_0 is the dominant mode [72]. While, the TE_0 mode gets partially canceled due to the current configuration in a full-wavelength loop (though much lesser than the grounded case, since 2a$\sim$ $\lambda_{TE0}/4$ instead of 2a$\sim$ $\lambda_{TE0}/2$), the TM_0 mode of the different antennas in the array add in phase and come out from the side of the chip, which is demonstrated by the presence of strong sidelobes along the x direction in the x-y plane, as illustrated in Fig. 7.6. We can compare this with the case, where the loop has a ground plane with an aperture. In this case, there are three modes existing, TM_0 (λ_{TM0}=309 μm), TE_0 (λ_{TE0}=346 μm) and TM_0 (λ_{TM0}=782 μm), of which TM_1 and TE_0 are the dominant modes, as explained in Chapter 4. TE_0 mode gets partially canceled with the full-wavelength loop, and the spacing in the array corresponds to nearly $\lambda_{TM1}/2$ which suppresses TM_1. The resultant pattern is much cleaner and sharper as also seen in Fig. 7.6.

The ground loop diameter is adjusted for maximizing the responsivity of the detector

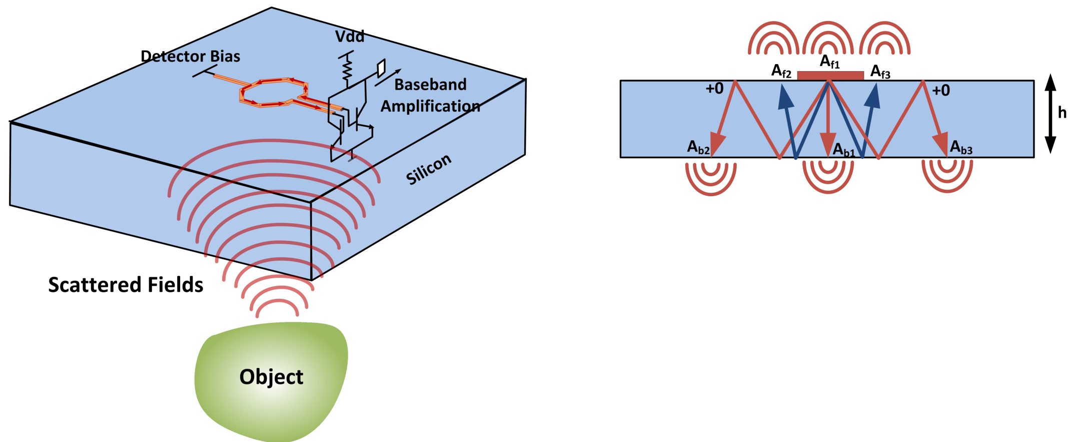

Figure 7.4: A full-wavelength loop antenna on an ungrounded substrate maximizes efficiency when front-side and back-side radiated power at the boresight are the same.

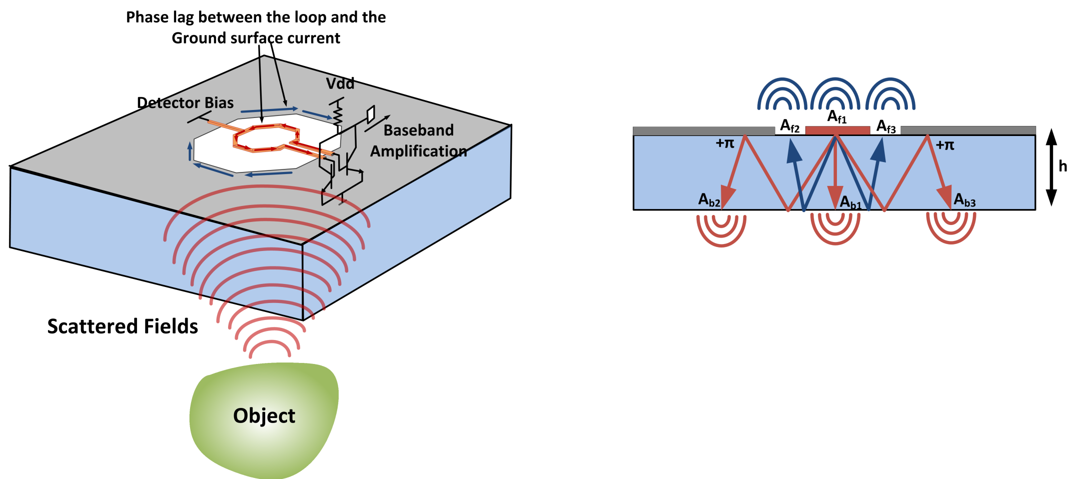

Figure 7.5: A ground plane with an aperture suppresses front-side radiation and increases gain, and therefore responsivity, from backside radiation.

from backside radiation. The ground aperture diameter results in a return current near the edge of the aperture, which is phase-lagged with respect to the radiation-induced current distribution on the loop. This can change the overall input impedance of the resonant antenna. A series inductance is provided by two extended arm lengths, 100 μm each, that allow near-conjugate match with the differential input of the detector for maximum radiative power transfer. The entire array structure of of 16 antennas with ground plane apertures in a lossy 2.5 mm $\times$ 2.5 mm lossy silicon substrate, is simulated in HFSS, to capture the coupling the the finite of the substrates. However, the differential input impedance of the antenna at the edges (Z_{in}=32+j59Ω) were almost same as the ones in the middle of the array Z_{in}=33.5+j58Ω.

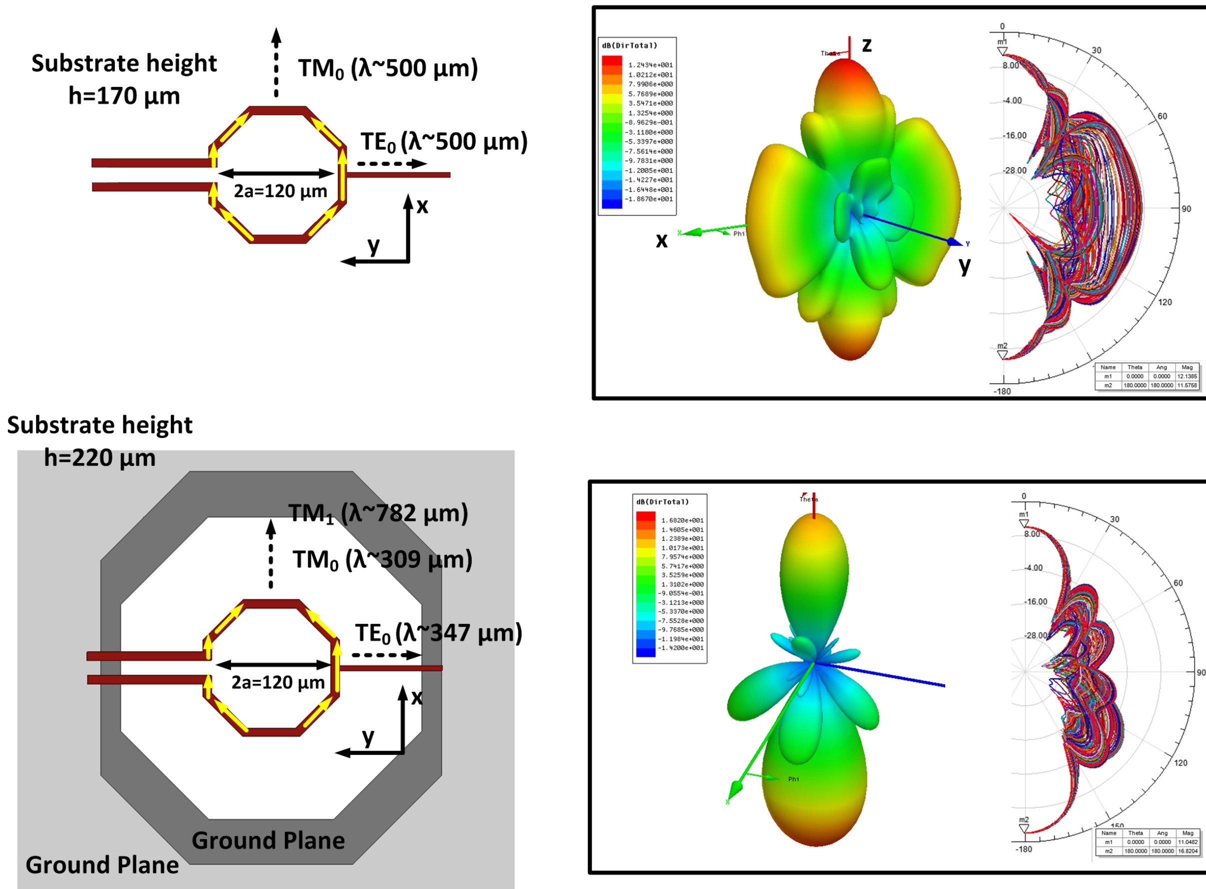

Figure 7.6: Comparison of radiation patterns in the absence and presence of the ground plane with aperture opening.

The differential ends of the antenna are connected to the detector, as shown in Fig. 7.7.

The front-end is based on square-law detection, which converts the incoming THz radiation into a change in output DC voltage. The detector consists of a differential SiGe pair, where the load resistance is attached to the common mode point. The biasing and the load are optimized for lowest noise performance. A low-cost low-power THz imager should have high responsivity and low NEP without the need for additional custom corrective measures. A simple analysis reveals that for 100 nW of THz power captured by the effective antenna aperture on-chip a SNR greater than 30 dB can be achieved with a 10 ms integration time if NEP is less than 10 pW/$\sqrt{Hz}$. The die photo and the PCB is shown in Fig. 7.8.

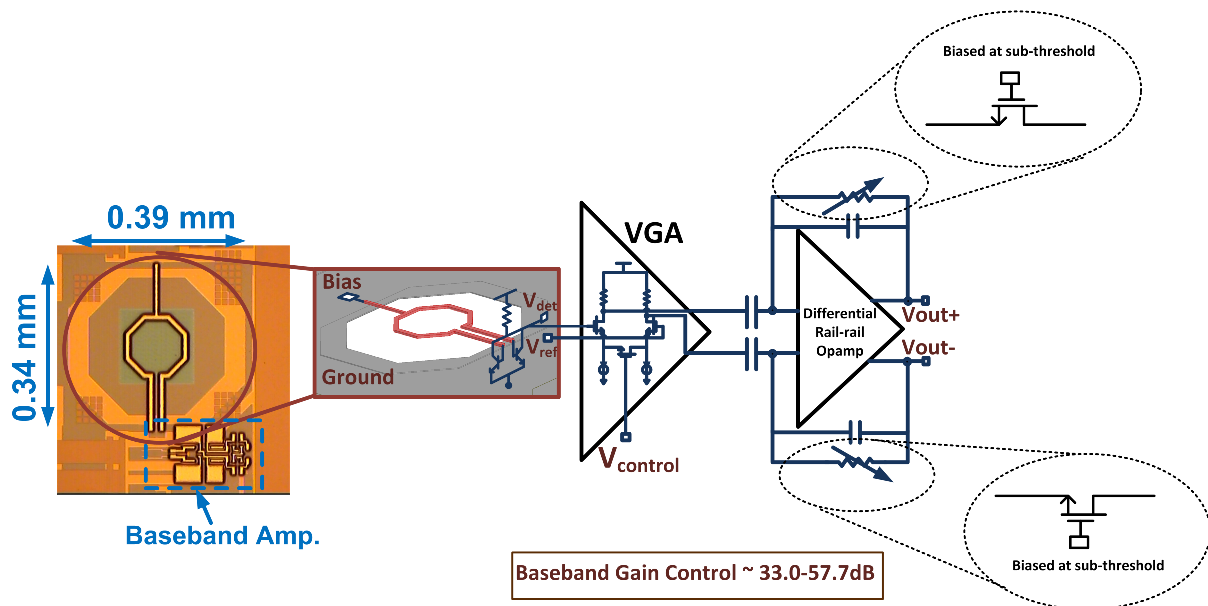

Figure 7.7: THz imaging receiver in silicon with on-chip antenna, front-end detector and baseband amplification with 24.7dB tuning range

7.2 Measurement Results at Room Temperature

The baseband is measured as a breakout structure. The results are shown in Fig. 7.9. The baseband has a peak voltage gain of 57.7 dB with a 3 dB bandwidth from 100 Hz–100 KHz. The gain can be varied from 33–57.7 dB using the VGA control.

The experimental set up for responsivity and NEP measurements is shown in Fig. 7.10. All measurements were done at room temperature. A custom WR-3 source, consisting of

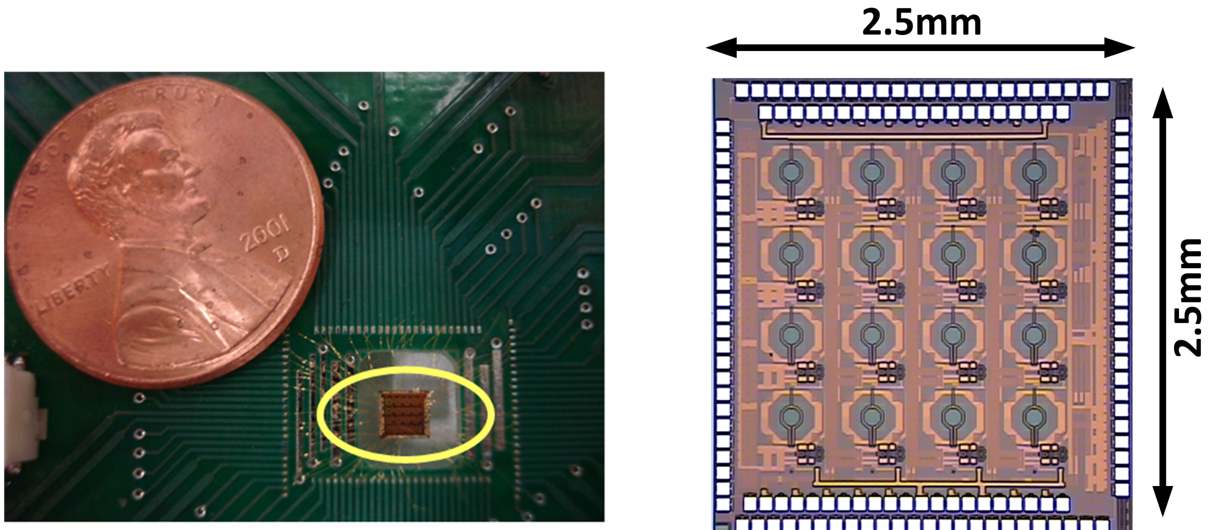

Figure 7.8: Die micrograph and PCB of the THz imager.

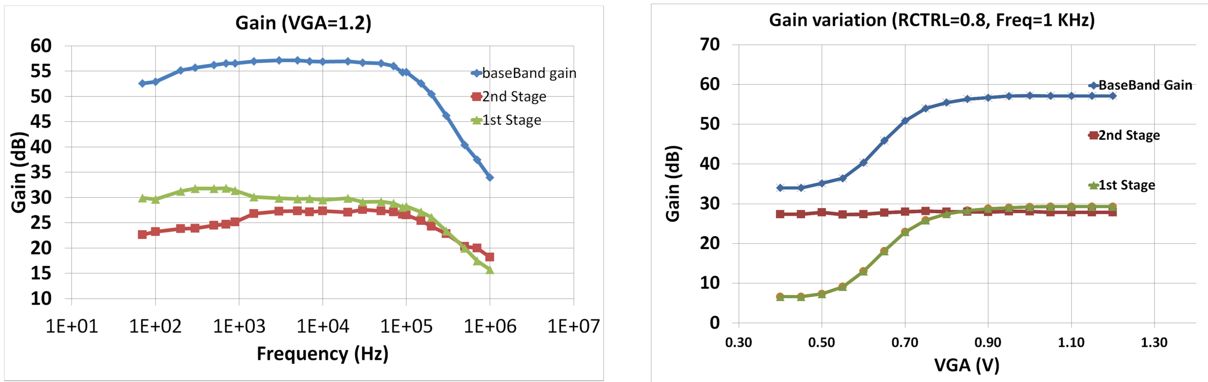

Figure 7.9: Frequency response of the baseband amplification showing a bandpass response which rejects DC offsets and low-frequency drifts. The gain variation with the VGA settings is also shown.

a chain of multipliers from Virginia Diodes, Inc. [35] is used as the THz source with a 25 dB standard gain WR-3 horn antenna. The radiation is captured by the chip from the backside of the substrate where it has the highest directivity. Responsivity is characterized in the far-field of a WR-3 source and the noise profile is measured using a spectrum analyzer, buffered by an external LNA. The THz radiation was chopped at a frequency of 5 KHz and the baseband output was observed in an oscilloscope. The whole setup was calibrated with an Erickson power meter [115]. The receiver was irradiated with measured 390 nW and 160 nW of power at 0.25 THz and 0.30 THz, respectively, at a far-field distance of 50 mm. The measured responsivity and NEP of the receiver in the WR-3 band is shown in Fig. 7.10. The receiver achieves a peak responsivity of 2.6 MV/W and 700 kV/W, and a NEP of 8.7 pW/$\sqrt{Hz}$ and 32.4 pW/$\sqrt{Hz}$ at 0.25 THz and 0.3 THz, respectively [62]. To the best of out knowledge, this is the lowest reported NEP in silicon at THz frequencies, without using expensive postprocessing or external silicon lens. Simulations predict that substrate thickness optimization through back-lapping can achieve a NEP of near 4 pW/$\sqrt{Hz}$, comparable to typical noise performance achieved in cooled microbolometers [123]. The entire chip draws approximately 93 mW of power. Each detector draws less than 1 mW of quiescent DC power.

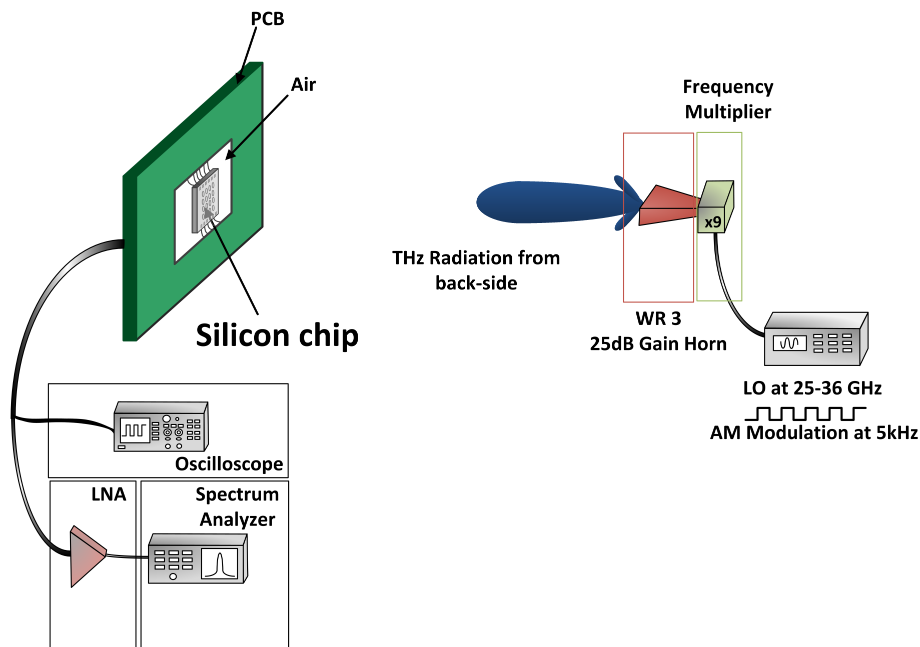

Figure 7.10: Set-up for measuring responsivity and NEP of the imager.

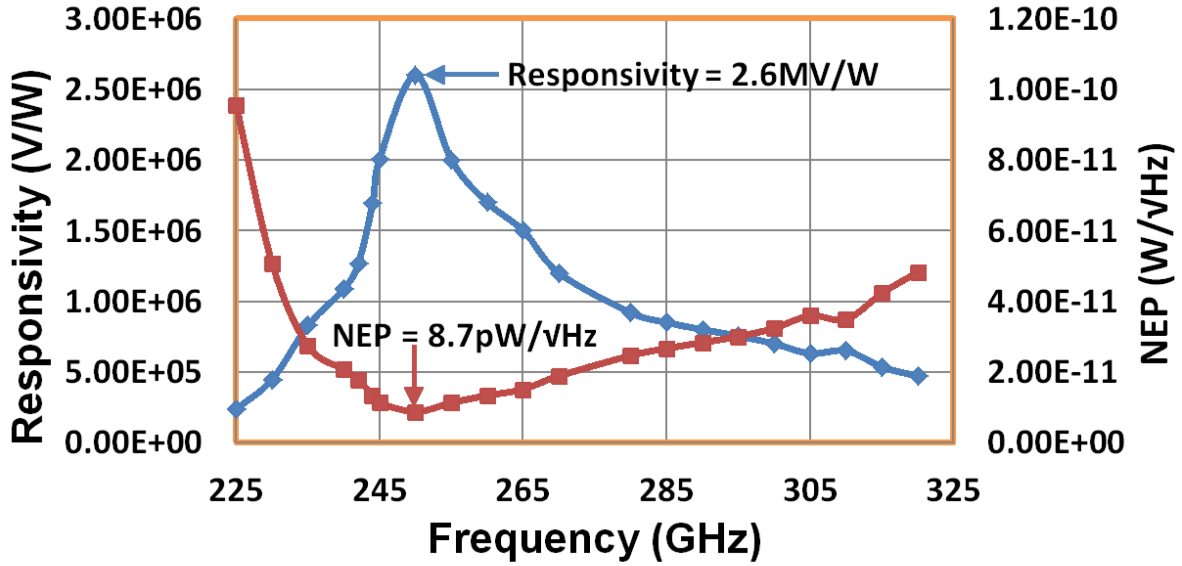

Figure 7.11: Measured responsivity and NEP of one pixel in the receiver.

The measured responsivities R_v of the 16 pixels across the chip, at 0.26 THz, for a chopping frequency of 5 KHz is shown in Fig. 7.12. The plot shows negligible variation across the 16 pixels of the chip. The responsivity variation across the chip occurs due to mismatches and also due to edge effects of the silicon die on the antenna response. The measured NEP of the 16 pixels are shown in Fig. 7.12, showing the maximum NEP to be below 10 pW/$\sqrt{Hz}$ for all pixels reaching a minimum of 6.8 pW/$\sqrt{Hz}$. Responsivity of a single pixel peaks at a frequency of 0.26 THz of the incoming radiation. The results indicate almost 10x improvement in sensitivity over previous results near 0.3 THz [122] in an un-thinned 250 μm bulk substrate with 11-16 Ω-cm. This corresponds to a 10x increase in acquisition speed at a modest power dissipation of 6 mW/pixel, which include baseband stages with variable gain from 33–57.7 dB, leading to higher SNR and better contrast in images, particularly important for biological specimens which have low-contrast variations.

Fig. 7.13 shows a measurement setup for imaging the focused THz beam to a diffraction limited spot. The radiation is again captured from the backside of the silicon die and the output is measured by a locking amplifier synchronized with the chopping signal. The PCB is connected to a motorized translational stage. The chip is raster scanned over the focal

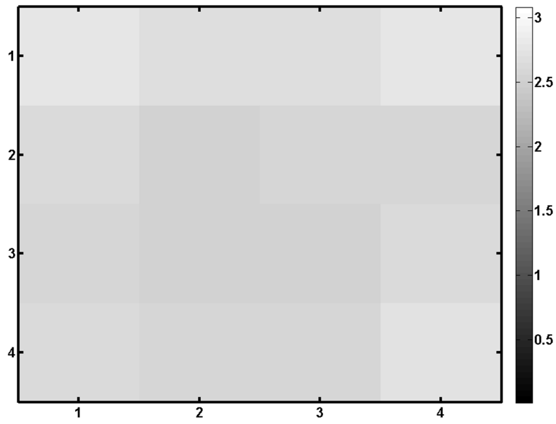

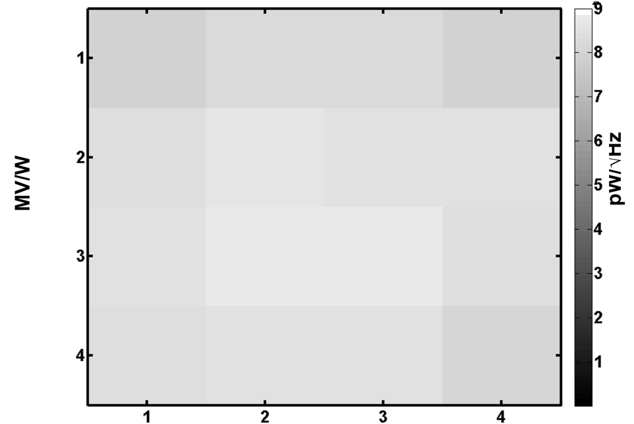

Variation of Responsivity across 16 pixels at 0.25 THz

Variation of NEP across 16 pixels at 0.25 THz

Figure 7.12: Responsivity and NEP measurements of 16 pixels at 0.25 THz showing sub-10 pW/$\sqrt{Hz}$ for all pixels.

plane of 5 mm × 5 mm, and the output voltage is plotted in a 2D plane. Thereby, the constructed image of the beam over the focal plane is shown in Fig. 7.14. The diffraction limited Gaussian focus spot for a 4-lens system at 0.26 THz , as shown in Fig. 7.14, follows closely the theoretical prediction. The full-width at half-maximum of the Gaussian beam is shown to be approximately 0.93 mm at 0.26 THz.

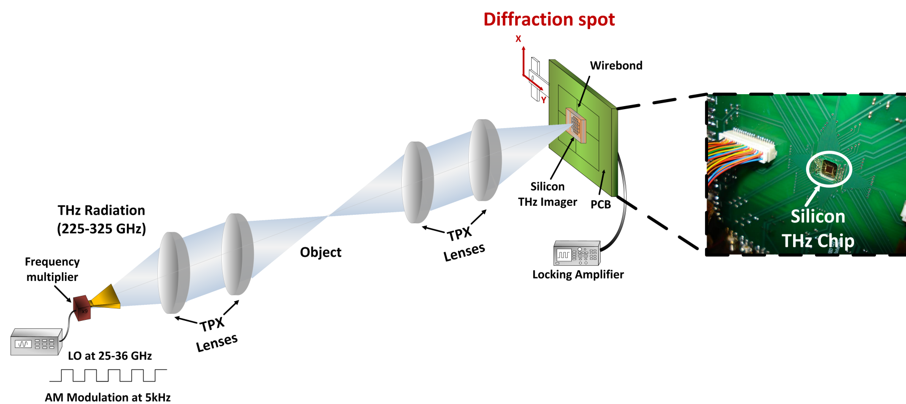

Figure 7.13: Measurement setup for focusing emitted THz beam to a diffraction-limited spot size on the focal plane which is imaged by the THz receiver by raster-scanning

Before proceeding to imaging, we demonstrate the sensitivity of the detector by demonstrating capability of imaging, even when the signal power is spread over a plane. This is

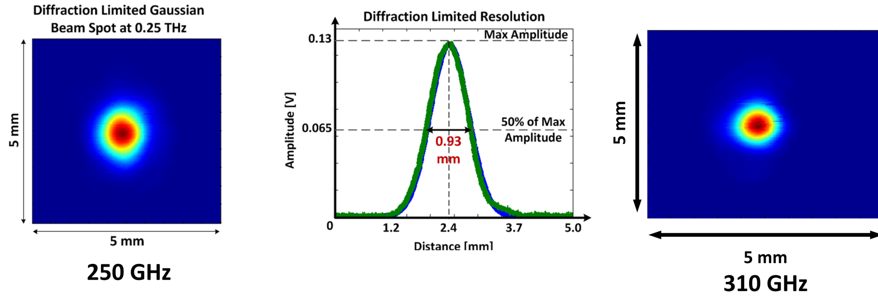

Figure 7.14: Measured spot size of the focused beam at 0.26 THz on the focal plane in transmission-mode setup.

shown in the demonstration of a 4f correlator, where we scan the imager across the Fourier transform plane of the object as shown in Fig. 7.15. The sensitivity of the imager allows us to obtain a high-SNR image of the Fourier transform of the object (made of three metallic slits) even though the power is spread over the imaging plane and not confined to a spot.

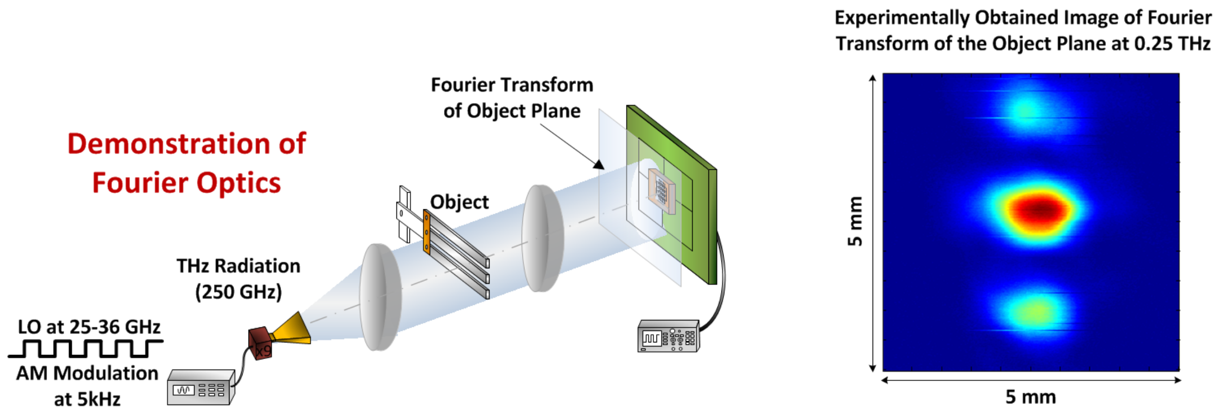

Figure 7.15: Demonstration of Fourier transform of the object on the focus plane of the lens at 0.26 THz.

We will now demonstrate imaging modalities and examples with the silicon-based chip. Transmission-mode and reflection-mode imaging reveal different properties of the specimen under investigation and offer different contrasting mechanisms. The transmission-based imaging set-up is shown in Fig. 7.16, where a THz source with output power of 0.8 mW at 0.26 THz has been used. A focused THz spot is irradiated on the object, which is scanned on the focal plane. The transmitted radiation is again captured from the backside of the silicon die and the output is measured by a locking amplifier synchronized with the chopping signal. The setup is aligned with a diode laser.

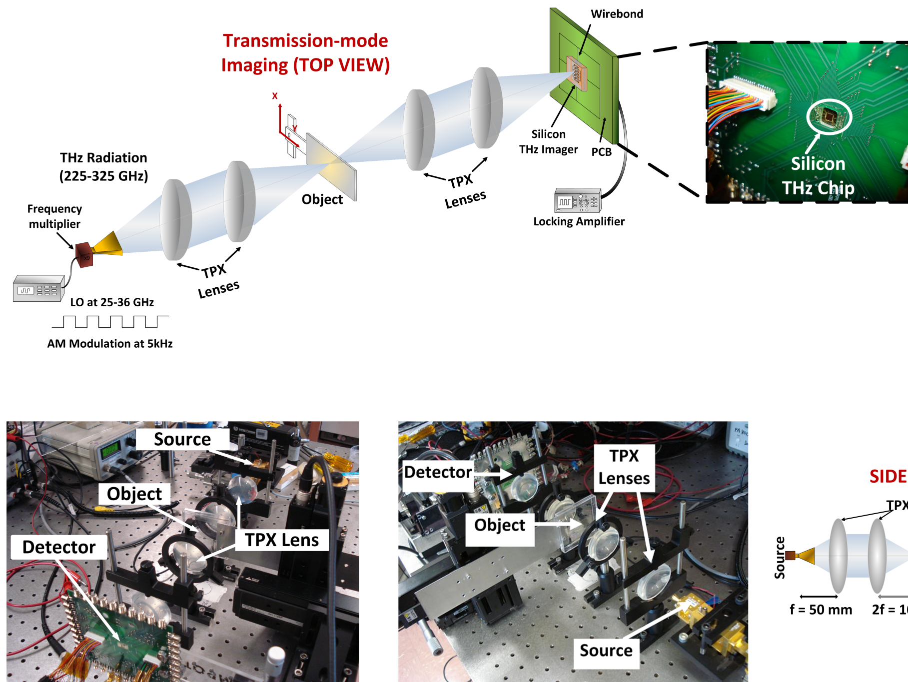

Figure 7.16: Transmission-mode imaging setup.

Fig. 7.17 and Fig. 7.18 show imaging results with various specimens under the transmission modes of imaging. THz waves can penetrate through plastic, paper ans packaging materials, all of which are demonstrated in Fig. 7.17 and Fig. 7.18. The electronic components inside a package or a drill bit inside a thick plastic capsule can be identified without opening the package. Fig. 7.17 also illustrates difference of interaction with scatterers of various sizes compared to the wavelength producing variant contrast at THz frequencies (sugar packets with fine and coarse grained sugar). This can be exploited for nondestructive quality control among other things. The image of the key inside the opaque envelope (inside can be only seen by holding against strong light) shows resolution nearing 1 mm, while the RFID chip and the loop antenna inside the conference ID card shows how far technology in conferences has come since the days of paper badges, not so long ago!

THz radiation is very sensitive to water absorption. This is one of the key features which is exploited in the contrast of healthy tissues against tumorous sites, where differences in water content and tissue density is purported to be a contrasting agent [8], [13], [23], [24]. Fig. 7.19 shows the contrast in the transmissive power of THz waves through a normal

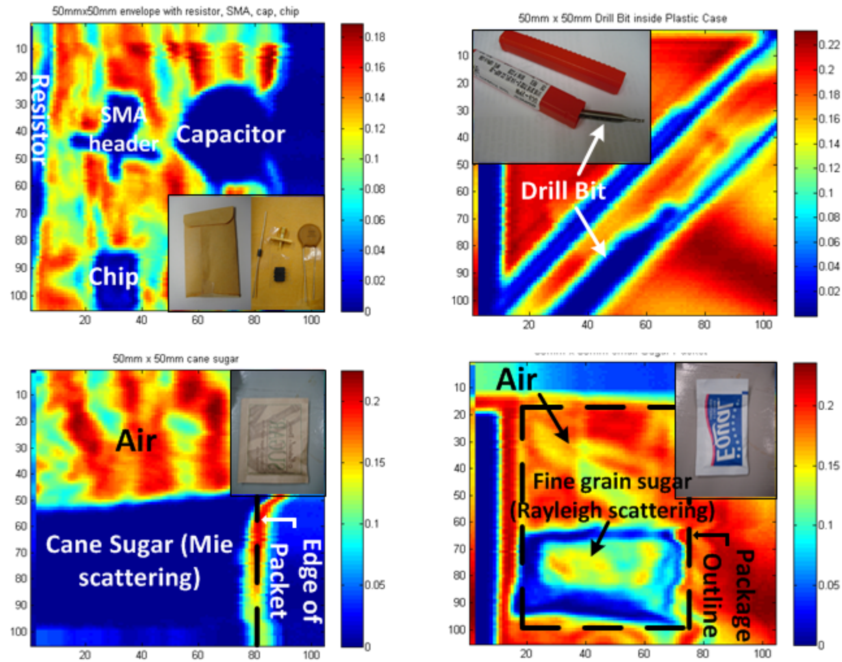

Figure 7.17: Transmission line imaging examples showing penetrative property of THz through paper, plastic and demonstrating difference of interaction with scatterers of various sizes compared to the wavelength (sugar packets with fine and coarse grained sugar).

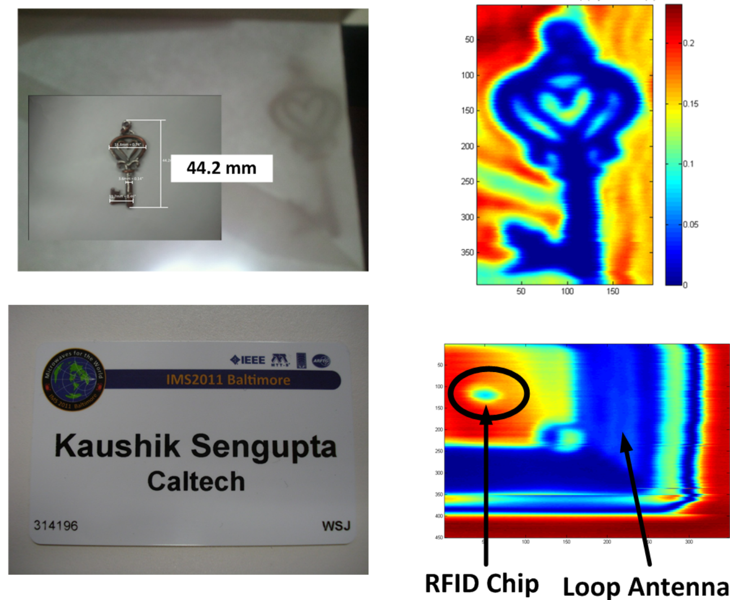

Figure 7.18: Transmission line imaging examples showing near-1-mm resolution, while the RFID chip and the loop antenna inside the conference ID card shows how far technology in conferences has come since the days of paper badges, not so long ago!

leaf with its regular water content and a dry leaf which hardly absorbs any radiation. The difference in absorption is the primary contrast mechanism in this mode, which is shown in the more than 10 dB of transmission difference between adipose and muscle in a sample of chicken tissue in Fig. 7.20.

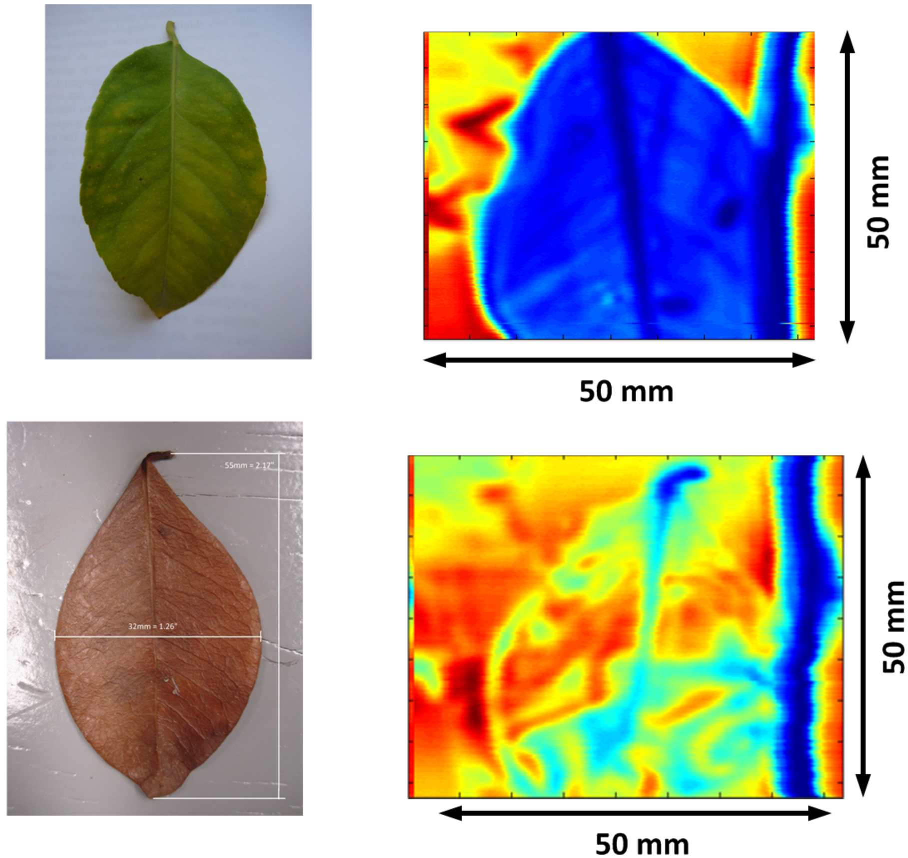

Figure 7.19: Contrast shown between dry and wet leaf due to absorption of THz signals by water.

THz imaging could also be a promising tool in noninvasive diagnostics, as different materials have different dielectric, absorptive and reflective properties. While in a transmission-mode imaging, only the transmitted power is captured, while reflected and absorbed power is lost, in a reflection-based imaging setting, only reflective power is capture while transmitted and absorbed power is lost. Reflection imaging can carry depth information and contrast between bones, muscles and cartilages from parts of a mouse leg is seen due to the differences in its dielectric properties. The setup is shown in Fig. 7.21. Due the angle of reflection, the gaussian spot is a little distorted, as shown in Fig. 7.22. This is also observed in the captured

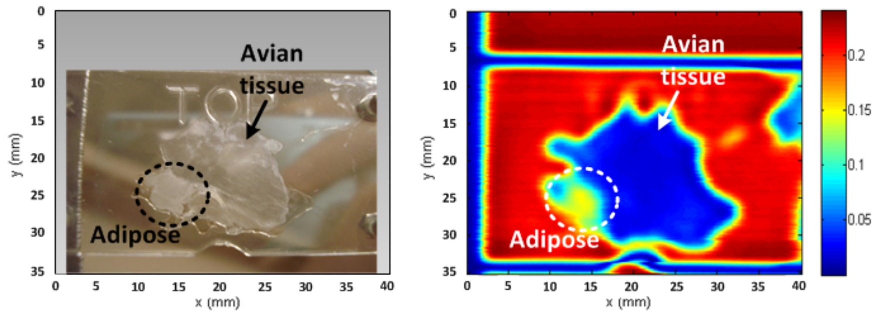

Figure 7.20: Transmission difference between adipose and muscle in a sample of chicken tissue at 0.26 THz.

image, illustrated in Fig. 7.22. Contrast in a biological specimen in reflection-mode imaging is demonstrated in Fig. 7.23. It can be observed that there is an appreciable contrast among bones, cartilages and muscles in of mouse leg, which is fixed on a glass slide, demonstrating feasibility of noninvasive imaging at THz frequencies.

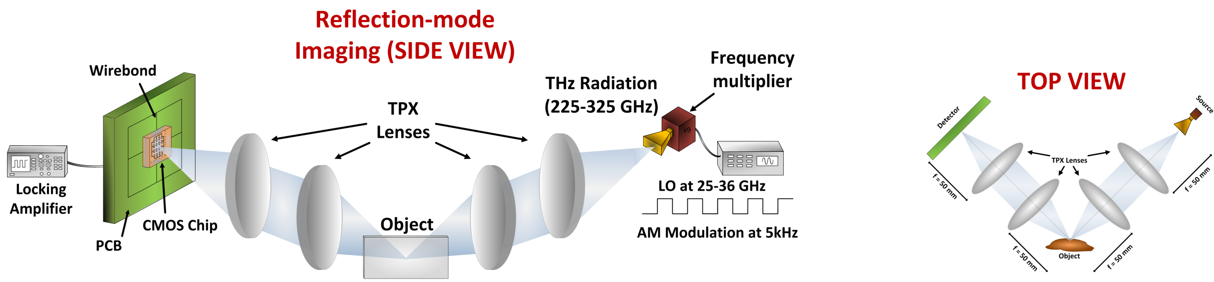

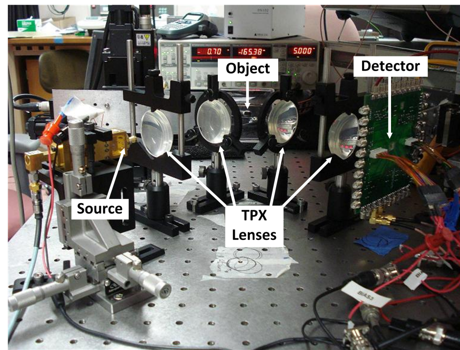

Figure 7.21: Reflection-mode imaging set-up.

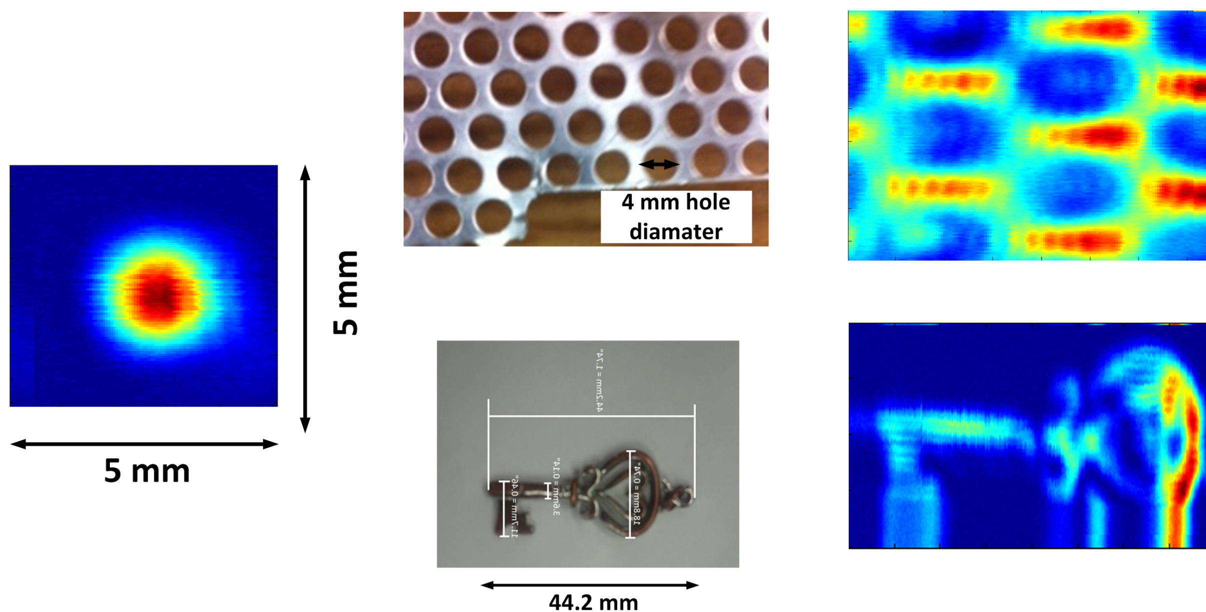

Figure 7.22: Reflection-based imaging examples.

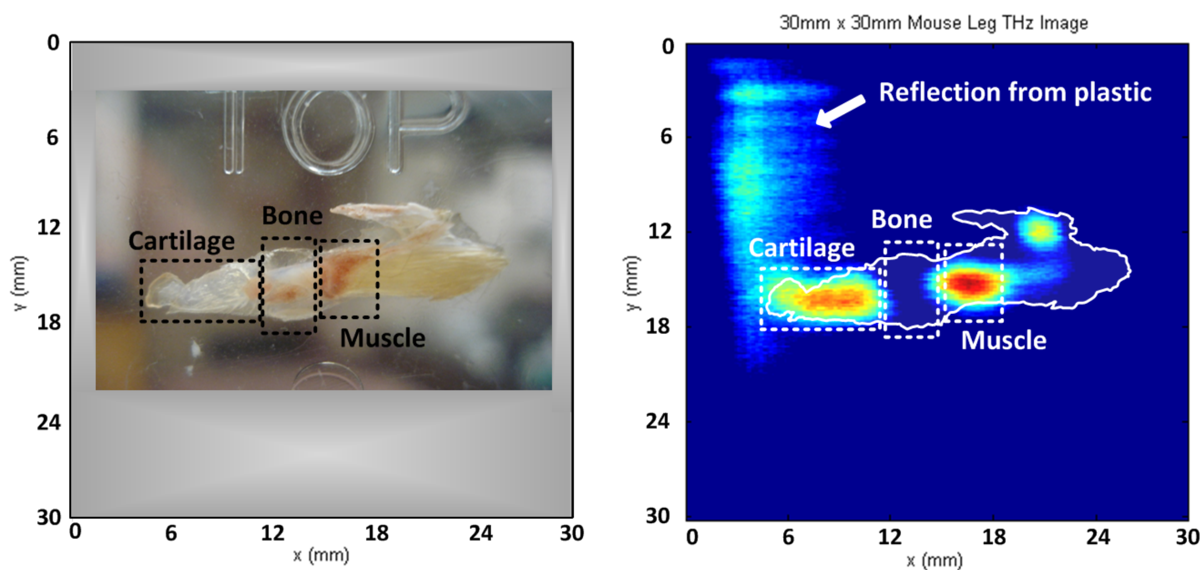

Figure 7.23: Contrast between bones, cartilages and muscles in of mouse leg, which is fixed on a glass slide, demonstrating feasibility of noninvasive imaging at THz frequencies.

7.3 All-Silicon THz Imaging

The previous examples showed using silicon-based THz detector array chip and a custom THz source. We, then, replaced the source with the CMOS chip reported in [57] and discussed in details in Chapter 5, which consists of a 2x2 array of free-running, mutually injection locked Distributed Active Radiators near 0.29 THz. This constitutes a fully integrated silicon-based THz imaging system. The imaging setup is shown in Fig. 7.24. The CMOS free-running frequency is near 0.29 THz and the radiation is chopped at a frequency of 5 KHz by modulating the supply voltage. The diffraction-limited spot of the CMOS source, as measured by the BiCMOS chip, is shown in Fig. 7.25. The spot size is near 1 mm diameter. The two PCB boards are then brought into each other's near field and the field profile is scanned again by the detector chip. The result is also shown in Fig. 7.25. Broadside spot and side-resonance fields due to the parallel plate waveguide effect can be seen in the field profile. We also demonstrate the first ever THz imaging demonstrated with a CMOS source at room temperature with no use of compound semiconductors or optics-based active devices for either signal generation or detection. This demonstration is shown in Fig. 7.26.

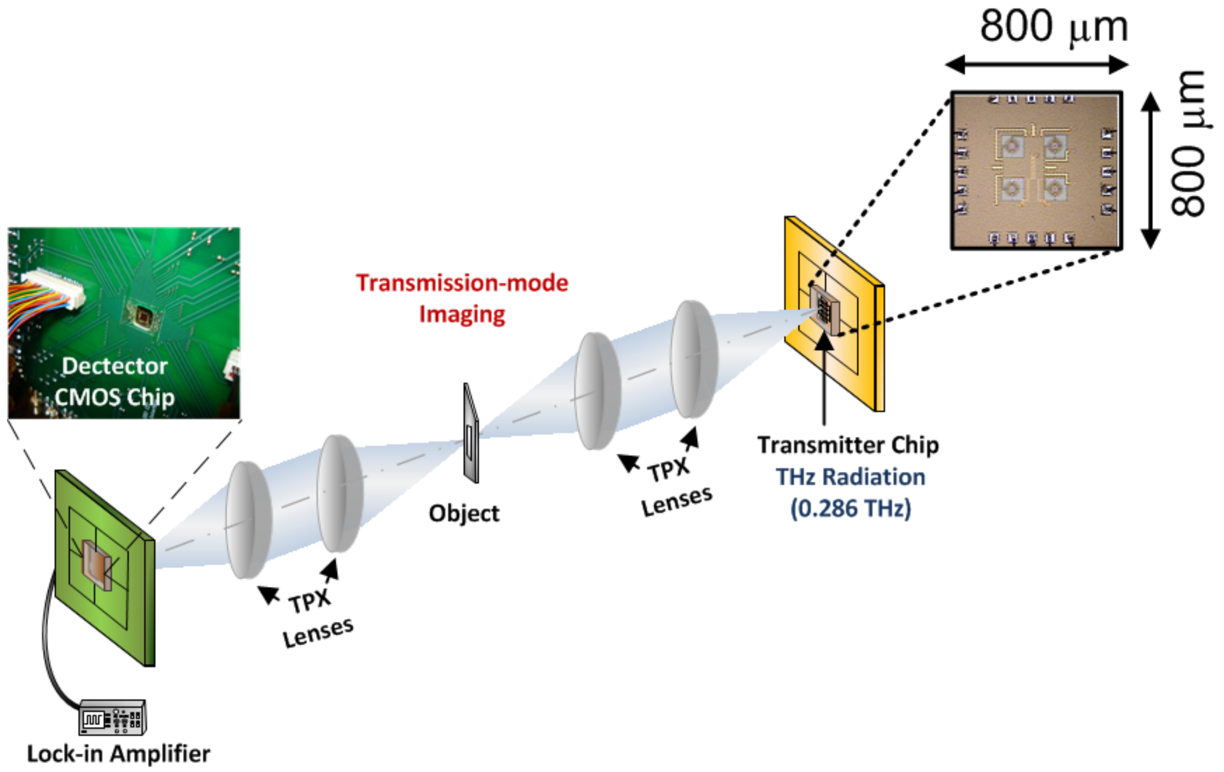

Figure 7.24: An all-silicon THz imaging setup with 16-pixel BiCMOS detector array and 2x2 array of locked CMOS DARs near 0.29 THz.

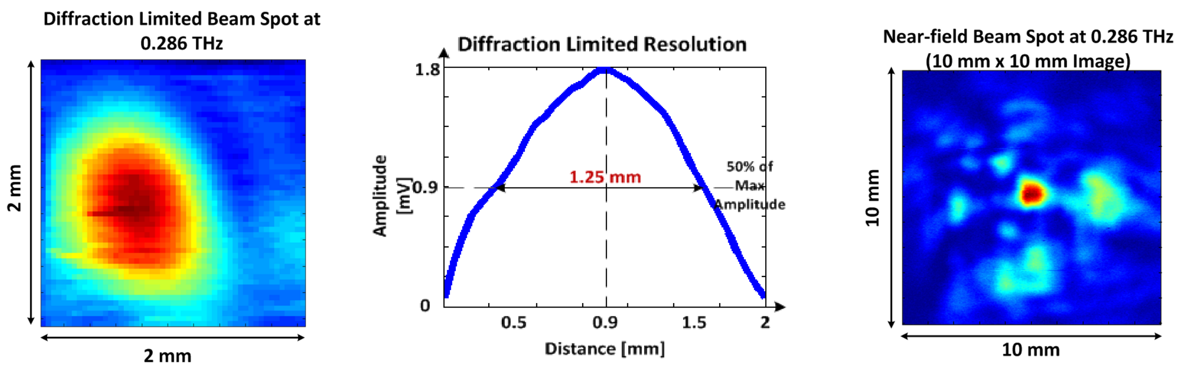

Figure 7.25: Diffraction-limited spot radiated by the CMOS source and imaged by the silicon detector array. The right figure shows the near-field profile, obtained by scanning the detector array chip, when the two PCBs with the silicon chips are brought into each other's near-fields.

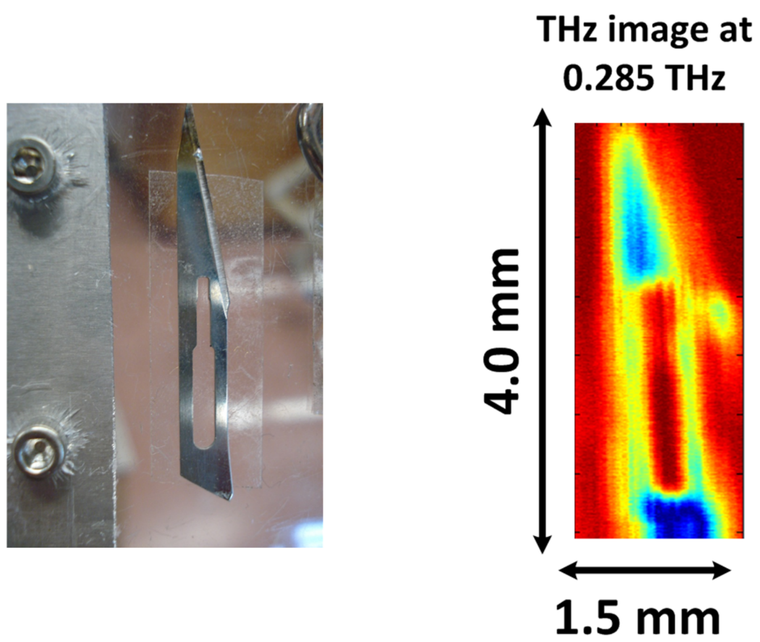

Figure 7.26: The first THz imaging demonstrated with a CMOS source.

Chapter 8

Robust and Self-Healing High-Frequency Integrated Systems

In Chapters 3-7, we have extensively discussed methods and techniques to push silicon technology into the terahertz frequency regime. While terahertz technology will take some more time to mature, there has been a surge of interest in research as well as in commercial viabilities of integrated silicon technology at slightly lower frequencies, namely in the millimeter wave part of the spectrum. The application span ranges from high-speed wireless communication to automotive radars, satellite communication, security and medical imaging. The possibility of integrating billions of transistors in silicon and sophisticated back-end digital processing with a mm-Wave front-end, all integrated in a single die, can be leveraged to make robust, low-cost, high-yield fully integrated systems at mm-Wave frequencies. This frequency outreach has been possible, in some ways, because of scaling that results in increasing f_t/f_{max} and high-frequency performance. However with scaling, as channel lengthshave reached atomic dimensions (22 nm, being state-of-the-art as of now), the oxide is only a few atoms thick and there are only countable number of dopant atoms in the channel (Fig. 8.1). As a result, atomistic and quantum-mechanical limitations have strong effects of transistor performances. Moreover, process variations, temperature significantly affect predictability in performance, both at the circuit and system level. Over many fabrication runs, therefore, yield may significantly go down, if designs are not oriented to address the challenges. At mm-wave frequencies, when performance margins, are small, the effects are more prominent.

A good exposition on CMOS variaitons and performance effects, albeit in the digital domain, can be found in [132].

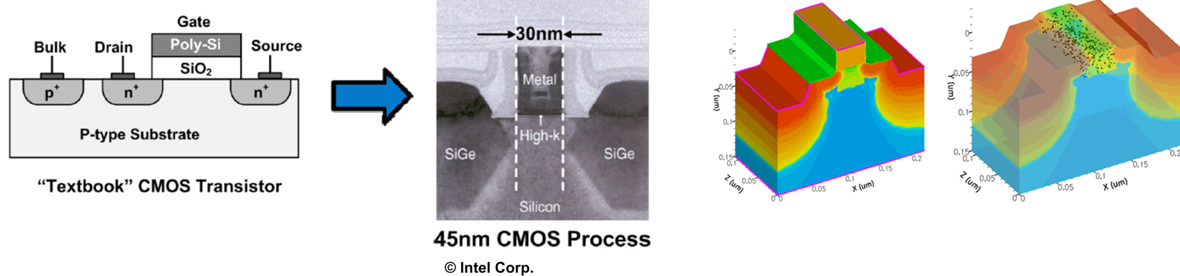

Figure 8.1: State-of-the-art transistor looks no longer like a textbook transistor. With scaling towards nanometer dimensions, fluctuations in process variations such as line edge roughness, number of dopant atoms can cause significant variations over predictability of transistor performance.

Added to it, the device models provided by the standard foundries are generally not validated in mm-wave frequencies because of the cost and expertise required and also since CMOS is yet to enter big into the commercial mm-wave market, the effort and expense does not justify the cost. As discussed before, the performance margin in mm-wave design is very small. For example, a 30 fF parasitic capacitance contributes to a reactance of j56 Ω at 94 GHz and therefore can completely detune the matching network unless the smallest of the parasitics is accurately modeled and accounted for. A design which relies on accuracy of device and passive modeling, therefore requires fabrication of test structures, custom active device modeling and several iterative runs (and therefore added expense) even which fails to guarantee optimum performance due to process variations. Finally, aging effects and environmental variations such as load mismatch and temperature can significantly degrade the performance of mm-wave front-ends, particularly the power amplifiers (PAs), where both output power and efficiency are strongly dependent on process and environmental parameters [133].

All these processes combine their effects to reduce the yield to an unacceptably low percentage which hurts its commercial viabilities. Digital system designs use redundancy as one method of overcoming transistor failures. In RF and mm-wave range, this is too power and area inefficient a process. One cannot really have a backup power amplifier or PLL, specially in a low-cost consumer product, without taking a hit at the cost, area

and power consumption. One way to work around the problem is to design conservatively to guarantee performance at all corners specially to meet stringent defense requirements or to use architecture which are inherently less prone to parasitics (wideband design for example). However this either comes at the cost of higher power or chip area or one needs to throw away transistor performance resulting in suboptimal performance. This approach completely overlooks the fundamental advantages of CMOS integration which comes with almost limitless computational abilities in digital domain and where transistor comes almost free of cost. In order to mitigate these issues, a systematic approach to the problem, which we call self-healing [135], [136], [137], takes advantage of the computing capabilities in the digital domain where transistors come almost free of cost. Instead of seeking to confront individual problems and devising custom solutions for them, self-healing mitigates process variations, modeling inaccuracies and environmental changes by constantly monitoring the system performance and employing subsequent on-chip correcting mechanisms and actuation controlled by optimization algorithms, running globally as well as locally. This is illustrated in Fig. 8.2, where onchip sensors characterize the system and onchip actuators optimize the performance, controlled by an onchip control loop.

In this Chapter, we will briefly discuss our collaborative work, with colleagues Steven Bowers and Kaushik Dasgupta, on the first self-healing mm-Wave power amplifier. The PA, designed at 28 GHz, has integrated low overhead sensors for on-chip characterization, actuators to reconfigure the parameters of the circuit on the fly, Analag-to-digital converters, Digital-to-analog converters, and an onchip communication link among all the components which is controlled by an on-chip digital core, that is also responsible for the self-healing algorithm. I was responsible for the design of the sensors and the digital core.

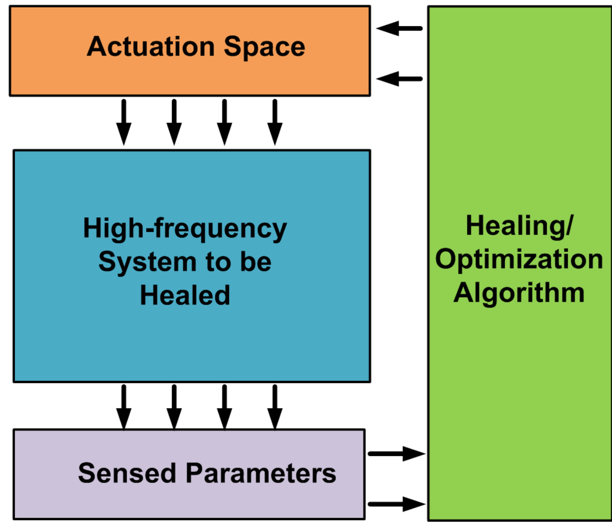

Figure 8.2: A mixed-signal feedback system that can characterize the performance of the system on-chip and has an actuation space to reconfigure the system to optimize performance over a range of random and systematic variations.

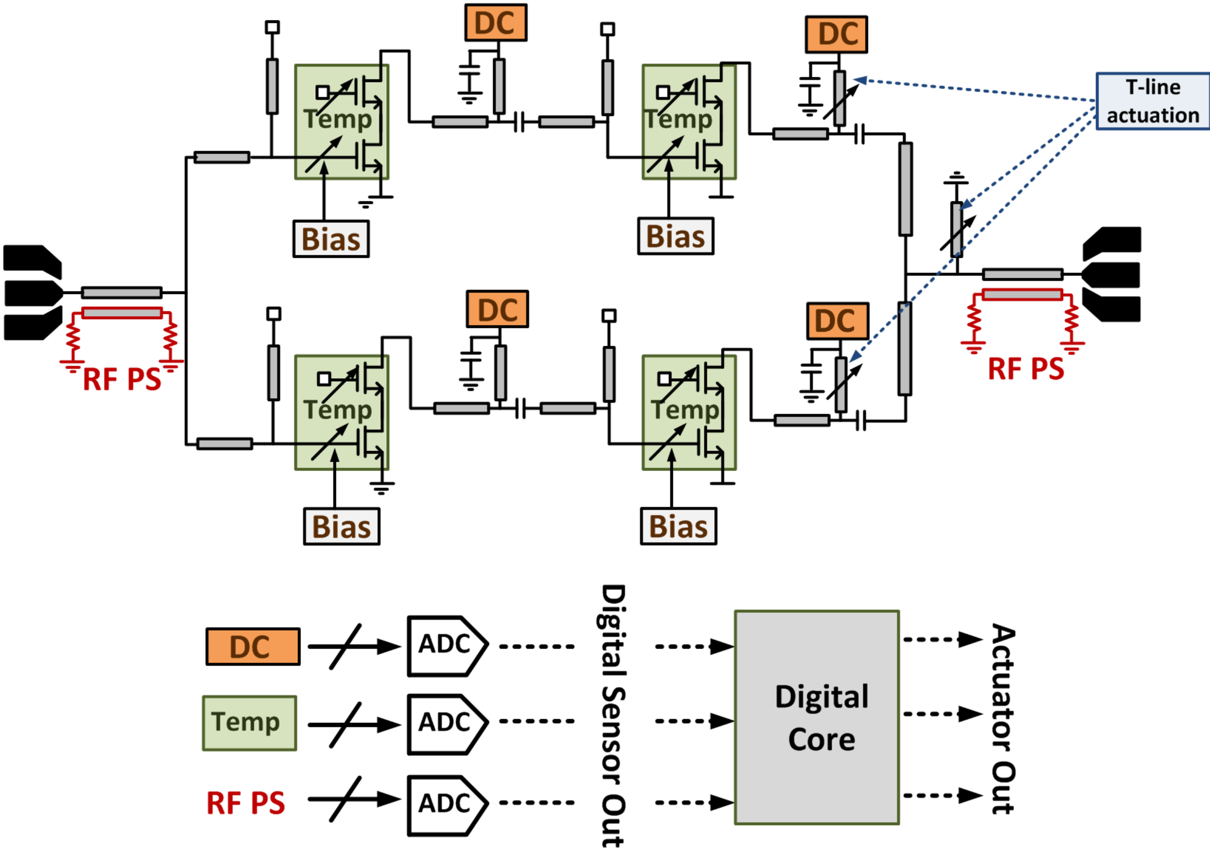

Figure 8.3: A transmission line based mm-Wave power amplifier with 2-to-1 combiner at 28 GHz with various sensors, ADC, actuators and digital core for on-chip sensing and actuation.

8.1 Sensors

8.1.1 DC Current Sensors

It is challenging to measure the DC drawn by a high power high frequency PA during operation. Mirroring the PA current through another transistor would require minimizing mismatches through careful layout techniques which, in turn, would increase interconnect lengths and parasitics, degrading performance at high frequencies. Additionally, since the current sensor will be operating in deep-triode to maintain efficiency, current mirrors need their terminal voltages accurately matched for high-fidelity current sensing. This is challenging to ensure over the range of actuation currents [138].

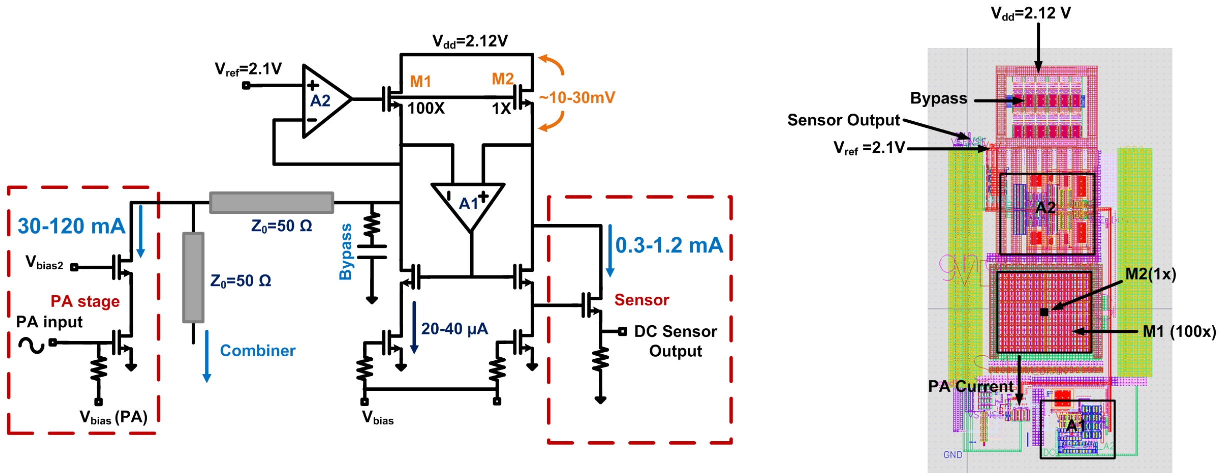

Figure 8.4: Schematic and layout of the DC sensor of the PA. The current through PA is mirrored by a factor of 100 and sensed, while accomplishing voltage regulation with a headroom of only 10-30 mV.

In order to mirror the current accurately without sacrificing efficiency, overhead transistors are kept in deep triode with Vds ranging between 10-30 mV as shown in Fig. 8.4 under a 2.12V supply. The current though a PA is scaled down by a factor of 100x and mirrored through matched transistors M1 and M2 as shown in Fig. 8.4. The op-amp A1 forces the source nodes of M1 and M2 to be at the same voltage for accurate mirroring of the current, while the sensor current through M2 is converted into the sensor DC voltage as shown in Fig. 8.4 [138]. The circuit accomplishes DC sensing and voltage regulation simultaneously since the voltage at the drain of the PA is controllable and set to V_{ref} by the op-amp A2

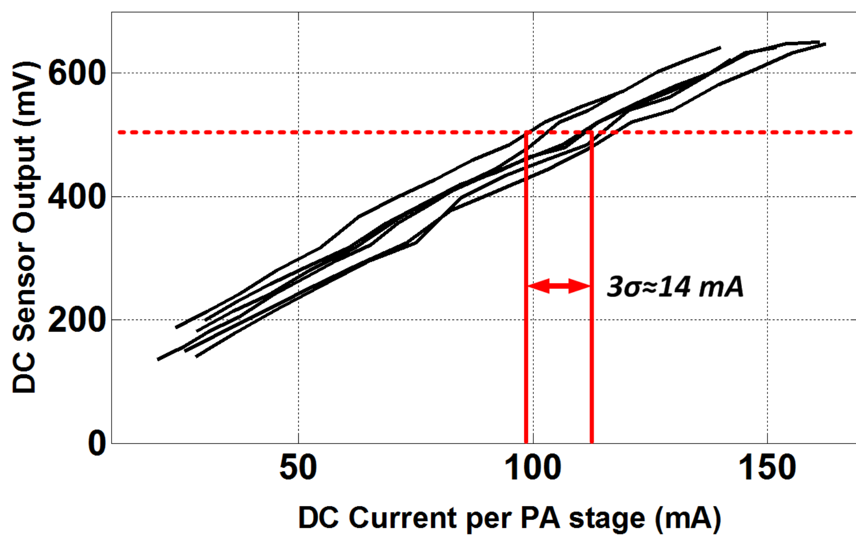

Figure 8.5: DC sensor response from measured ADC data, against PA output current showing the spread over 5 chips.

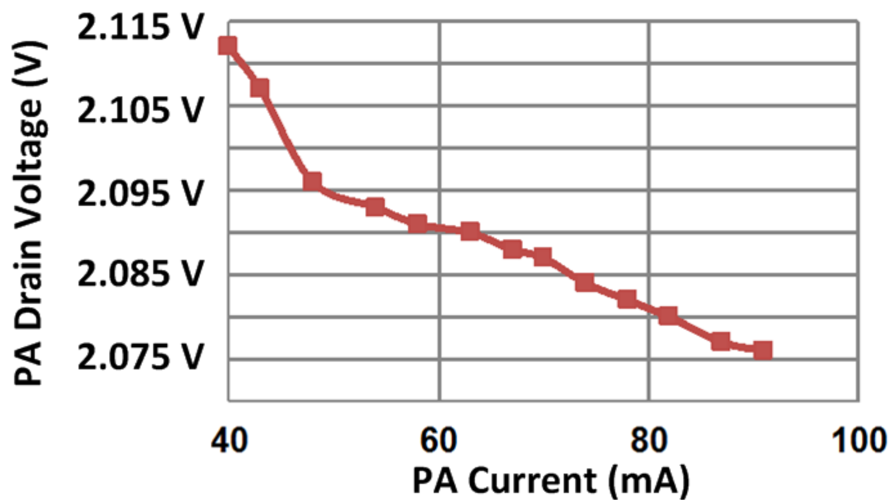

Figure 8.6: Measured PA drain voltage regulation with DC drawn. The maximum headroom is less than 45 mV over a 2.12 V supply, thereby, not affecting PA efficiency significantly.

as shown in Fig. 8.4. Fig. 8.5 shows a measured responsivity of 4.2 mV/mA current drawn based on 5 chips, derived from digitized sensor outputs. The 3σ spread of the PA current for a measured sense voltage, which also includes ADC variations, is less than 14% over all chips. Each sensor consumes less than 3 mW. Fig. 8.6 shows the voltage regulation as the PA is actuated to draw more DC. The headroom stays below 45 mV within the entire actuation space, thereby enabling, voltage regulation and DC sensing without significantly affecting efficiency.

8.1.2 Input and Output True RF Power Sensing

Input and output RF power sensors, which sense the forward and reflected power from the load, can measure the true RF power in presence of load mismatches. Two coupled transmission lines are implemented for the input and output ports of the PA as shown in Fig. 8.3 and Fig. 8.7. The input and output couplers were designed to have coupling coefficients of 15dB and 21dB at 28 GHz so that only a small fraction of the input and output power is sensed by the couplers to estimate gain and the power delivered. The lengths of the couplers are kept short at 220 μm for low insertion loss of 0.4dB. The transmission lines are implemented with 2.1 μm thick top aluminum metal in a ground tub as shown in Fig. 8.7. The power detector circuit at the isolated and coupled ports is also shown in Fig. 8.7. The RF power is rectified by M1 biased at cut-off. The rectified signal is then low pass filtered and amplified in the current domain, and measured across a resistor as shown in Fig. 8.7. Based on ADC data, the responsivity for output and input coupler and power detectors are measured to be 8.3mV/mW and 54mV/mW respectively. Each detector consumes a maximum DC power of 1.2 mW. The 3σ spreads of the true RF power for a measured sensor output, which also includes ADC variations, are approximately 1.1 dB and 2.2 dB for output and input sensors respectively over 6 chips.

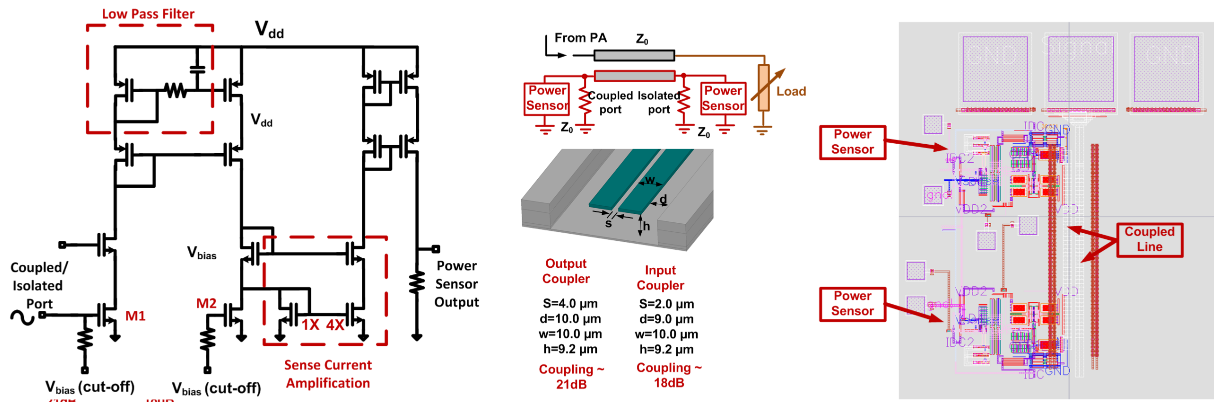

Figure 8.7: RF power sensor schematic and layout showing rectification, low-pass filtering and detection current amplification.

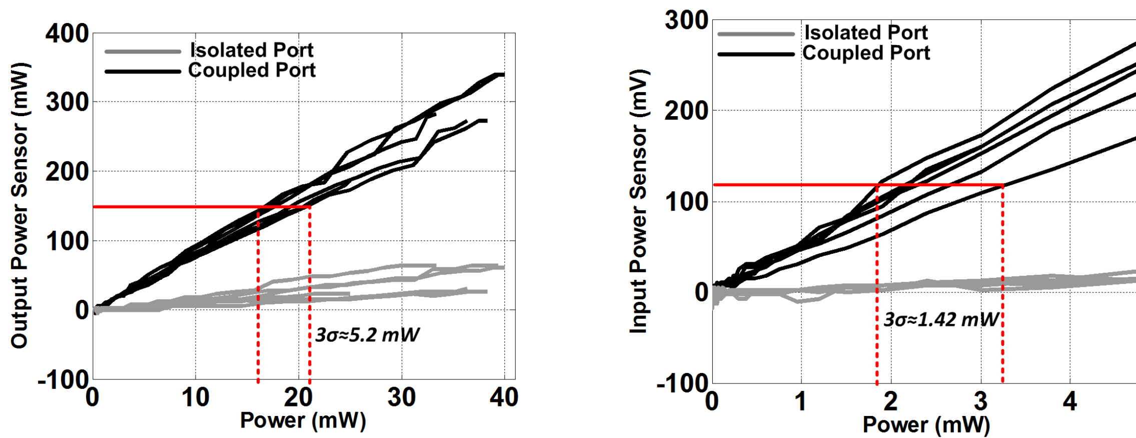

Figure 8.8: Output and Input RF power sensor response at 28 GHz, from measured ADC data over 6 chips.

8.1.3 Local Temperature Sensing to measure PA Efficiency

Instead of measuring the PA current directly, a low overhead method of measuring PA efficiency is to sense the local temperature rise proportional to the power dissipated during the PA operation. Simulations in ePhysics 2.0 predicted that during PA operation, an active region of 20-30 μm surrounding the amplifier core experiences temperature rise with the core rising by 10°C [139]. Hence, p-n junction sensor diodes were laid within the input and output PA transistors (thermally active region), both at the common source and the cascode transistor as shown in Fig. 8.9 and Fig. 8.10. In order to increase the responsivity, the x1 diode is placed outside the local thermally sensitive region ($\sim$ 40 μm away) as shown in Fig. 8.9, leading to a factor of 10x increase in responsivity. It can be proved that if diodes of sizes x1 and xN are kept at two different temperatures T and $T + \Delta T$, and if the same currents are forced through them, the difference between their V_{be} is given by

$$\Delta V_{be} = V_T(m+4)\ln\left(1 + \frac{\Delta T}{T}\right) + V_T \ln N + \left(\frac{E_g}{q} - V_{be,n}\right)\frac{\Delta T}{T + \Delta T} \tag{8.1}$$

where $V_T \approx 26$ mV, $V_{be,n} \approx 700$ mV, $E_g \approx 1.12$ eV (bandgap of silicon), m$\approx -\frac{3}{2}$ [140].

A regular temperature sensor, where both the diodes experience the same global temperature change, takes advantage of the term $V_T \ln N$ to establish $\frac{\partial V_{be}}{\partial T} \approx \frac{k}{q} \approx 8.67 \times 10^{-5}$ V/K. By placing the x1 diode in a constant temperature region, the designed local temperature sensor takes advantage of the last term $\left(\frac{E_g}{q} - V_{be,n}\right)\frac{\Delta T}{T+\Delta T}$ to establish $\frac{\partial V_{be}}{\partial T} \approx \frac{\frac{E_g}{q} - V_{be,n}}{T} \approx 1.33 \times 10^{-3}$ V/K. Since the range of temperature change is limited, we sacrifice linearity over large range with sensitivity.

Fig. 8.11 shows the measured responsivity of 2 mV/mW of dissipated power under a 2.1 V supply. The thermal and as well as the DC sensor show similar monotonic variation with DC power drawn by the PA. The response of the thermal sensor is, however, limited by the thermal time constant. The measured results are in close agreement with predicted results from thermal and circuit simulations. The sensor performances are summarized in Table. 8.1.3.

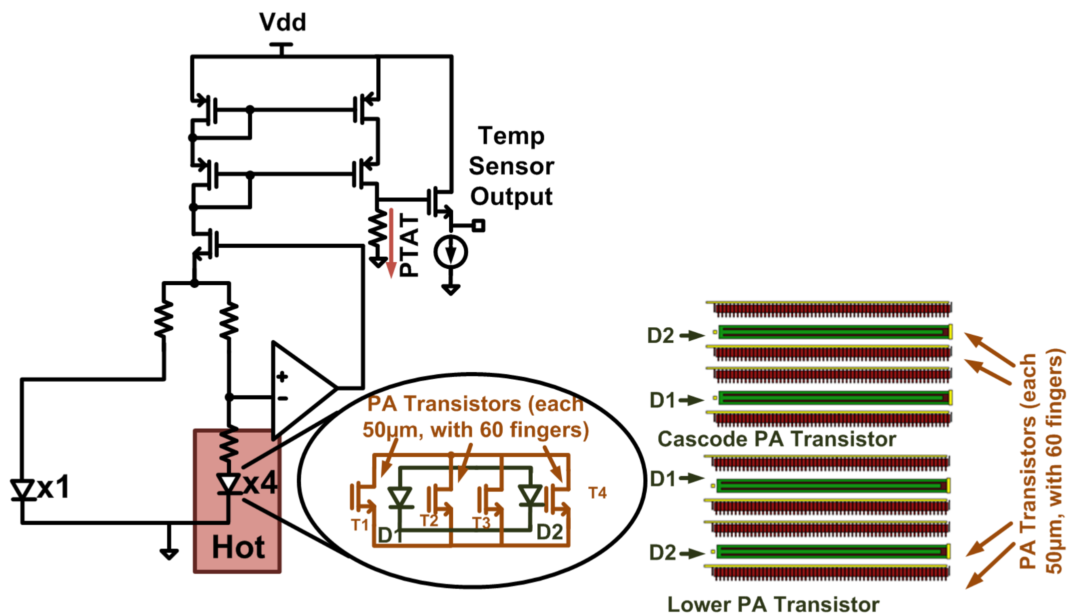

Figure 8.9: Schematic of temperature sensor showing 'hot' sensor diodes interspersed within PA transistor and the simulated thermal profile for 80mW power dissipation in the process.

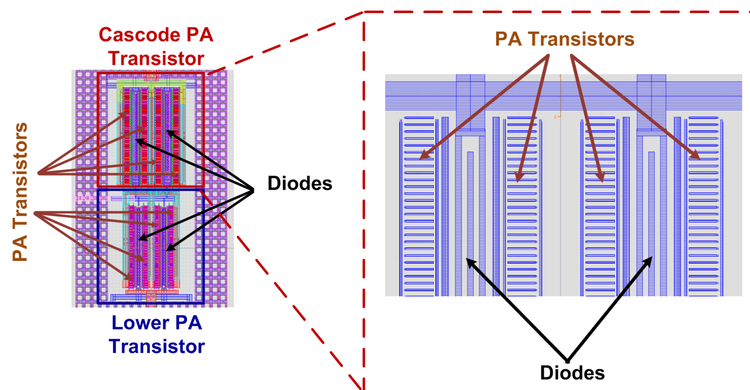

Figure 8.10: Layout of the PA transistor with the inter-spaced diodes in between.

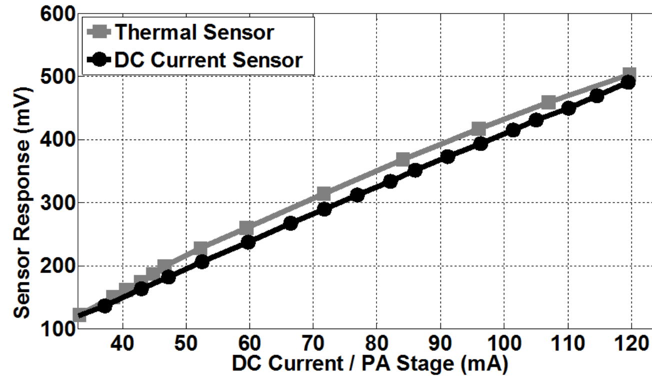

Figure 8.11: Measured temperature sensor output and DC sensor output with increasing DC power dissipation in PA.

Sensors	Measured Entities	Responsivity	Range	Sensor 1-b resolution
RF Power	True In/Op	54 mV/mW (in)	0-10 mW (in)	55 μW (in)
	Power	8.3 mV/mW (op)	0-100 mW (op)	360 μW (op)
DC	DC drawn	8.5 mV/mA (in)	0-60 mA (in)	280 μA (in)
Sensor	by PA	4.2 mV/mA (op)	0-120 mA (op)	560 μA (op)
	(in, op stages)			
Thermal	Power dissipated	4.0 mV/mA (in)	0-130 mW (in)	0.75 mW (in)
Sensor	by PA	2.0 mV/mA (op)	0-260 mW (op)	1.5 mW (op)

8.2 Actuators

[1]

The actuation space of the PA is composed of individual biasing controls for both the common source and cascode transistors, for each stage of the PA as well as output combiner tuning with tunable transmission lines. The tunability is achieved by allowing transmission line stubs to be shorted at different lengths using active transistors and digital control. More details are available in the papers [134] and [137].

[1] Designed by Steven Bowers and Kaushik Dasgupta

8.3 Digital Algorithm

An on-chip healing algorithm is synthesized with IBM library digital cells and consists of a global state machine that controls communication with all component blocks for changing actuation states, reading sensor data and performing the optimization of PA operation [2]. The iteration runs on automatically till the optimized state is run. To the user, it looks alike a black box where the user specifies the desired output power and the algorithm finds the most efficient state that generates the desired RF power with minimum DC power consumption. Because of this modular code setup, many different types of complex optimization algorithms can be incorporated into this general fully-integrated self-healing framework. Two such optimization strategies have been synthesized in the current implementation that finds the optimum solution within the search space of 262,144 possible states. One finds the state with maximum output power, and the other finds the state with the lowest DC power for a given output power. The convergence of the algorithm using a low frequency clock of 25 MHz (limited by the measurement setup) takes up to a maximum of 0.8 second. At its full speed of 400 MHz, the maximum healing time would be 0.1 second. The digital core structure and the state-machine are explained in Fig. 8.12 and Fig. 8.13. The digital core is equipped with several instruction sets, which help in debugging. The instruction sets have different modes such as complete automated optimization, manual actuation set loading, only reading sensor data, as well as set-by-step optimization so that sensor data at every step of the optimization can be monitored.

8.4 Measurement Results Demonstrating Healing

[3]

The self-healing PA is fabricated in IBM 45 nm SOI CMOS. The chip is probed with high-frequency GSG probes and communication with the on-chip digital core is achieved through

[2] We would like to thank Ben Parker for digital synthesis support.
[3] Measurements were performed by Steven Bowers and Kaushik Dasgupta

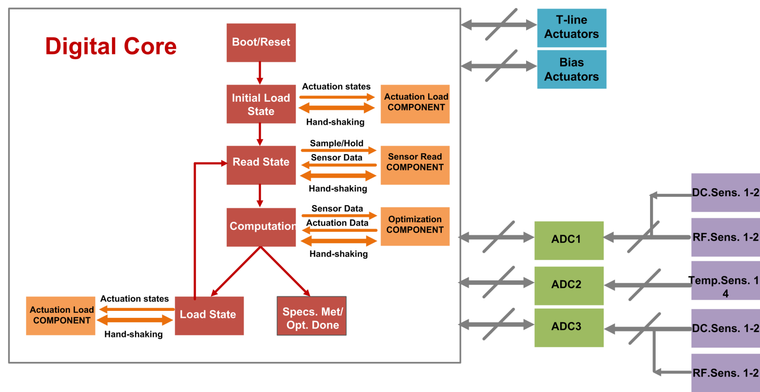

Figure 8.12: Digital core structure.

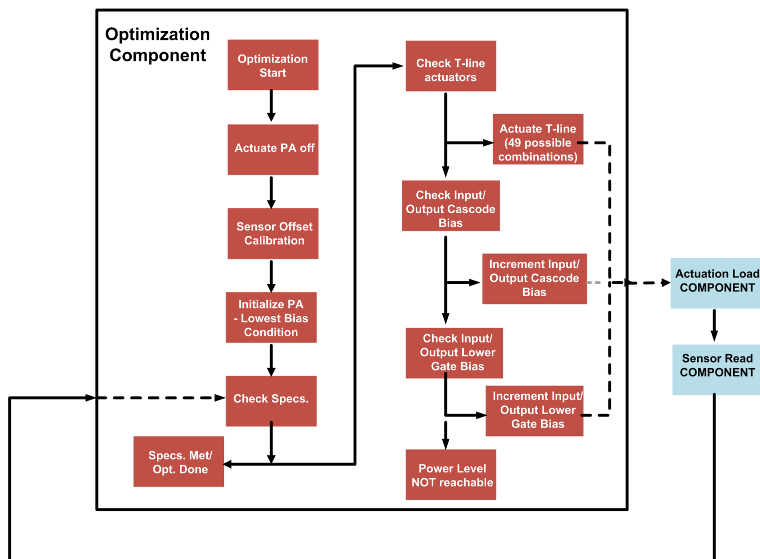

Figure 8.13: State-machine description.

an on-chip serial interface. The die micrograph with sensor placements and measurement setup photo is shown in Fig. 8.14. FPGA and Matlab interface are used only for reading sensor data out of the chip and loading the instruction set into the core.

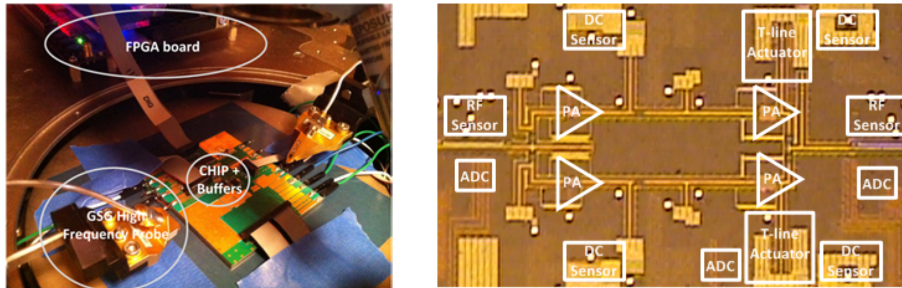

Figure 8.14: Measurement set-up and die micrograph showing PA with sensors, ADC and actuators.

20 chips were measured and Fig. 8.15 shows that healing improvement at different input power levels at 28 GHz. Since self-healing allows us a reconfigurable PA which can be optimized for different drive levels, Fig. 8.15 shows considerable improvement over a non-healed PA, specially at the back-off. The non-healed PA has been designed for saturated output power, but the optimum impedance for maximizing output power changes at lower drive levels. Due to impedance tuning facilitated by the actuation space, we achieve almost 3 dB increase in output power at lower input power levels. The histogram shows, that due to self-healing, random variations in the performance space, due to variations in fabrication processes can be reduced to a considerable extent, as shown by narrowing of the distribution over 20 chips in Fig. 8.15. If we are interested in a constant RF output power, then self-healing allows us to optimize efficiency using a combination of DC control and combiner tuning. Fig. 8.16 shows almost 50% decrease in DC power consumption for a constant output of P_{out}=12.5 dBm at 28 GHz. The narrowing of the distribution shows the efficacy of self-healing countering against process variations. Due to aging and environmental changes, such as absorptions and reflections from nearby surfaces, the output loading may be considerably different from the designed load of 50 Ω. [4] Fig. 8.17 shows that self-healing helps us to overcome some effects of load variations by optimizing the performance of the PA over the actuation space. The details of the measurement results can be found in [137].

[4] This is the case when cell-phone is held against our ear or near our head or even placed on a table.

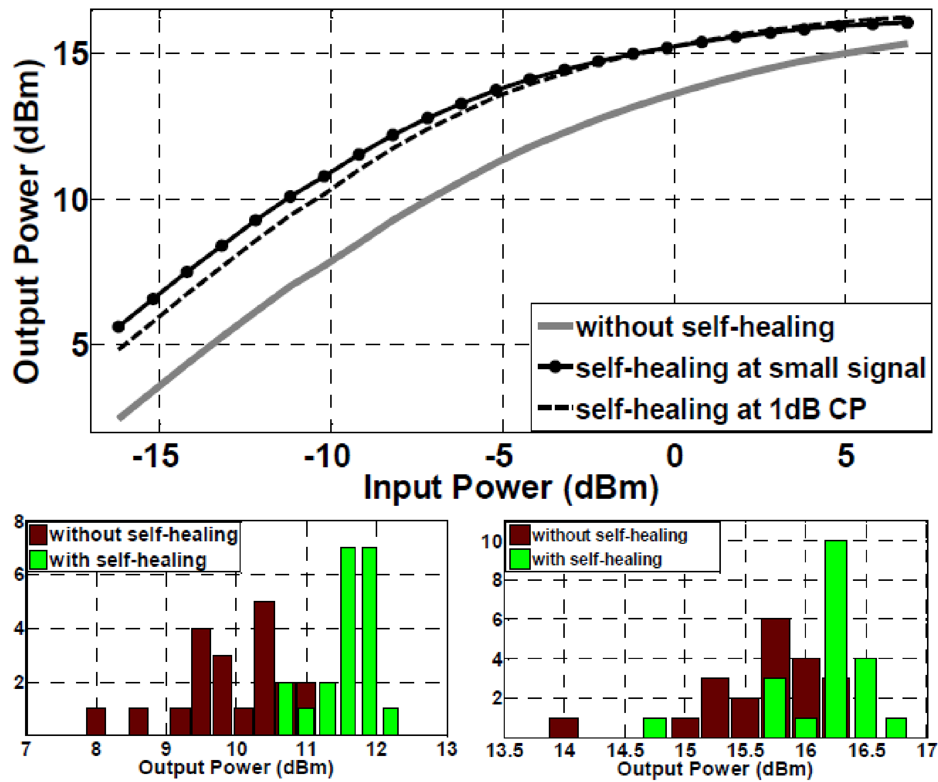

Figure 8.15: Output power healing for different input power and histogram showing effect of self-healing in narrowing distribution and yield increase.

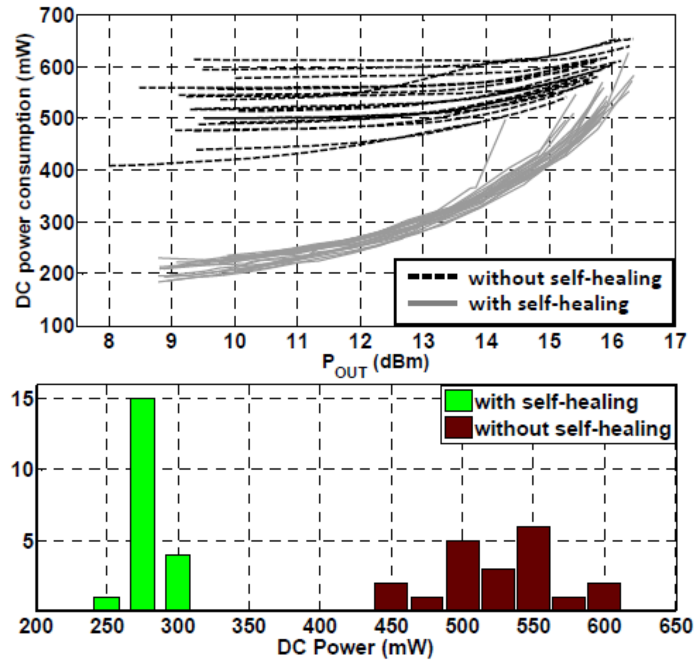

Figure 8.16: Self-Healing demonstrating almost 50% less DC power consumption for a constant output power of P_{out}=12.5 dB.

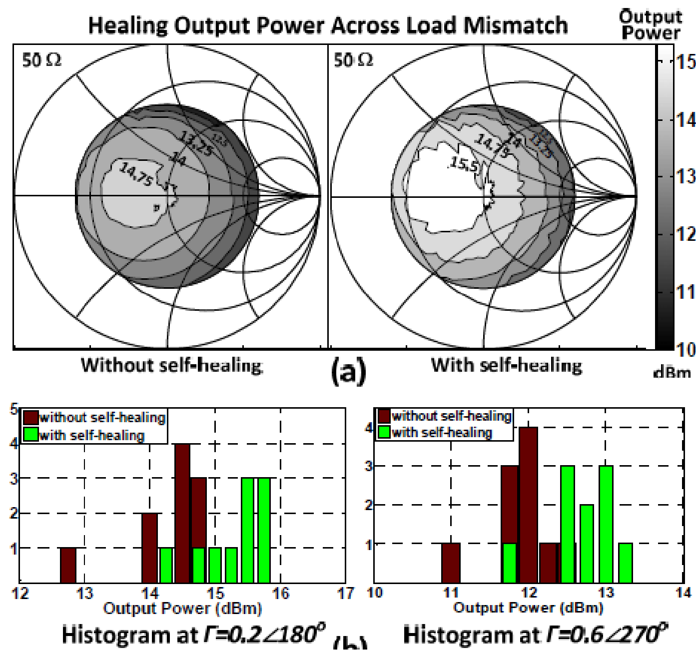

Figure 8.17: Self-Healing showing improved output power performance over the 4-1 VSWR cycle and histogram showing yield increases for a constant load mismatch at $\Gamma_L = -0.2$

Chapter 9

Other Work

In a mm-Wave transceiver, the integrated power amplifier (PA) still remains the most challenging block because of low breakdown voltages and reliability issues like hot carrier injection (HCI) [141]. This fundamentally limits the maximum power that can be extracted from a single stage without sacrificing efficiency, gain, and stability. It therefore becomes inevitable that the output power of several stages must be combined in order to achieve the desired power level. Also since available gain is limited and ohmic losses are high at mm-wave frequencies, it becomes necessary to cascade several stages to boost up the power gain, often at the cost of efficiency.

In this Chapter, we will discuss our work on a scalable compact combiner topology which is based on a self-similar modular design. The design is an effort towards realizing the broader concept illustrated in Fig. 9.1 where the entire combiner network is similar to a part of itself. The output currents of four stages driven in phase combine with four similar output stages which again combine with four similar stages and the self-replication continues. Such self-similarity will not only make the design more modular, flexible and compact for lower loss, but will also make it more scalable than a more conventional current combing corporate network where physical distance of separation between the stages increases rapidly with number of stages [143]. The symmetry of this design also ensures a symmetric thermal profile in the die which affects each of the 4-way combining stages in a similar way, unlike a conventional corporate combiner where the temperature rise experienced by the middle stages is higher. As a proof of concept, we present the design of a 16-way combiner which

combines the power of 16 output stages to achieve a P_{sat} of +11.4dBm at 77 GHz on a 0.7 V supply. This was the highest reported P_{sat} in this frequency band in CMOS with a sub 1V supply at the time of publication [142], that is necessary for long term reliability of the devices.

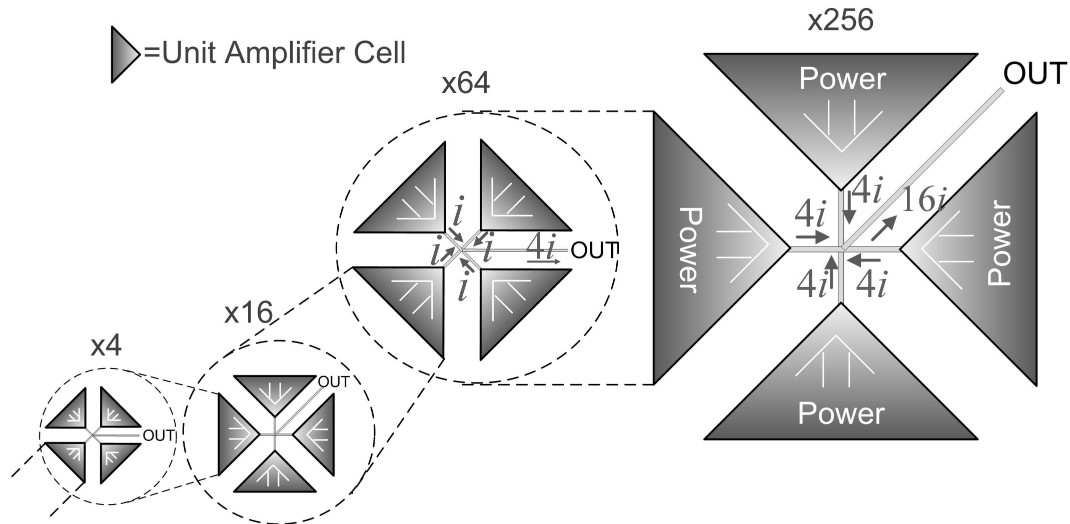

Figure 9.1: A conceptual self-similar output combiner for combining currents from four output stages where each output stage is a scaled self-replicated version of the four output stages in an iterative way

9.1 Power Combining

Given a technology, there is an optimum value of power which can be reliably obtained from a single stage without sacrificing power gain, stability and bandwidth. It is important to understand the trade-offs in order to appreciate the relevance of power combining.

9.1.1 Importance of Power Combining

When the transistor is operated at a frequency near its f_{max}, the gain is limited by the quality factor of its input impedance. The resistive part of this impedance which sinks the input RF power, is contributed by the resistance of the polysilicon, the gate contacts and also by the delayed trans-conductance caused due to the transit delay between the charge induction in the channel and the instantaneous gate voltage, commonly known as 'nonquasistatic'

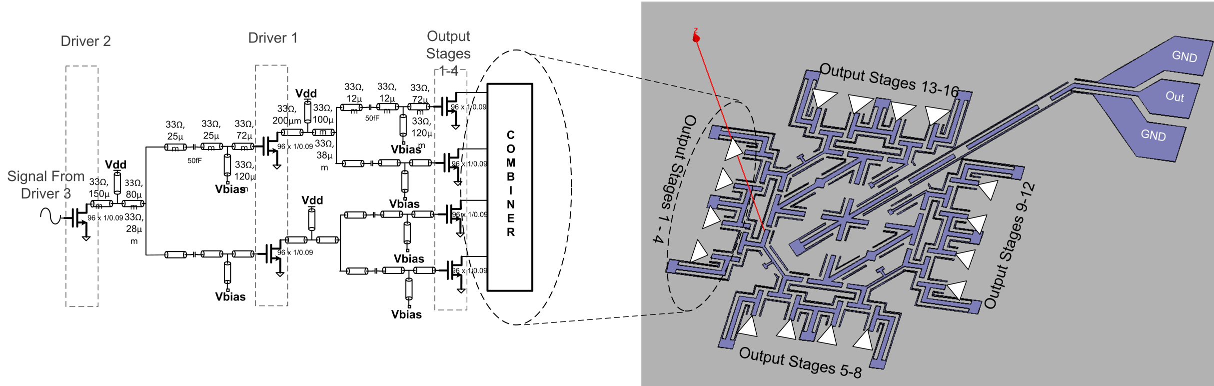

Figure 9.2: Output combiner design for combining current from 16 output stages driven in phase. The combiner also achieves impedance transformation. The spaces in the transmission line network of the combiner represent ports where capacitors were placed as parts of the matching network. It also shows the schematic of the last three stages in each of the four arms of the combiner. It consists of Driver 1, Driver 2 and Output stage which have been illustrated in Fig. 9.4 and Fig. 9.5

effect [144]. The quality factor and therefore, the power gain and f_{max}, can be increased by reducing the gate width per finger until the transistor becomes unstable from the output port for a conjugate input match. Thus, for a optimum gate width per finger, the power gain of a transistor biased at its maximum f_{max} is fixed by technology. In this design, for a finger width of $1\mu m$, the MAG was 5dB at 77 GHz at a bias of 0.16mA/μm.

For an optimal finger width and bias, the output voltage swing will be limited by the breakdown of the devices and the long term reliability issues like HCI and time-dependent dielectric breakdown. The device time to failure is exponential with the voltage swing and it is imperative to operate far away from this region. This fixes the supply voltage, which in this design is set at 0.7V. The output power, however, can be increased in theory by adding fingers in parallel and scaling down the desired output impedance for a proportionately higher current swing. In practice, such an optimistic scaling fails beyond a point primarily due to the following factors.

The low input and output impedance of a 'giant' output stage will imply a high impedance transformation ratio in the interstage as well as the output matching network leading to high loss and possible instability into the preceding stage [145]. This also reduces bandwidth and makes the design more sensitive to modeling errors. Also beyond a point, the connecting and feeding wiring resistance and inductance would overwhelm the benefit of adding irrationally

large number of elements. In this technology, for a $96\mu m$ finger wide transistor, the saturated output power is around 5.5 dBm for a large signal load-pull match.

9.1.2 Efficient Power Combining

In order to increase the net output power, therefore, it is evident that power combining is necessary. Any loss in the output combiner, however, is critical and directly reduces efficiency and cannot be compensated for, unlike interstage losses. Assuming around 4 dB of combiner loss, around 16 output stages each delivering 5.5dBm need to be combined in order to generate +13dBm of output power. The problem of designing a combiner to ensure maximum large signal power transfer to a 50Ω load through a lossy matching network is a multi-dimensional optimization procedure [141]. We know, however, that in silicon ICs, high-frequency loss is primarily dominated by metal loss due to storage of magnetic energy (as opposed to storage of electrical energy in the dielectric). Hence, in order to achieve a given inductive impedance transformation and store a given amount of net reactive energy, the average capacitive energy stored in the passive network has to be minimized, since any electrical energy needs to be compensated by an excess magnetic energy leading to higher loss. Ideally, therefore we should use only inductors with no capacitors to achieve the impedance transformation. However since inductors have finite self-resonant frequencies and transformer geometry also includes distributed capacitance, we use transmission lines in the combiner, splitter as well as in inter-stage matching networks. T-lines have predictable return paths and also scale up more readily with frequency. When a transmission line is terminated with a load of reflection coefficient, $|\Gamma_L|\ e^{j\theta}$, the average magnetic energy stored inside the line is given by $W_m = \frac{1}{2}\int_0^l L|I(x)|^2 dx = f(l, |\Gamma_L|, \theta)$ and the average electrical energy is given by $W_e = \frac{1}{2}\int_0^l C|V(x)|^2 dx = g(l, |\Gamma_L|, \theta)$ and the impedance transforming network with the highest W_m/W_e ratio will be the most efficient.

In this design, we combine the power of 16 such output stages driven in phase and current combine the output progressively though a modular matching network which realizes the power combining and impedance transformation at the same time. In order to minimize loss,

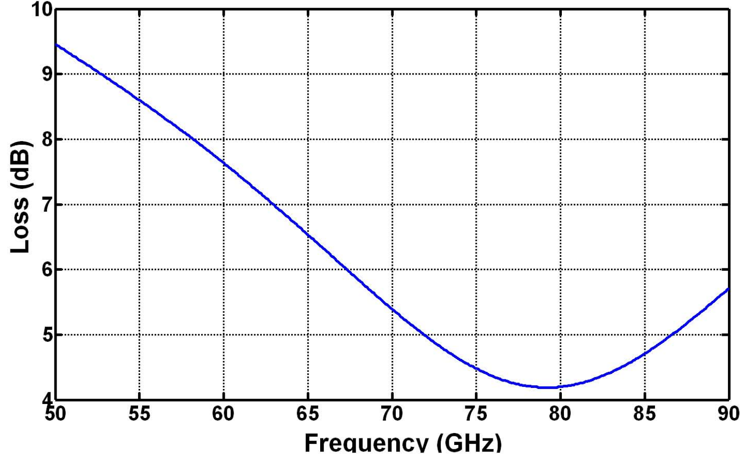

Figure 9.3: Simulated loss (passive efficiency) of the combiner

and to the make the layout compact, the combiner is made symmetrical and equidistant from 16 output stages as shown in Fig. 9.2. It has a binary tree-like structure and progressively adds current from the previous two stages finally adding 16 in phase currents in the center node. At each intersection point of the combiner, current gets added with the impedance looking into it doubled at each branch, while the combiner brings the impedance down again through a network of t-lines and capacitors to achieve the desired load-pull impedance. This approach leads to a combiner with a simulated passive efficiency of 38% at 77 GHz as shown in Fig. 9.3. Each of the feeding arms in the 16-way combiner is also fed through a series of self-similar driver amplifiers and matching networks as shown in Fig. 9.4 and explained in the next section. In theory, each such combiner can be self-replicated to make four such combiners combining the output power after having transformed the terminating 50Ω to 200Ω.

9.2 Architecture and Amplifier Design

The entire PA architecture, along with power splitting and combining, has been shown in Fig. 9.4. For the driver amplifiers typically, the transistors are sized in the ratio of 1:2 in a cascaded chain so that the output saturates when it has atleast 3 dB of gain. Therefore the driver stages (each 48μm) of two output stages (each 96μm) can be combined into a

single stage of width 96μm. The same procedure can be carried out on the initial driver stages to enable a binary tree scaling. This concept is illustrated in Fig. 9.4 which shows the combining network and the self-similar active power splitting among different stages through transmission lines . In this way, a modular design methodology can be established and laying out separate optimized transistors and separate transformation networks for each stage can be avoided. However, layout constraints entail using slightly different matching network for different stages. The power flow among various branches at saturation is also shown in Fig. 9.4, assuming each stage has 3dB of gain at saturation and branches are lossless. Let P_{out} be the power delivered by each output stage consuming P_{DC} of DC power and let L be the combiner loss factor in the such a N cascaded binary corporate combiner [143](here $N = 5$). Then the drain efficiency (E_{nw}) of the entire network is given by

$$E_{nw} = \frac{L \sum_{i=0}^{2^{N-1}} P_{out}}{\sum_{i=0}^{N-1} 2^i P_{DC}} = \frac{L}{2} \frac{2^N}{2^N - 1} \frac{P_{out}}{P_{DC}} \approx \frac{1}{2} L E_{single} \tag{9.1}$$

where E_{single} is the drain efficiency of a single output stage. It can be seen that the efficiency gets reduced to less than 50% for such cascaded combiners; however such a reduction is unavoidable in order to achieve a higher saturation gain and a higher saturated output power.

The whole network consists of six stages and the input transistors have a width 48μm. Each 96 finger transistor is laid out as 8 parallel transistors, each of 12 fingers, to distribute the gate resistance and maximize gain ensuring minimum gate-drain side-wall capacitance for improved stability. The input and output CPW tapers are absorbed as parts of the matching network. All impedance transforming networks are designed using microstrip tub structure [141] with the 1.49μm thick top Al metal being used as the signal path. Spacing and width of the ground lines are optimized for loss and transmission line length. Although most of the return current is forced through the ground plane, the ground wall provides isolation necessary to make the combiner layout compact and low-loss. The schematic of the

Figure 9.4: The PA architecture showing the power splitting, combining networks and power flow among various branches at saturation assuming each stage has 3dB of saturated gain and branches are lossless

last three stages with detailed matching network is shown in Fig. 9.2.

Metal-oxide-Metal (MOM) capacitors were employed in the matching network and for bypass. Extensive 3D EM simulations (Ansoft HFSS) were performed to accurately predict self-resonance frequency (SRF) of the capacitors A wide-band model (1-110 GHz) was then fitted which matched simulations within 0.5% over the entire frequency range. 200fF capacitors were simulated to resonate around 80 GHz. They were used in series with suitable resistors to achieve low impedance bypass.

9.3 Measurement Results

The die microphotograph is shown in Fig. 9.5. The chip occupies an area of 1.3x1.3mm^2. Small-signal measurements are carried on wafer through WR-10 GSG Infinity probes connected to Agilent PNA 8361A through TX-RX modules. The Agilent 8316A vector network analyzer is calibrated using W-band calibration substrates since the pads have been assimilated in the matching networks. The PA is biased in class AB mode and the DC current

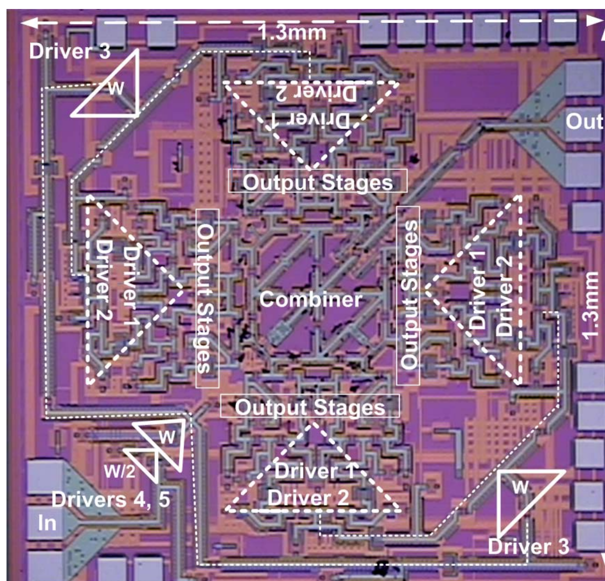

Figure 9.5: Die microphotograph of the 77 GHz amplifier showing the layout placements of the different stages and the power splitting and combining network.

drawn is 472mA from a 0.7V supply. The measured small-signal parameters are shown in Fig. 9.6. The input match is below -19dB at 77 GHz and is below -10dB between 70-82 GHz. S_{22} is below -8dB at 77 GHz. The small signal gain of the amplifier is around 9.4 dB at 77GHz and has 3dB bandwidth between 72.5-83.5 GHz and has gain upto 87 GHz. No instability was observed and the measured K-factor is greater than 3.8 between 50-90 GHz.

The large signal performance of the PA at 77GHz is shown in Fig. 9.7. The input signal is provided through WR-10 GSG probes and attenuator using a quadrupler (Spaceklabs AE-4XW) which can deliver 12.3dBm output power at 77 GHz, enough to saturate the PA. The input signal at 19.25 GHz to the quadrupler was provided by Agilent 8257D. The output power was measured with W-band Agilent W8486A power sensor connected to Agilent 4418B power meter after de-embedding the probe loss. The PA has a saturation output power of 11.4 dBm and a saturated gain of 5dB. To the best of the authors' knowledge, the PA achieves the highest P_{sat} among reported work in CMOS at this frequency with a sub 1V quiescent V_{ds}, despite being implemented in a 90nm process with a relatively lower f_{max} compared to finer line processes used in other implementations [146]- [151]. In general, although higher P_{sat} and efficiency can be obtained by operating at higher supply voltages, it was kept low

at 0.7V to operate far away from low breakdown and ensure long term reliability.

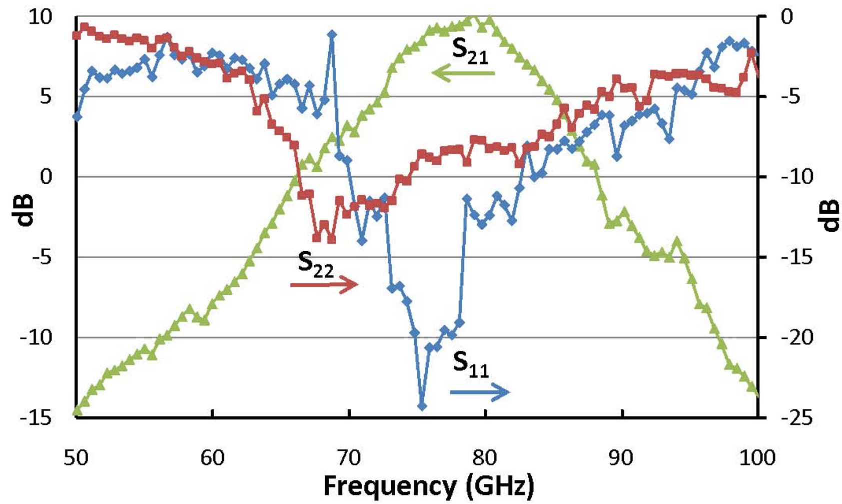

Figure 9.6: . Measured S-parameters of the power amplifier

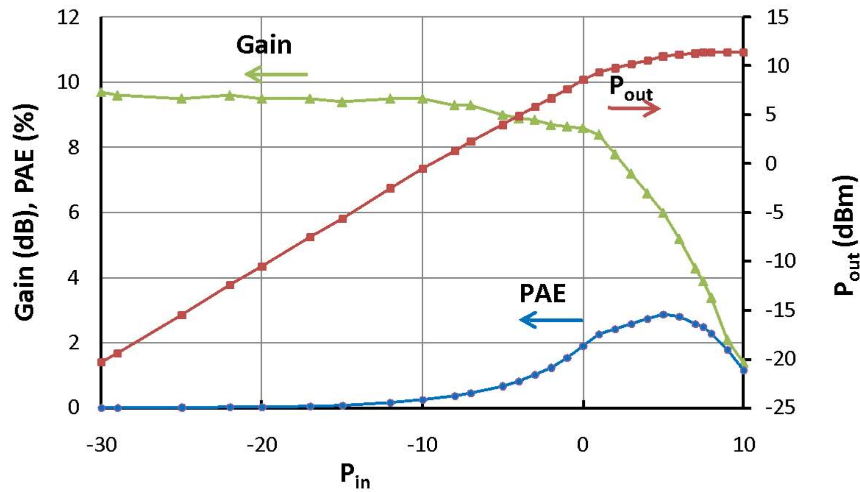

Figure 9.7: Measured output power, gain and PAE at 77 GHz.

Chapter 10

Conclusion

In this thesis, we discussed our approach towards development of integrated terahertz technology in silicon-based processes. Up until recently, the terahertz frequency range has been mostly addressed by high mobility custom III-V processes, expensive nonlinear optics, or cryogenically cooled quantum cascade lasers. A low cost room temperature alternative can enable the development of such a wide array of applications, such as disease diagnostics, label-free genetics, security screening for concealed weapons and contraband detection, global environmental monitoring, nondestructive quality control and ultra-fast wireless communication, not currently accessible due to cost and size limitations

However, THz power generation in silicon-based integrated circuit technology is challenging due to lower carrier mobility, lower cut-off frequencies compared to compound III-V processes, lower breakdown voltages and lossy passives. Radiation from silicon chip is also challenging due to lossy substrates and high dielectric constant of silicon. In this work, we propose novel ways of combining circuit and electromagnetics in a holistic design approach, which can overcome limitations of conventional partitioned and block-by-block design methodology for high-frequency power generation above the classical definition of cut-off frequencies (f_{max}). We demonstrate this design philosophy in an active electromagnetic structure, which we call Distributed Active Radiation. It is inspired by an Inverse Maxwell approach, where instead of using classical circuits and electromagnetics block to generate and radiate THz frequencies, we formulate surface (metal) currents in silicon chip for a desired THz field profile and develop active means of controlling different harmonic currents to perform signal generation,

frequency multiplication, radiation and lossless filtering, simultaneously in a compact footprint. By removing the artificial partitions among circuits, electromagnetics and antenna, we open ourselves to a broader design space. This enabled us to demonstrate the first 1 mW Effective-isotropic-radiated-power(EIRP) THz (0.29 THz) source in CMOS with total radiated power being three orders of magnitude more than previously demonstrated. We also proposed a near-field synchronization mechanism, which is a scalable method of realizing synchronized large arrays of autonomous radiating sources in silicon. We also demonstrated the first THz CMOS array with digitally controlled beam-scanning in 2D space and near 10 mW EIRP at 0.28 THz.

We use a similar electronics and electromagnetics co-design approach to realize a 4x4 pixel integrated silicon Terahertz camera demonstrating to the best of our knowledge, the most sensitive silicon THz detector array without using post-processing, silicon lens or high-resistivity substrate options (NEP $\sim$ 10 pW$\sqrt{Hz}$ at 0.26 THz). Together with the CMOS DAR arrays, we demonstrated, for the first time, an all silicon THz imaging system with a CMOS source.

Chapter 11

Appendix

11.1 On the possibility of false locking

The near-field sense antenna gauges the current configuration in the radiating sources through a near-field electromagnetic coupling mechanism. The coupling network between multiple distributed active radiators tries to bring back the system into a state where the sense antenna voltages of all the radiator cores equalize. We have shown the locked state is a lowest energy and stable state, *i.e.* any small perturbation around the steady state will die down exponentially. It is possible though, that two current configurations in a DAR result in the same sense antenna voltage and we explored if such a false locking state can occur in practice. It is seen that in silicon implementation, any spurious substrate mode coupling is enough to suppress this undesired locking state and this is verified in simulations and experiments.

This is illustrated in Fig. 11.1. If we fix the direction of traveling wave and the phase at any point on the DAR, then the current configuration for any other point on the DAR is fixed. If we now advance the phase of that chosen point through 360°, it will be reflected *uniquely* in the sense antenna voltage whose phase will also follow through 360°. If we now reverse the direction of wave travel, and again advance the phase of the current distribution on thee DAR, the phase of the sense antenna voltage will once again follow through 360°. This implies for every current configuration there is another state where the traveling wave oscillation is in the reverse direction, which results in the same sense antenna voltage. This is shown in Fig. 11.1, where the magnetic flux remains same with time for the two states. If observed

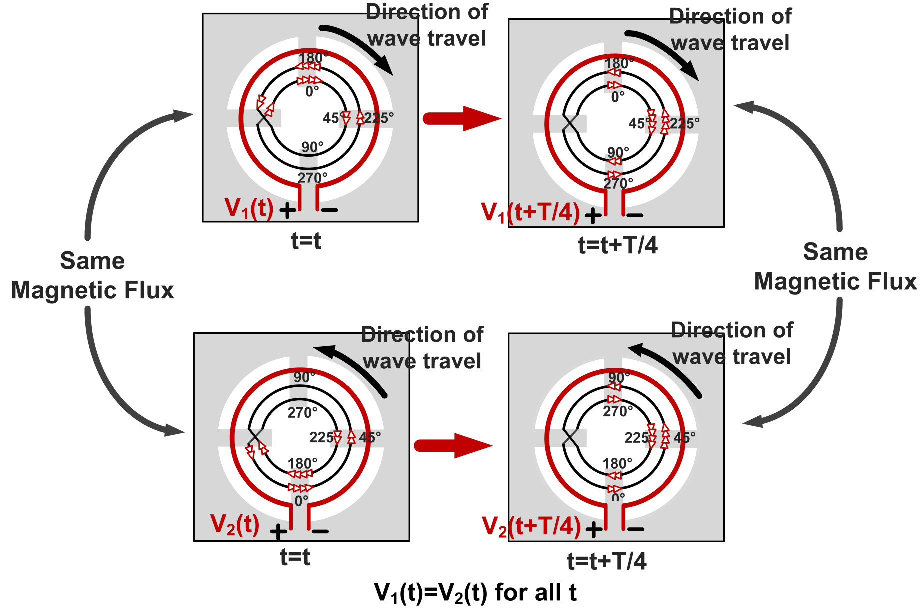

Figure 11.1: On the possibility of false locking.

carefully, it can be seen that all times, the current elements in one DAR are rotational transformation of the elements in the other DAR, which results in the same magnetic flux. However, as discussed before, in practical realization, any form of coupling through substrate or otherwise, renders two of these states existing in two coupled DARs unstable.

11.2 Derivation of State Equations in the transformed domain for stability analysis

We will try to derive(5.16a) and (5.16b) form (5.8) using the transformations(5.15a) and (5.15b). Assuming $z = \frac{1}{\omega_0}\frac{dv}{dt}$, we have $r^2 = v^2 + z^2$ and $tan(\phi) = \frac{z}{v}$. This gives us

$$r\frac{dr}{dt} = v\frac{dv}{dt} + z\frac{dz}{dt} \tag{11.1a}$$

$$r^2\frac{d\phi}{dt} = v\frac{dz}{dt} - z\frac{dv}{dt} \tag{11.1b}$$

(11.1a) and (11.1b) when applied to (5.8) gives (5.16a) and (5.16b).

11.3 Derivation of linearized state space matrix for stability analysis

Here, we will derive the state-space matrix in (5.21) from (5.17)-(5.20) using the steady state solutions. From, (5.17)-(5.18), we have

$$\begin{aligned}
\left.\frac{\partial F_{1,T}}{\partial r_{1,T}}\right|_{r^0_{1,T},\phi^0_{1,T},r^0_{2,T},\phi^0_{2,T}} &= -\frac{\omega_{t,1}}{2Q}(1-g_mR) \\
&- \frac{9}{8Q}\omega_{t,1}\alpha_3^2 R(r^0_{1,T})^2 - \frac{C\omega_0}{2} \\
&= -\frac{2\omega_{t,1}}{Q}(g_mR-1) - \frac{C\omega_0}{2} && (11.2a) \\
\left.\frac{\partial F_{1,T}}{\partial \phi_{1,T}}\right|_{r^0_{1,T},\phi^0_{1,T},r^0_{2,T},\phi^0_{2,T}} &= \frac{C\omega_0}{2} r^0_{2,T} sin(\phi^0_{1,T}-\phi^0_{2,T}) \\
&= r^0_{2,T}\Delta\omega_t && (11.2b) \\
\left.\frac{\partial F_{1,T}}{\partial r_{2,T}}\right|_{r^0_{1,T},\phi^0_{1,T},r^0_{2,T},\phi^0_{2,T}} &= \frac{C\omega_0}{2} cos(\phi^0_{2,T}-\phi^0_{1,T}) && (11.2c) \\
\left.\frac{\partial F_{1,T}}{\partial \phi_{2,T}}\right|_{r^0_{1,T},\phi^0_{1,T},r^0_{2,T},\phi^0_{2,T}} &= -\frac{C\omega_0}{2} r^0_{2,T} sin(\phi^0_{1,T}-\phi^0_{2,T}) \\
&= -r^0_{2,T}\Delta\omega_t && (11.2d)
\end{aligned}$$

$$\left.\frac{\partial G_{1,T}}{\partial r_{1,T}}\right|_{r^0_{1,T},\phi^0_{1,T},r^0_{2,T},\phi^0_{2,T}} = -\frac{C\omega_0}{2}\frac{r^0_{2,T}}{(r^0_{1,T})^2}sin(\phi^0_{2,T}-\phi^0_{1,T})$$

$$= \frac{r^0_{2,T}}{(r^0_{1,T})^2}\Delta\omega_t \tag{11.3a}$$

$$\left.\frac{\partial G_{1,T}}{\partial \phi_{1,T}}\right|_{r^0_{1,T},\phi^0_{1,T},r^0_{2,T},\phi^0_{2,T}} = -\frac{C\omega_0}{2}\frac{r^0_{2,T}}{r^0_{1,T}}cos(\phi^0_{1,T}-\phi^0_{2,T}) \tag{11.3b}$$

$$\left.\frac{\partial G_{1,T}}{\partial r_{2,T}}\right|_{r^0_{1,T},\phi^0_{1,T},r^0_{2,T},\phi^0_{2,T}} = \frac{C\omega_0}{2r^0_{1,T}}sin(\phi^0_{2,T}-\phi^0_{1,T})$$

$$= -\frac{\Delta\omega_t}{r^0_{1,T}} \tag{11.3c}$$

$$\left.\frac{\partial G_{1,T}}{\partial \phi_{2,T}}\right|_{r^0_{1,T},\phi^0_{1,T},r^0_{2,T},\phi^0_{2,T}} = \frac{C\omega_0}{2}cos(\phi^0_{2,T}-\phi^0_{1,T}) \tag{11.3d}$$

(11.3e)

We can similarly derive the state-space coefficients corresponding to $F_{2,T}$ and $G_{2,T}$ from (5.19)-(5.20). The final results are shown in (5.21).

Bibliography

Bibliography

[1] H. Rubens *et al.*, “Heat rays of great wave length,” *Phys. Rev.* vol. 4, 1897.

[2] P.H. Siegel, “Terahertz technology,” *IEEE Trans. Microw. Theory Tech.*, vol. 50, no. 3, pp.910-928 , 2002.

[3] M. Tonouchi, “Cutting-edge terahertz technology”, *Nature Photonics*, vol.1, 97-105, 2007.

[4] “Highlights of Telecom Subscription Data as on 31st March, 2012,” TRAI. 03 May 2012. http://www.trai.gov.in/WriteReadData/WhatsNew/Documents/PR-TSD-Mar03052012.pdf

[5] Teraview. http://www.teraview.com/.

[6] I. Duling and D. Zimdars, “Terahertz imaging: Revealing hidden defects”, *Nature Photonics*, vol.3, pp.630-632, 2009.

[7] B. Ferguson and X-C. Zheng, “Materials for terahertz science and technology,” *Nature Photonics*, **1**, 630-632, (2002).

[8] P.H. Siegel,“Terahertz technology in biology and medicine,” *IEEE Trans. Microw. Theory Tech.*, vol. 52, no. 10, pp. 2438-2447, 2004.

[9] R.E. Miles *et al.*, *Terahertz sources and systems*, Kluwer Academic Publishers, London, June 2000.

[10] D.L. Woolard *et al.*, “Terahertz Frequency Sensing and Imaging: A Time of Reckoning Future Applications?,” *Proc. IEEE*, vol. 93, no. 10, Oct. 2005.

[11] B. Hu and M. Nuss, "Imaging with terahertz waves," *Optics Letters*, vol.20, pp. 1716–1718, 1995.

[12] R.M. Woodward *et al.*, "Terahertz pulse imaging in reflection geometry of human skin cancer and skin tissue," *Phys. Med. Biol.*, vol.47, pp. 3853-3863, 2002.

[13] E. Pickwell and V.P. Wallace, "Biomedical applications of terahertz technology," *J. Phys. D: Appl. Phys.*, vol.39, R301-R310, 2006.

[14] C. P. Vlahacos *et al.*,"Near-field scanning microwave microscope with 100 μm resolution," *Appl. Phys. Lett.* vol. 69, pp.3272-3274, 1996.

[15] B. Knoll *et al.*,"Contrast of microwave near-field microscopy," *Appl. Phys. Lett.*, vol.70, pp. 2667-2669, 1997.

[16] Chun Yu *et al.*, "Active Microwave Imaging II: 3-D System Prototype and Image Reconstruction From Experimental Data," *IEEE Trans. Microw. Theory Tech.*, vol. 56, no. 4, pp. 991-1000, Apr. 2008.

[17] E. Grossman *et al.*,"Passive terahertz camera for standoff security screening," *Appl. Opt.*, vol. 49, Issue 19, pp. 106-120, 2010.

[18] X-C Zhang, "Terahertz wave imaging: horizons and hurdles," *Phys. Med. Biol.*, **47**, 3667-3677, 2002.

[19] W.L. Chan *et al.*,"Imaging with terahertz radiation," *Rep. Prog. Phys.*, **70**, 1325-1379, 2007.

[20] S. Hunsche *et al.*, "THz near-fieldimaging," *Optics Comm.*, vol. 150, issues 1–6, pp. 22-26, 1 May 1998.

[21] D.M. Mittleman *et al.*,"Recent advances in terahertz imaging," *Appl. Phys. B* **68**, pp. 1085–1094, 1999.

[22] C. Haber and D. Wirtz, "Magnetic tweezers for DNA micromanipulation," *Rev. Sci. Instrum.* vol. 71, no.12, pp. 4561-4570.

[23] J-H Son, "Terahertz electromagnetic interactions with biological matter and their applications," *J. Appl. Phys.* **105**, 102033, 2009.

[24] Philip C. Ashworth *et al.*,"Terahertz pulsed spectroscopy of freshly excised human breast cancer," *Optics Express*, vol. 17, issue 15, pp. 12444-12454, 2009.

[25] M. Woodward *et al.*,"Terahertz Pulse Imaging of ex vivo Basal Cell Carcinoma," *Jour. Investigative Dermatology*, **120**, 72–78, 2003.

[26] M. Wallace *et al.*, "Dermatological Surgery and Lasers Terahertz pulsed imaging of basal cell carcinoma ex vivo and in vivo," *British Jour. Dermatology*, **151**, 424-432, 2004.

[27] L. Yujiri *et al.*, "Passive millimeter wave imaging," *IEEE Microw. Mag*, vol. 4, no. 3, pp. 39-50.

[28] Cooper *et al.*, "THz Imaging Radar for Standoff Personnel Screening," *IEEE Trans. Terahertz Sc. Tech.*, vol. 1, no. 1, Sept. 2011.

[29] D.M. Sheen *et al.*,"Three-dimensional millimeter-Wave imaging for concealed weapon detection," vol. 49, no.9, Sept. 2001.

[30] R. Appleby and H.B. Wallace, "Standoff Detection of Weapons and Contraband in the 100 GHz to 1 THz Region," *IEEE Trans. Antennas Propag.*, vol. 55, no. 11, pp. 2944-2955, Nov. 2007.

[31] Hai-Bo Liu *et al.*, "Terahertz Spectroscopy and Imaging for Defense and Security Applications," *Proc. IEEE*, vol. 95, no.8, pp. 1514-1527.

[32] P. H. Bolivar, *et al.*, "Label-free probing of genes by time domain terahertz sensing," *Phys. Med. Biol.*, vol. 47, no. 21, pp. 3815–3821, Nov. 2002

[33] M. Brucherseifer *et al.*, "Label-free probing of the binding state of DNA by timedomain terahertz sensing," *Appl. Phys. Lett.*,**77**, 4049 –4051 (2000).

[34] M.A. Belkin *et al.*, "High-Temperature Operation of Terahertz Quantum Cascade Laser Sources," *IEEE Jour. Sel. Top. Quantum Elec.*, vol. 15, no. 3, May, June 2009.

[35] Virginia Diodes, Inc. http://www.vadiodes.com

[36] M.B. Johnston, "Plasmonics: Superfocusing of terahertz waves," *Nature Photonics* **1**, pp. 14 - 15, 2007.

[37] C.R. Williams *et al.*,"Highly confined guiding of terahertz surface plasmon polaritons on structured metal surfaces," *Nature Photonics* **2**, pp. 175 - 179, 2008.

[38] Hou-Tong Chen *et al.*, "Experimental demonstration of frequency-agile terahertz metamaterials," *Nature Photonics* **2**, pp. 295-298, 2008.

[39] Seongsin M. Kim *et al.*,"Biomedical terahertz imaging with a quantum cascade laser," *Appl. Phys. Lett.* **88**, 153903, 2006.

[40] M. Rodwell *et al.*, "A Future of Integrated Electronics: Moving Beyond Moore's Law and Off the Roadmap," *Proc. IEEE*, vol. 96, no.2, pp. 271-286, Feb. 2008.

[41] W. Knap *et al.*,"Field Effect Transistors for Terahertz Detection: Physics and First Imaging Applications," *Intl. Jour. Infrared Millimeter Waves.*, vol. 30, no. 12, pp. 1319-1337, 2009.

[42] D. Glaab *et al.*,"Terahertz heterodyne detection with silicon field-effect transistors," *Appl. Phys. Lett.*, **96**, 042106, 2010.

[43] G. Gonzalez, *Microwave Transistor Amplifiers*, 2nd Ed., Prentice Hall, 1996.

[44] T.H. Lee, *The Design of CMOS Radio-Frequency Integrated Circuits*, 2nd Ed., Cambridge University Press, 2003.

[45] Van Der Ziel, *Noise in Solid-State Device and Circuits*, Wiley, New York. 1986.

[46] M.S. Gupta, "Power Gain in Feedback Amplifiers, a Classic Revisited," *IEEE Trans. Microw. Theory Tech.*, vol. 40, no. 5, May 1992.

[47] O. Momeni *et al.*, "High Power Terahertz and Millimeter-Wave Oscillator Design: A Systematic Approach,"*IEEE J. Solid-State Circuits*, vol. 46, no. 3, pp. 583-597, Mar. 2011.

[48] Erik Öjefors *et al.*, "A 820GHz SiGe Chipset for Terahertz Active Imaging Applications," *ISSCC Dig. Tech. Paper*, pp. 224-225, Feb. 2011.

[49] R. Lai *et al.* "Sub 50nm InP HEMT device with f_{max} greater than 1 THz," *IEEE 2007 IEDM Conf. Dig.*, pp. 609-611, Dec. 2007.

[50] W.R. Deal *et al.*,"Demonstration of a S-MMIC LNA with 16-dB gain at 340-GHz," *IEEE 2007 CSIC Conf. Dig.*, pp. 1-4, Oct. 2007

[51] E. Bava *et al.*, "Analysis of Varactor Frequency Multipliers: Nonlinear Behavior and Hysteresis Phenomena," *IEEE Trans. Microw. Theory Tech.*, vol. 27, no. 2, Feb. 1979.

[52] M. Li *et al.*,"A fully distributed heterostructure-barrier varactor nonlinear transmission-line frequency multiplier and pulse sharpener," *IEEE Trans. Microw. Theory Tech.*, vol. 46, no. 12, Feb. 1998.

[53] "Frequency Multipliers for Millimeter and Submillimeter Wavelengths," *Proc. IEEE*, vol.80, no. 11, Nov. 1992.

[54] A. Babakhani *et al.* "A 77-GHz Phased-Array Transceiver With On-Chip Antennas in Silicon: Receiver and Antennas," *IEEE J. Solid-State Circuits*, vol. 41, no. 12, pp. 2795-2806, Dec. 2006.

[55] A. Hajimiri, "mm-Wave silicon ICs: An opportunity for holistic design,"*RFIC Symp. Dig.*, pp. 357-360, Jun. 2008.

[56] J. Wood *et al.*, "Rotary Traveling-Wave Oscillator Arrays: A New Clock Technology," *IEEE J. Solid-State Circuits*, vol. 36, No. 11, pp 1654-1665, Nov. 2001.

[57] K. Sengupta and A. Hajimiri, "Distributed Active Radiator for THz Signal Generation," *ISSCC Dig. Tech. Paper*, pp. 288-289, Feb. 2011.

[58] K. Sengupta and A. Hajimiri, "Sub-THz Beam-forming using Near-field Coupling of Distributed Active Radiator Arrays," *RFIC Symp. Dig.*, pp. 357-360, Jun. 2011.

[59] K. Sengupta and A. Hajimiri, "A 0.28 THz 4x4 power-generation and beamsteering array for THz applications," *ISSCC Dig. Tech. Paper*, pp. 256-258 , Feb. 2012.

[60] K. Sengupta and A. Hajimiri, "A 0.28 THz Power-Generation and Beam-Steering Array in CMOS based on Distributed Active Radiators," invited for special ISSCC issue in *IEEE J. Solid-State Circuits*, Dec. 2012.

[61] K. Sengupta and A. Hajimiri, "Distributed Active Radiator: Combining Power Generation and Radiation," in preparation *IEEE Trans. Microw. Theory Tech.*

[62] K. Sengupta and A. Hajimiri, "A Terahertz Imaging Receiver in 0.13μm SiGe BiCMOS Technology," *Intl. Conf. Infrared, mm, THz Waves (IRMMW-THz)*, June 2011.

[63] D.J. Seo, K. Sengupta and A. Hajimiri, "Distributed Active Radiator Arrays for Efficient Doubling, Filtering and Beam-forming," *Intl. Microwave Symp.*, June 2011.

[64] D. Huang *et al.*, "Terahertz CMOS Frequency Generator Using Linear Superposition Technique," *IEEE J. Solid-State Circuits*, pp. 2730-2738, Dec. 2008.

[65] D. Huang *et al.*, "324 GHz CMOS Frequency Generator Using Linear Superposition Technique," *ISSCC Dig. Tech. Papers*, pp. 476-477, Feb. 2008.

[66] E. Seok *et al.*, "A 410 GHz CMOS Push-Push Oscillator with an On-Chip Patch Antenna," *ISSCC Dig. Tech. Papers*, pp. 472-473, Feb. 2008.

[67] C.A. Balanis,*Antenna Theory: Analysis and Design*, John Wiley Sons, Inc., 3rd edition, New Jersey, 2005.

[68] J.D. Krauss,*Antennas*, Mcgraw-Hill, New York, 1988.

[69] S. Drabowitch *et al.*, *Modern Antennas*, Springer, 2nd edition, Netherlands, 2005.

[70] C.E. Baum,"General Properties of Antennas," *IEEE Trans. Electromag. Compat.*, vol. 44, no. 1, Feb 2002.

[71] S.A. Schelkunoff,"Theory of Antennas of Arbitrary Size and Shape," *Proc.of the IRE*, vol.29, no.9, pp. 493-521, 1941.

[72] D. B. Rutledge *et al.*, "Integrated-circuit antennas," *Infrared and Millimeter-Waves*, New York: Academic, 1983, pp. 1–90.

[73] N. G. Alexopoulos, P. B. Katehi, and D. B. Rutledge, "Substrate optimization for integrated circuit antennas," *IEEE Trans. Microw. Theory Tech.*, vol. 83, no. 7, pp. 550–557, Jul. 1983.

[74] H. Kogelnik, "Theory of dielectric waveguides," in *Integrated Optics*, T. Tamir, Ed. New York: Springer-Verlag, Ch. 2.

[75] G.M. Rebeiz, "Millimeter-wave and terahertz integrated circuit antennas," *Proc. of the IEEE* , vol.80, no.11, pp.1748-1770, Nov 1992.

[76] D. F. Filipovic, G. P. Gauthier, S. Raman, and G. M. Rebeiz, "Off axis properties of silicon and quartz dielectric lens antennas," *IEEE Trans. Antennas Propagat.*, vol. 45, no. 5, pp. 760–766, May 1997.

[77] A. Sommerfeld, *Über die Ausbreitung der Wellen in der drahtlosen Telegraphie*, *Ann.Physik* , vol.28, pp.665-737, 1909.

[78] A. Banos, *Dipole Radiation in the presence of conducting half-space*, Oxford: pergammon Press, 1966.

[79] R.E. Collin, *Field Theory of Guided Waves*, Wiley-IEEE Press, 2nd edition, 1990.

[80] R.O. King, "The electromagnetic field of a horizontal electric dipole in the presence of a three-layered region," *J. Appl. Phys.* **69**,7987, 1991.

[81] S.R.J. Brueck,"Radiation from a dipole embedded in a dielectric slab," *", IEEE Jour. on Selec. Top. Quantum Elec.*, vol. 6, no. 6, pp. 899-910, 2000.

[82] Kai Li and Yilong Lu, "Electromagnetic field generated by a horizontal electric dipole near the surface of a planar perfect conductor coated with a uniaxial layer ," *IEEE Trans. Antennas Propag.*, vol. 38, no. 10, pp. 1719–1723, 1990.

[83] Liang Li and Kai Li, "Radiation From a Vertical Electric Dipole in the Presence of a Three-Layered Region," *IEEE Trans. Antennas Propag.*, vol. 55, no. 12, pp. 3469-3475, 2007.

[84] A.K. Bhattacharyya, " Characteristics of Space and Surface Waves in a Multilayered Structure ," *IEEE Trans. Antennas Propag.*, vol. 38, no. 8, pp. 1231-1238, 1990.

[85] C.E. Tong and R. Blundell, "An annular slot antenna on a dielectric half-space," *IEEE Trans. Antennas Propag.*, vol. 42, no. 7, pp. 967-974, July 1994.

[86] D.R. Jackson and N.G. Alexopoulos, "Microstrip dipoles on electrically thick substrates," *Intl. Jour. Infrared Millimeter Waves.*, vol. 7, no. 1, pp. 1-26, 1986.

[87] P.B. Katehi and N.G. Alexopoulos, "On the Effect of Substrate Thickness and Permittivity on Printed Circuit Dipole Properties," *IEEE Trans. Antennas Propag.*, vol. AP-31, no. 1, pp. 34-39, Jan. 1983.

[88] N Uzunoglu, N.G. Alexopoulos and J Fikioris, "Radiation properties of microstrip dipoles," *IEEE Trans. Antennas Propag.*, vol. AP-27, no. 6, pp. 853-858, Nov. 1979.

[89] G. V. Eleftheriades and M.Qiu, "Efficiency and gain of slot antennas and arrays on thick dielectric substrates for millimeter-Wave applications: A unified approach, " *IEEE Trans. Antennas Propag.*, vol. 50, no. 8, pp. 1088-1098, Aug 2002.

[90] W.B. Dou and Z.L. Sun, "Surface wave fields and power in millimeter wave integrated dipole antennas ," *Intl. Jour. Infrared Millimeter Waves.*, vol. 18, no. 3, pp. 711-721, 1997.

[91] S.F. Mahmoud *et al.*, "Theoretical Considerations in the Optimization of Surface Waves on a Planar Structure," *IEEE Trans. Antennas Propag.*, vol. 52, no. 8, pp. 2057-2063, Aug 2004.

[92] D.M. Pozar, " Considerations for millimeter wave prointed antennas," *IEEE Trans. Antennas Propag.*, vol. AP-31, no. 5, pp. 740-747, 1983.

[93] D.M. Pozar,"Dipole and Slot Elements and Arrays on Semi-Infinite Substrates," *IEEE Trans. Antennas Propag.*, vol. AP-33, no. 6, pp. 600-607, 1985.

[94] J-G. Youk and L.P.B. Katehi, "Micromachined microstrip patch antenna with controlled mutual coupling and surface waves," *IEEE Trans. Antennas Propag.*, vol. 49, no. 9, pp. 1282-1289, Sep 2001.

[95] R.L. Rogers and D.P. Neikirk,"Radiation properties of slot and dipole elements on layered substrates," *Intl. Jour. Infrared Millimeter Waves.*, vol. 10, no. 6, pp. 697-728, 1989.

[96] W. Lukosz and R.E. Kunz,"Light emission by magnetic and electric dipoles close to a plane interface. I. Total radiated power," *J. Opt. Sot. Amer.*, vol.67, no. 12, pp. 1607-1615, Dec. 1977.

[97] W.Lukosz and R.E. Kunz,"Light emission by magnetic and electric dipoles close to a plane dielectric interface.II. Radiation patterns of perpendicular oriented dipoles," *J. Opt. Sot. Amer.*, vol.67, no. 12, pp. 1615-1619, Dec. 1977.

[98] W.Lukosz and R.E. Kunz,"Light emission by magnetic and electric dipoles close to a plane dielectric interface. III. Radiation patterns of dipoles with arbitrary orientation," *J. Opt. Sot. Amer.*, vol.69 , no. 11, pp. 1495-1503, 1979.

[99] W. Lnkosz and R. E. Kunz, " Fluorescencelifetime of magnetic and electric dipcdesnear a dielectric interface," *Opt.Comm.*, vol. 20, pp. 195-199, Feb. 1977.

[100] D.M.Pozar,*Microwave Engineering*, Wiley, 3rd edition, 2004.

[101] MoM-Based Electromagnetic Simulator (IE3D. http://www.mentor.com/electromagnetic-simulation/products/ie3d-ssd

[102] R.C. Hansen,*Phased Array Antennas*, Wiley, 2009.

[103] R.S. Elliott,"The Theory of Antenna Arrays", in *Microwave Scanning Antennas*, Vol II, R.C.Hansen, Ed., Academic Press, 1966 [Peninsula Publishing, 1985], Chapter 1.

[104] W.H. Von Aulock, "Properties of Phased Arrays," *Proc. IRE*, vol. 48, pp. 1715-1727, Oct. 1960.

[105] R. A. York and R. C. Compton, "Quasi-optical power combining using mutually synchronized oscillator array," *IEEE Trans. Microw. Theory Tech.*, vol. 39, no. 6, pp. 1000–1009, Jun. 1991.

[106] P. Liao and R. A. York, "A new phase-shifterless beam-scanning technique using array of coupled oscillators," *IEEE Trans. Microw. Theory Tech.*, vol. 41, no. 10, pp. 1810–1815, Oct. 1993.

[107] R. A. York and Z. B. Popovic´, *Active and Quasi-Optical Arrays for Solid-State Power Combining*. New York: Wiley, 1997.

[108] J. Hwang and N. Myung, "A new beam-scanning technique by controlling the coupling angle in a coupled oscillator array," *IEEE Microw. Guided Wave Lett.*, vol. 8, no. 5, pp. 191–193, May 1998.

[109] R. York and R. Compton, "Measurement and Modelling of radiative Coupling in Oscillator Arrays," *IEEE Tran. Microw. Theory Tech*, vol. 41, no.10, pp. 438-444, Mar. 1993.

[110] R. Adler, "A Study of Locking Phenomena in Oscillators," *Proc. IRE*, vol.34, no.2 , pp. 351-357, June 1946.

[111] K. Sengupta, T. K. Bhattacharyya, and H. Hashemi,"A Nonlinear Transient Analysis of Regenerative Frequency Dividers," *IEEE Trans. Circuits Syst. I, Reg. Papers*, vol. 54, no. 12, pp. 2646–2660, Dec. 2007.

[112] B. Cetinoneri *et al.*, "W-Band Amplifiers with 6-dB Noise Figure and Milliwatt-Level 170-200 GHz Doublers in 45nm CMOS," *IEEE Trans. Microw. Theory Tech.*,vol. 60, pp. 692-701, Mar. 2012.

[113] C-L Wu *et al.*, "I-Gate Body-Tied Silicon-on-Insulator MOSFETs with Improved High-Frequency Performance,"*IEEE Electron Device Lett.*, vol. 32, no. 4, pp. 443-445, Apr. 2011.

[114] O. Inac *et al.*, [U+0081]"Millimeter-Wave and THz Circuits in 45-nm SOI CMOS,"*Proc. CSICS*, Oct. 2011.

[115] Erickson Power Meter operating manual, Virginia Diodes Inc.,http://vadiodes.com/Erickson/PM4 Manual.pdf

[116] H. Wang and A. Hajimiri,"A Wideband CMOS Linear Digital Phase Rotator," *Proc. IEEE CICC*, Sep. 2007, pp. 671–674.

[117] Z. Chen and P. Heydari, "A 85-95.2 GHz transformer-based injection-locked frequency tripler in 65nm CMOS,"*IEEE International Microwave Symp. Dig.*, pp. 776-779, May 2010.

[118] P.H. Siegel and R.J. Dengler, "Terahertz heterodyne imaging part I: Introduction and Techniques," *Intl. Jour. Infrared Millimeter Waves.*, vol. 27, no. 4, pp. 465-477, Apr. 2006.

[119] P.H. Siegel and R.J. Dengler, "Terahertz heterodyne imaging part II: Instruments ," *Intl. Jour. Infrared Millimeter Waves.*, vol. 27, no. 5, pp. 631-655, May. 2006.

[120] E. Öjefors, U.R. Pfeiffer, "A 650GHz SiGe Receiver Front-End for Terahertz Imaging Arrays", *ISSCC Dig. Tech. Papers*, pp. 430-431, Feb. 2010.

[121] H. Sherry et al.," Lens-Integrated THz Imaging Arrays in 65nm CMOS Technologies," *RFIC Symp. Dig.*, pp. 1-4, Jun. 2011.

[122] F. Schuster et al.," A Broadband THz Imager in a Low-Cost CMOS Technology," *ISSCC Dig. Tech. Papers*, pp. 42-43, Feb 2011.

[123] U.R. Pfeiffer, *et al.*, "Terahertz Imaging with CMOS/BiCMOS Process Technologies," in *Proceedings of ESSRIC*, Sep 2010, pp. 52-60.

[124] J.W. May and G. Rebeiz, "Design and Characterization of W-Band SiGe RFICs for Passive Millimeter-Wave Imaging," *IEEE Tran. Microw. Theory Tech*, vol. 58, no.5, pp. 1420-1430, May. 2010.

[125] "OAD-7 Golay Detector Operating Manual," QMC Instruments Ltd.,Cardiff, U.K., Jan. 4, 2005.

[126] S. Eminoglu, M. Tanrikulu, and T. Akin, "A low-cost 128 x 128 uncooled infrared detector array in CMOS process," *J.Microelectromechan. Syst.*, vol. 17, no. 1, pp. 20–30, Feb. 2008.

[127] C. Middleton *et al.*, "Passive millimeter-wave focal plane array," in *Conf. Dig. 2004 Joint 29th Int. Conf. Infrared and Millimeter Waves*, 12th Int. Conf. Terahertz Electronics, 2004, pp. 745–746.

[128] J. L. Hesler and T. W. Crowe, "Responsivity and noise measurements of zero-bias schottky diode detectors," in Proc. 18rd Int. Symp. Space Terahertz Techn., Pasadena, CA, Mar. 2007, pp. 89–92. http://www.isstt2007.caltech.edu .

[129] Pyroelectric Detector, Product Sheet for Model SPH-62. Spectrum Detector Inc., Lake Oswego, www.spectrumdetector.com

[130] Erik Öjefors *et al.*, "0.65 THz Focal-Plane Array in a Quarter-Micron CMOS Process Technology," *IEEE J. Solid-State Circuits*, vol. 44, no. 7, pp. 1968-1976, Jul. 2009.

[131] S. R. Nassif, N. Mehta, Y. Cao, "A Resilience Roadmap," *IEEE DATE Dig. Tech. Papers*, 2011.

[132] K. Bernstein *et al.*, "High-performance CMOS variability in the 65-nm regime and beyond," *IBM Journal of Research and Development*, vol. 50, no 4.5, pp. 433-449, July 2006.

[133] A. Keerti and A.V.H. Pham, "RF Characterization of SiGe HBT Power Amplifiers," *IEEE Tran. Microw. Theory Tech*, vol. 55, no.2, pp. 207-214, Feb. 2007.

[134] K.Sengupta, K.Dasgupta, S.M.Bowers and A.Hajimiri,"On-chip Sensing and Actuation Methods for Integrated Self-healing mm-Wave CMOS Power Amplifier," *Intl. Microwave Symp.*, June 2012.

[135] Kaushik Sengupta, Steven Bowers, Arthur H.Chang and Ali Hajimiri, "Self-healing Power Amplifier: Methods and Apparatus," US Patent application number: 12/964,281, publication number: US 2011/0140772 A1, Dec. 9, 2010.

[136] Steven Bowers, Kaushik Sengupta and Ali Hajimiri, "Self Healing Technique for High Frequency Circuit," US Patent application number: 12/877,743 publication number: US 2011/0057712 A1, Sep. 8, 2010.

[137] S.M.Bowers, K.Sengupta, K.Dasgupta and A.Hajimiri, "A Fully- Integrated Self-Healing Power Amplifier," *RFIC Symp. Dig.*, June 2012.

[138] C.F. Lee and P.T. Mok, "A monolithic current-mode CMOS DC-DC converted with on-chip current sensing technique," *IEEE J.Solid-State Circuit*, vol. 39, no.1 pp. 3-14, Jan 2004.

[139] S.-S Lee and D.J. Allstot, "Electrothermal simulations of integrated circuits," *IEEE J.Solid-State Circuit*, vol. 28, no.12 pp. 1283-1293, Dec 1993.

[140] B.Razavi, *Design of Analog CMOS Integrated Circuits*, McGraw-Hill Science, 2000.

[141] A. Komijani and Ali Hajimiri, "A wideband 77 GHz, 17.5 dBm power amplifier in silicon," in *Proc. Custom Integr. Circuits. Conf.*, Sept. 2005, pp. 561-564.

[142] K. Sengupta and A. Hajimiri, "A Compact Self-similar Power Combining Topology," *Intl. Microw. Symp.*, pp. 244-247, May 2010.

[143] K.J. Russell, "Microwave Power Combining Techniques," *IEEE Trans. Microwave Theory Tech.*, vol. 27, no. 5, pp. 472-478, May. 1979.

[144] Van der Ziel, " Noise in Solid State Devices," Wiley, New York, 1986.

[145] I. Aoki, Scott D. Kee, David B. Rutledge and A. Hajimiri, "Distributed Active Transformer - A New Power-Combining and Impedance-Transformation Technique," *IEEE Trans. Microwave Theory Tech.*, vol. 50, no. 1, pp. 316-331, Jan. 2002.

[146] Toshihide Suzuki et al., "60 and 77 GHz Power Amplifiers in Standard 90nm CMOS," *ISSCC Dig. Tech. Papers*, pp. 562-563, Feb. 2008.

[147] Jhe-Jia Kuo et al., "A 71-76 GHz Chip Set for Wireless Communication in 65-nm CMOS Technology," *IEEE MTT-S Int. Dig.*, pp. 189-192, June 2009.

[148] Jeffrey Lee et al., "A 68-83 GHz Power Amplifier in 90 nm CMOS," *IEEE MTT-S Int. Dig.*, pp. 437-440, June 2009.

[149] N. Kurita and H. Kondoh, "60 GHz and 80 GHz Wide Band Power Amplifier MMICs in 90nm CMOS Technology," *RFIC Symp. Dig.*, pp. 39-42, June 2009.

[150] Y. Hamada et al, "A High Gain 77 GHz Power Amplifier Operating at 0.7 V Based on 90 nm CMOS Technology," *IEEE Microw. Wireless Compon. Lett.*, vol 19, no. 5, pp. 329-331, May 2009.

[151] B.Wicks, E.Skafidas, R. Evans, "A 75 – 95 GHz Wideband CMOS Power Amplifier," *Proc. European Microwave. IC. Conf.*, pp 554-557, Oct. 2008.